LBL-37825
UC-404

Lawrence Berkeley Laboratory
UNIVERSITY OF CALIFORNIA

Materials Sciences Division

NMR Investigations of Surfaces and Interfaces Using Spin-Polarized Xenon

H.C. Gaede
(Ph.D. Thesis)

July 1995

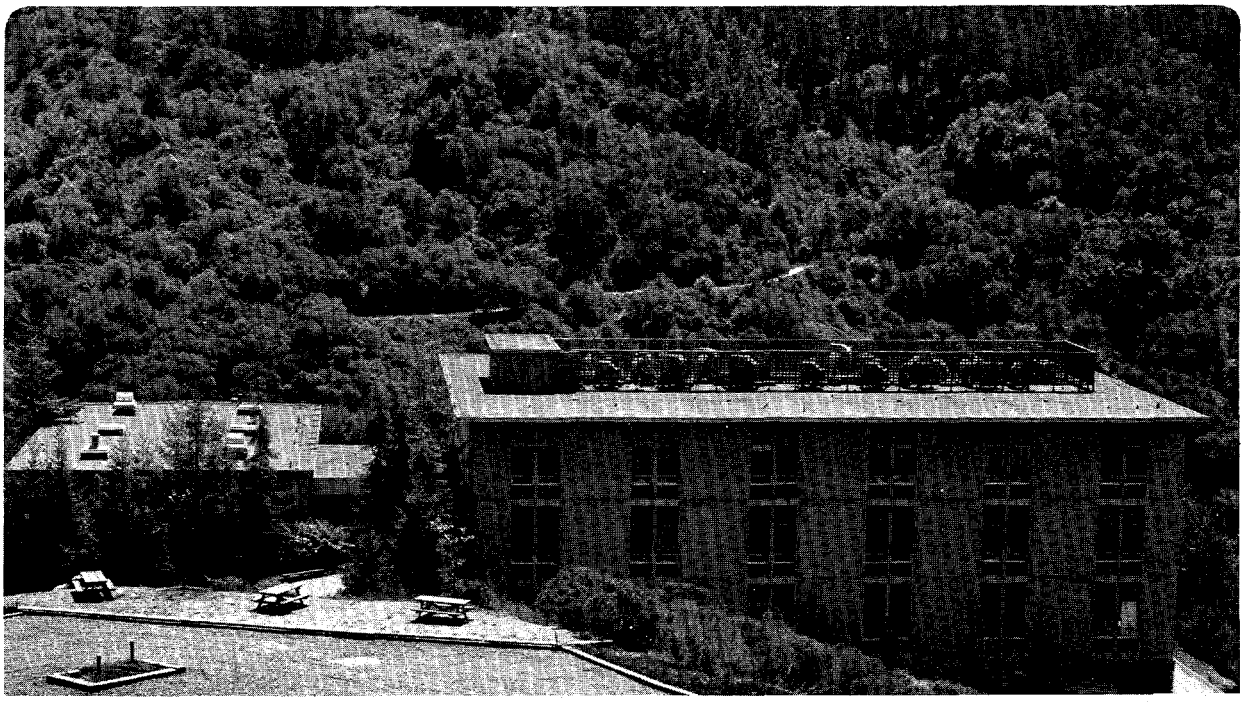

Prepared for the U.S. Department of Energy under Contract Number DE-AC03-76SF00098

LBL-37825
UC-404

NMR Investigations of Surfaces and Interfaces Using Spin-Polarized Xenon

Holly Caroline Gaede
Ph.D. Thesis

Department of Chemistry
University of California, Berkeley

and

Materials Sciences Division
Lawrence Berkeley Laboratory
University of California
Berkeley, CA 94720

July 1995

DISCLAIMER

This work was supported by the Director, Office of Energy Research, Office of Basic Energy Sciences, Materials Sciences Division, of the U.S. Department of Energy under Contract No. DE-AC03-76SF00098.

DISCLAIMER

Portions of this document may be illegible electronic image products. Images are produced from the best available original document.

NMR Investigations of Surfaces and Interfaces Using Spin-Polarized Xenon

by

Holly Caroline Gaede

B.S. (University of Delaware) 1991

A dissertation submitted in partial satisfaction of the

requirements for the degree of

Doctor of Philosophy

in

Physical Chemistry

in the

GRADUATE DIVISION

of the

UNIVERSITY of CALIFORNIA at BERKELEY

Committee in charge:

Professor Alexander Pines, Chair

Professor Gabor A. Somorjai

Professor Jeffrey A. Reimer

1995

NMR Investigations of Surfaces and Interfaces Using Spin-Polarized Xenon

by

Holly Caroline Gaede

Abstract

NMR Investigations of Surfaces and Interfaces using Spin-Polarized Xenon

by

Holly Caroline Gaede

Doctor of Philosophy in Physical Chemistry

University of California at Berkeley

Professor Alexander Pines, Chair

^{129}Xe NMR is potentially useful for the investigation of material surfaces, but has been limited to high surface area samples (hundreds of m^2/g) in which sufficient xenon can be loaded to achieve acceptable signal to noise ratios. In Chapter 2 conventional ^{129}Xe NMR is used to study a high surface area polymer, a catalyst, and a confined liquid crystal to determine the topology of these systems. Further information about the spatial proximity of different sites of the catalyst and liquid crystal systems is determined through two dimensional exchange NMR in Chapter 3.

Lower surface area systems (on the order of 10 m^2/g) may be investigated with spin-polarized xenon, which may be achieved through optical pumping and spin exchange. Optically polarized xenon can be up to 10^5 times more sensitive than thermally polarized xenon. In Chapter 4 highly polarized xenon is used to examine the surface of poly(acrylonitrile) and the formation of xenon clathrate hydrates.

An attractive use of polarized xenon is as a magnetization source in cross polarization experiments. Cross polarization from adsorbed polarized xenon may allow detection of surface nuclei with drastic enhancements. A non-selective low field thermal mixing technique is used to enhance the ^{13}C signal of CO_2 of xenon occluded in solid CO_2 by a factor of 200. High-field cross polarization from xenon to proton on the surface of high surface area polymers has enabled signal enhancements of ~1000. These

studies, together with investigations of the efficiency of the cross polarization process from polarized xenon, are discussed in Chapter 5.

Another use of polarized xenon is as an imaging contrast agent in systems that are not compatible with traditional contrast agents. The resolution attainable with this method is determined through images of structured phantoms in Chapter 6 . A demonstration of the ability of this method to detect material inhomogeneity is presented through images of silica aerogels. The thesis concludes with an outlook to the future of this technique. Additionally, appendices are included which detail the experimental approach.

Table of Contents

List of Figures

List of Symbols

Symbol	Description
B_0	Static magnetic field
B_1	Applied magnetic field
BHAT	Beam height adjustment tool
β	Inverse spin temperature
c	Speed of light
CP	Cross polarization
δ	Chemical shift
ΔE	Energy difference
e	Electron charge
FID	Free induction decay
FT	Fourier Transform
γ	Nuclear gyromagnetic ratio
$\mathcal{H}$	Hamiltonian
$\hbar$	Planck's constant
IR	Infrared
$\vec{I}$	Spin operator for the nucleus
$I_{\pm 1}$	Ladder spin operators
k	Boltzmann constants
$\vec{K}$	Spin operator
$\vec{\mu}$	Nuclear moment
μ_B	Bohr magneton
m	Eigenvalue of I_z
M	Magnetization

NMR ..... Nuclear magnetic resonance

n_a ..... Population of magnetic sub-level

N ..... Total nuclear spin population

p(n) ..... Fractional probability

r ..... Internuclear distance

rf ..... Radiofrequency

ρ ..... Density matrix

$\vec{S}$ ..... Spin operator for the electron

σ_{ex} ..... Spin exchange cross section

$\ddot{\Sigma}$ ..... Chemical shielding tensor

t ..... Time

T ..... Temperature

T_1 ..... Spin-lattice relaxation time

T_2 ..... Spin-Spin relaxation time

τ ..... Time

Θ ..... Coverage

ω ..... Angular frequency

ω_l ..... Larmor frequency

Z ..... Partition function

Acknowledgments

I first thank Alex Pines for insisting on excellence and for providing the tools to achieve it. I have tremendously enjoyed being a part of his research group and am proud to be a pinenut. I also thank Jeff Reimer for his active involvement with the pumping project. I always benefited from his suggestions, advice, and support.

I was fortunate to have joined a (mostly) working project, so for that I must thank those who went before me, especially Dan Raftery and Henry Long. The pumping project has been a parade of postdocs, but I have learned valuable lessons from each one, scientific and otherwise. I thank them all. Special thanks go out to Jay Shore, who taught me everything I know about double resonance, Tanja Pietraß, who made pumping fun, and Yi-Qiao Song, who gave the project a needed push. I wish the pumpers every continued success.

I am also thankful to the non-pumping postdocs of the group who were great resources of experience and information. I am especially grateful to Russell Larsen, who always had answers for my questions. I enjoyed learning with and from the graduate students with whom I shared the past four years, including (but not nearly limited to!) Geoff Barrall, Sheryl Gann, Marcia Ziegeweid, Susan DePaul, Mei Hong, Eyal Barash, ShuanHu Wang, Bin He, Yung-Ya Lin, Seth Bush, and David deGraw. It was fun being part of the soon-to-be disbanded "female gang" at ENCs. One of the best parts of this group is its cultural diversity. I will greatly miss the non-scientific discussions we enjoyed at the 4 p.m. Strada gatherings, which were greatly enriched by the multitude of perspectives.

I would be greatly remiss if I failed to acknowledge Dione Carmichael for keeping the group running. Everyone knows the group would fall to pieces without her. I am also

thankful to Tom Lawhead and Cathy Sigler in the glass shop for their expert glassblowing, and for dropping everything on several occasions to repair broken pumping glassware.

The government and its various agencies must be thanked for funding these endeavors.: The NSF has generously paid me and, more importantly, spared me from much of the Berkeley bureaucracy. This research was funded by the Director, Office of Basic Energy Sciences, Materials Sciences Division, of the U. S. Department of Energy under Contract No. DE-AC03-76SF00098.

Finally, my undying love and gratitude goes out to those who kept me sane through the madness that is graduate school: my family, my friend Sue Onuschak, and my husband James Batteas.

Chapter 1

Introduction

1.1 A Historical Perspective

In the fifty years that have intervened since Purcell, Torrey, and Pound[1] observed the proton resonance in paraffin and Bloch, Hansen, and Packard[2] independently observed the proton resonance in water, Nuclear Magnetic Resonance (NMR) Spectroscopy has blossomed as an investigative tool. The discovery of the Chemical Shift by Proctor and Yu[3] in 1950 provided chemists with a convenient, non-destructive method for structural determination of chemical compounds. The advent of Fourier Transform and multi-dimensional NMR methods extended the applicability of NMR to protein structure determination and dynamical studies. And, with the invention of Nuclear Magnetic Resonance Imaging, the use of NMR has even spread to the medical community! Few techniques have seen such widespread acceptance and utility. Excitingly, new methods that improve both resolution and sensitivity are continually being developed, allowing the application of NMR to even more systems and samples.

The focus of this work is Optically Polarized ^{129}Xe NMR Spectroscopy, a method which enables the investigation of insensitive systems typically inaccessible to NMR, such as surfaces. The remainder of Chapter 1 outlines the basic theory of NMR. Chapter 2 introduces the field of Xenon NMR with some examples of conventional Xenon NMR. Chapter 3 introduces two-dimensional NMR techniques, with particular examples of xenon exchange in two systems. Chapter 4 presents the theory of Optical Pumping and Spin Exchange with examples of optically polarized Xenon NMR. Chapter 5 describes the application of polarization transfer techniques, particularly as they are applied to spin-polarized xenon. In Chapter 6, the application of polarized xenon as an NMR imaging contrast agent is described. Chapter 7 concludes with a look to the future of this technique. Finally, appendices are included which describe the experimental approach in great detail.

1.2 Classical Description of NMR

1.2.1 Nuclear Magnetic Moments

NMR can be performed on any nucleus with a magnetic moment, or non-zero spin. When a nucleus with $I \neq 0$ is placed in a static magnetic field B_0 along the z direction, the nuclei are distributed among the available energy levels according to the Boltzmann law. The small excess of nuclei with their moments in the direction of B_0 gives the sample a permanent macroscopic magnetic moment M_0 in the z direction. In the magnetic field, a torque is exerted on the nuclear magnetic moment which tends to align it perpendicular to the field. The net result of this torque is a rotation of the direction of the magnetic moment at a characteristic frequency, called the Larmor frequency, ω_l, where $\omega_l = \gamma B_o$, (1.1)

and γ is the gyromagnetic ratio of the nuclei. Due to the randomness of the precession, there is no net magnetic moment in the xy plane.

1.2.2 The Bloch Equations

In an NMR spectrometer, the nuclei are subjected to an additional weak magnetic field, B_1, perpendicular to B_0. We can regard the oscillating field as composed of two vectors rotating in opposite directions.

$$B_{cw} = B_1(\hat{i}\cos\omega t + \hat{j}\sin\omega t) \tag{1.2}$$

$$B_{ccw} = B_1(\hat{i}\cos\omega t - \hat{j}\sin\omega t) \tag{1.3}$$

One component rotates in the same sense as the precession of the moment, and the other in the opposite sense; the resonance counter rotating may be neglected. We will assume only the field B_{cw} contributes and will call it B_1. Such a field also exerts a torque on the magnetic moment of the nuclei. The magnetic moment of the nuclei will precess along the effective magnetic field which is the vector sum of the static magnetic field B_0 and B_1. The interaction thereby causes the appearance of a magnetic moment rotating in the xy plane. If the frequency of the B_1 field is varied until it equals the Larmor frequency of the nuclei, transitions between the magnetic energy levels are induced. The transitions tend to decrease the magnitude of M_z, since most transitions occur to the less populated energy level, anti-parallel to M_z. The Boltzmann distribution of the spins is restored through interaction with the fluctuating magnetic field of neighboring nuclei. The process occurs with the time constant T_1, and is called the *longitudinal* or *spin lattice* relaxation time. The x,y magnetization will also return to its equilibrium value (zero) due to interactions with fluctuating local fields. This process is characterized by T_2, and is called *spin-spin* or *transverse relaxation* time. T_1 and T_2 are described by the following equations.

$$\frac{dM_x}{dt} = -\frac{M_x}{T_2} \tag{1.4}$$

$$\frac{dM_y}{dt} = -\frac{M_y}{T_2} \tag{1.5}$$

$$\frac{dM_z}{dt} = -\frac{M_z - M_o}{T_1} \tag{1.6}$$

These equations describe what happens when B_1 is turned off. The Bloch equations below describe the changing components of the magnetization along the axes when B_1 is present.

$$\frac{dM_x}{dt} = \gamma M_y B_o + \gamma M_z B_1 \sin\omega t - \frac{M_x}{T_2} \tag{1.7}$$

$$\frac{dM_y}{dt} = -\gamma M_x B_o + \gamma M_z B_1 \cos\omega t - \frac{M_y}{T_2} \tag{1.8}$$

$$\frac{dM_z}{dt} = -\gamma M_x B_1 \sin\omega t - \gamma M_y B_1 \cos\omega t - \frac{M_z - M_o}{T_1} \tag{1.9}$$

These equations take a simpler form when using a coordinate system in which the z-axis remains parallel with B_0, but the x and y axes rotate about the z-axis with a frequency ω. This coordinate system is called the rotating frame.

$$x_{rot} = x_{lab}\cos\omega t + y_{lab}\sin\omega t \tag{1.10}$$

$$y_{rot} = y_{lab}\cos\omega t - x_{lab}\sin\omega t \tag{1.11}$$

$$z_{rot} = z_{lab} \tag{1.12}$$

The field is exactly cancelled when $\omega = \omega_l$, and appears as a much smaller field $b_o = B_o + \frac{\omega}{\gamma}$, when $\omega \neq \omega_l$. The rotating frame Bloch equations are

$$\frac{dM_x}{dt} = \gamma M_y b_o - \frac{M_x}{T_2} \tag{1.13}$$

$$\frac{dM_y}{dt} = -\gamma(M_z B_1 - M_x b_o) - \frac{M_y}{T_2} \tag{1.14}$$

$$\frac{dM_z}{dt} = -\gamma M_y B_1 - \frac{M_z - M_o}{T_1} \tag{1.15}$$

These equations show the basic behavior of nuclei interacting with magnetic fields; however, a quantum mechanical description is needed to fully understand complex systems.

1.2.3 Spin Temperature

A system with a set of energies E_a and E_b that is at thermal equilibrium with a lattice of temperature T occupies the levels with the probabilities p(Ea), which are given by

$$\frac{p(E_a)}{p(E_b)} = \frac{\exp\left(\frac{-E_a}{kT}\right)}{\exp\left(\frac{-E_b}{kT}\right)}. \tag{1.16}$$

$$\text{Since } \sum_{E_a} p(E_a) = 1 \tag{1.17}$$

$$\frac{p(E_a)}{p(E_b)} = \frac{\exp\left(\frac{-E_a}{kT}\right)}{\sum_c \exp\left(\frac{-E_c}{kT}\right)} = \frac{\exp\left(\frac{-E_a}{kT}\right)}{Z} \tag{1.18}$$

$$\text{where } Z = \sum_c \exp\left(\frac{-E_c}{kT}\right) \tag{1.19}$$

Any system that obeys (1.18) is described by a spin temperature T. For a spin-1/2 system in a magnetic field B_0 at thermal equilibrium with the lattice, the population can be described by the Boltzmann distribution

$$\frac{n_b}{n_a} = \exp\left(\frac{-\Delta E}{kT}\right) = \exp\left(\frac{-\gamma\hbar B_o}{kT}\right), \tag{1.20}$$

where n_a and n_b are the populations of energy levels E_a and E_b, respectively and T is the temperature of the lattice. The population difference between these sublevels, i.e. the polarization, can be described by

$$\frac{\Delta n}{N} \approx \frac{\gamma\hbar B_o}{2kT} \tag{1.21}$$

If a non-thermal polarization is established (for example through an rf pulse), the system can no longer be described by the lattice temperature. However, the new polarization may be defined in equation (1.21) with a new spin temperature. In this way the spin temperature can be used to describe the polarization of a system.

1.3 Quantum Mechanical Description of NMR

1.3.1 The Angular Momentum Operators

$\vec{I}$ is the angular momentum vector operator (I_x, I_y, I_z). I_x, I_y, and I_z for spin-$^1/_2$ nuclei are the Pauli spin matrices given below.

$$I_x = \frac{\hbar}{2}\begin{pmatrix} 0 & 1 \\ 1 & 0 \end{pmatrix} \tag{1.22}$$

$$I_y = \frac{\hbar}{2}\begin{pmatrix} 0 & -i \\ i & 0 \end{pmatrix} \tag{1.23}$$

$$I_z = \frac{\hbar}{2}\begin{pmatrix} 1 & 0 \\ 0 & -1 \end{pmatrix} \tag{1.24}$$

It is sometimes convenient to use the following operators instead of the Cartesian spin operators.

$$I_0 = I_z \tag{1.25}$$

$$I_{\pm 1} = \pm \tfrac{1}{\sqrt{2}}(I_x \pm iI_y) \tag{1.26}$$

$I_{\pm 1}$ are called ladder operators because they connect states differing in their quantum number by one. Important relations that hold are

$$\vec{I}^2|\psi\rangle = I(I+1)|\psi\rangle \tag{1.27}$$

$$I_z|\psi\rangle = m|\psi\rangle \tag{1.28}$$

$$[I_p, I_q] = iI_r \tag{1.29}$$

where p, q, r = x, y, z or cyclic permutations.

$$\vec{I}_{\pm 1}|\psi\rangle = \tfrac{\pm 1}{\sqrt{2}}\sqrt{(I \mp m)(I \pm m + 1)}|\psi\rangle \tag{1.30}$$

1.3.2 The Zeeman Interaction

The Zeeman Hamiltonian describes the interaction of the nuclear magnetic dipoles with the externally applied magnetic field. It is written as

$$\mathcal{H}_Z = -\gamma\hbar B_o I_z \tag{1.31}$$

The eigenvalues of this Hamiltonian are multiples of the eigenvalues of I_z, so the allowed energies are $E_m = -m\gamma\hbar B_o$, with m = I, I-1, ..., -(I-1), -I

The Zeeman interaction is usually the largest interaction in the nuclear spin Hamiltonian.

1.3.3 Radiofrequency Hamiltonian

As described earlier, transitions can be excited between the levels by irradiating the nuclei with an oscillating magnetic field perpendicular to the static field. The interaction between the rf field and spin I is given by

$$\mathcal{H}_{rf} = -\hbar\gamma B_1 \cos(\omega t + \phi) I_x^{lab} \tag{1.32}$$

The oscillating field has frequency ω, phase ϕ, with intensity B_1. This Hamiltonian may also be expressed in the rotating frame:

$$\begin{aligned}\mathcal{H}_{rf} &= -\frac{\hbar\gamma B_1}{2}[I_x\cos\phi - I_y\sin\phi] \\ &-\frac{\hbar\gamma B_1}{2}[\cos(2\omega t+\phi)I_x - \sin(2\omega t+\phi)I_y] \\ &\approx -\frac{\hbar\gamma B_1}{2}[I_x\cos\phi - I_y\sin\phi]\end{aligned} \tag{1.33}$$

In the rotating frame, transverse magnetization appears to oscillate at zero frequency and 2ω. These 2ω terms effectively average out to zero since they are oscillating twice as fast, i.e. in the opposite direction of the rotating frame.

1.3.4 Chemical Shift Interaction

The chemical shift is the most important interaction discussed in this thesis, and is covered in great detail in Chapter 2. Chemical shifts arise from the interaction of the magnetic moment of the nucleus and magnetic field. The form of the Hamiltonian is

$$\mathcal{H} = -\gamma\vec{B}_o \cdot \vec{\vec{\Sigma}} \cdot \vec{I} \tag{1.34}$$

where $\vec{\vec{\Sigma}}$ is the chemical shielding tensor.

1.3.5 Dipolar Interaction

The dipolar coupling is the through-space direct magnetic dipolar interaction between pairs of nuclei. The general form of the Hamiltonian is

$$\mathcal{H}_D = \frac{\gamma_1\gamma_2\hbar^2}{r_{12}^3}\left\{\vec{I}_1\cdot\vec{I}_2 - \frac{3(\vec{I}_1\cdot\vec{r})(\vec{I}_2\cdot\vec{r})}{r_{12}^2}\right\} \tag{1.35}$$

Alternatively, this Hamiltonian can be expressed as

$$\mathcal{H}_D = \frac{\gamma_1\gamma_2\hbar^2}{r_{12}^3}\{A+B+C+D+E+F\} \tag{1.36}$$

where

$$A = I_{1z}I_{2z}(1-3\cos^2\theta) \tag{1.37}$$

$$B = -\tfrac{1}{4}(\vec{I}_{1+}\vec{I}_{2-} + \vec{I}_{1-}\vec{I}_{2+})(1-3\cos^2\theta) \tag{1.38}$$

$$C = -\tfrac{3}{2}(\vec{I}_{1z}\vec{I}_{2+} + \vec{I}_{1+}\vec{I}_{2z})\sin\theta\cos\theta\exp(-i\phi) \tag{1.39}$$

$$D = -\tfrac{3}{2}(\vec{I}_{1z}\vec{I}_{2-} + \vec{I}_{1-}\vec{I}_{2z})\sin\theta\cos\theta\exp(i\phi) \tag{1.40}$$

$$E = -\tfrac{3}{4}\vec{I}_{1+}\vec{I}_{2+}\sin^2\theta\exp(-2i\phi) \tag{1.41}$$

$$F = -\tfrac{3}{4}\vec{I}_{1-}\vec{I}_{2-}\sin^2\theta\exp(2i\phi) \tag{1.42}$$

In high field, the Hamiltonian is truncated by the static field.

$$\mathcal{H}_D = \frac{\gamma_1\gamma_2\hbar^2}{r_{12}^3}\{A+B\} \tag{1.43}$$

$$\mathcal{H}_D^0 = \frac{\gamma_1\gamma_2\hbar^2}{4r_{12}^3}(1-3\cos^2\theta)(3\vec{I}_{1z}\vec{I}_{2z} - \vec{I}_1\cdot\vec{I}_2) \tag{1.44}$$

There are many other interaction important to NMR, particularly the quadrupolar and scalar interactions. They are not relevant to this thesis, however, and will not be discussed here.

1.3.6 Thermodynamic Treatment

If a spin system is at thermal equilibrium with a lattice of temperature T, the n states of the total system will be occupied with fractional probabilities p_n given by the Boltzmann factor.

$$p_n = \frac{\exp\left(\frac{-E_n}{kT}\right)}{Z}, \tag{1.45}$$

where the partition function is given by $Z = \sum_n \exp\left(\frac{-E_n}{kT}\right)$. (1.46)

Quantities such as the average energy $\overline{E}$ and magnetization $\overline{M}_z$ are given by

$$\overline{E} = \sum_n p_n E_n \tag{1.47}$$

$$\overline{M}_z = \sum_n \gamma\hbar\langle n|I_z|n\rangle p_n \tag{1.48}$$

The Schrödinger equation need not be evaluated because (1.47) and (1.48) can be expressed as traces. For example, the partition function may be denoted as

$$Z = \sum_n \exp\left(\frac{-E_n}{kT}\right) = \langle n|\exp\left(\frac{-\mathcal{H}}{kT}\right)|n\rangle = \mathrm{Tr}\left\{\exp\left(\frac{-\mathcal{H}}{kT}\right)\right\}. \tag{1.49}$$

The exponential may be expanded into a power series:

$$Z = \mathrm{Tr}\left\{\exp\left(\frac{-\mathcal{H}}{kT}\right)\right\} = \mathrm{Tr}\left\{1 - \frac{\mathcal{H}}{kT} + \frac{1}{2}\frac{\mathcal{H}^2}{k^2T^2} - \ldots\right\}. \tag{1.50}$$

In the high temperature approximation, only the leading terms are kept.

$$Z = (2I+1)^N + \frac{1}{2k^2T^2}\mathrm{Tr}\{\mathcal{H}^2\}, \tag{1.51}$$

for an N spin system. In a similar manner, the energy may be calculated.

$$\bar{E} = -\frac{C(B_o^2 + B_L^2)}{T} \tag{1.52}$$

$$\text{where } C = \frac{N\gamma^2\hbar^2 I(I+1)}{3k} \tag{1.53}$$

is the Curie constant, and B_L is the local field , which is defined by

$$CB_L = \frac{\mathrm{Tr}\{\mathcal{H}_d^2\}}{k(2I+1)^N} \tag{1.54}$$

Calculating the trace of (1.52) gives $B_L^2 = \gamma^2\hbar^2 I(I+1)\sum_j \left(\frac{1}{r_{jk}}\right)^6$ (1.55)

The magnetization is

$$\vec{M} = \frac{C\vec{B}_o}{T} \tag{1.56}$$

This approach will be used in Chapter 5 to discuss cross polarization.

1.3.7 The Density Matrix

The density matrix formalism is useful for the following the evolution of a spin system under a set of pulses and delays. A wave function can be expanded in the orthonormal basis set $|n\rangle$ with complex coefficients c_n.

$$|\psi\rangle = \sum_n c_n |n\rangle \tag{1.57}$$

This state evolves under a time-independent Hamiltonian according to the Schrödinger equation. $i\hbar\frac{d\psi(t)}{dt} = \mathcal{H}\psi(t)$ (1.58)

$$\psi(t) = \exp\left(\frac{-i\mathcal{H}t}{\hbar}\right)\psi(0) \tag{1.59}$$

The same information can be presented in a density matrix formalism

$$\rho(t) = \psi(t)\psi^{\dagger}(t) = \sum_{n,m} c_n(t)c^{\dagger}{}_m(t)|n\rangle\langle m| \tag{1.60}$$

$$\rho(t) = \exp\left(\frac{-i\mathrm{H}t}{\hbar}\right)\psi(0)\,\psi^{\dagger}(0)\exp\left(\frac{i\mathrm{H}t}{\hbar}\right) = \exp\left(\frac{-i\mathrm{H}t}{\hbar}\right)\rho(0)\exp\left(\frac{i\mathrm{H}t}{\hbar}\right) \tag{1.61}$$

The initial density matrix at thermal equilibrium in a high magnetic field is

$$\rho_{eq} = \frac{1}{\mathrm{Z}}\exp\left(\frac{-\mathcal{H}_{\mathrm{Z}}}{k\mathrm{T}}\right), \tag{1.62}$$

Substituting in (1.51) into (1.62) and expanding the exponential gives:

$$\rho_{eq} \approx \frac{1}{(2\mathrm{I}+1)}\left(\hat{1} + \frac{-\mathcal{H}_{\mathrm{Z}}}{k\mathrm{T}}\right), \tag{1.63}$$

where 1 is a (2I+1 x 2I+1) matrix. (In NMR the magnitude of $\mathrm{H} \ll k\mathrm{T}$, so the series is truncated after the second term.) The constant term is ignored in calculations of time evolution. The equilibrium density matrix can be written as $\rho_{eq} = \kappa \mathrm{I}_z$, (1.64)

where $\kappa = \dfrac{\hbar\gamma \mathrm{B}_o}{(2\mathrm{I}+1)^{\mathrm{N}} k\mathrm{T}}$. (1.65)

The time-dependence of the density matrix under a time-dependent Hamiltonian is given by the Liouville equation $\dfrac{d\rho}{dt} = -\dfrac{i}{\hbar}[\mathcal{H}(t), \rho(t)]$ (1.66)

This gives $\rho(t) = \exp\left(\dfrac{-i\mathcal{H}t}{\hbar}\right)\rho\exp\left(\dfrac{i\mathcal{H}t}{\hbar}\right)$ (1.67)

1.3.8 Rotations

NMR relies heavily on rotations. One application of rotations is to change between frames of reference, which is not relevant to this thesis. Rotations are also involved in the manipulation of magnetic moments. In general,

$$e^{-i\theta I_p} I_q e^{i\theta I_p} = I_q \cos\theta + I_r \sin\theta \tag{1.68}$$

and

$$e^{-i\theta I_p} I_r e^{i\theta I_p} = I_r \cos\theta - I_q \sin\theta \tag{1.69}$$

where p, q, r = x, y, z or cyclic permutations.

1.4 The One Pulse Experiment

The basic Fourier transform NMR experiment begins with the application of a $\pi/2$ pulse to an equilibrium spin system. (A $\pi/2$ pulse is an rf field applied for such a time that $\frac{\pi}{2} = \gamma B_1 t$.) Recall that the equilibrium density matrix is given by $, \rho_{eq} = \kappa I_z$ (1.70)

where κ is defined in (1.65). Application of a $(\pi/2)_y$ pulse gives, according to (1.69)

$$\rho(0) = \kappa I_x \tag{1.71}$$

The evolution is given by (1.67) $\rho(t) = \beta e^{-i\mathcal{H}t/\hbar} I_x e^{i\mathcal{H}t/\hbar}$ (1.72)

The signal detected during time t for a spectrometer operating in quadrature is given by

$$S(t) = \varepsilon \mathrm{Tr}\{\rho(t) I_+\} \tag{1.73}$$

where ε is a factor accounting for signal amplitude and depends on experimental considerations. Expanding in the eigenbasis of H gives

$$S(t) = \varepsilon \sum_i \langle i | e^{-i\mathcal{H}t/\hbar} \beta I_x e^{i\mathcal{H}t/\hbar} I_+ | i \rangle. \tag{1.74}$$

Inserting $\sum_j |j\rangle\langle j| = 1$ and operating on the states gives

$$S(t) = \varepsilon\beta \sum_i \sum_j e^{-iE_i t/\hbar} e^{iE_j t/\hbar} [I_x]_{ij} [I_+]_{ji}. \tag{1.75}$$

$$S(t) = \frac{1}{2}\varepsilon\beta \sum_i \sum_j e^{-i\omega_{ij}t} \left| [I_+]_{ji} \right|^2 \tag{1.76}$$

Fourier transform gives $S(t) = \varepsilon\beta \sum_i \sum_j \delta(\omega - \omega_{ij}) \left| [I_+]_{ji} \right|^2$ (1.77)

with lines occurring at frequencies ω_{ij} and intensities $\left| [I_+]_{ji} \right|^2$. This clearly shows why only single quantum transitions can be detected in the FID, since the operator I_+ connects states differing by 1 in their Zeeman quantum number.

This is only a brief glimpse at the beauty of NMR. Much more detail is available in the many books on the subject.[4-10] Also the theses of Dan Raftery[11] and Henry Long[12] address Xenon and Optical Pumping NMR and complement the information contained in the rest of this thesis.

Chapter 2

Xenon in NMR

2.1 Introduction

Xenon may seem an odd nucleus on which to perform NMR investigations. As a noble gas, it is rather inert, forming only a few compounds, primarily with fluorine and oxygen [13-18]. However, atomic xenon possesses characteristics which make it an ideal probe of its environment. It is *precisely* xenon's inertness that enables NMR spectroscopists to insert either NMR-active isotope of xenon, ^{129}Xe (I=1/2) or ^{131}Xe (I=3/2), into systems of interest and monitor xenon NMR parameters with little concern that xenon is perturbing the sample. Additionally, xenon has good adsorption properties, which facilitate studies of surfaces. Finally, xenon has a very large chemical shift range which is very diagnostic of its environment. This chapter continues with a detailed discussion of the chemical shift interaction, which is the parameter most often measured in xenon NMR investigations. This is followed by with a brief background of xenon in NMR. The chapter concludes with detailed

discussions of xenon NMR investigations of representative systems including a polymer, catalysts, and a confined liquid crystal.

2.2 Chemical Shift Interaction

2.2.1 Introduction

Chemical shifts arise because of the simultaneous interaction of a nucleus with an electron and the electron with an applied field $\vec{B}_o$. The chemical shift Hamiltonian will therefore have the form $\mathcal{H}_{cs} = \vec{I} \cdot \vec{\Sigma} \cdot \vec{B}_o$, where $\vec{I}$ is the spin operator for the nucleus and $\vec{\Sigma}$ is the chemical shielding tensor. The electron-nucleus interaction has the following effects. In an applied field $\vec{B}_o$, the Larmor precession of the electronic charge around the nucleus is equivalent to an electric current producing a magnetic field $\vec{B}_d$ at the nucleus which adds to the applied field and is proportional to it. Additionally, the applied field polarizes the electronic shells. The distorted shells produce a magnetic field $\vec{B}_p$ at the nucleus which is also proportional to $\vec{B}_o$. The total field seen by the nucleus is $\vec{B} = \vec{B}_o + \vec{B}_d + \vec{B}_p$ or $\vec{B} = \vec{B}_o(1-\sigma)$ where σ is the relative resonance frequency shift independent of the magnitude of $\vec{B}_o$.

This shift depends on the distribution of electrons around the nucleus and has different values in different chemical compounds, hence the name chemical shift. The chemical shift is sensitive to the geometry and identity of the atoms surrounding a particular nucleus and is one of the most chemically diagnostic tools of NMR. The values of chemical shifts for ^{1}H, ^{13}C, and ^{15}N are often used in an entirely empirical way for structure determination in organic molecules. This treatment will discuss the theoretical attempts to understand this nuclear interaction, from an isolated xenon atom to the condensed phase.

2.2.2 Theory

Given a molecule containing N nuclear moments and n electrons, its Hamiltonian in the presence of an applied magnetic field $\vec{B}_o$ can be written, given that m is the mass of the electron, $\vec{p}_k$ is the momentum of the k_{th} electron, e is the charge of the electron, c is the speed of light, μ_β is the Bohr magneton, $\vec{S}_k$ is the spin operator of the electron, and V is the electrostatic energy of the system. Furthermore, in this equation $\vec{A}_k^o = \frac{1}{2}\left(\vec{B}_o \times \vec{r}_k\right)$ is the value of the vector potential of the external field $\vec{B}_o$ at the position r_k of the kth electron. $\vec{A}_k^q = \frac{\left(\vec{\mu}_q \times \vec{r}_{qk}\right)}{r_{qk}^3}$ is the value of the vector potential produced by the nuclear moment $\vec{\mu}_q = \gamma\hbar\vec{I}$ situated at R_q. The origin of r_k and R_q is left unspecified, but clearly all physical results must be independent of the choice of origin.

$$\mathcal{H} - \mathrm{V} = \frac{1}{2\mathrm{m}}\sum_{\mathrm{k=1}}^{\mathrm{n}}\left(\vec{\mathrm{p}}_\mathrm{k} + \frac{\mathrm{e}}{\mathrm{c}}\vec{\mathrm{A}}_\mathrm{k}^\circ + \frac{\mathrm{e}}{\mathrm{c}}\sum_{\mathrm{q=1}}^{\mathrm{N}}\vec{\mathrm{A}}_\mathrm{k}^\mathrm{q}\right)^2 + 2\mu_\beta\sum_{\mathrm{k=1}}^{\mathrm{n}}\vec{\mathrm{S}}_\mathrm{k}\cdot\nabla\times\vec{\mathrm{A}}_\mathrm{k}^\circ + 2\mu_\beta\sum_{\mathrm{k=1}}^{\mathrm{n}}\sum_{\mathrm{q=1}}^{\mathrm{N}}\vec{\mathrm{S}}_\mathrm{k}\cdot\nabla\times\vec{\mathrm{A}}_\mathrm{k}^\mathrm{q} \qquad (2.1)$$

The magnetic couplings between electrons, the Zeeman couplings of the nuclei with the applied field, and the dipolar couplings have been omitted since they are unimportant in this consideration.[4]

An expansion of (2.1) gives the following terms:

$$\mathcal{H} - \mathrm{V} - \mathrm{T} - \mathrm{D} = (\mathrm{Z_L} + \mathrm{Z_S}) + (\mathrm{O_1} + \mathrm{S_1} + \mathrm{S_2}) + (\mathrm{O_2} + \mathrm{O_3}) \qquad (2.2)$$

where the kinetic energy of the electrons is given by $T = \frac{1}{2m}\sum_{k=1}^{n}\vec{p}_k^2$, (2.3)

and the diamagnetic energy of the electrons by $D = \frac{e^2}{mc^2}\sum_{k=1}^{n}\left(\vec{A}_k^o\right)^2$. (2.4)

The Zeeman energy of the electrons in the applied field is given by $\mathrm{Z_S} = 2\mu_\beta\cdot\vec{\mathrm{S}}$. (2.5)

The orbital Zeeman energy of the electrons is given by

$$Z_L = \frac{e}{2mc}\left(\vec{p}_k \cdot \vec{A}_k^o + \vec{A}_k^o \cdot \vec{p}_k\right) = \mu_\beta \vec{B}_o \cdot \vec{L} \tag{2.6}$$

$O_1+S_1+S_2$ is the sum of magnetic couplings between the n electrons and N nuclei.

$$O_1 = 2\mu_\beta \sum_{k=1}^{n}\sum_{q=1}^{N} \frac{\vec{\mu}_k \cdot \vec{l}_{qk}}{r_{qk}^3} \text{ with } \hbar \vec{l}_{qk} = \vec{r}_{qk} \times \vec{p}_{qk} \tag{2.7}$$

$$S_1 = 2\mu_\beta \sum_{k=1}^{n}\sum_{q=1}^{N} \frac{1}{r_{qk}^3}\left\{\frac{3(\vec{S}_k \cdot \vec{r}_{qk})(\vec{\mu}_q \cdot \vec{r}_{qk}) - (\vec{S}_k \cdot \vec{\mu}_q)}{r_{qk}^2}\right\} \tag{2.8}$$

$$S_2 = \frac{16\pi}{3}\mu_\beta \sum_{k=1}^{n}\sum_{q=1}^{N} (\vec{S}_k \cdot \vec{\mu}_q)\delta(\vec{r}_{qk}) \tag{2.9}$$

O_2 represents the coupling between the nuclear moments and the magnetic fields of the currents induced by the Larmor precession in the applied field. O_3 represents the coupling between different nuclear moments.

$$O_2 = \frac{e^2}{2mc^2}\sum_{k=1}^{n}\sum_{q=1}^{N} \frac{(\vec{B}_o \times \vec{r}_{qk}) \cdot (\vec{\mu}_q \times \vec{r}_{qk})}{r_{qk}^3} \tag{2.10}$$

$$O_3 = \frac{e^2}{2mc^2}\sum_{kqq'} \frac{(\vec{\mu}_q \times \vec{r}_{qk}) \cdot (\vec{\mu}_{q'} \times \vec{r}_{q'k})}{r_{qk}^3 r_{q'k}^3} \tag{2.11}$$

The chemical shift corresponds to small modifications of energy of the system and is calculated by perturbation theory. The ground state is given by $|0\lambda>$, where λ refers to the orientations of the molecule. $|0>$ refers to the other degrees of freedom (electronic, vibrational). In a diamagnetic substance the only terms on the right hand side of (2.2) for which the expectation value $<0\lambda| \cdots |0\lambda>$ does not vanish are O_2 and O_3.

Isolated Atom

As required for the chemical shift interaction, the term O_2 is bilinear in $\vec{\mu}$ and $\vec{B}_o$. Its expectation value may be expressed, selecting the particular nuclear moment N_o for which the shift is being calculated as the origin, so $\vec{r}_{ok}$ becomes $\vec{r}_k$:

$$\langle O_2 \rangle = \frac{e^2}{2mc^2} \langle 0\lambda | \sum_k \frac{(\vec{B}_o \times \vec{r}_k) \cdot (\vec{\mu} \times \vec{r}_k)}{r_k^3} | 0\lambda \rangle \tag{2.12}$$

Equation (2.12) may be rewritten in the functional form for the chemical shift given in the introduction: $\langle O_2 \rangle = \vec{\mu} \cdot \vec{\vec{\Sigma}}_d \cdot \vec{B}_o$, where d represents diamagnetism. (2.13)

The chemical shift tensor $\vec{\vec{\Sigma}}_d$ may be decomposed into a traceless part Σ_d' and a scalar part Σ_d''.

$$\Sigma_d'^{pq} = \frac{-e^2}{2mc^2} \langle 0\lambda | \sum_k \frac{x_k^p x_k^q}{r_k^3} - \frac{1}{3} \frac{\delta^{pq}}{r_k} | 0\lambda \rangle \tag{2.14}$$

$$\Sigma_d''^{pq} = \sigma_d \delta_{pq}, \tag{2.15}$$

$$\text{where } \sigma_d = \frac{e^2}{3mc^2} \langle 0\lambda | \sum_k \frac{1}{r_k} | 0\lambda \rangle \tag{2.16}$$

Since the scalar part is independent of the rotational state of the molecule, the λ index may be dropped.

$$\sigma_d = \frac{e^2}{3mc^2} \langle 0 | \sum_k \frac{1}{r_k} | 0 \rangle \tag{2.17}$$

This expression is called Lamb's formula[19] and represents the entire chemical shift of a closed-shell atom. It may be calculated explicitly if the electron distribution is known. The resonance for an isolated xenon atom has been estimated to be 5642 ppm more shielded than the bare xenon nucleus.[20]

Isolated Molecule

In a molecular system there exists, in addition to the Lamb term, another contribution to shielding which normally opposes the diamagnetic effect and is therefore known as the paramagnetic term.[21,22] The paramagnetic contribution to shielding may be estimated by finding the way in which the electronic wave functions are modified by the magnetic field. When a field is applied new energy terms appear, and the electronic wave functions calculated in the absence of the field are no longer eigenfunctions of the electronic Hamiltonian. The new electronic wave functions may be obtained as linear combinations of the eigenfunctions of the original Hamiltonian. The field can be considered to mix excited electronic states into the ground state wave function. Physically, the paramagnetic term corresponds to the fact that the presence of attracting centers from several different massive nuclei prevents a simple circular diamagnetic circulation of the electrons about any one nucleus.

An energy term Δ, bilinear in μ and Bo, can be obtained through second order perturbation theory by combining a term A of (2) which is proportional to $\vec{\mu}$ and a term B proportional to $\vec{B}_o$ such that:

$$\Delta = \sum_n \cdot \frac{\langle 0|A|n\rangle\langle n|B|0\rangle}{E_o - E_n} + c.c., \text{ where } \lambda \text{ has been omitted for simplicity.} \qquad (2.18)$$

A and B must both have non-vanishing matrix elements between the ground state and an excited electronic state. There are three terms proportional to $\vec{\mu}$ (O_1, S_1, S_2) and two terms proportional to $\vec{B}_o$ (Z_L and Z_S). There are six possible cases to be used in the perturbation theory approach. However, it can be shown that (O_1, Z_L) is the only combination which differs from zero.

The lack of contribution from Z_S arises because the ground state is an eigenstate of S=0. Therefore, $Z_S|0\rangle = 0$. Hence, B is necessarily Z_L.

An operator C may be defined $C \equiv \sum' \frac{|n\rangle\langle n|}{E_o - E_n}$ (2.19)

If it is assumed that the energies are independent of spin, then C is purely an orbital operator. If the energy levels do not depend on the orientation of a molecule then C is invariant under rotation. The contribution from S_1 and S_2 together can be represented:

$$\Delta = \langle 0|(S_1 + S_2)CZ_L|0\rangle + c.c. \tag{2.20}$$

Since $|0\rangle$ is an eigenstate of S=0 , and S_1 and S_2 are linear combinations of the components of electronic spin, the above expression for Δ vanishes.

The only non-zero expression for Δ is given with $A = O_1$, and $B = Z_L$ as follows, with the orientation index reintroduced and the origin chosen such that it corresponds to the nuclear moment $\vec{\mu}$ considered:

$$\begin{aligned}\Delta &= 2\mu_\beta^2 \sum_{n,k}' \frac{\langle 0\lambda|\vec{L}\cdot\vec{B}_o|n\rangle\langle n|\frac{\vec{\mu}\cdot\vec{l}_k}{r_k^3}|0\lambda\rangle}{E_o - E_n} + c.c. \\ &= 2\mu_\beta^2 \sum_k \langle 0\lambda|(\vec{L}\cdot\vec{B}_o)C\left(\frac{\vec{\mu}\cdot\vec{l}_k}{r_k^3}\right)|0\lambda\rangle + c.c.\end{aligned} \tag{2.21}$$

This can be expressed $\Delta = \vec{\mu}\cdot\vec{\vec{\Sigma}}_p\cdot\vec{B}_o$ (2.22)

Again, $\vec{\vec{\Sigma}}_p$ can be reduced to a traceless, Σ_p', and scalar Σ_p'' part.

$$\Sigma_p'^{mn} = 2\mu_\beta^2 \sum_k \langle 0\lambda|\sum_k \vec{L}^m C\frac{l_k^n}{r_k^3} - \frac{1}{3}\vec{L}C\frac{\vec{l}_k}{r_k^3}|0\lambda\rangle + c.c. \tag{2.23}$$

$$\Sigma_p''^{mn} = \sigma_p\delta_{mn} \tag{2.24}$$

$$\text{where } \sigma_p = \frac{2\mu_\beta^2}{3}\langle 0|\frac{\vec{L}\cdot C\cdot\vec{l}_k + \vec{l}_k\cdot C\cdot\vec{L}}{r_k^3}|0\rangle \tag{2.25}$$

Calculating the paramagnetic chemical shift is difficult because a knowledge of the excited states is required. Furthermore, while the choice of origin can not affect what is observed, it will affect the magnitudes of $\ddot{\Sigma}_d$ and $\ddot{\Sigma}_p$. This is important because $\ddot{\Sigma}_d$ and $\ddot{\Sigma}_p$ tend to be very large and opposite in sign, making the errors in chemical shift calculation very high. These terms are very closely related and the separation is largely superficial.

Gas

The characteristic value of nuclear shielding for an isolated molecule is modified by interactions between pairs of molecules and multiple interactions. A virial-type expansion may be made for a dilute gas[23]

$$\sigma(T,\rho) = \sigma_0(T) + \sigma_1(T)\rho + \sigma_2(T)\rho^2 + \sigma_3(T)\rho^3 + \ldots \qquad (2.26)$$

$\sigma_0(T)$ represents the chemical shielding parameter for an isolated molecule. The temperature dependence arises from averaging of intramolecular motions. $\sigma_1(T)$ may be called the second virial coefficient of the nuclear shielding, in analogy to the second virial coefficient of the normal expansion PV/RT. For xenon,[23]

$$\sigma_1(298.15\ \text{K}) = -0.548 \pm 0.004\ \text{ppm/amagat} \qquad (2.27)$$

Studies of gaseous ^1H, ^{19}F, and ^{129}Xe systems show that the chemical shift dependence is essentially linear with density up to about 100 amagats. (An amagat is the density of an ideal gas at 0°C and 1 atm, 2.689×10^{19} atoms/cm^3.) This implies that at these densities the interactions that are important are binary, and only the $\sigma_0(T)$ and $\sigma_1(T)$ terms contribute.

A functional form for $\sigma_1(T)$ may be obtained by taking the statistical average over the radial distribution function.

$$\sigma_1(T) = \int_0^\infty 4\Pi R^2 dR[\sigma(R) - \sigma(\infty)]\exp\left[\frac{-V(R)}{kT}\right], \quad (2.28)$$

where $\sigma(\infty)$ is the shielding function for the isolated atom, $\sigma(R)$ is the shielding function for a dimer, and V(R) is the two-body interaction potential. The observed sign for $\sigma_1(T)$ is the same for all systems. At a fixed magnetic field the resonance frequency is found to increase with increasing density at a given temperature. Intermolecular interactions have a net deshielding effect on the nucleus in the molecule.[24]

That is, $\left[\sigma(T,\rho) - \sigma_0(T)\right] < 0 \quad (2.29)$

Since $\sigma_1(T)$ involves binary interactions, it can be related to the shielding function for linear diatomic molecules and calculated with a knowledge of spin-rotation coupling as in the previous section.[25] In the case of Xe gas it has been shown that exchange interactions are the source of the chemical shift.[26] The net paramagnetic shielding due to exchange interaction between xenon atoms is

$$\sigma_p = \frac{16(S_{\sigma\sigma} + S_{\pi\pi})^2 \sin^2\theta}{\mu_\beta^2 \Delta E}\left\langle\left(\frac{1}{r}\right)^3\right\rangle, \quad (2.30)$$

where $S_{\sigma\sigma} = -\langle a_{z,0}|b_{z,0}\rangle$ and $S_{\pi\pi} = \langle a_{y,0}|b_{y,0}\rangle$ with $a_{z,0}$ and $a_{y,0}$ as 5p orbitals of atom A, and $b_{z,0}$ and $b_{y,0}$ as the corresponding orbitals of atom B. $\left\langle\left(\frac{1}{r}\right)^3\right\rangle$ is the expectation value for a Xe 5p orbital and $\Delta E = \langle E_0 - E_n\rangle_{av}$.

At higher densities many-body interactions become important. Higher order terms in density are generally opposite in sign to $\sigma_1(T)\rho$. That is, although the shifts are generally still deshielding, the shift is somewhat smaller than would be expected from two-body terms alone.[27] For xenon,

$\sigma_2(298.15) = -1.69 \pm 0.2 \times 10^{-4}$ ppm/amagat^2 (2.31)

and $\sigma_3(298.15) = 1.63 \pm 0.1 \times 10^{-6}$ ppm/amagat^3 (2.32)

From gas to liquid shifts, an effective term can be obtained which contains the many-body terms.

$$\sigma_{1\text{effective}}(T) = \frac{[\sigma(T,\ell) - \sigma(T,\text{vapor})]}{[\rho_\ell - \rho_{\text{vapor}}]T} \tag{2.33}$$

Gas in Pores

The chemical shift data for the high surface area polymer is interpreted using the established empirical guidelines for xenon NMR.[28] The chemical shift can be represented be written as the following function of density (ρ) when the adsorption sites are weak:

$$\sigma = \sigma_0(T,r) + \sigma_1(T)\rho + \cdots \tag{2.34}$$

Here the chemical shift in the limit of low density, σ_0, is explicitly written as a function of temperature (T) and pore size (r). Although the exact functional dependence is not known, σ_0 is empirically found to be inversely dependent on pore size from zeolite studies.[28]

Adsorbing Gas

Raftery et al.[29] have shown that the shielding due to xenon interactions at the surface can be written in a virial-type expansion

$$\sigma_s(T,\theta) = \sigma_0 + \sigma_1\theta\, P_s(T) + \sigma_2(\theta\, P_s(T))^2 + \sigma_3(\theta\, P_s(T))^3 + \ldots \tag{2.35}$$

where σ are the virial coefficients of the nuclear shielding[23] and θ is the coverage in monolayers. The first term in the expansion (σ_0) is due to interactions between xenon and the surface. The second term results from xenon-xenon interactions at or

near the surface. The slope of the shift as a function of coverage results from the binary xenon-xenon collisions at or near the surface.[29]

Exchanging Systems

In cases where atomic xenon has been inserted into a material as a spin spy, the possibility that xenon is sampling more than one environment must be considered. If this is indeed the case, the spectra will depend on the rate of exchange between the distinct sites and the chemical shift of xenon at each site. In cases of slow exchange between two sites, $\tau\delta\omega >> 1$, where τ is the lifetime of xenon at each site and $\delta\omega$ is the chemical shift difference between the two sites, the observed spectrum will be the superposition of the sub-spectra of xenon at each site. In cases of slow exchange, rate information may be derived from two-dimensional NMR. This will be addressed in Chapter 3. In cases of fast exchange, where $\tau\delta\omega << 1$, the observed spectrum will consist of a resonance at the time-weighted average chemical shift of the two sites. NMR spectroscopy determines the time-averaged shift

$$\langle\delta\rangle = \frac{t_A}{t_A + t_B}\cdot\delta_A + \frac{t_B}{t_A + t_B}\cdot\delta_B \qquad (2.36)$$

where δ_A and δ_B are the shifts of xenon when it resides at the two sites, respectively. t_A and t_B are the average lifetimes of xenon at the two sites. Whatever the nature of the two sites, the chemical shift of the two sites must be measurably different from each other, and there must be rapid exchange between the two sites on the NMR time scale. If the system is at dynamic equilibrium then the lifetime factors can be replaced by probabilities of occupancy:

$$\langle\delta\rangle = \frac{N_A}{N}\cdot\delta_A + \frac{N - N_A}{N}\cdot\delta_B \qquad (2.37)$$

where N_A is the equilibrium population of site A and N is the total amount of xenon in the two sites.

Condensed Phases

In the solid state the shift will be dependent on the orientation of the molecule in the magnetic field. The complete three-dimensional shielding of the nucleus may be determined, giving much more information about structure and bonding than can be obtained in liquid-state or solution studies. The three dimensional nature of shielding may be expressed:

$$B_s(i) = \vec{\mu} \cdot \vec{\vec{\Sigma}} \cdot \vec{B}_0. \tag{2.38}$$

$\vec{\vec{\Sigma}}$ is a 3x3 matrix, or a second-rank tensor. $\vec{\vec{\Sigma}}$ may be converted to diagonal form with the components on the axis labeled σ_{11}, σ_{22}, and σ_{33}. The important quantities $\Delta\sigma$, shielding anisotropy, and η, asymmetry factor may be defined as follows:

$$\Delta\sigma = \sigma_{33} - \frac{1}{2}(\sigma_{11} + \sigma_{22}) \tag{2.39}$$

$$\eta = \frac{\sigma_{22} - \sigma_{11}}{\sigma_{33} - \sigma_{Ave}} \tag{2.40}$$

In solids, two extreme types of samples may be studied: single crystals and powdered samples. Semi-crystalline polymers is an example of a material which falls in between the two extremes. In a single crystal each nuclei has a fixed orientation to the magnetic field. A single sharp line will be observed for each magnetically unique orientation of a particular nucleus to the field direction. For a powdered sample, signals will be observed for every random orientation of the crystallite, resulting in a very broad signal with singularities at the principal elements of the shielding tensor. Powder patterns for axially symmetric molecules have only two singularities, with

$\sigma_{11} = \sigma_{22} = \sigma_{\perp}$ and $\sigma_{33} = \sigma_{\parallel}$. Since in liquid samples the molecules are rapidly tumbling, what is observed is the isotropic or average value of the chemical shift.

$$\sigma_{Ave} = \frac{1}{3}(\sigma_{11} + \sigma_{22} + \sigma_{33}) \tag{2.41}$$

2.3 Xenon in NMR

As described in the previous sections, the chemical shift of xenon is sensitive to the dynamics and the local structure surrounding the xenon atom. Because of this sensitivity and the favorable NMR properties of ^{129}Xe (natural abundance 26.8% and magnetic moment -0.77247 μ_N) atomic xenon is a convenient NMR probe. NMR investigations of Xe began in the early eighties, pioneered by Fraissard in zeolites,[30] Ripmeester in anisotropic environments,[31] and Williamson in liquids.[32] The use of xenon as a spin spy has spread to many samples of technological interest in the nearly fifteen years that have followed since the introduction of xenon to the NMR community. Figure 2.1 shows the large chemical shift range of xenon, with several representative samples indicated. Several excellent reviews have been written recently which outline the use of ^{129}Xe NMR for the investigation of zeolites,[33] confined spaces,[34] microporous solids,[35] materials research,[36] and isotropic and anisotropic liquids.[37] This chapter continues with examples of Xenon NMR carried out in the Pines lab. The systems studied include a microporous polymer, a catalyst, and a microconfined liquid crystal.

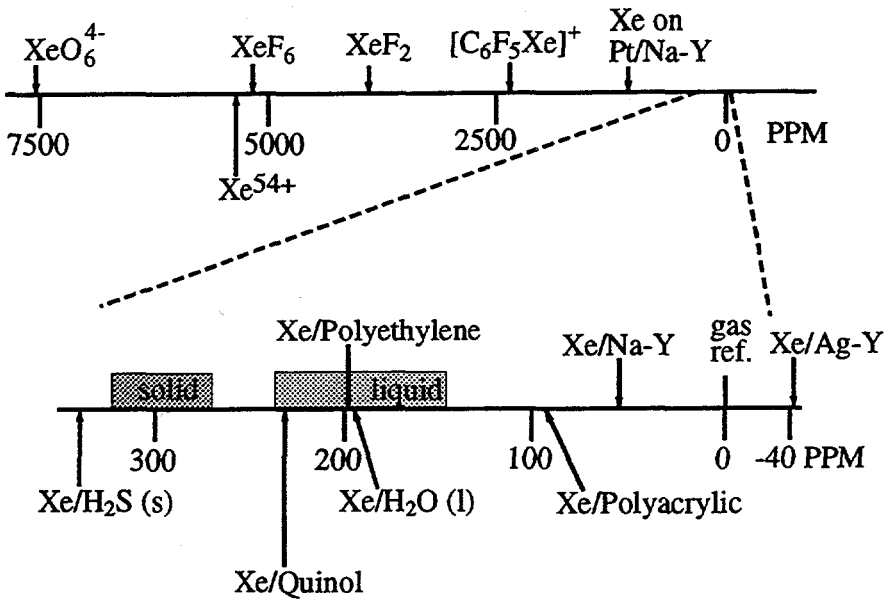

Figure 2.1 Xenon chemical shift range. Dilute xenon gas is used as the reference at 0 ppm. The chemical shift of xenon adsorbed on or absorbed in several representative materials are indicated.

2.4 Xenon NMR Studies of Polytriarylcarbinol

2.4.1 Background

The search for new polymer topologies and architectures is driven by the need to improve the thermal and mechanical properties of known polymers, as well as the desire to develop completely new polymer chemistry. Often the physical and chemical properties of these new structures prove to be superior to those of existing materials. Hypercrosslinked poly(triarylcarbinol),[38-40] comprised of a framework of rigid rod connecting units held together by trifunctional tiepoints (Figure 2.2), represent such a

new topology and give rise to a number of unusual properties, such as microporosity and swellability. Due to the nature of the crosslinking process, a structural framework possessing a high number of internal voids is formed. This results in surface areas as high as 1000 m^2/g, which compares with other high surface area materials like carbon black.

In addition, these hypercrosslinked polymers, unlike other highly crosslinked materials, swell 200-300 % in most organic solvents. This unique combination of high surface area and controlled cavities of molecular dimensions yields promising new materials for use as catalysts supports and adsorbents.

The unusual swelling behavior is poorly understood and, since they neither dissolve nor melt, very little information is available concerning their detailed pore structure and morphology. One explanation, model 1, involves the formation of highly crosslinked particles having a high microporosity during the early polymerization stages that give rise to the observed high surface area. These micro-gel particles (with diameter estimated to be 100-300 Å) crosslink later in the polymerization reaction via more or less loose crosslinks, rendering the resulting material insoluble. These loose crosslinks would, according to this model, allow for some flexibility between the crosslinked particles and account for the observed high swellability.[40]

Alternatively, in model 2, the swelling can be explained based on the assumption that

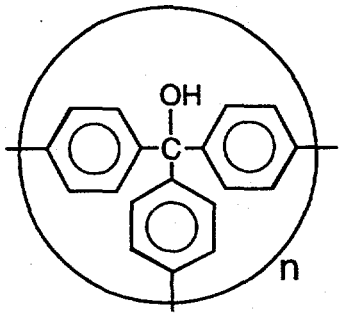

Figure 2.2 The structure of poly(triarylcarbinol)

solvent-filled micropores formed during polymerization contract when the polymer is dried and the solvent evaporates. Since the network structure is rigid, the pores cannot collapse completely, thus imposing a very high strain on the dry network. To release this strain, the crosslinked polymers swell, even in thermodynamically bad solvents, in order to regain the conformation they had during the crosslinking reaction, i.e., it is thermodynamically favorable to fill the pores with solvent and thus release strain. Such a model was proposed by Davenkov et al.[41] to explain the swelling of polystyrene-based hypercrosslinked materials. The main difference between these two models is that the first assumes loosely crosslinked microporous particles, implying two different pore sizes or distributions (micropores within the particles and larger pores between them), whereas the latter implies a homogeneous polymer with a uniform pore size distribution throughout the polymer.

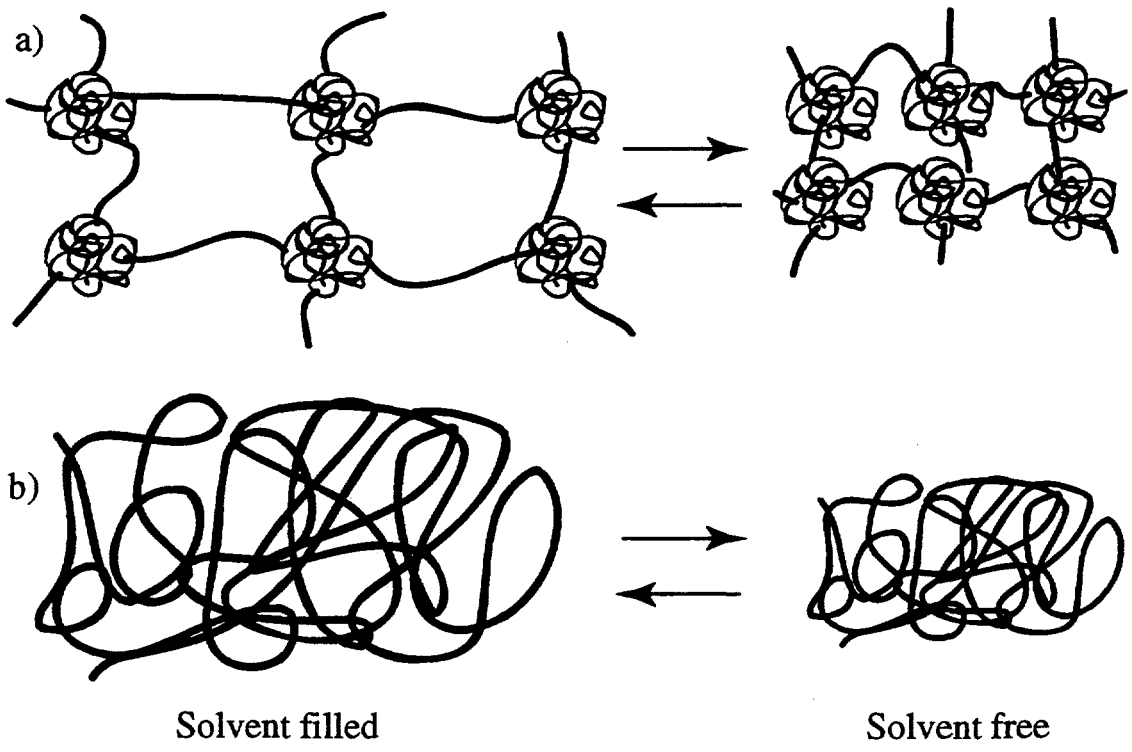

Figure 2.3 Two models developed to explain porosity and swelling of poly(triarylcarbinol) polymers. (a) Model 1 and (b) Model 2. For details see text.

^{129}Xe NMR spectroscopy is a very useful method for characterizing polymers.[42-45] Xenon NMR has been used to characterize polymer blends,[45-47] amorphous polymer regions,[42] nascent polymerized material on catalyst surfaces,[44] cross-linked elastomers,[43] and, with optical polarization, polymer surfaces.[29] Reported values of the chemical shifts of xenon dissolved in polymers range from 190 to 213 ppm at pressures from 2 – 12 atm[48] and temperatures from ambient to 363 K. There has been no reported data on the pressure dependence of the chemical shift in polymers. Most workers use very high pressures (8–12 atm) to obtain sufficient xenon dissolved in the polymer to give an observable xenon NMR signal. In phase separated polymer blends two signals can be seen if the domain size in the blend is larger than about 0.6 μm (and the chemical shift of xenon is different in the two components of the blend).[45]

In the present study, ^{129}Xe NMR spectroscopy was used to determine the microstructure of the system in the context of the two models discussed above.

2.4.2 Experimental

A powdered sample of poly(triarylcarbinol) was evacuated at $<10^{-5}$ torr while heating at 313 - 333 K for several hours before loading with xenon (80% enriched, Isotec Inc.) at a pressure of 375 torr (confirmed by comparison with chemical shift pressure data in Figure 2.4). Measurements on the sealed sample were made either on a Nalorac spectrometer operating at 51.4 MHz or a Chemagnetics based spectrometer operating at 49.5 MHz. Typical acquisition parameters were a sweepwidth of 40 kHz, recycle delay of 15 s (at ambient temperature) or 60 s (at low temperatures), using 6 μs 90° pulses. All spectra were referenced to low pressure xenon gas. The variable pressure measurements, as well as the experiments performed by introducing the

xenon directly at low temperatures, used the optically pumped xenon NMR spectrometer to be described in detail in Chapter 4. The essential features relevant to these studies is that the sample in a dewared region of the probe is connected through glassware to a xenon reservoir outside the magnet. Such a setup allows *in situ* variable pressure measurements to be performed rapidly and accurately over a range of temperatures. Temperature measurements were accurate to ± 2 K with a precision of ± 0.5 K, and chemical shift measurements have a precision of ± 1 ppm (slightly less at low temperatures due to broader lines and lower signal to noise).

2.4.3 Results

The surface area of the polymer was measured by the BET method to be 834 m^2/g, as reported earlier.[40] The xenon chemical shift as a function of pressure measured at

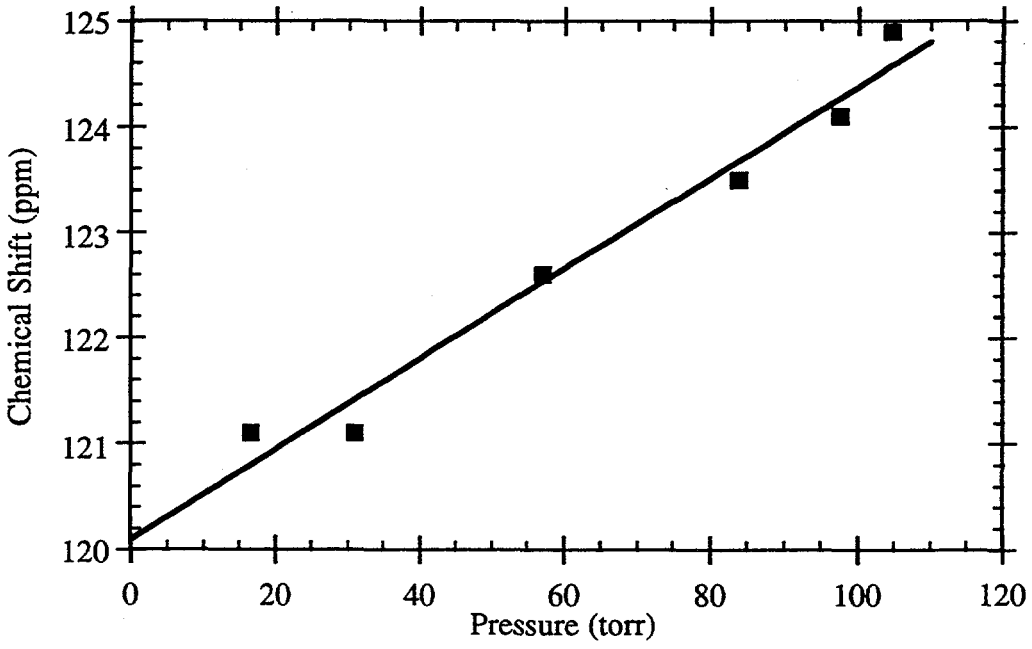

Figure 2.4 Chemical Shift vs. Pressure of xenon in poly(triarylcarbinol) at room temperature.

room temperature is shown in Figure 2.4. The intercept is 120.1 ppm and the slope is 0.04 ppm/torr (30 ppm/atm) and is linear in the range shown, but at higher pressures, above about 600 torr, it begins to show some negative curvature in contrast to the strictly linear behavior observed in zeolites with monovalent cations. Some negative curvature is seen in pure xenon studies at high densities (> 100 amagats).[49]

In the sealed sample with 375 torr of xenon the line width was measured to be 300 Hz. The chemical shift was measured to be 135 ppm at room temperature. At low temperature the chemical shift increases only slightly, reaching 149 ppm at 95 K, the lowest temperature that can be obtained on the variable temperature xenon probe. The line width increases sharply below 143 K and is equal to approximately 4.5 kHz at 95 K (Figure 2.5). Here the motion of the xenon is clearly being reduced, and the xenon is no longer rapidly averaging over many pores. There was no discernible change in the line width when using high power proton decoupling; therefore the line width is presumably dominated by a chemical shift distribution due to the different sites and pore sizes within the polymer.

The sealed samples in all of the above experiments were slowly cooled in the probe (typical cooling rates were ≈0.3 K/s below 173 K) and allowed to equilibrate for 5 - 10 minutes at the final temperature. Experiments were also performed on this polymers using a setup designed for optical pumping experiments, where the experimental procedure is quite different (described in Chapter 4). The important points of the procedure as it relates to these experiments is that the sample is allowed to equilibrate at the desired temperature and then an aliquot of xenon is added. For optically polarized xenon, the spectra are acquired a few seconds later (within the T_1 of the xenon) after the pressure had stabilized.

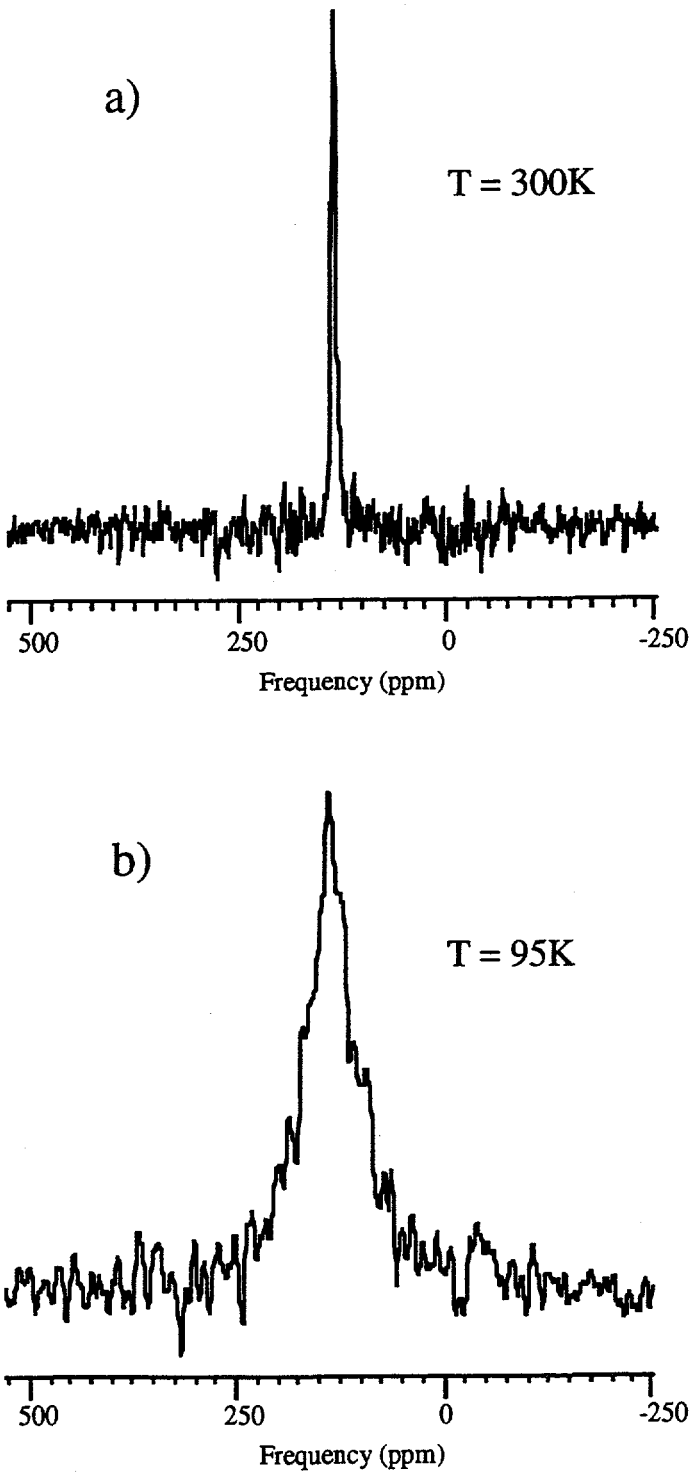

Figure 2.5 ^{129}Xe NMR spectra of rigid polymer in a sealed ampoule with 375 torr overpressure at a) toom temperature and b) low temperature .

The question of equilibration in such experiments is a problematic one; however, for some low surface area materials (< 20 m^2/g, nonporous) it has been reasonably well established.[12] For a microporous material, however, a few seconds is clearly insufficient, especially at low temperatures. Migration times may be on the order of hours in carbon black. However, the xenon establishes a quasi-static equilibrium within a few minutes that shows no time dependence on a time scale of hours at some temperatures. This observation allows an investigation of the nonequilibrium dynamics in this system, albeit a qualitative one.

Figure 2.6 shows the results of an experiment displaying the dramatic nonequilibrium effects in this system. Xenon is added at room temperature to the polymer and the system is slowly cooled to 105 K (typical cooling rates were 0.3 K/s below 173 K). The xenon spectrum at this point is shown in Figure 2.6a and is quite similar to the low temperature spectrum the sealed sample, shown in Figure 2.5b. Next a second aliquot is added; five minutes later the spectrum in 2.6b is obtained (average of 4 scans, 4 minute acquisition time). The second peak corresponding to the xenon just added is at ~250 ppm, about 100 ppm higher than the equilibrated xenon! This spectrum showed no changes over a two hour period, which in itself is a powerful demonstration of equilibration times in high surface area materials.

The sample is then warmed to 121 K and after another 5 minute equilibration period the spectrum in Figure 2.6c is obtained. Both peaks have narrowed somewhat and the "nonequilibrium" peak has shifted to 235 ppm. Again no time dependence is seen over an hour period. The sample is then warmed to 149 K; at this temperature the peaks begin to coalesce and the spectra are time dependent. Two representative spectra are shown: Figure 2.6d is taken 15 minutes after reaching the set temperature and Figure 2.6e is taken 45 minutes later.

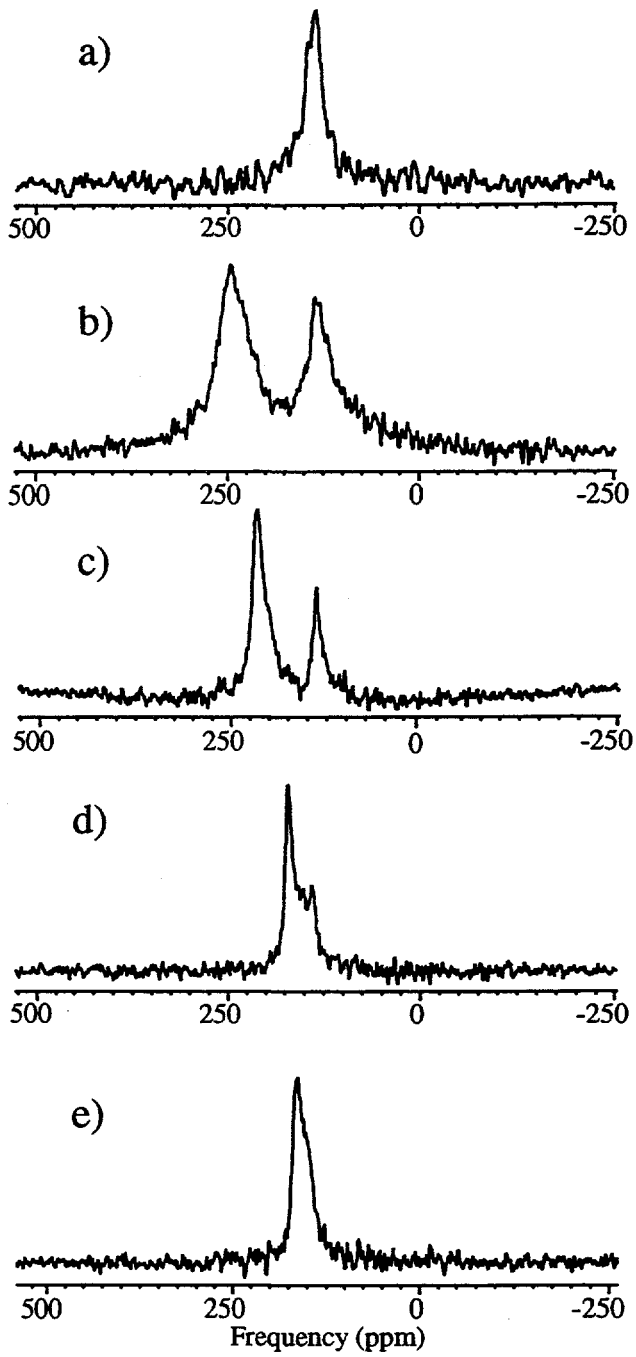

Figure 2.6 Nonequilibrium spectra of xenon in poly(triarlycarbinol) (a) Spectrum at 105 K showing peak from xenon loaded at room temperature. (b) An aliquot of xenon is added at 105 K and a second peak appears. (c) The sample is warmed to 121 K and equilibrated for 5 min. (d) The sample is warmed to 149 K and equilibrated for 15 min. (e) The sample is equilibrated at this temperature for 45 more minutes.

This behavior was found to be irreversible, that is recooling the sample did not result in the return of a second peak. Recooling resulted in the behavior seen in the sealed sample, a slight downfield shift and increased linewidth. Furthermore, in a separate experiment, the procedure was repeated (with identical results) up to the state represented in Figure 2.6c and then cooled to the original temperature (105 K). The nonequilibrium peak remained at the position it attained at 121 K, and thus even the shifts of the well separated peaks are irreversible. The intensity ratio of the two peaks also remained constant.

At low temperatures, where the two xenon peaks are completely separated, an inversion recovery experiment was performed. The data shows a large difference between the spin-lattice relaxation times of the two sites (Figure 2.7). A least squares fit to a semilog plot of the data (Figure 2.8) shows that the low frequency ("equilibrium") peak has a T_1 of 12.5 s, about one half that of the high frequency ("non equilibrium") peak, 24.0 s. Fluctuating chemical shift anisotropy is the most likely relaxation mechanism.

2.4.4 Discussion

This polymer shows a chemical shift that is consistent with xenon gas in micropores, rather than dissolved in the bulk polymer. The pressure dependence of the chemical shift makes it clear that the xenon occupies an interconnected pore volume where xenon-xenon collisions occur. The small change in chemical shift with decreasing temperature is characteristic of microporous substances due to the large number of surface collisions that occur even at room temperature. The increase in line width as the temperature is lowered has been observed for both polymers and zeolites. It suggests site heterogeneity; sites with different chemical shifts are observed as the exchange rate of xenon between these sites is slowed at the lower temperature.

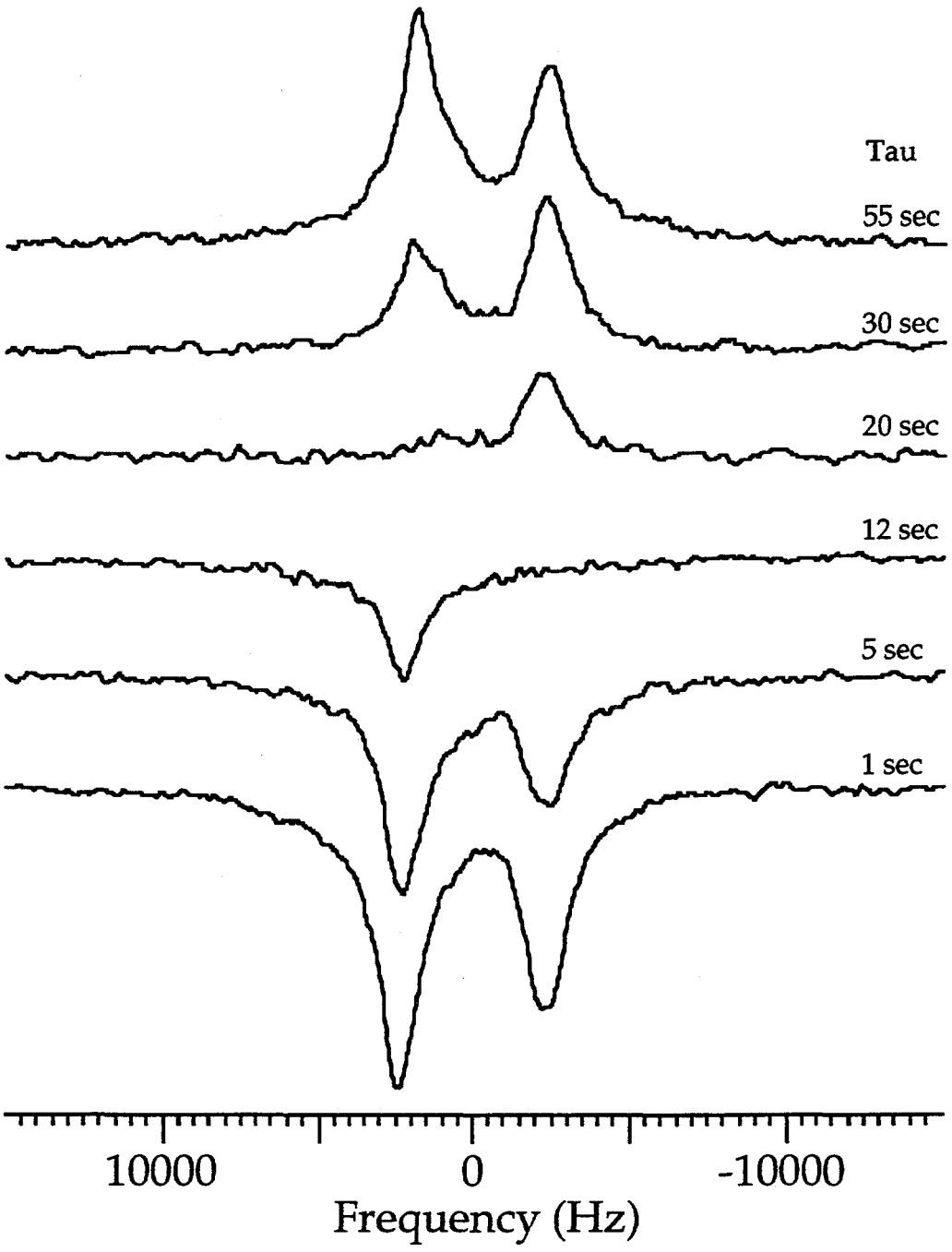

Figure 2.7 Inversion recovery spectra of xenon in poly(triarylcarbinol). Xenon was added at two different temperatures as described in the text.

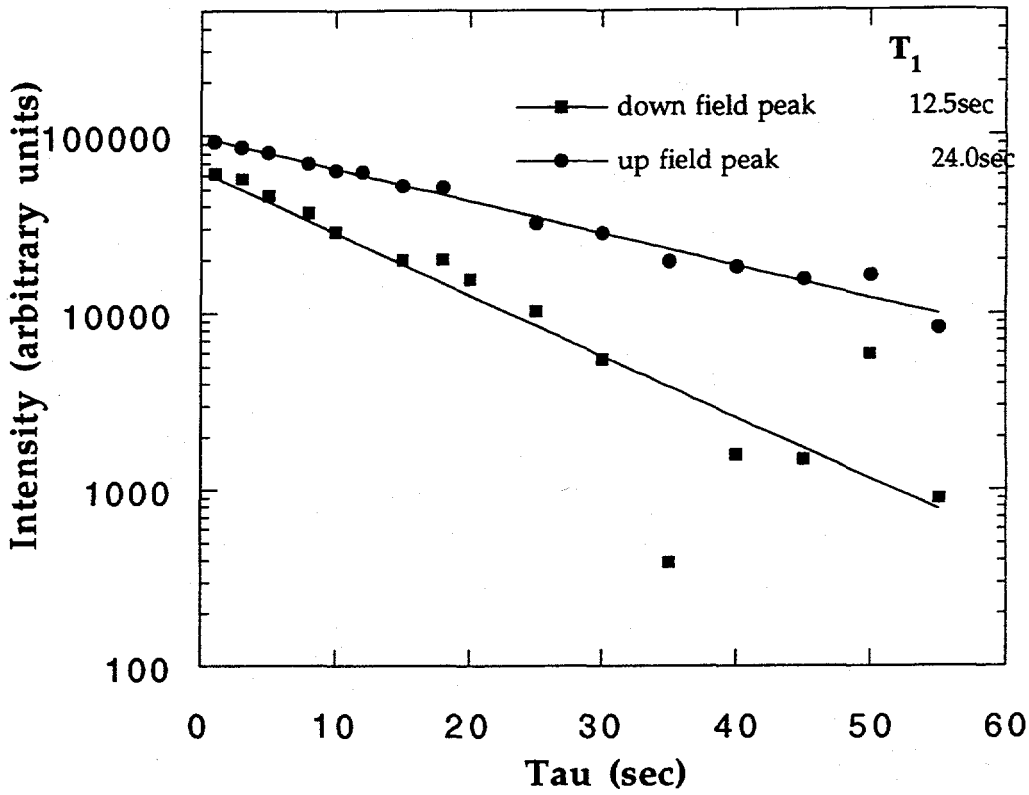

Figure 2.8 Semilog plot of the full inversion-recovery dataset, showing integrated xenon signals from the relaxation data of Figure 2.7.

The chemical shift data for the high surface area polymer is interpreted using the established empirical guidelines for xenon NMR.[28] The chemical shift can be represented be written as the following function of density (ρ) when the adsorption sites are weak:

$$\sigma = \sigma_0(T,r) + \sigma_1(T)\rho + \cdots \tag{2.42}$$

Here the chemical shift in the limit of low density, σ_0, is explicitly written as a function of temperature (T) and pore size (r). Although the exact functional dependence is not known, σ_0 is empirically found to be inversely dependent on pore size from zeolite studies.[28] It is therefore tempting to assign the two peaks as resulting from two

different pore sizes, however, it is very difficult to rationalize why the xenon should exclusively occupy large pores when in thermodynamic equilibrium with the polymer. Due to the greater van der Waals interaction (overlap) with the surface having greater curvature, the xenon should occupy the smaller cages if the intrinsic adsorption energies of the different cages are the same. There also appears to be no structural rationalization for having small pores only on the surface of the polymer particles, where the xenon that is rapidly introduced at low temperatures first comes into contact with the polymer.

An alternative explanation lies in the second term of equation 2.42. When the xenon initially comes into contact with the polymer at low temperatures, it cannot rapidly diffuse through the pores into the particle, otherwise it would equilibrate. Thus the xenon must be kinetically trapped in the pores at or near the surface. The local density of xenon in these pores may be quite high, and, if there are several xenon atoms per pore, then the xenon-xenon interactions can cause the large observed chemical shift. Cheung and coworkers[50] have observed non-equilibrium xenon resonances in zeolites, which they attributed to a macroscopic xenon density gradient introduced by rapid cooling. They have observed a chemical shift difference between the equilibrium site of about 25 ppm. This effect disappears at 144 K in about 20 min. They have attributed the non-equilibrium chemical shifts as arising from a xenon dimer in a non-equilibrium distribution. The results presented here are quite similar to theirs at the highest temperature (149 K). The major difference between the experiments reported here and theirs is that Cheung and coworkers believe that a temperature gradient existed in their sample due to rapid cooling, where the samples presented here are at a uniform temperature and still display non-equilibrium behavior. In this case, a non-equilibrium peak is observed that differs from the equilibrium peak by 30 ppm at 149 K, and are attributing the non-equilibrium

resonance to xenon in large pores near the surface. At lower temperatures, a much larger chemical shift difference is observed between the equilibrium and non-equilibrium peaks, with the non-equilibrium shift occurring at 250 ppm. There are precedents of shifts of this magnitude in the literature. Xenon occluded in NaA zeolite[51,52] show a discrete distribution of xenon pore occupancies and the difference in chemical shift from one xenon per cage to six xenon per cage is approximately 100 ppm. The zeolite supercages have a diameter of 11.4 Å. One xenon/cage has a resonance at ~75 ppm reflective of the interaction with the cage. Two xenons/cage has a resonance at ~95 ppm, up to seven xenons/cage, which has a resonance at 225 ppm. In this system, xenon-xenon interactions increase the observed chemical shift by 150 ppm. In studies of spin polarized xenon adsorbed onto poly(acrylic acid) at low temperatures, the chemical shift in the limit of zero coverage is 95 ppm, but increased to 195 ppm at high coverage.[29] Clearly, xenon-xenon interactions can be of comparable magnitude to xenon-surface interactions. Unfortunately, it is extremely difficult to quantify the xenon pore occupancy in these experiments, even in the bulk, let alone purely at surface sites. Measurement times for xenon isotherms would clearly be prohibitively long at these temperatures due to the equilibration times involved (no observable progress toward equilibrium in 2 hours!). Qualitatively, however, this model provides a plausible mechanism to describe the adsorption behavior. After the xenon has been added at low temperatures and during the subsequent warming (Figures 2.6 c, d, e) the xenon gradually begins to diffuse into the particle. This model explains directly why the behavior is irreversible as the equilibration process increases the entropy of the system.

It is possible to speculate on how the different relaxation times may also be rationalized by this model. If the relaxation is dominated by fluctuating chemical shift anisotropy, the xenon in the highly occupied cages have a much smaller effective

volume to move in and thus a much shorter correlation time. In the short correlation time limit, the relaxation time is inversely proportional to the correlation time and thus cages with a shorter correlation time (the pores with high xenon occupancy at higher chemical shift) will have a longer spin-lattice relaxation time, as observed experimentally. The greater homonuclear dipolar interaction in the filled cages will most not likely not contribute to the relaxation, even with the enriched xenon used in some of the experiments, as the T_1 in pure frozen xenon is extremely long (tens of minutes at least) over the entire temperature (and thus correlation time) range of the solid.[53] Experiments at different magnetic field strengths would have to be done to confirm this relaxation mechanism.

The two models discussed in the introduction to account of the high swellability of hypercrosslinked polymers should result in different xenon NMR spectra: the model assuming loosely crosslinked microgel particles (Figure 2.2a) implies two different environments, one within the gel particle and the other in voids between the gel particles. However, given the presumed size of the microgel particles, 100 - 30 Å, fast exchange will undoubtedly lead to a single average line, which is to be expected from the homogeneous model as well. At low temperatures the xenon will most likely equilibrate within the smallest pores of both models. However, the low temperature adsorption of xenon and the observed nonequilibrium adsorption dynamics can distinguish between the polymer topologies of the two models. When the xenon is rapidly introduced at low temperatures it must be trapped at or near the surface of the polymer. If the homogeneous model the external surface area would be only 10 m^2/g for 10 μm particles and would not be sufficient to rapidly sorb all the xenon. In the microgel model the external surface area of the polymer would likely be in excess of 100 m^2/g and the larger void spaces would allow the xenon to access more of this surface. Thus in the microgel model the bottleneck for xenon adsorption is *not*

entering the pore system, but diffusion within it, as appears to be the case experimentally. However, other possibilities such as an unusual surface structure cannot be ruled out; Experiments on this system at higher pressures would be desirable, especially if the loading could be calibrated. It might also be interesting to study the dynamics in a solvent-swelled system.

2.4.5 Conclusions

The adsorption of xenon at low temperatures in microporous samples is dramatically far from equilibrium and does not approach equilibrium on the timescale of hours. Thus the xenon NMR supports a polymer topology of a microgel of highly porous particles loosely crosslinked together forming larger voids between them.

2.5 Xenon NMR on Dispersed Vanadia Catalysts

2.5.1 Introduction

Vanadia Catalysts

Supported V_2O_5 is used as a catalyst for the selective oxidation of hydrocarbons[54-56] and for the selective reduction of nitrogen oxides.[57] A high catalytic activity and selectivity are achieved when vanadia is present as a highly dispersed, amorphous species.[54,58,59] The exact structure of the amorphous vanadia and bonding to the support is the focus of several recent reports.[60-64] *In situ* laser Raman spectroscopy[65] indicates that V_2O_5/TiO_2 (anatase) catalysts contain monomeric vanadyl and polymeric vanadate species, as well as crystallites of V_2O_5. At low vanadia loadings the monomeric species predominate and with increasing loading, polymeric vanadates are formed. Crystallites of V_2O_5 are formed if the vanadia loading is larger than the monolayer capacity of the support.

Xenon NMR of Catalysts

Xenon NMR has been used extensively to characterize zeolites. Bansal and Dybowski[66] have measured the diffusivity of water in Ni-NaY by observing the change of chemical shift with time. ^{129}Xe NMR also provides information about the distribution and sites of adsorbed species and was used to study the distribution of different organic molecules in zeolite NaY.[51,67,68]

In contrast to the extensive work in the field of zeolites, there are only a few ^{129}Xe NMR studies of amorphous materials. Cheung[69] has reported the effects of pore size distribution of silica, alumina, and silica-alumina on the xenon chemical shift. Conner et al.[70] have used xenon as a probe of the pore structure created by compression of nonporous silica.

The use of xenon as a probe of metal cluster formation in zeolites is facilitated by the presence of strong adsorption sites for the xenon atoms on the metal particles. The non-linear behavior of the chemical shift at low xenon loadings is a useful tool for the study of the exchange of cations in zeolites and metal cluster formation and growth on zeolites.[71-76] Boudart et al.[77-79] have extended this method to amorphous materials. In these studies xenon was used as a probe of the chemisorption of H_2 and O_2 on platinum particles supported on alumina. The work reported here utilizes ^{129}Xe NMR to probe dispersed vanadia catalysts.

2.5.2 Experimental

Apparatus

The experimental apparatus consists of a xenon reservoir connected by glass tubing to a sample ampoule located in a 4.2 Tesla superconducting magnet. A connection to a

vacuum rack allows the sample region to be evacuated. The pressure in the sample region is measured by a thermocouple pressure gauge. The NMR-probe consists of a Macor ceramic coil support, glass dewar, dewared stainless-steel transfer line for the nitrogen cooling gas, and a glass transfer line for the xenon. The sample region contains an rf-shielded thermocouple for monitoring and controlling the temperature during the experiments. The probe head is depicted in Figure 2.9. A temperature range between 133 K and 300 K, which could be controlled within ±1 K, was used for these experiments.

The sample was slowly cooled and brought to thermal equilibrium at the desired experimental temperature. After adding a certain amount of xenon, two minutes were typically waited before acquiring data. For the pressure-dependent NMR

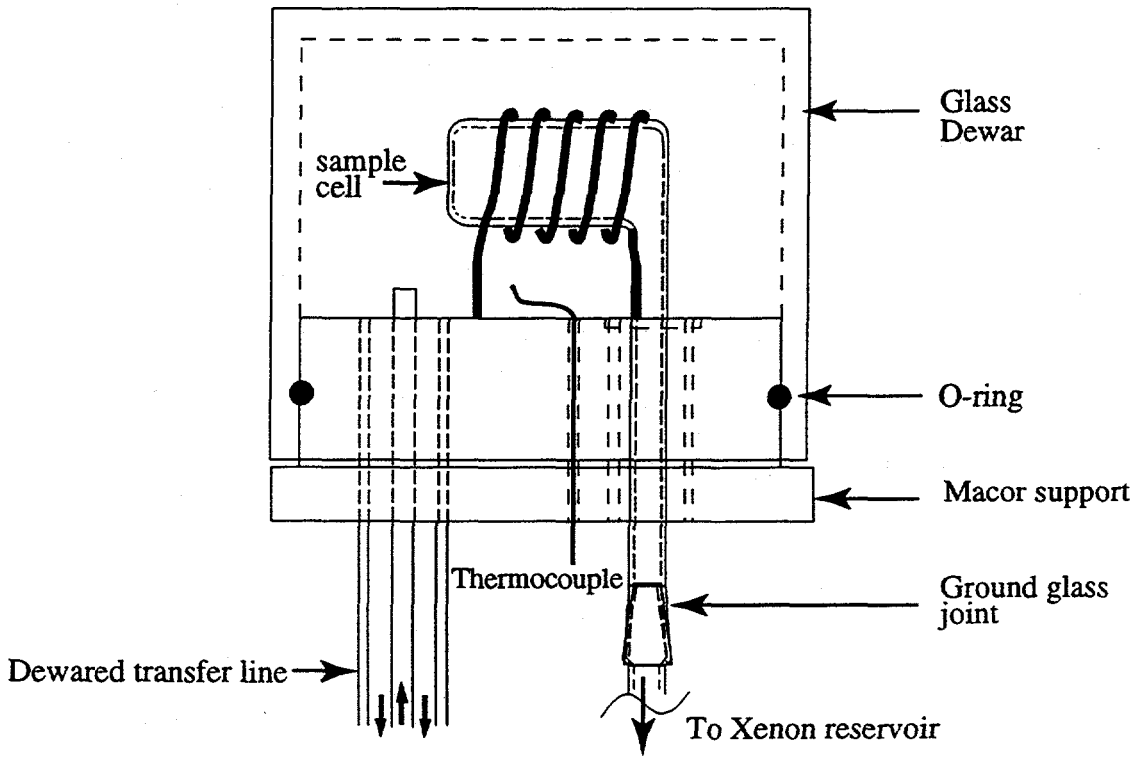

Figure 2.9 Schematic diagram of probehead used in variable pressure ^{129}Xe NMR experiments. Key features include a dewared sample region, dewared transfer line, and glassware connecting sample to xenon reservoir.

experiments 80% enriched xenon-129 (EG+G Mound Miamisburg, OH) was used. After acquisition of an NMR spectrum, the sample was allowed to warm, and the xenon was recovered by condensing it with liquid nitrogen.

The spectra were acquired by Fourier transformation of the signal obtained after a 90° rf pulse. The chemical shifts are referenced to an external standard of dilute gas-phase xenon.[49] The number of scans necessary to achieve a good signal-to-noise ratio was strongly dependent on the surface area of the sample, temperature, and xenon pressure. For example, 64 scans were required for the 1.3% V_2O_5/TiO_2 sample at 153 K and 32,768 scans were required for the pure V_2O_5 sample at 300 K. Typical NMR pulse recycle times were between 0.1 and 1 s.

Catalyst Pretreatment

The preparation of the V_2O_5/TiO_2 samples is described in detail elsewhere.[65] The weight percent loading of V_2O_5 on the surface of TiO_2 (anatase) is shown as X% V_2O_5/TiO_2 (X = 1.3, 3.0, or 9.8). Commercially available TiO_2 (anatase) (Aldrich Gold Label, 99.9%) and V_2O_5 (Aldrich, 98%+) were used. Contamination by water is the main obstacle in the preparation of clean metal oxide surfaces.[80,81] The samples were heated to 673 K under vacuum (< 10^{-4} torr) to remove surface bound water and then heated in an O_2-atmosphere (300 torr) at the same temperature for 1 hour to produce a fully oxidized surface. The samples were then loaded into the NMR probe and immediately evacuated to 10^{-5} torr. When loading the samples into the probe, the samples were exposed to atmosphere for approximately 1 minute. To remove any water adsorbed during this time, the samples were heated to 473 K under vacuum (< 10^{-5} torr) for 2 hours. It was possible to monitor the desorption of water with a pressure gauge. After a short time of heating an increase in pressure was observed,

followed by a slow decrease to the original value (< 10^{-5} torr). The sample was then heated (473 K) for 1 hour under oxygen (300 torr), the probe was transferred into the magnet, and the sample was evacuated to a pressure below 10^{-5} torr for 12 hours at room temperature.

Isotherms

Nitrogen and xenon isotherms were carried out to measure the surface areas and adsorption energies of xenon on the metal oxide samples. Details of the experimental procedure can be found in Shoemaker, Garland, and Nibler.[82] The data show a BET[83] like behavior (Figure 2.10). The equation for a BET isotherm is

$$V = \frac{V_{mon}\, c\, x}{(1-x)[1+x(c-1)]}. \tag{2.43}$$

where V is the volume of adsorbed gas at STP, $x = {}^{p}/_{p_0}$ is the reduced pressure, and V_{mon} is the volume that would be occupied at STP by the amount of gas needed to form a monolayer on 1g of sample. The quantity c is related to the surface adsorption energy by the equation $\ln c = (\Delta H_{ads} - \Delta H_l)/RT$, (2.44)

where ΔH_l is the heat of liquefaction of the adsorbate (3.57 kcal/mole).[84] The nitrogen and xenon isotherms were measured on a glass vacuum rack using a silicone oil diffusion pump capable of achieving pressures below 10^{-5} Torr. For the xenon isotherms cold-temperature baths of the following organic solvents cooled with liquid nitrogen: n-pentane (143 K), methanol (172 K), and ethyl acetate (190 K) were used. For accuracy, the dead-volume measurements using helium gas were made at each temperature for which an isotherm was measured. In Figure 2.10 the xenon isotherms of the 3.0% V_2O_5/TiO_2 sample are presented. The isotherms at 143, 172, and 190 K show characteristic BET behavior for all samples used in this study. The parameters used for the xenon and nitrogen isotherms are listed in Table 2.1.

In accord with the BET theory, the heat of adsorption (ΔH_{ads}) was determined from the linear region of the isotherm (reduced pressure $0.05 \leq x \leq 0.3$). Note that in this pressure range the isotherms are insensitive to the presence of a small number of strong adsorption sites. The absence of hysteresis for the xenon isotherm taken at 143 K indicates that the sample does not contain pores. In contrast, for V_2O_5 the nitrogen adsorption and desorption isotherms display extreme hysteresis, indicating the presence of dead ended and ink-bottle pores with a wide range of pore sizes.[85,86] To analyze the chemical shift data for xenon on the V_2O_5/TiO_2 samples, V_{mon} was determined from the surface areas obtained by the N_2-isotherms. Knowing p_0 from saturated vapor pressure measurements,[87,88] equation (2.44) was used to calculate the coverage θ, which is equal to V/V_{mon}. Values for c were obtained from fits of the isotherms to equation (2.44) for each of the temperatures used in the NMR experiments. The heats of adsorption were determined using equation (2.44) and are presented in Table 2.1.

2.5.3 Results and Discussion

Representative spectra of ^{129}Xe adsorbed on V_2O_5 (spectrum a), on V_2O_5/TiO_2 with different V_2O_5 weight loadings (spectra b-d), and on TiO_2 (spectrum e) are presented in Figure 2.11. For the pure TiO_2 (anatase) as well as for the V_2O_5/TiO_2 catalysts there is a single xenon peak. In contrast, two distinct resonances for xenon on V_2O_5 are observed. The poor signal-to-noise ratios of spectra a and e are due to the low surface areas of the TiO_2 (anatase) and the V_2O_5 samples (see Table 2.1). At the temperatures at which the spectra were acquired, xenon is mobile and on the NMR time scale (~10^{-3} s) samples both the surface and gas phase. Because of this motion, ^{129}Xe NMR spectra do not usually contain anisotropic lineshapes from adsorption interactions, however anisotropic lineshapes have been observed for xenon in

Sample	Gas	Temperature (K)	ΔH_{ads} (kcal/mol)	Surface area (m^2/g)
TiO_2	N_2	77	2.1	9
	Xe	143	4.5	7
	Xe	172	4.6	8
	Xe	190	4.2	18
1.3% V_2O_5/TiO_2	N_2	77	2.0	86
	Xe	143	4.8	81
	Xe	172	4.8	73
	Xe	190	4.9	79
3.0% V_2O_5/TiO_2	N_2	77	2.1	69
	Xe	143	4.9	59
	Xe	172	4.8	63
	Xe	190	4.7	70
9.8% V_2O_5/TiO_2	N_2	77	2.1	27
	Xe	143	4.9	24
	Xe	172	4.9	24
	Xe	190	4.7	28
V_2O_5	N_2	77	2.1	6
	Xe	143	5.0	5
	Xe	172	4.4	7
	Xe	190	4.3	11

Table 2.1 Summary of the isotherm data for Nitrogen and Xenon adsorbed onto TiO_2 (anatase), 1.3% V_2O_5/TiO_2 (anatase), 3.0% V_2O_5/TiO_2 (anatase), 9.8% V_2O_5/TiO_2 (anatase), and V_2O_5

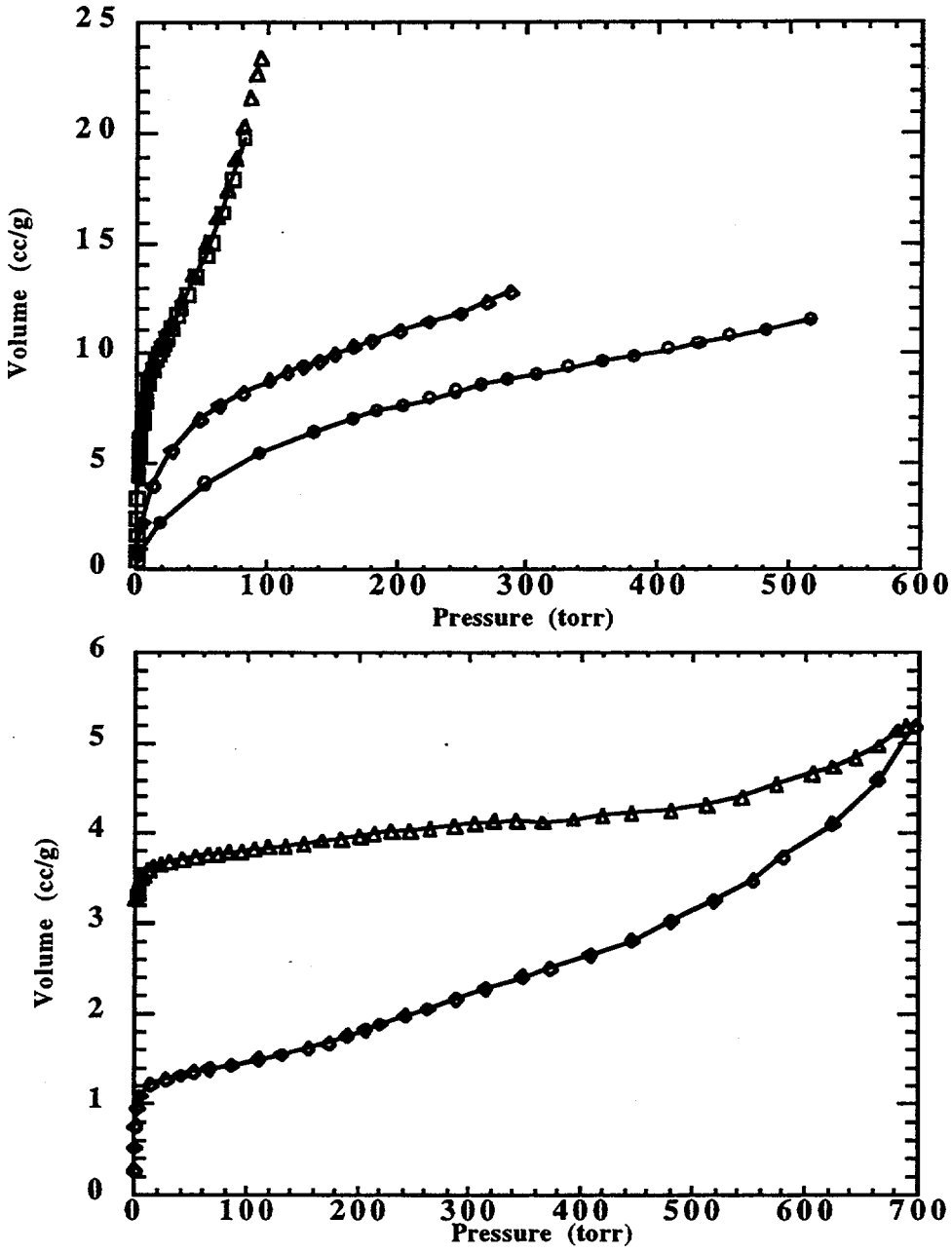

Figure 2.10 Representative isotherms of xenon on metal oxides (top) BET isotherms of xenon on 3.0% V_2O_5/TiO_2 (anatase) at 143 K (adsorption and desorption), 172 K (adsorption), and 190 K (adsorption). (bottom) BET adsorption and desorption isotherm of nitrogen on V_2O_5. In both Figures, lines connect the points to guide the eye.

cavities.[89,90] The spectra displayed in Figure 2.11 were obtained using xenon coverages, θ, between 0.34 and 0.63.

The chemical shift of xenon adsorbed on the surfaces of TiO_2 (anatase), V_2O_5/TiO_2 and V_2O_5 as a function of temperature and coverage are displayed in Figures 2.12, 2.13, 2.15, 2.16, and 2.17. The chemical shift of ^{129}Xe adsorbed on the surface of pure TiO_2 (anatase) as well as pure V_2O_5 shows a linear dependence on the xenon coverage. In contrast, the shifts of xenon adsorbed on V_2O_5/TiO_2 catalysts initially decrease with increasing coverage, and then with greater coverage, increase due to xenon-xenon interactions near the surface.[29]

Xenon adsorbed on TiO_2 (anatase)

The shift of xenon adsorbed on pure TiO_2 (anatase) results from rapid exchange of the xenon atoms between the gas phase and the surface adsorbed phase. Hence, the total chemical shift is equal to the shift due to interactions at the surface (δ_s) plus that of the gas phase (δ_g), weighted by the relative probabilities of the xenon atom being on the surface, ($P_s(T)$) and in the gas phase ($P_s(T)$).

$$\delta(T,\theta) = \delta_g(T,\theta)\, P_g(T) + \delta_s(T,\theta)\, P_s(T) \qquad (2.45)$$

The shift of xenon at low pressure is used as an external standard and defined as 0 ppm. The temperature and pressure dependences of the chemical shift of xenon gas has been found to be small[23] and can be neglected in this study. Hence, the measured shift is simply the shift due to interactions at the surface (δ_s) multiplied by the probability of being at the surface ($P_s(T)$).

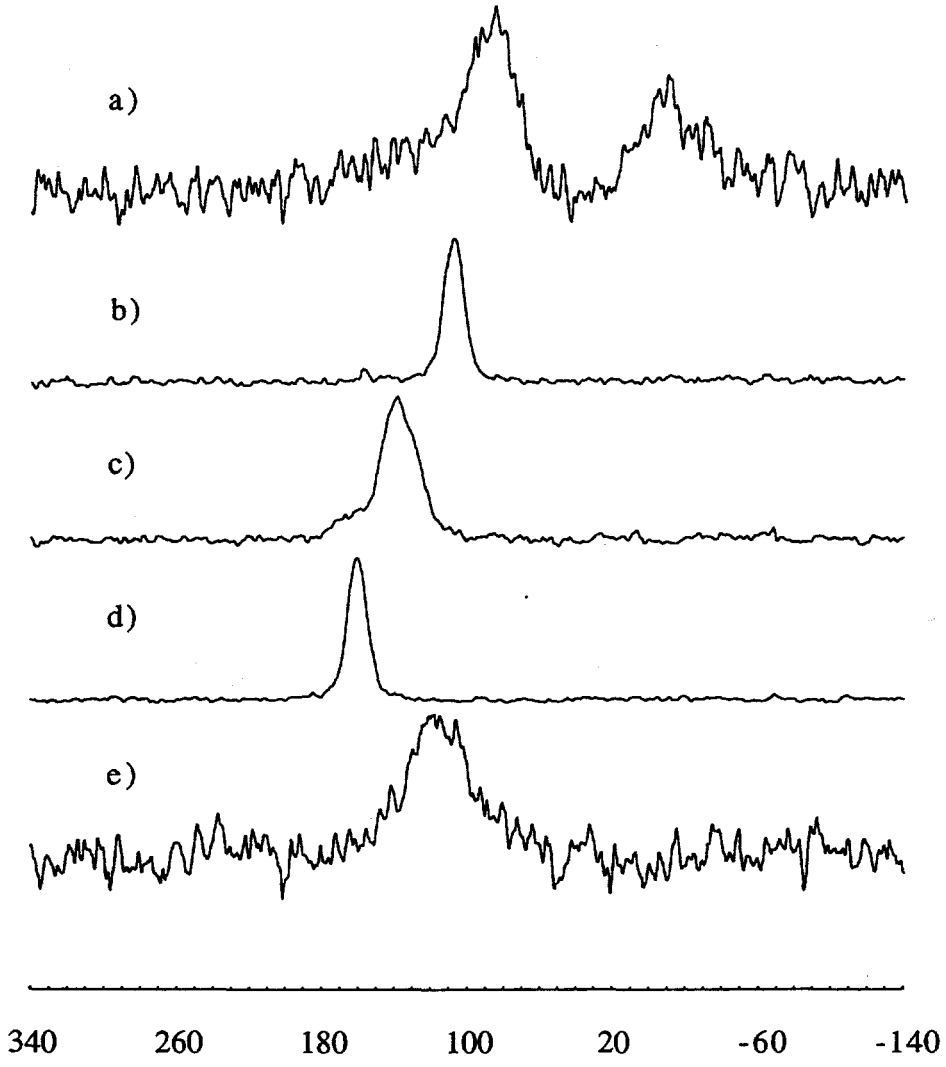

Figure 2.11 Representative ^{129}Xe NMR spectra of xenon adsorbed onto metal oxides. (a) V_2O_5 (T = 213 K, θ = 0.34) ; (b) 9.8% V_2O_5/TiO_2 (T = 173 K, θ = 0.58); (c) 3.0% V_2O_5/TiO_2 (T = 173 K, θ = 0.63); (d) 1.3% V_2O_5/TiO_2 (T = 172 K, θ = 0.62); (e) TiO_2 (T = 172 K, θ = 0.59); the poor S/N of spectra a and e is due to the low surface area of the TiO2 anatase and V_2O_5 sample (see Table 2.1).

Raftery et al. [29] has shown that the shift due to interactions at the surface can be written in a virial-type expansion

$$\delta_s(T,\theta) = \sigma_0 + \sigma_1\theta\, P_s(T) + \sigma_2(\theta\, P_s(T))^2 + \sigma_3(\theta\, P_s(T))^3 + \ldots \quad (2.46)$$

where σ are the virial coefficients of the nuclear shielding, and for this work, are considered temperature independent.[23] The first term in the expansion (σ_0) is due to interactions between xenon and the surface. The second term results from xenon-xenon interactions at or near the surface. The linear dependence of the chemical shift on coverage (Figure 2.12a) indicates that higher order terms can be neglected, and that only binary collisions between xenon atoms near the surface appear to be important at the xenon coverages studied. The slope of the shift as a function of coverage results from the binary xenon-xenon collisions at or near the surface.[29]

The chemical shift of the adsorbed xenon resonances extrapolated to zero coverage ($\delta(T,\theta=0)$) is $\delta(T,\theta=0) = \sigma_0 P_s(T)$, (2.47)

dependent on only the xenon-surface interactions and probability of the xenon being on the surface. The probability of finding a xenon atom at the surface can be written as[29]

$$P_s(T) = \tau_s/(\tau_s + \tau_v), \quad (2.48)$$

where τ_s is the sticking time and τ_v is the mean time between sticking collisions of xenon with the surface. The average sticking time is given by $\tau_s = \tau_0\, e^{\Delta H_{ads}/kT}$. (2.49) where τ_0 is the preexponential factor and ΔH_{ads} is the energy of adsorption. Combining equations (2.47) - (2.49) yields

$$\delta(T,\theta=0) = \sigma_0 \frac{e^{\Delta H_{ads}/kT}}{\tau_v/\tau_0 + e^{\Delta H_{ads}/kT}}. \quad (2.50)$$

With the heat of adsorption given in Table 2.1, the chemical shift extrapolated to zero coverage, $\delta(T,\theta=0)$, as a function of temperature, is fit to (2.50). The fit and data are presented in Figure 2.12b. The contribution to the chemical shift due to xenon-surface interactions (σ_0) is found to be 109 ppm for TiO_2 (anatase) which is similar to 86 ppm measured for xenon in NaY zeolite at 144 K[50] and 120 to 150 ppm for amorphous silica, silica-alumina, and alumina at 144 K.[69] For the ratio τ_0/τ_0 we find a value of $4 \cdot 10^4$, which is comparable to that determined for xenon on a polymer surface ($3 \cdot 10^4$).[29]

Xenon adsorbed on V_2O_5/TiO_2 catalysts

The chemical shifts as a function of coverages for the loaded V_2O_5/TiO_2 samples are shown in Figures 2.12 , 2.14, 2.15. An initial decrease in the chemical shift with coverage is attributed to interactions of xenon atoms with a limited number of strong adsorption sites.[71-76] The most attractive adsorption sites are occupied first and cause an initial high shift value. With increasing coverage only less attractive sites are available for xenon, which causes a decrease in the average chemical shift.

This proceeds until the increasing xenon-xenon interactions begin to dominate the xenon-surface interactions and cause an increase in the chemical shift at higher coverages. On a pure TiO_2 surface the chemical shift of xenon shows a linear dependence on the coverage. A dramatic change in the chemical shift behavior of xenon occurs if a small amount of V_2O_5 is introduced to the surface (Figure 2.13). Compared to pure TiO_2, the chemical shift values of xenon extrapolated to zero pressure are larger by 50 ppm at 153 K and by 100 ppm at room temperature. In addition, the chemical shift of xenon decreases at low xenon coverages, which suggests the presence of strong adsorption sites. According to Went et al.[65] the surface of the 1.3% V_2O_5/TiO_2 catalyst is composed of 80% monomeric vanadium

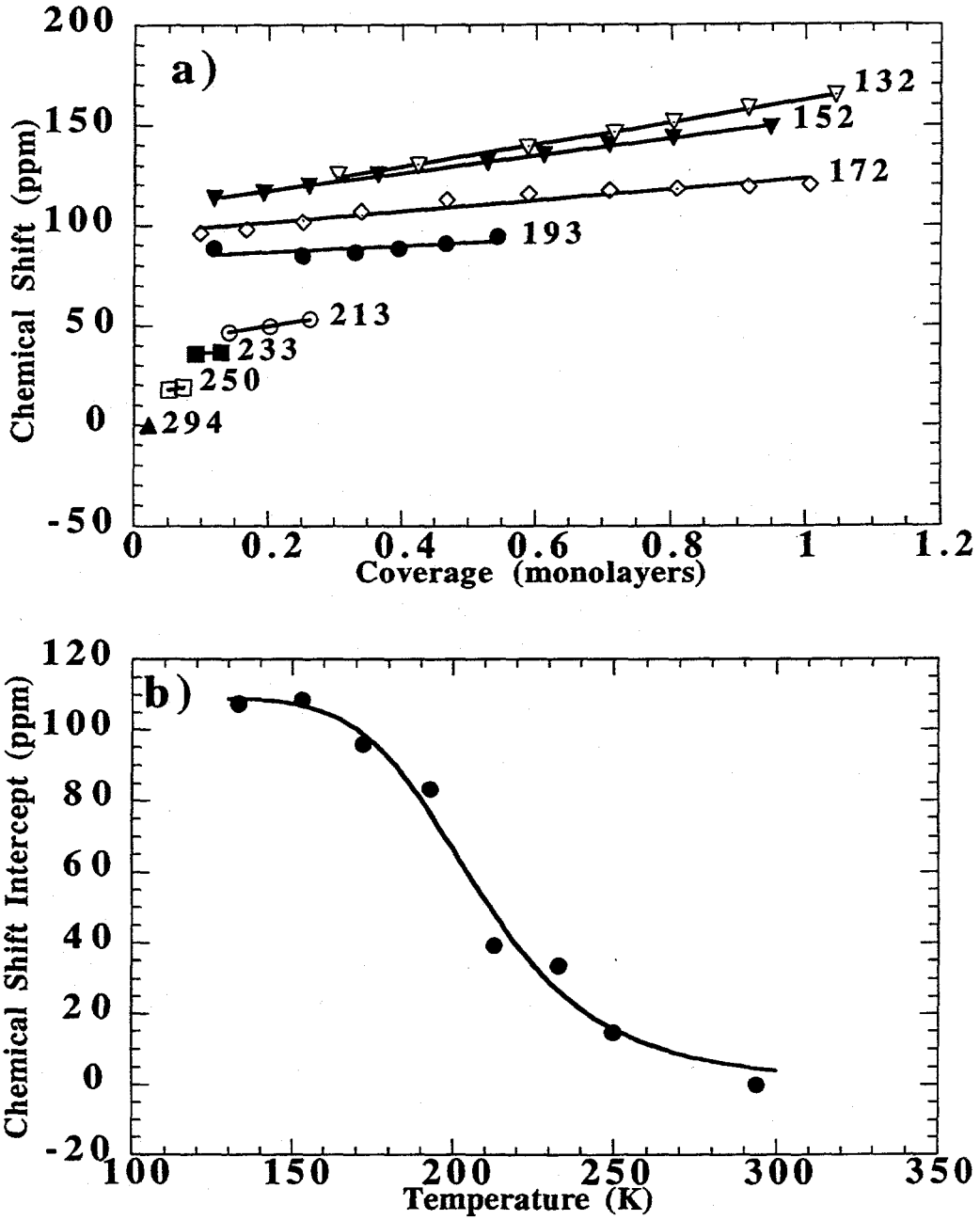

Figure 2.12 Xenon chemical shift data of xenon adsorbed on TiO_2 (**a**) ^{129}Xe chemical shifts (ppm) of xenon adsorbed on TiO_2 (anatase) as a function of the temperature (K) and coverage (in monolayers). Lines represent linear least-squares fits to the data at each temperature. (**b**) ^{129}Xe chemical shift intercepts (ppm) of xenon adsorbed on TiO_2 (anatase) versus temperature.

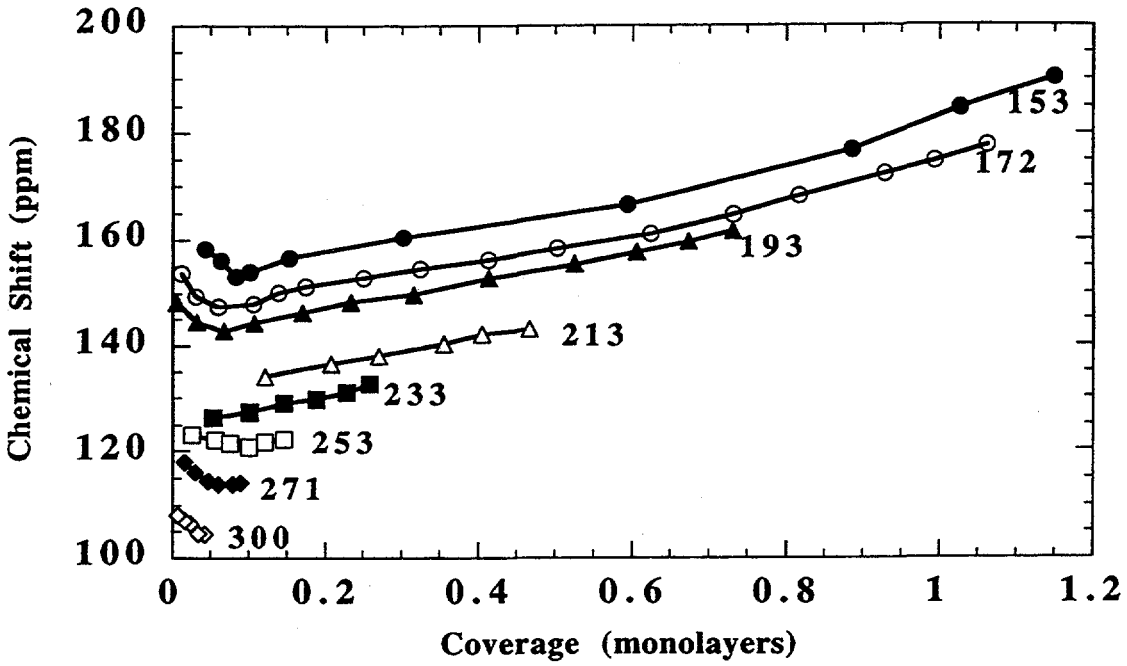

Figure 2.13 ^{129}Xe chemical shifts (ppm) of xenon adsorbed on 1.3% V_2O_5/TiO_2 (anatase) as a function of temperature (K) and coverage (in monolayers). Lines connect the points at each temperature to guide the eye.

oxide units and 20% polymeric units. The vanadium atoms of the surface vanadium oxide are accessible to the xenon atoms and provide strong adsorption sites for xenon (Figure 2.14).

With increasing V_2O_5 loading, the space between the vanadium oxide units decreases and correspondingly the capacity for xenon atoms in contact with strong adsorption sites decreases (Figure 2.14). Additionally, the increased loading causes a decrease of the fraction of monomeric species and an increase of the fraction of polymeric species.[65] However, the space between monomeric units is drastically reduced, hence the average time xenon spends close to vanadium atoms is increased. Increased

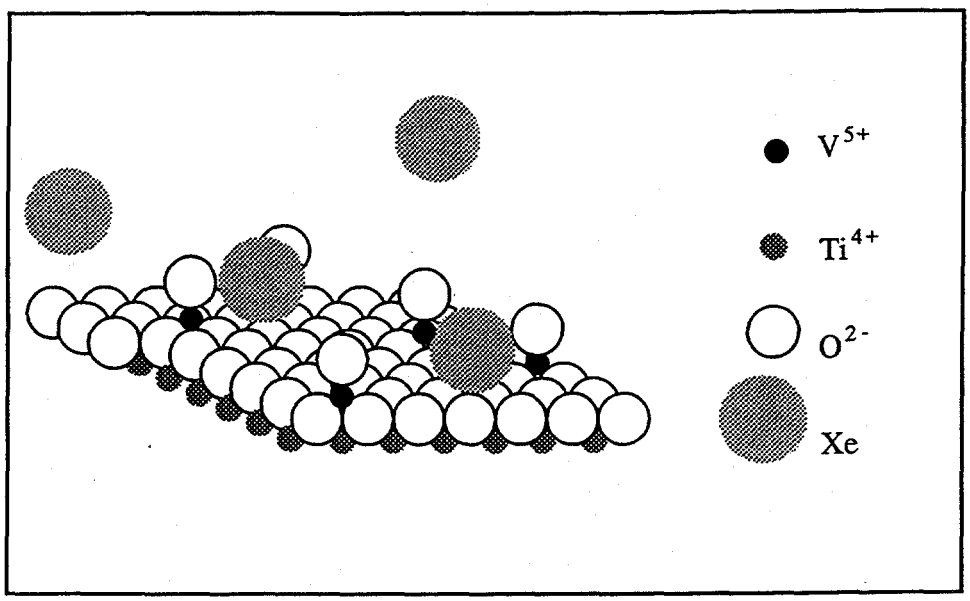

Figure 2.14 Schematic drawing of xenon exposed to a TiO_2 surface loaded with monomeric vanadia units. The radii 0.59 Å for V^{5+},[91] 0.68 Å for Ti^{4+},[91] 1.32 Å for O^{2},[91] and 2.2 Å for Xe[35,72] were used to represent the different elements.

loading of vanadia is expected to have two effects on the chemical shift of xenon: there will be fewer strong sites available for the xenon; however, the chemical shift due to these sites is greater because the xenon is spending more time on or near these sites.

A comparison of the chemical shift data of the 3.0% V_2O_5/TiO_2 sample (Figure 2.15) to that of the 1.3% V_2O_5/TiO_2 sample (Figure 2.13) seems to confirm this hypothesis. The xenon chemical shift values on the 3.0% V_2O_5/TiO_2 sample are larger at very low coverages and smaller at higher coverages than for xenon on the 1.3% V_2O_5/TiO_2 sample (Figure 2.13). This initial larger chemical shift implies that the xenon interacts more strongly with the 3.0% V_2O_5/TiO_2 surface than the 1.3% V_2O_5/TiO_2 surface. The smaller shift at higher coverages may indicate, however, that there are fewer total adsorption sites available for xenon on the 3.0% V_2O_5/TiO_2 sample.

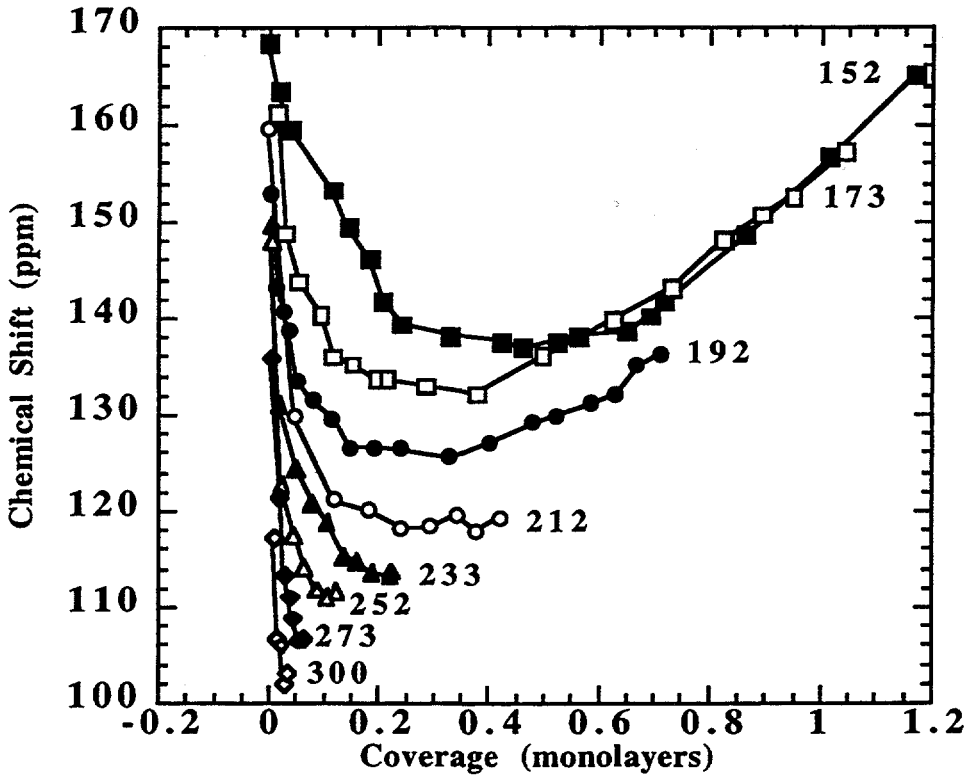

Figure 2.15 ^{129}Xe chemical shifts (ppm) of xenon adsorbed on 3.0% V_2O_5/TiO_2 (anatase) as a function of temperature (K) and coverage (in monolayers). Lines connect the points at each temperature to guide the eye.

A further increase of the vanadium content to 9.8 weight % V_2O_5 produces a monolayer of vanadium oxide on TiO_2 and V_2O_5 crystallites are formed.[65] A complete layer of vanadium oxide on the surface decreases the accessibility of xenon to strong adsorption sites (vanadium atoms), which is reflected in the shift data (Figure 2.16). There is no decrease of the xenon chemical shift for low xenon loadings and the

chemical shift is almost linearly dependent on coverage, both observations are expected for surfaces without a limited number of strong adsorption sites.

Unfortunately it is not currently possible to develop a quantitative interpretation of our xenon shift data due to the complex nature of the xenon-surface interactions. The chemical shift of a xenon atom on the surface of V_2O_5/TiO_2 is influenced not only by the total number of vanadium atoms present, but also by the distance between the vanadia groups and the actual structure of the surface.

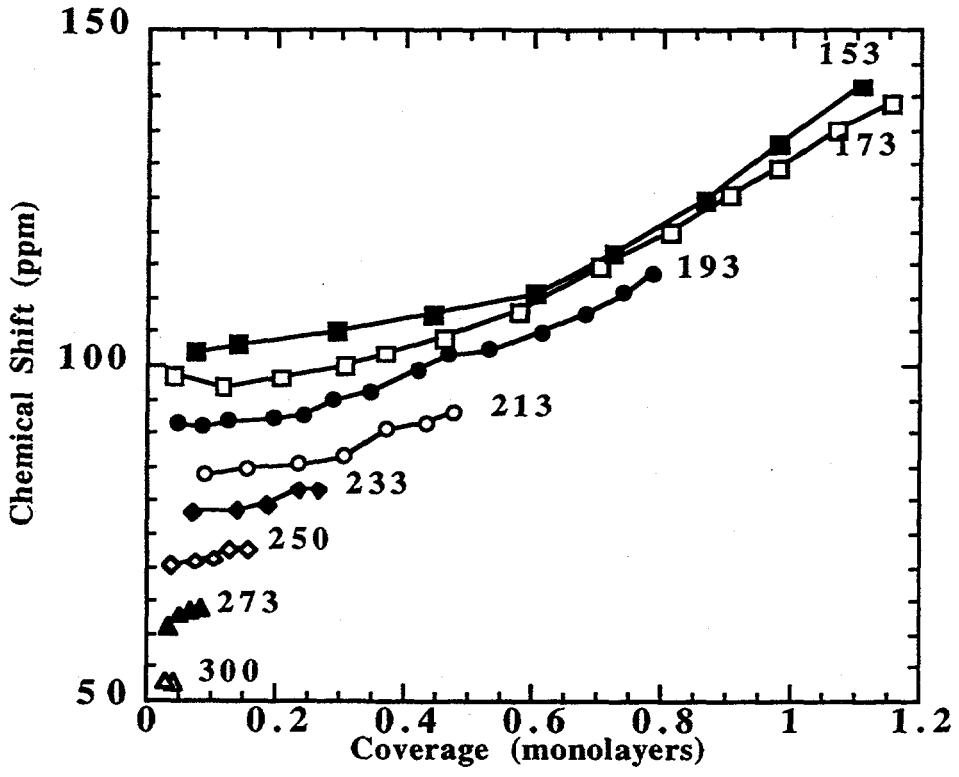

Figure 2.16 ^{129}Xe chemical shifts (ppm) of xenon adsorbed on 9.8% V_2O_5/TiO_2 (anatase) as a function of temperature (K) and coverage (in monolayers). Lines connect the points at each temperature to guide the eye.

Xenon adsorbed on V_2O_5

The ^{129}Xe NMR spectrum of xenon adsorbed on V_2O_5 has two well resolved peaks (Figure 2.11 a), due to two distinct environments for xenon. The relative intensity of the peaks change with temperature. At 173 K, only the peak at higher frequency is detected. With increasing temperature the relative intensity of this peak decreases, which is characteristic of an adsorbed species. Also, this resonance shows a pressure and temperature dependence similar to that of xenon adsorbed on TiO_2. Hence, it is attributed to xenon adsorbed on the surface of V_2O_5 in rapid exchange with gas phase xenon. The resonance at ~0 ppm appears to be from xenon in a gas-like environment, as evidenced by the chemical shift. The peak assignments are further discussed in Chapter 3.

For xenon adsorbed on V_2O_5 in rapid exchange with gas phase xenon (the peak at higher frequency), it is possible to apply the same formalism used to interpret the xenon chemical shift of xenon adsorbed on TiO_2 (Figure 2.12). As in the case of TiO_2 the chemical shift shows a linear dependence on coverage (Figure 2.17), which indicates that only binary collisions between xenon atoms are important at the xenon coverages studied. Figure 2.17 shows the temperature dependence of the chemical shift intercepts, $\delta(T,\theta=0)$, for this resonance. The fit to equation (2.50), yields a chemical shift due to xenon-surface interactions (σ_0) for V_2O_5 of 93 ppm. For the ratio τ_v/τ_0 a value of $9 \cdot 10^3$ is obtained.

Ripmeester and Ratcliffe[89] measured the ^{129}Xe NMR spectrum of xenon sorbed in porous vycor glass obtaining two distinct peaks. The authors attribute the high frequency resonance (~80 ppm) to xenon inside the pores and attribute a resonance near 0 ppm to xenon gas and a "surface phase." Their spectra appear very similar to that of xenon adsorbed on V_2O_5; both spectra have a resonance with a large shift due to strong interactions with the surface, and a peak due to gas-like xenon in slow

exchange with the strongly adsorbed xenon. Although similar, a direct comparison of the spectra should be approached with caution due to the possible differences in adsorption energy and pore size, both of which directly effect the dynamics that govern the xenon chemical shift.

2.5.4 Conclusions

The chemical shift of ^{129}Xe adsorbed on the surface of TiO_2 (anatase) and on V_2O_5 depends linearly on the xenon coverage, indicating a lack of strong adsorption sites. The contributions to ^{129}Xe chemical shift due to xenon-surface interactions are 109 ± 3 ppm for TiO_2 (anatase) and 93 ± 5 ppm for V_2O_5. V_2O_5/TiO_2 catalysts, particularly those with a high proportion of monomeric vanadyl sites, exhibit strong adsorptive interactions with xenon. The presence of strong adsorption sites on 1.3% and 3.0% V_2O_5/TiO_2 samples excludes the existence of large vanadia domains indicating that the vanadia units are dispersed on the TiO_2 (anatase) support. Isotherm data shows that crystallites of pure V_2O_5 contain a large number of pores. ^{129}Xe NMR of xenon sorbed on V_2O_5 reveals the existence of two distinct environments for xenon.

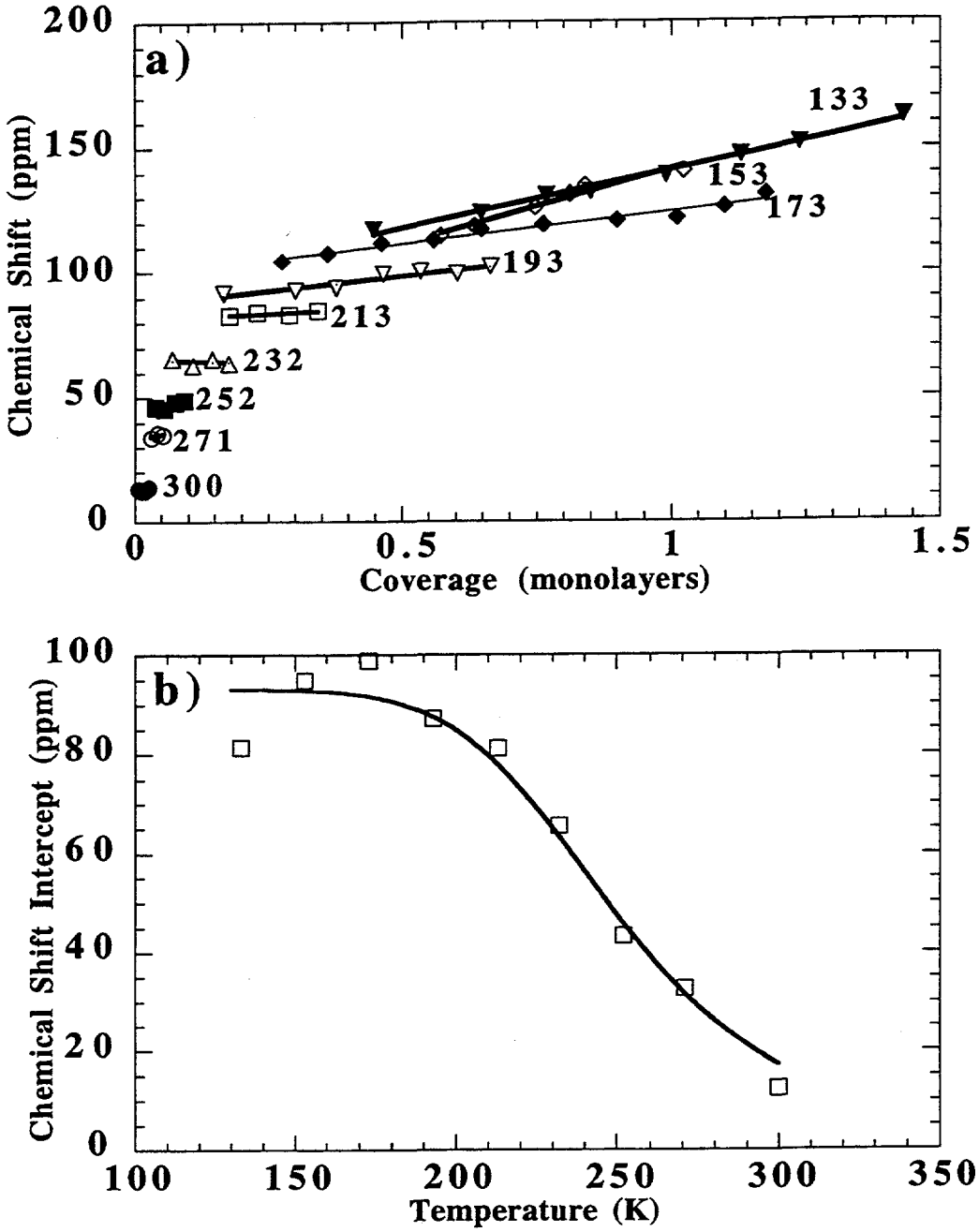

Figure 2.17 Chemical shift data for xenon adsorbed on V_2O_5 (**a**) ^{129}Xe chemical shifts of xenon adsorbed on V_2O_5 as a function of the temperature and coverage. Lines represent linear least-squares fits to the data at each temperature. (**b**) ^{129}Xe chemical shift intercepts (ppm) of xenon adsorbed on V_2O_5 versus temperature.

2.6 Xenon NMR Study of a Nematic Liquid Crystal Confined to Cylindrical Submicron Cavities

2.6.1 Introduction

Liquid crystals are technologically important due to their widespread use in displays (LCDs) and their potential applicability in nonlinear optical devices.[92-94] Liquid crystalline phases exhibit long range molecular orientational order, in contrast to normal liquids which lack positional and orientational order. Devices based on liquid crystals are able to exploit the anisotropy of the medium for the control of alignment and switching of the director axis formed by the liquid crystalline phases. Characterization of the orientational order and the factors that govern it are therefore of considerable scientific and commercial interest.

Nuclear magnetic resonance (NMR) is useful for studying liquid crystals[95] due to the sensitivity of the NMR spectrum to orientational order. Anisotropic interactions such as chemical shift anisotropy, quadrupolar interactions, and magnetic dipolar couplings make it possible to measure the degree of orientational order. However, spectra can be extremely complicated and intractable for abundant spins in multiple sites, e.g. protons in the liquid crystal molecules. A common simplifying approach is to study small probe molecules dissolved in the liquid crystal, or the use of liquid crystal molecules which have been isotopically labeled at specific sites. For solute molecules within a liquid crystalline environment, the ordering of the solute by dispersive and steric forces can be described by an order tensor that relates the average alignment of the solute molecular frame to the liquid crystal director frame.[96] A particularly simple example is the case of an atom dissolved in a liquid crystal solvent; in this case the principal axis system of the probe is completely determined by the liquid crystal director field.

In a nematic liquid crystal, ^{131}Xe was observed to have a spectrum composed of a sharp triplet indicative of a quadrupolar splitting from an orientationally ordered, homogeneous average electric field gradient at the nucleus.[97] More recently Diehl, Jokisaari, and coworkers have used several noble gases[98,99] possessing quadrupolar nuclei to perform a systematic study of several nematics and have attempted to explain the observed electric field gradients in bulk liquid crystals and mixtures.[98] Similarly, several NMR studies have attempted to exploit the high sensitivity of ^{129}Xe chemical shift to its local environment and structure. These studies have sought to correlate various contributions to the total chemical shift to liquid crystal environments by following the temperature dependence of chemical shift of ^{129}Xe dissolved in various liquid crystals and liquid crystalline mixtures.[100,101] Again, the area of noble gas studies of isotropic and anisotropic fluids has recently been reviewed.[37]

An interesting and potentially important aspect of liquid crystal behavior is the effect of confined geometry.[102] In this paper we report the application of xenon NMR to the study of a liquid crystal (ZLI 1132) confined to cylindrical cavities of submicron diameter. Both NMR active isotopes of xenon ^{129}Xe and ^{131}Xe are used, and spectra of xenon dissolved in the confined liquid crystal are compared to the spectra of xenon dissolved in the bulk liquid crystal. The examination of the surface induced alignment effects is facilitated by the ability to control the orientation of the long axis of the cylinders with respect to the field.

2.6.2 Background

The ordering of a liquid crystal confined to a small volume is a consequence of the competition between the elastic forces within the liquid crystal and the molecular interactions with the surface, in addition to alignment induced by externally applied electric or magnetic fields. A grooved surface can strongly anchor the molecules in a

preferred direction and various surface coatings can also exert effects on the alignment of the molecules by changing the surface interaction energy.[103] Optical techniques, such as surface ellipsometry, have long been used to investigate these effects,[104] but NMR, lacking sufficient sensitivity to probe a surface area which is generally a few square centimeters, has typically been relevant only to studies of bulk phases. Liquid crystals confined in submicron structures, however, are high surface area systems in which sufficient liquid crystalline material can be loaded to allow NMR studies. Surface orientation effects in these systems have been observed previously using NMR of site-selectively deuterated liquid crystals.[105] It has been shown that in these submicron sized systems, liquid crystals behave quite differently than in the bulk, as might be anticipated from the potential for strong liquid crystal-surface interactions. Xenon NMR has the advantage over previous deuterium NMR studies of microconfined liquid crystals that no special synthesis is required for the liquid crystal.

Although magnetic fields also are capable of orienting liquid crystals, in these confined systems the effect is expected to be much weaker than effects due to surface interactions. The magnetic coherence length, ξ_m,[106] is determined by the magnetic field strength B, the susceptibility anisotropy $\Delta\chi$, and the elastic constant of the medium K through $\xi_m=\sqrt{(K/\Delta\chi)}/B$. In a field of 11.7 T, the magnetic coherence length is on the order of 1 micron. Since the magnetic field coherence length is larger than the cavity diameter (0.2 μ), the formation and orientation of the local director axis is dominated by the surface interactions in these confined systems, with the magnetic field playing only a secondary role. The dominance of the surface effects enables observations to be made with different angles of the director axis with respect to the magnetic field, which is typically not possible in the bulk because of fast realignment of the director along the magnetic field.

The liquid crystal studied here is loaded into a high surface area anopore membrane shown schematically in Figure 2.18. These membranes are composed of aluminum oxide that has been electrochemically treated to create a non-interconnected set of highly parallel pores through the membrane. The membranes have a very narrow distribution of pore diameters, with an average diameter of 0.2 μ.[102] The extremely high pore density (up to 10^9 pores/cm^2) results in BET surface areas of approximately 10 m^2/g.[102] Each membrane is 60 μ thick and may be cut into square sheets.

Previous deuterium NMR studies have shown that the alignment axis of the director is perpendicular to the wall.[107] Although several director configurations are possible; in this case it is known that a lecithin coating reduces the surface interaction energy, making a planar-polar configuration a relative energy minimum.[107] This structure is sketched above the membrane in Figure 2.18. Deuterium NMR has shown that in lecithin treated anopores the director axis of the configurations do not align along the magnetic field, but instead remain pinned at random orientations within the plane perpendicular to the cylinder axis.

2.6.3 Experimental

The anopore membranes were cut into square strips 2.0 x 1.0 cm and treated with lecithin before being loaded with ZLI 1132 (Merck, a mixture of trans-4-n-alkyl-(4'-cyanophenyl)-cyclohexanes and trans-4-n-pentyl-(4'-cyanobiphenyl) cyclohexane). The coating and loading procedure has been described in detail.[102] ZLI 1132 was chosen due to its convenient nematic range and since it has been characterized previously in the bulk by xenon NMR.[101,108] Several glass sample cells were constructed from square tubing (1.0 x 1.0 cm ID) to accommodate the membranes tightly and facilitate orientational studies. Approximately 100 membranes were

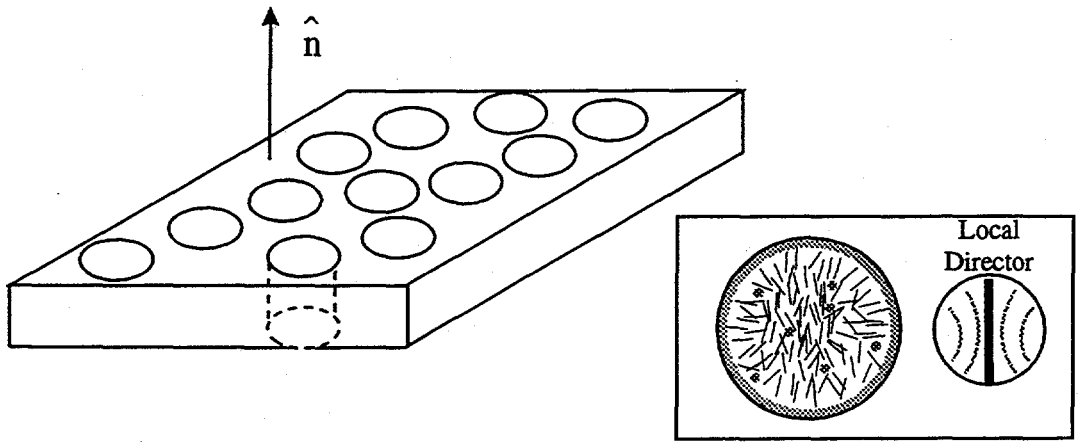

Figure 2.18 Schematic picture of an anopore membrane whose unit normal is denoted n̂. The lecithin induced "planar polar" director field within the pores is sketched beside the membrane. The membrane size is 15 x 10 x 0.06 mm, and the cylinder diameters are 0.2 μm.

stacked into each cell. One cell was loaded with 6 atm enriched ^{129}Xe (EG+G Mound, 80%) and another with 5 atm enriched ^{131}Xe (EG+G Mound, 70%) and flame sealed. Before starting the experiments the cells were briefly heated to above 100 °C to allow the xenon to dissolve rapidly into the isotropic phase of the liquid crystal. For comparison, samples of bulk ZLI 1132 were also prepared with 3 - 5 atm of enriched ^{131}Xe and ^{129}Xe.

The spectra were recorded on a 500 MHz (11.7 T) CMX spectrometer operating at 138 MHz for ^{129}Xe and 41 MHz for ^{131}Xe nuclei and a 400 MHz Bruker (9.4 T) with a ^{129}Xe frequency of 110 MHz. The 90° pulse for ^{129}Xe was 10 μs. Typical relaxation delays were 30 s for ^{129}Xe and 50 ms for ^{131}Xe, and sufficient S/N was achieved with 200 - 400 and 100,000 - 500,000 scans, respectively. All reported chemical shifts are referenced to an external standard of low pressure Xe gas.[49]

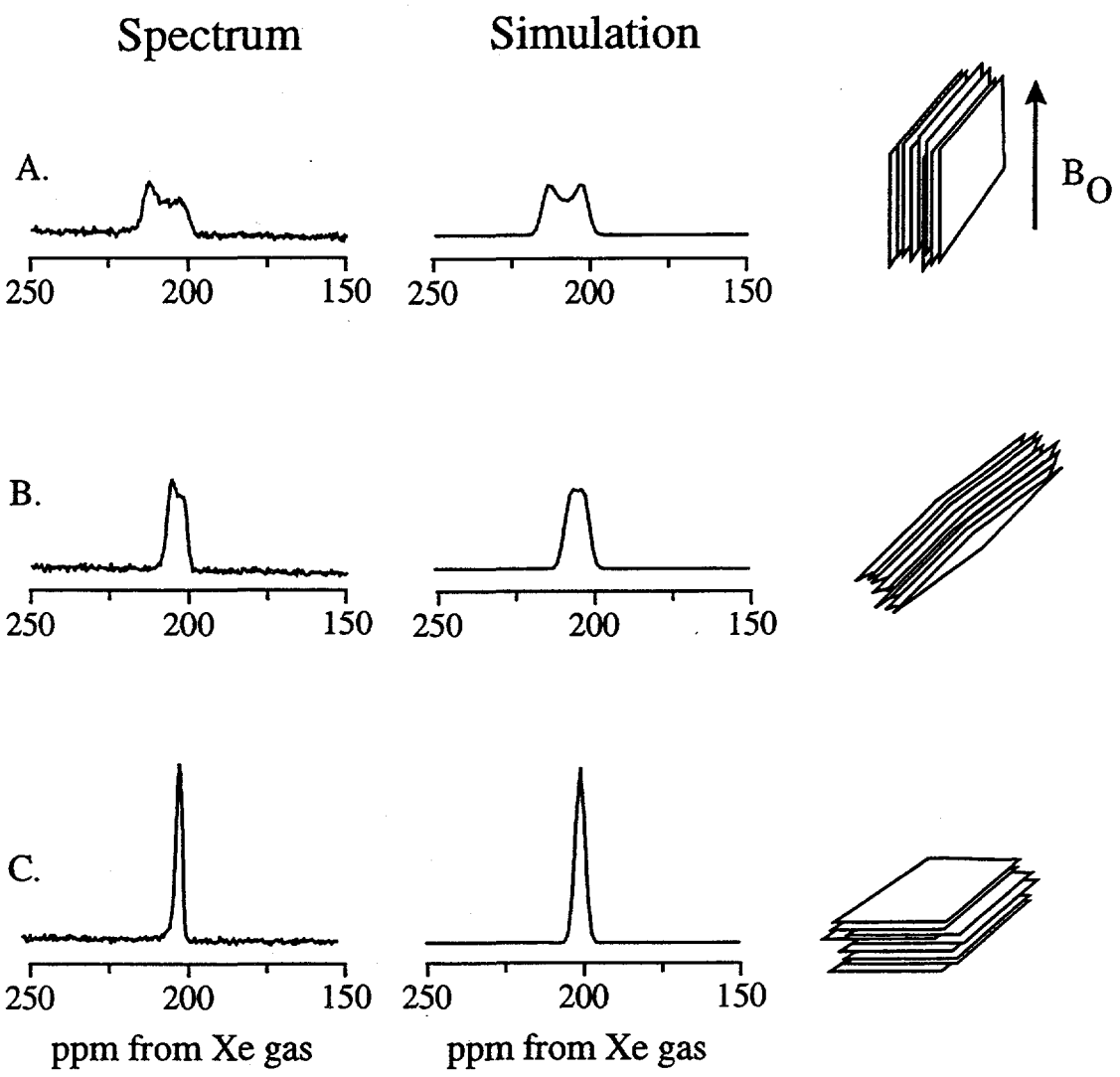

Figure 2.19 Experimental and simulated ^{129}Xe spectra in ZLI 1132 confined within anopore membranes (T= 19°C and P = 5 atm) at various orientations with respect to the magnetic field. (a) $\hat{n} \perp \vec{B}$ (b) 45° (c) $\hat{n} \parallel \vec{B}$.

Diffusion measurements of xenon in ZLI 1132 at room temperature were performed using a pulsed field gradient spin echo technique on a sample of ZLI 1132 sealed with 5 atm of 80% ^{129}Xe (EG + G Mound) and ~50 torr O_2 (Matheson). The experiments were performed with a 180 MHz (4.3 T) micro-imaging spectrometer (Quest 4300, Nalorac Cyrogenics Inc) operating at 51 MHz for ^{129}Xe and using cylindrical micro-imaging gradients (Nalorac Cryogenics Inc.) and a homebuilt probe. A 500 μs slice-selective pulse was used. Gradients from 5 kHz/mm to -5 kHz/mm in 64 steps were applied for a 1 ms duration with a 500 ms delay between the end of the first gradient pulse and the application of the 180° refocussing pulse. Eight acquisitions were made at each gradient value. Diffusion measurements were made both parallel and perpendicular to the director axis.

Numerical simulations of spectral lineshapes were carried out for a random distribution of directors within a plane (transverse isotropy) as a function of the angle between the magnetic field axis and the plane. Line shapes were calculated using an axial chemical shift tensor and were convolved with Gaussian line broadening to mimic the broadening observed in the experimental spectra.

2.6.4 Results

In the bulk sample of ZLI 1132 at 27 °C, the chemical shift of ^{129}Xe was measured to be 222 ppm with a linewidth of 1.5 ppm, approximately equal to that expected from the magnetic field inhomogeneity. Figure 2.19 shows the spectra of ^{129}Xe in ZLI 1132 confined to the cavities of the anopore sample with various orientations of $\hat{\mathbf{n}}$. The vector $\hat{\mathbf{n}}$ is the normal to the membrane surface; $\hat{\mathbf{n}}$ is parallel to the long cylinder axis and perpendicular to the directors (Figure 2.19). With $\hat{n}\|\vec{B}$ a single line is observed at 201 ppm. With $\hat{n}\perp\vec{B}$ a much broader signal is observed and exhibits a lineshape that is characteristic of a random distribution of director axes in a two-dimensional

plane, a distribution also known as "transverse isotropy."[109] The simulated lineshapes show satisfactory agreement with the experiment; the slight distortions from the theoretical shape are likely due to misalignment of the membranes with respect to the field. The splitting, corresponding to the separation between singularities in the line shape, represents the anisotropy of the chemical shift interaction and is found to be 15 ppm at 21 °C. As in bulk samples,[110] the chemical shift anisotropy of ^{129}Xe within the confined liquid crystal is temperature dependent, monotonically decreasing with increasing temperature, from 15 ppm at 21 °C to 8 ppm at 90 °C. The isotropic chemical shift moves upfield with increasing temperature at 0.23 ppm K^{-1}, compared to the 0.25 ppm K^{-1} found in bulk studies.[101]

The chemical shift anisotropy has been previously measured in several liquid crystals by observing the change in chemical shift at the nematic-isotropic transition.[100] This method is affected by the temperature and phase dependence of σ_{iso}; however, from the data of Jokisaari and Diehl (Figure 2 in reference [101]), the anisotropy near the transition temperature appears to be 11 ppm for bulk ZLI 1132, compared to 8 ppm in the present confined system.

The nematic-isotropic transition in our bulk samples without xenon was measured to be 74 ± 1 °C, by observation of the clearing temperature. It has been observed previously that the transition temperature depends on the total pressure of xenon dissolved.[100] The transition temperature is further altered in the restricted geometry. In the anopores, the transition was found to be 96 ± 3 °C for the sample which includes ^{129}Xe gas dissolved under a pressure of ~6 atm. This transition is shown in Figure 2.20, where the anisotropic line shape at 190 ppm collapses to a narrow isotropic line. The resonance assigned to the xenon gas near 0 ppm also shows structure. The gas resonance is composed of two partially resolved peaks whose separation is independent of temperature over the range 0 - 100 °C. There is a very narrow

component identified with the gas in regions of the tube that contain no sample, and a broader component most likely due to gas that experiences magnetic susceptibility shifts between the plates and interactions with the aluminum oxide surface.

The quadrupolar splitting (defined as the frequency separation of the satellite transitions) of ^{131}Xe in the bulk sample at 29 °C was measured to be 207 kHz, in agreement with the results of previous work.[108] Figure 2.21 shows the spectrum of ^{131}Xe in ZLI 1132 in the anopore sample at the orientation $\hat{n}\|\vec{B}$. The quadrupolar splitting has been measured as 230 kHz at 49 °C in the bulk.[108] In the anopore™ membrane at 49 °C the quadrupolar splitting is reduced to 120 kHz. The quadrupolar splitting scales as $P_2(\cos\vartheta)$, where ϑ is the angle between the director and the magnetic field, thus a scaling of 0.5 is anticipated because, with this macroscopic

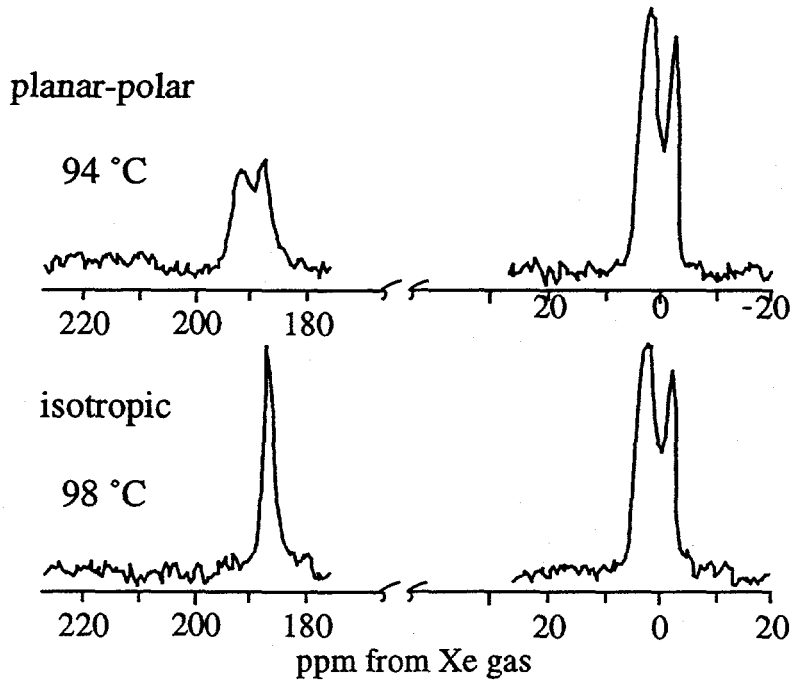

Figure 2.20 ^{129}Xe spectra of ZLI 1132 confined within anopore membranes, at temperatures just below (94 °C) and above (98 °C) the isotropic to nematic phase transition.

orientation of the membranes, all of the directors are perpendicular to the field (Figure 2.19). Since the splitting is slightly more than one half of the bulk value, it appears that the electric field gradient experienced by the xenon is slightly higher in the confined liquid crystal than in the bulk. The linewidth is 1.2 kHz for the central transition and 4.5 kHz for the satellites. The satellite transitions are difficult to observe in the ^{131}Xe spectrum since they are broadened by slight misalignments of the membranes, temperature gradients over the sample, and small temperature fluctuations over the acquisition time. The satellites broaden out rapidly upon rotating the sample and are unobservable at more than a few degrees of misalignment from the magnetic field.

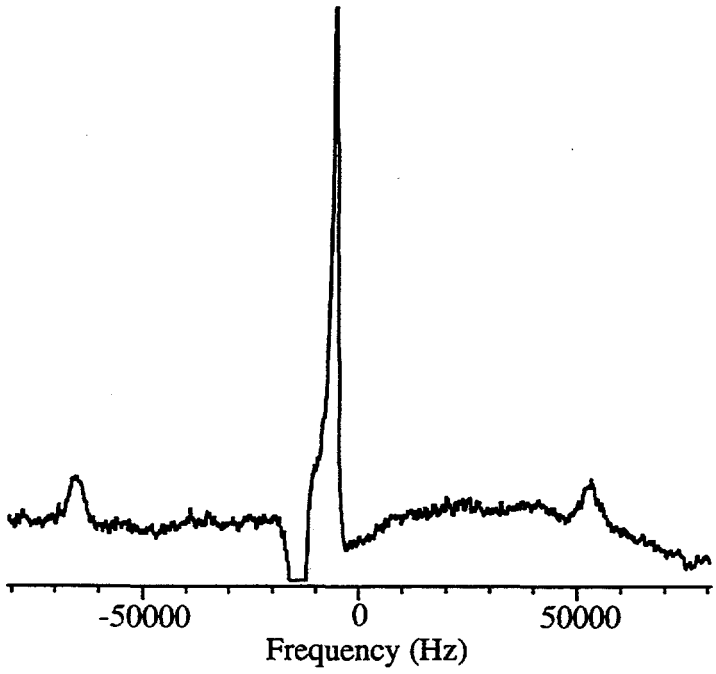

Figure 2.21 ^{131}Xe spectra in ZLI 1132 within anopore membranes shows the entire triplet (and the gas phase peak which is inverted and truncated), T=48 °C, splitting = 120 kHz. NA= 206,450.

The diffusion measurements of xenon within bulk ZLI 1132 yielded a value of $2.0 \pm 0.3 \times 10^{-10}$ m^2/s with no observable anisotropy.

2.6.5 Discussion

Liquid crystals confined to the cylindrical cavities with dimensions much less than the magnetic coherence length allow measurements that are not normally possible in bulk liquid crystals. In these systems, rotation of the cylinders with respect to the direction of the magnetic field can provide a direct measurement of anisotropic interactions in these systems. In the case of the lecithin treated membranes, perpendicular anchoring of the liquid crystal molecules is obtained,[111] and a random distribution of the director configurations in the plane perpendicular to the long cylinder axes has been observed. The anisotropy of the ^{129}Xe chemical shift can be *directly* determined from the splitting of the transverse isotropic powder pattern. This enables a direct determination of the anisotropy of a particular configuration over a broad temperature range, compared to other methods which only infer the anisotropy from the change in chemical shift at the nematic-isotropic transition.

Using the measured diffusion constant of the xenon in ZLI 1132, $D = 2.0 \times 10^{-10}$ m^2/s, it can be estimated that it takes only ~ 25 μs for the root mean square distance travelled by dissolved xenon in the cross-sectional plane of the cylinders to approach the 0.1 μm radius of the cylinder. Given that the observed anisotropy is on the order of 1-2 kHz, this rate of diffusion ensures that the exchange within this plane is in the fast exchange regime, and that the observed chemical shift represents the average chemical shift in the cross-sectional plane. Thus, the observed decrease in chemical shift anisotropy with increasing temperature indicates either a temperature dependent change in planar polar configuration or a reduction in the order parameter of the liquid crystal. The xenon chemical shift line shape can be viewed as a complement to the

deuterium lineshape analysis used previously to identify and assign liquid crystalline configurations in these system; whereas deuterium NMR provides a detailed view of individual molecular orientations in the plane, xenon NMR gives an average over the cylinder cross section and makes possible the study of greater length scales.

2.6.6 Conclusions

It has been shown that xenon NMR studies of microconfined liquid crystals are feasible and supply new information about such systems. The two xenon isotopes offer different observables with which to probe the liquid crystal system. Additional insight is gained when studies of confined liquid crystals are compared to bulk studies. The main difference between confined and bulk liquid crystal is the slightly decreased chemical shift anisotropy of ^{129}Xe at the nematic-to-isotropic transition and slightly enhanced quadrupolar splittings of ^{131}Xe. The difference in quadrupolar splitting could be due to the additional effects of the cavity walls on the polarization of xenon atoms or a change of the liquid crystal order parameter at the wall.

2.7 Conclusions

Xenon NMR can be used to study a large variety of systems. The interactions of xenon atoms with their environments perturb the xenon electron density; these interactions can be monitored by observing the xenon chemical shift. When ^{129}Xe is in fast exchange between different sites, a series of one dimensional experiments may be performed to extract dynamical information. In cases when ^{129}Xe is in slow exchange between different sites, i.e. multiple peaks are observed in a one-dimensional experiment, two-dimensional NMR may be used to extract additional dynamical information. Two dimensional xenon exchange experiments are the subject of the next chapter.

Chapter 3

Two-Dimensional Xenon Exchange NMR

3.1 Introduction

One of the most exciting advances since the original discovery of NMR has been two-dimensional Fourier Transform NMR. Multidimensional NMR has enabled complicated protein structure elucidation, correlation between different NMR interactions of the same type or different kinds of nuclei, and enabled dynamical studies of the motion of molecules on time scales approaching the T_1s of the molecules. An extraordinary number of two dimensional experiments have been applied to problems in physics, chemistry, biology and medicine. One particular type of 2D experiment which monitors chemical exchange is known as exchange NMR. This chapter introduces exchange NMR, outlines how it has been used with xenon, and presents two examples of 2D xenon exchange NMR.

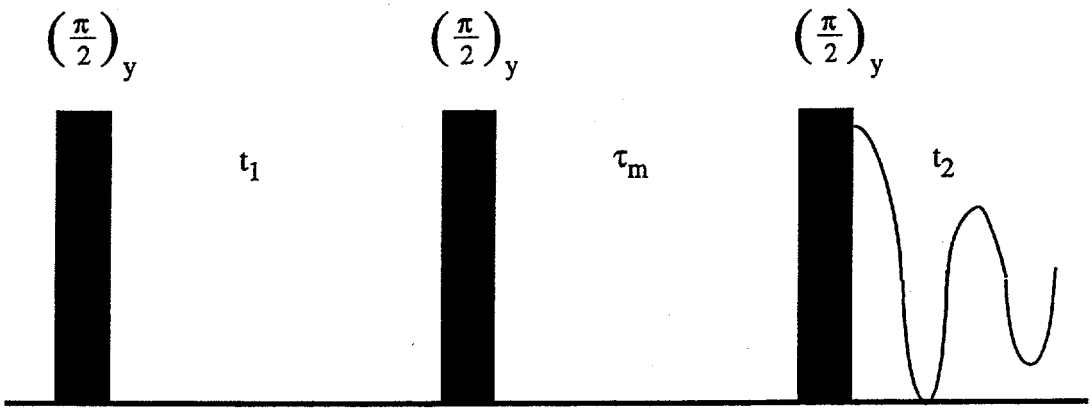

Figure 3.1 Basic pulse sequence for 2D exchange spectroscopy, where t_1 and t_2 indicate the evolution and detection periods. The exchange time τ_m is normally kept constant in a 2D experiment.

3.2 Theory

The idea of two dimensional NMR spectroscopy was first introduced by Jeener at a conference, though Ernst was the first to exploit the great potential of the method.[5,112] A signal $S(t_1, t_2)$ is measured as a function of two independent time variables and is converted by a 2D Fourier Transform into a 2D frequency domain spectra $S(\omega_1, \omega_2)$. In 2D exchange NMR, the general idea is to label the frequency of various sites before exchange takes place and then observe how the frequencies change after a mixing time. The pulse sequence used for the experiments described in this chapter is pictured in Figure 3.1. It involves a 90° pulse, evolution for a time t_1, application of a second 90° pulse, followed a mixing time τ_m, and a third 90° pulse for detection of single quantum coherence in t_2. A symmetrical two site chemical exchange case with

equal concentrations, equal spin-lattice relaxation rates, and equal transverse relaxation rates is analyzed below. The transverse magnetization, excited by the initial $(\frac{\pi}{2})_y$ pulse precesses freely in the t_1 interval. If the exchange is slow, its effect on the lineshape in this period may be neglected. Two complex magnetization components are obtained.

$$M_A^+(t_1) = M_{A0}\exp\{i\Omega_A t_1 - t_1 / T_2\} \tag{3.1}$$

$$M_B^+(t_1) = M_{B0}\exp\{i\Omega_B t_1 - t_1 / T_2\} \tag{3.2}$$

If the second pulse is applied along the y-axis the real components of the transverse magnetization are converted into longitudinal magnetization.

$$M_{Az}(\tau_m = 0) = -M_{A0}\cos\Omega_A t_1 \exp\{-t_1 / T_2\} \tag{3.3}$$

$$M_{Bz}(\tau_m = 0) = -M_{B0}\cos\Omega_B t_1 \exp\{-t_1 / T_2\} \tag{3.4}$$

The t_1-modulated longitudinal components in (3.3) and (3.4) migrate from one site to another because of chemical exchange or cross-relaxation, while spin-lattice relaxation attenuates the "memory" of the initial labeling.

$$\begin{aligned} M_{Az}(\tau_m) &= M_{Az}(\tau_m = 0)\frac{1}{2}[1+\exp\{-2k\tau_m\}]\exp\{-\tau_m / T_1\} \\ &+M_{Bz}(\tau_m = 0)\frac{1}{2}[1-\exp\{-2k\tau_m\}]\exp\{-\tau_m / T_1\} \end{aligned} \tag{3.5}$$

$$\begin{aligned} M_{Bz}(\tau_m) &= M_{Az}(\tau_m = 0)\frac{1}{2}[1-\exp\{-2k\tau_m\}]\exp\{-\tau_m / T_1\} \\ &+M_{Bz}(\tau_m = 0)\frac{1}{2}[1+\exp\{-2k\tau_m\}]\exp\{-\tau_m / T_1\} \end{aligned} \tag{3.6}$$

where k is the rate constant of the exchange process. The final $(\frac{\pi}{2})_y$ pulse converts the longitudinal components into observable transverse magnetization. After 2D Fourier Transformation, cross peaks at $(\omega_1, \omega_2) = (\Omega_A, \Omega_B)$ with an integrated

amplitude $I_{BA}(\tau_m)$ appears if a magnetization component that precessed at Ω_A in t_1 precesses at Ω_B in t_2. The amplitudes $I_{kl}(\tau_m)$ of the diagonal and cross peaks depend on the equilibrium magnetization M_{l0} and on mixing coefficients $a_{kl}(\tau_m)$.

$$I_{AA}(\tau_m) = a_{AA}(\tau_m)M_{A0} \tag{3.7}$$

$$I_{BB}(\tau_m) = a_{BB}(\tau_m)M_{B0} \tag{3.8}$$

$$I_{AB}(\tau_m) = a_{AB}(\tau_m)M_{B0} \tag{3.9}$$

$$I_{BA}(\tau_m) = a_{BA}(\tau_m)M_{A0} \tag{3.10}$$

The mixing coefficients correspond to the factors in (3.5) and (3.6). In the symmetrical two-site case discussed above for $M_{A0}=M_{B0}$, the exchange rate can be determined from the ratio of the peak intensities.

$$\frac{I_{AA}}{I_{AB}} = \frac{a_{AA}}{a_{AB}} = \frac{1+\exp\{-2k\tau_m\}}{1-\exp\{-2k\tau_m\}} \cong \frac{1-k\tau_m}{k\tau_m} \tag{3.11}$$

This treatment can be generalized to N sites with different relaxation and exchange rates for systems without resolved couplings using modified classical Bloch equations.[5] Again, the initial $(\frac{\pi}{2})_y$ pulse generates transverse magnetization along the x-axis:

$$M^+(t_1 = 0) = M_x(t_1 = 0) + iM_y(t_1 = 0) = M_0. \tag{3.12}$$

with $M_y(t_1=0)=0$. The evolution of the complex transverse magnetization is governed by a set of N coupled differential equations: $\frac{dM^+}{dt} = L^+M^+$ (3.13)

where $L^+ = i\Omega - \Lambda + K$ (3.14)

The diagonal matrices Ω and L contain the chemical shifts Ω_I and the transverse relaxation rates $\lambda_1 = 1/T_{2I}$. The kinetic matrix K represents the effects of chemical exchange. The precession in the t_1 period is described by

$$M^+(t_1) = \exp\{L^+ t_1\} M^+(t_1 = 0). \tag{3.15}$$

The second $(\frac{\pi}{2})_y$ pulse converts the x-component into longitudinal magnetization.

$$M_z(\tau_m = 0) = -\mathrm{Re}\{M^+(t_1)\} \tag{3.16}$$

The evolution of the longitudinal magnetization is described by

$$\frac{d\Delta M_z(\tau_m)}{d\tau_m} = L\Delta M_z(\tau_m) \tag{3.17}$$

$$\text{with} \quad \Delta M_z(\tau_m) = M_z(\tau_m) - M_0, \tag{3.18}$$

$$\text{and} \quad L = -R + K. \tag{3.19}$$

where the diagonal elements of R account for the effects of spin-lattice relaxation and the off-diagonal elements account for cross-relaxation. The solution for (3.17) shows that the magnetization components recover towards equilibrium M_0 in the course of τ_m.

$$M_z(\tau_m) = M_0 = \exp\{L\tau_m\} \Delta M_z(\tau_m = 0) \tag{3.20}$$

The final $(\frac{\pi}{2})_y$ pulse regenerates transverse magnetization:

$$M^+(t_2 = 0) = M_z(\tau_m). \tag{3.21}$$

The overall time dependence can be summarized in the following expression:

$$M^+(t_1, \tau_m, t_2) = \exp\{L^+ t_2\}\left[1 - \exp\{L\tau_m\}\left(\mathrm{Re}\left[\exp\{L^+ t_1\}\right] + 1\right)\right] M_0 \tag{3.22}$$

Terms which do not depend on t_1 give rise to axial peaks and are usually eliminated by phase cycling. Neglecting these terms the time dependence takes the form:

$$M^+(t_1,\tau_m,t_2) = \exp\{L^+t_2\}\exp\{L\tau_m\}\mathrm{Re}\left[\exp\{L^+t_1\}\right]M_0. \quad (3.23)$$

If the experiment is phase cycled to transfer all transverse magnetization, the time dependence can be written as $M^+(t_1,\tau_m,t_2) = \exp\{L^+t_2\}\exp\{L\tau_m\}\exp\{L^+t_1\}M_0$. (3.24)

If the exchange is slow, the contributions of K may be neglected in the evolution and detection periods and the dynamic matrix L can be represented as

$$L^{+(\mathrm{slow})} = i\Omega - \Lambda. \quad (3.25)$$

In this case, the transverse terms develop independently.

$$M_l^+(t_1) = \exp(i\Omega_l t_1 - \lambda_l t_1)M_{l0} \quad (3.26)$$

The time domain signal simplifies to

$$S(t_1,\tau_m,t_2) = -\sum_k\sum_l \exp(i\Omega_l t_2 - \lambda_k t_2)\left[\exp\{L\tau_m\}\right]_{kl} \times \exp(i\Omega_l t_1 - \lambda_l t_1)M_{l0}. \quad (3.27)$$

After 2D Fourier transformation, the integrated amplitude of a signal with frequency coordinates $(\omega_1, \omega_2)=(\Omega_l, \Omega_k)$ is $I_{kl}(\tau_m) = a_{kl}(\tau_m)M_{l0}$. (3.28)

with $a_{kl}(\tau_m) = \left[\exp\{L\tau_m\}\right]_{kl}$. (3.29)

The 2D spectrum is essentially a pictorial representation of the exponential mixing operator.

3.3 Xenon Exchange NMR

Two-dimensional xenon exchange NMR has been used to probe polymer domains, the liquid-gas coexistence curve, and the dynamics of NaA zeolite.[52,113,114] Using 2D exchange xenon NMR it is possible to obtain information on the average domain size

of polymer blends. Such experiments on monoatomic systems may serve for calibration of theoretical models and of numerical simulations of the liquid-gas equilibrium dynamics. In the case of xenon atoms adsorbed in NaA zeolite, two-dimensional exchange NMR was used to determine the microscopic rates of intercage motion and to relate them to the adsorption and activation energies of the xenon atoms. In the following sections 2D xenon exchange NMR is used to gain information about the morphology of two of the systems discussed in Chapter 2: the V_2O_5 catalysts and the microconfined liquid crystals.

3.4 2D Xenon Exchange NMR Experiments of Xe Adsorbed on V_2O_5

3.4.1 Introduction

To further investigate the relationship of the two peaks observed in the ^{129}Xe NMR spectrum for V_2O_5 discussed in the previous chapter, two-dimensional (2D) exchange spectroscopy[112,115] was used to study the dynamics of xenon motion between the two sites.

3.4.2 Experimental Details

A sample of pure V_2O_5 (Aldrich) was used. Approximatley 2 atm of 80% enriched xenon-129 was added and the sample was flame-sealed in a Pyrex ampoule (10 mm O. D.). The ^{129}Xe NMR spectra were acquired at 11.7 T (138.3 MHz) with a Chemagnetics CMX-500 spectrometer and a $\pi/2$ pulse of 5 μs. A typical recycle time was 500 ms. The standard NOESY pulse sequence and the method of States et al. was used.[115] Typically, 128 and 256 points were acquired in t_1 and t_2, respectively, with increments of 0.1, 0.5, 1, 2, 4, 10, and 50 ms and 256 scans per t_1 value. During

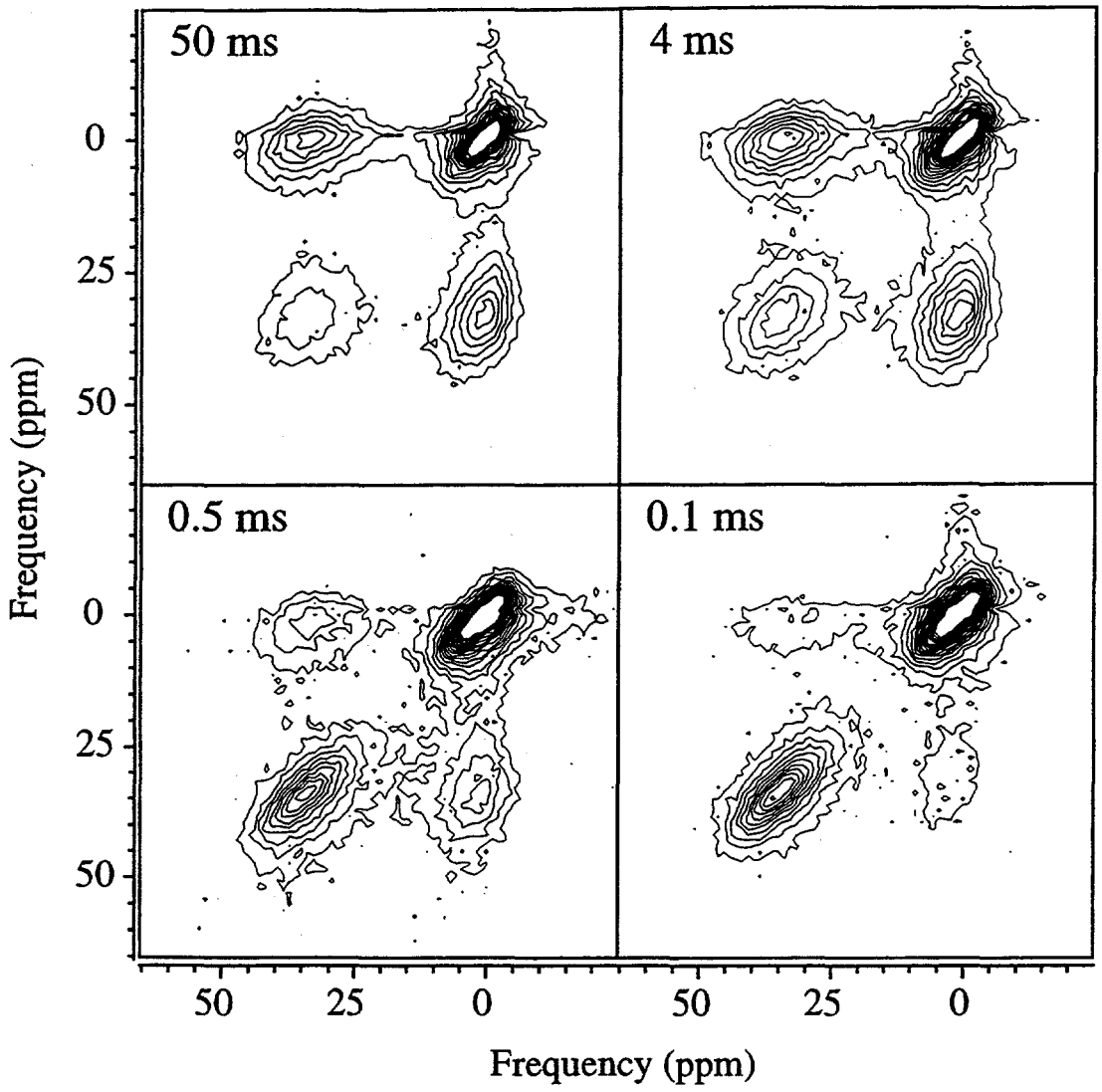

Figure 3.2 ^{129}Xe 2D exchange NMR spectra of xenon adsorbed on V_2O_5 at 290 K and a xenon pressure of approximately 2 atmospheres. The spectra were recorded using mixing times of 50, 4, 0.5, and 0.1 ms and a recycle delay of 300 ms. The contour lines represent 1% to 20% of the maximum intensity.

data processing, the t_1 dimension was zero filled to 256 points and 100 Hz Gaussian line-broadening was applied in both dimensions. The T_1 relaxation time was determined using the saturation recovery pulse sequence and fitting the intensity as a function of delay time to an exponential function.

3.4.3 Results and Discussion

In Figures 3.2 and 3.3 the ^{129}Xe two-dimensional exchange NMR spectra of xenon adsorbed on V_2O_5 using the mixing times indicated is presented. The diagonal peaks correspond to ^{129}Xe resonances from xenon atoms in two different environments. The cross-peaks result from motion of xenon between the two distinct environments during the mixing time of the 2D experiment and have intensities that are proportional to the number of xenon that exchanged. By fitting the intensity of the cross-peak divided by the intensity of the adsorbed peak as a function of mixing time to an exponential function and obtained the following rate constants ($1/\tau$) for the exchange of xenon between the two environments: 0.78, 0.91, and 1.45 ms^{-1} for temperatures of 210, 250, and 290 K, respectively. These rate constants are consistent with an activation energy of 0.24 ± 0.09 kcal/mole. A distance between the two xenon environments of $5 \cdot 10^{-5}$ m can be estimated from the rate constants assuming non-activated diffusion. The diameter of the particles of the V_2O_5, are between $1.5 \cdot 10^{-4}$ m and $3.0 \cdot 10^{-4}$ m. Also, using these rates, the width of the peaks due to exchange broadening can be approximated by $(\tau\pi)^{-1}$. The width of the low frequency peak appears to be dominated by exchange broadening, which is supported by the observed field and temperature dependences. From the shift and exchange data it is evident that the xenon of the low frequency peak is gas-like and in slow exchange with the adsorbed xenon. The existence of pores is indicated by the hysteresis of the isotherm data and may be related to the presence of two distinct sites for xenon.

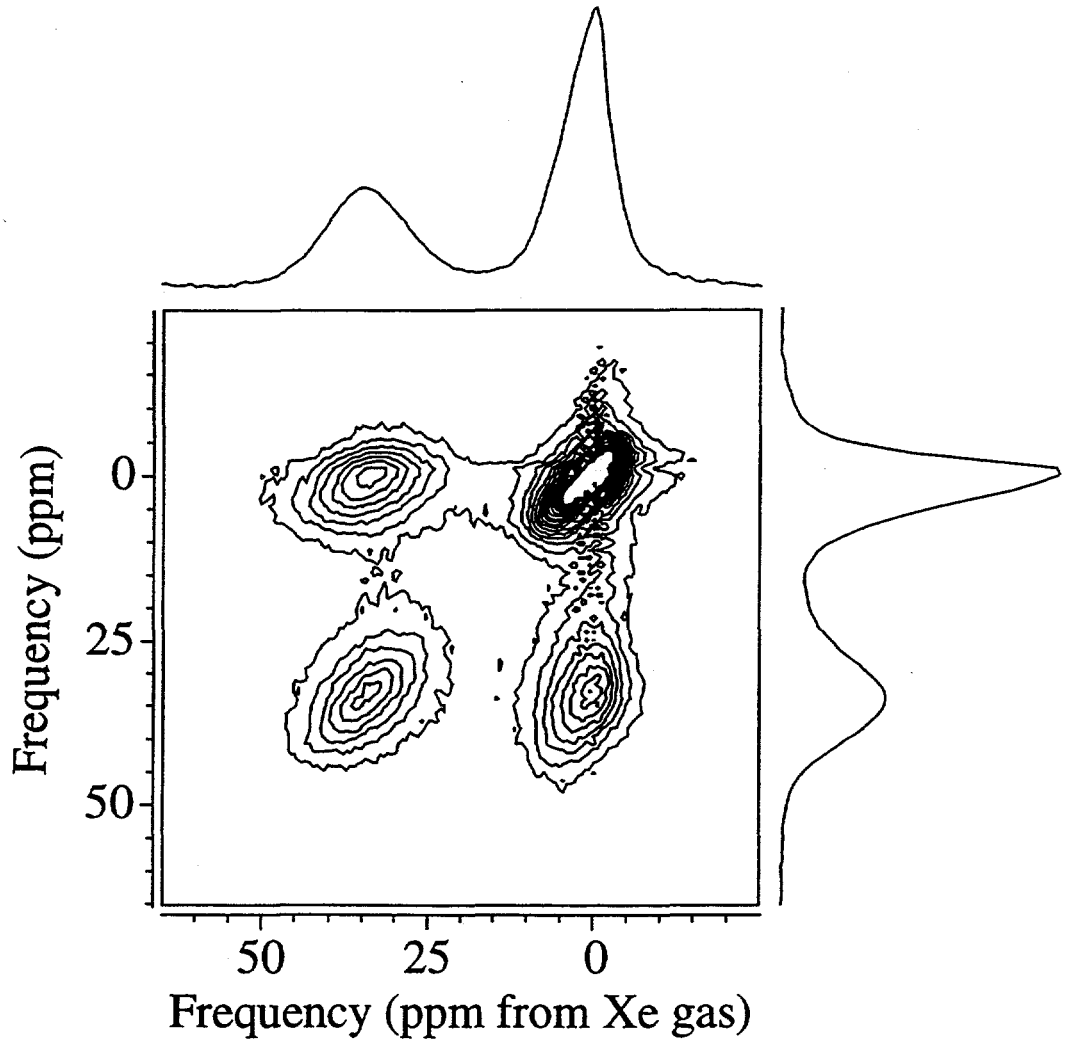

Figure 3.3 ^{129}Xe 2D exchange NMR spectrum of xenon adsorbed on V_2O_5 at 290 K and a xenon pressure of approximately 2 atmospheres. The spectrum was recorded using a mixing time of 2 ms and a recycle delay of 300 ms. The contour lines represent 1% to 20% of the maximum intensity.

3.4.4 Conclusions

^{129}Xe NMR of xenon sorbed on V_2O_5 reveals the existence of two distinct environments for xenon. The xenon adsorption and desorption isotherms of V_2O_5 point to the existence of pores. Therefore, the two sites may be attributed to gas-like xenon in pores, susceptibility-shifted from the true gas peak, and xenon adsorbed on the surface of the V_2O_5. Two-dimensional exchange spectroscopy reveals that xenon diffuses between these two environments; the rates of 0.78, 0.91, and 1.45 ms^{-1} at temperatures of 210, 250, and 290 K show that these environments are within close proximity.

3.5 Xenon Exchange in Confined Liquid Crystals

3.5.1 Introduction

Two-dimensional xenon NMR spectroscopy can also reveal information about the confined liquid crystal system discussed in the previous chapter. Since the xenon resonance is sensitive to the director orientation, further information about the spatial proximity of different director orientations can be obtained by following xenon magnetization exchange between the different components of the xenon spectrum.

3.5.2 Experimental

The anopore membranes were cut into square strips 2.0 x 1.0 cm and treated with lecithin before being loaded with ZLI 1132 (Merck, a mixture of trans - 4 - n - alkyl-(4'-cyanophenyl) - cyclohexanes and trans - 4 - n - pentyl - (4' - cyanobiphenyl) cyclohexane).The coating and loading procedure has been described in detail.[102] A square pyrex cell in which approximately 100 membranes were tightly packed was loaded with 6 atm enriched ^{129}Xe (EG+G Mound, 80%) and flame sealed. Before

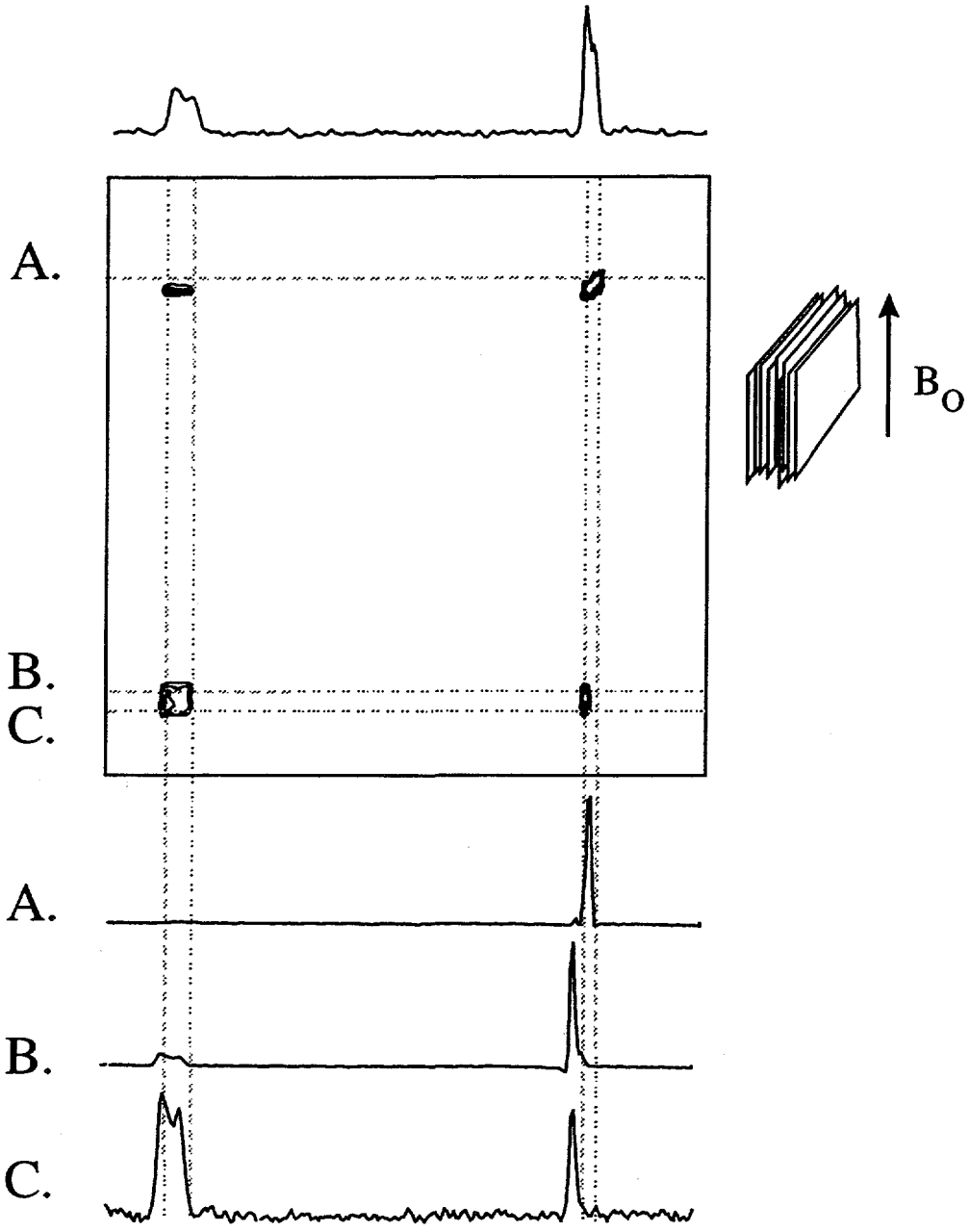

Figure 3.4 2D exchange spectra of xenon in ZLI 1132 loaded into anopore membranes at T= 33 °C with τ_m = 400 msec. The projection is shown. (A), (B), and (C) Three different slices indicated by the dashed lines are shown. The largest peaks are normalized to the same height.

starting the experiments the cells were briefly heated to above 100 °C. A standard pulse sequence and the method of States *et al.* [115] or TPPI[116,117] were used to obtain pure absorption spectra. Typically, 128 and 256 points were acquired in t_1 and t_2, respectively, with 8 scans per t_1 value. During data processing, the t_1 dimension was zero-filled to 256 points and 100 Hz. Gaussian line-broadening was applied in both dimensions.

3.5.3 Results and Discussion

Figure 3.4 shows the two-dimensional ^{129}Xe exchange spectrum obtained with a mixing time of 400 ms. The spectrum has off diagonal peaks connecting the gas and liquid crystal resonances, indicating that exchange is occurring between these two regions on this time scale. The observed exchange at 400 ms occurs only with the second, broad gas component, associated with xenon near the membranes. Figure 3.5 a indicates the exchange occurring with a τ_m of 20 ms. Figure 3.5 b shows the detail of the liquid crystal region and displays the effects of exchange among the different components of the inhomogeneous dissolved xenon lineshape, indicating that exchange among the different components of the xenon dissolved in a liquid crystal at 25 °C also takes place on a time scale of 20 ms.

Two-dimensional exchange experiments as a function of mixing time indicate that exchange between liquid crystal-director axes is faster than gas to liquid crystal exchange. Xenon atoms are therefore exchanging between different environments within a single pore. One possible mechanism for this is that if the observed 1D line shape is representative of a single pore, then the xenon may remain bound near the liquid crystal/anopore interface for times around 20 ms and then rapidly diffuse through the pore until binding at another interface site where there is a different director

orientation. This possibility relies on unreasonably long surface residence times, and thus appears unlikely.

If the distribution of directors were from different pores, the observed exchange would dictate that the average environment experienced by the xenon within each pore must be varying on the time scale of ~20 ms. Director order fluctuations of the liquid crystals within a pore appear unlikely because of the timescale of the slowest reorientation mode, $1/\tau \approx Kq^2/\eta$ where $q \equiv \pi/r = 30\mu^{-1}$.[106] Inserting typical values for K=10^{-11} N and $\eta = 10^{-2}$ N s/m^2, one obtains $\tau = 10$ μs, which is much too short to

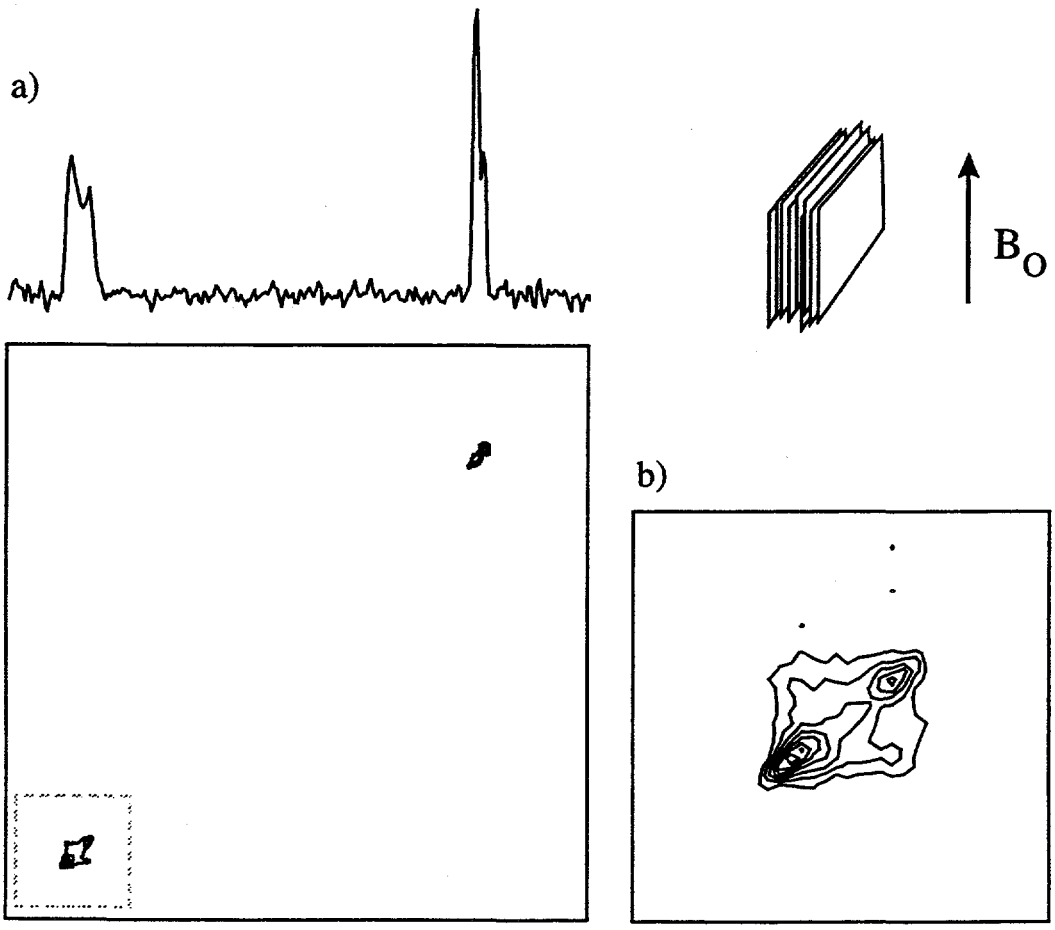

Figure 3.5 2D exchange spectra of xenon in ZLI 1132 loaded into anopore membranes a) Entire spectrum at T= 25 °C with τ_m = 20 msec. b) An expansion of the liquid crystal region (boxed).

account for the appearance of off diagonal intensity (~20 ms).

A third, more probable, mechanism is a change in the orientation of the symmetry axis of the configuration along the cylinder axis due to random changes in surface roughness and ellipticity of the cylinders. These deviations are thought to be the cause of the random distribution of director axes observed in this study as well as previous deuterium NMR studies.[111] At τ_m = 20 ms an estimated 25% of the xenon has undergone a reorientation of its director axis. Using the diffusion constant of 2 x 10^{-10} m^2/s, the root mean square distance traveled by a xenon atom along the cylinder is 2 μm in 20 ms. This defines the length scale between random variations of director domains within each pore. Such an exchange mechanism is illustrated schematically in Figure 3.6.

Diffusion is also responsible for the appearance of exchange between the dissolved and gas phase xenon. At a mixing time of 400 ms, about 20% of the dissolved xenon has appeared in the peak assigned to the susceptibility-shifted gas between the membranes. The root mean square distance along the cylinder axis during this time interval is calculated to be 9 μm (of the 60 μm total length), a reasonable estimate

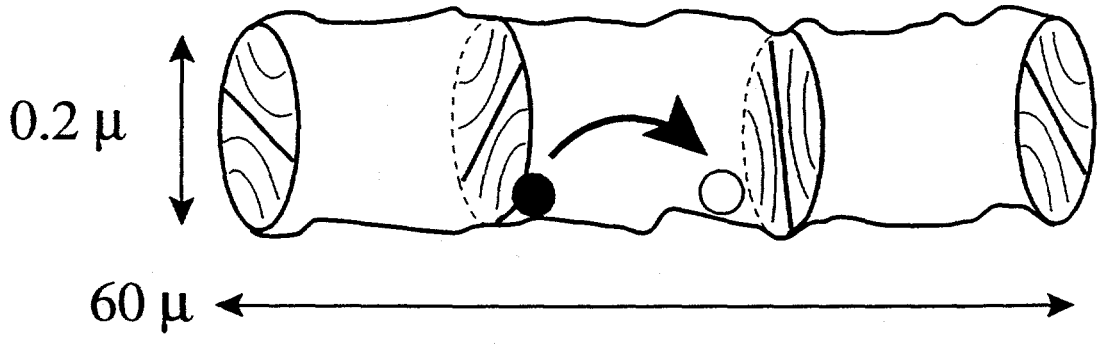

Figure 3.6 Schematic picture of the director structure within a single pore experienced by the xenon atom in the 2D exchange experiment.

given the rough nature of the calculation.

3.5.4 Conclusions

Multi-dimensional experiments offer new possibilities for obtaining information on confined liquid crystal systems. Two-dimensional exchange spectroscopy allows much longer time scales (and thus length scales) to be probed and suggests the presence of variations of the symmetry axis of the director field within a single cavity on a length scale of 2 μm. Finally, the xenon NMR methods discussed in this chapter and the previous chapter could be used to investigate surface induced order in the isotropic phase[118] and studies of other confined systems such as liquid crystals loaded in silica aerogels.[119]

3.6 Conclusions

Two-dimensional xenon exchange NMR can provide complementary information to one-dimensional xenon studies. In addition to obtaining direct dynamical information about xenon motion, in favorable cases, information can be obtained about the morphology of the system studied. In addition to obtaining mix-time dependences, temperature dependences can be performed in order to find a regime where the exchange rate is fast compared to the T_1 but slow compared to the spectral parameters affected by the exchange. Although 2D NMR can provide this additional information, it does not address a fundamental problem of xenon NMR: lack of sensitivity. To solve this problem, we turn to another technique, optical pumping, which will be discussed in the next chapter.

Chapter 4

Optically Polarized Xenon NMR

4.1 Introduction

4.1.1. Sensitivity Considerations

Sensitivity limitations are a major obstacle in the application of NMR to many systems of interest, such as surfaces. Typically, the NMR detection limit is 10^{20} spins. However, for typical organic molecules, the surface is composed of only 10^{15} spins.[120] The signal intensities in NMR are proportional to the population differences between the magnetic sublevels. This population is described by the Boltzmann distribution. For a spin-1/2 nucleus,

$$\frac{n_b}{n_a} = \exp\left(\frac{-\Delta E}{kT}\right) = \exp\left(\frac{-\gamma\hbar B_o}{kT}\right), \tag{4.1}$$

where n_a and n_b are the populations of the magnetic sub-level a and sub-level b, respectively. ΔE is the energy difference between the sub-levels, k is the Boltzmann constant, T is the temperature, γ is the gyromagnetic ratio of the nucleus, $\hbar$ is Planck's

constant, and B_0 is the magnetic field. By expanding the exponential in equation (4.1), the following expression may be obtained:

$$\frac{\Delta n}{N} \approx \frac{\gamma \hbar B_o}{2kT}, \tag{4.2}$$

where N is the total number of nuclei in a sample and Δn is the difference in population between sub-levels a and b. For ^{129}Xe at room temperature in a magnetic field of 4.2 T, the population difference is only on the order of 10 ppm! Obvious approaches to increasing this population difference for a given nucleus are apparent from equation (4.2): increasing B_0 or decreasing T. Additional tactics include polarization transfer from more sensitive nuclei or electrons.[121-124] These methods are very valuable, and in the most favorable case of DNP, signal enhancements on the order of 10^2 have been achieved.[125] These polarization transfer methods will be discussed in Chapter 5. However, in the case of xenon, an alternative approach may be utilized. Drastic signal enhancements may be obtained by establishing a non-equilibrium (non-Boltzmann) distribution through optical pumping.

4.1.2 Nuclear Spin Polarization

Highly nuclear spin polarized xenon has become relatively easily available with the development of optical pumping and spin exchange. With the use of commercially available lasers, ^{129}Xe NMR signals may be enhanced by four to five orders of magnitude. The enhancement of xenon gas is shown in Figure 4.1. The use of optically polarized xenon enables many types of investigations that are inaccessible to conventional xenon NMR, including surface studies. A major limitation of conventional ^{129}Xe NMR is the prohibitively long relaxation time of xenon in the presence of many materials. For instance,xenon adsorbed on poly(acrylic) acid has a ^{129}Xe T_1 of 30 s.[29]

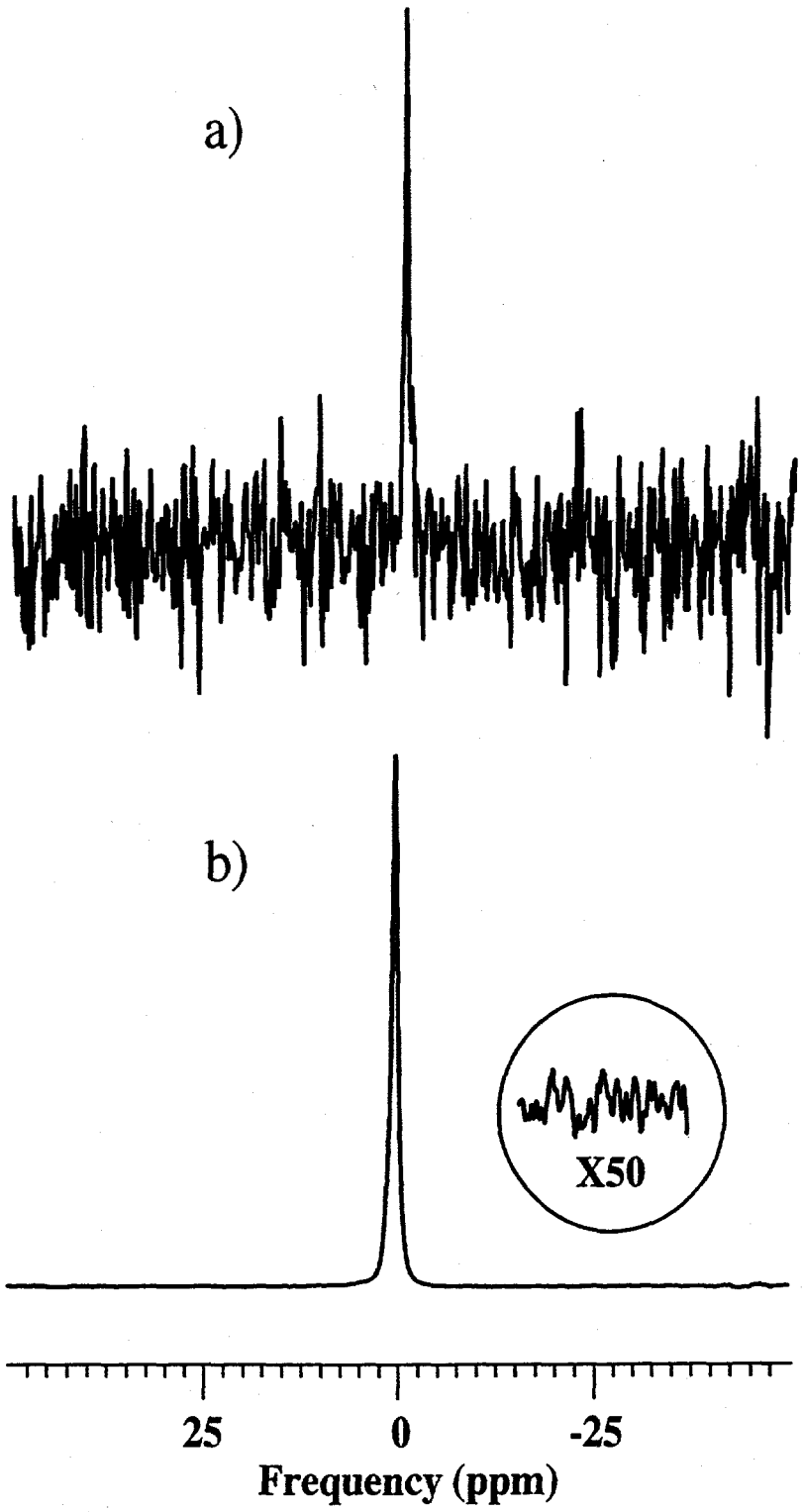

Figure 4.1 Signal enhancement attainable through optical pumping (a) One scan of 5 x 10^{19} xenon atoms. (b) One scan of 2 x 10^{17} optically polarized xenon atoms. (b) represents a signal enhancement of 55,000 over (a).

The use of optically polarized xenon circumvents this problem, as signal averaging is not required. In fact, signal averaging is generally avoided, as the xenon nuclear spin polarization is not replenished by T_1 processes. However, materials with extremely short relaxation times are not ideally suited for investigations using polarized xenon, as the polarized xenon may relax before equilibrating with the sample. For this reason, conventional and optically polarized xenon NMR are complementary techniques. Materials in which dissolved or adsorbed xenon has a long relaxation time are best studied by optically polarized xenon NMR; conversely, materials in which xenon has very short relaxation times may be best investigated through conventional xenon NMR. The depletion of the high, non-equilibrium polarization with pulsing and relaxation requires careful experimental design and interpretation for multipulse and multidimensional experiments. This chapter continues with an introduction to the theory of optical pumping and spin exchange. The experimental approach will then be detailed in the following section. In Section 4.4, a study of polarized xenon on poly(acrylonitrile) will be detailed. The chapter will end with a description of a study of a reaction with polarized xenon as a reactant: the enclathration of xenon in a hydrate lattice.

4.2 Theory of Optical Pumping and Spin Exchange

4.2.1 Optical Pumping

Alfred Kastler received the Nobel Prize in 1966 for his discovery that a non-equilibrium population of spin energy levels in a magnetic field may be created by irradiating a sample with polarized light.[126] This method, dubbed optical pumping, relies on the conservation of angular momentum. When a photon is absorbed by an atom, its angular momentum is transferred to the electrons. Photons have spin I = 1

with m = 1 and m = -1. If the electric vector of the light is a right-handed helix, the light is said to be right circularly polarized, and by convention this corresponds to m = 1. The selection rules for the electric dipole transmission are $\Delta\ell = \pm 1$ and $\Delta m = 0; \pm 1$. The latter rule is polarization dependent: $\Delta m = 0$ for linearly polarized light and $\Delta m = \pm 1$ for circularly polarized light. Furthermore, right and left circularly polarized light have different selection rules, (one corresponds to $\Delta m = +1$ and the other corresponds to $\Delta m = -1$) depending on the direction of the magnetic field with respect to the direction of the propagation of the light. Right circularly polarized light is given the notation $\sigma+$ if it produces $\Delta m = +1$ transitions. These selection rules give rise to the production of a population imbalance of one electron spin state versus the other.[126]

Alkali metal atoms, in particular Rb, represent good systems for optical pumping. Rubidium is mainly a mixture of two isotopes, ^{85}Rb (I = 5/2; 72.12% abundant) and ^{87}Rb (I = 3/2; 27.85% abundant). Both isotopes possess a $^2S_{1/2}$ ground state and a first excited state of $^2P_{1/2}$. The D1 transition ($^2S_{1/2} \rightarrow {}^2P_{1/2}$), used for optical pumping, corresponds to a wavelength of 794.7 nm, which is close to the wavelength of maximum output of the commercially available Ti-Sapphire laser. In a magnetic field the $^2S_{1/2}$ and $^2P_{1/2}$ energy levels are each split into two-magnetic sub-levels. The interaction of the nucleus and electrons result in hyperfine splittings, which are indicated F in Figure 4.2 . The resulting fluorescence spectrum for the D1 transition of Rb is shown schematically in Figure 4.3. However, due to Doppler broadening above 40 °C, only three maxima can be observed.

Illuminating Rb along the direction of a static magnetic field with $\sigma+$ light produces transitions where the following selection rules apply:

$$\langle m = -1/2 | \sigma^+ | m = -1/2 \rangle = 0 \tag{4.3}$$

$$\langle m = +1/2 | \sigma^+ | m = -1/2 \rangle = 0 \tag{4.4}$$

$$\langle m = -1/2 | \sigma^+ | m = +1/2 \rangle \neq 0 \tag{4.5}$$

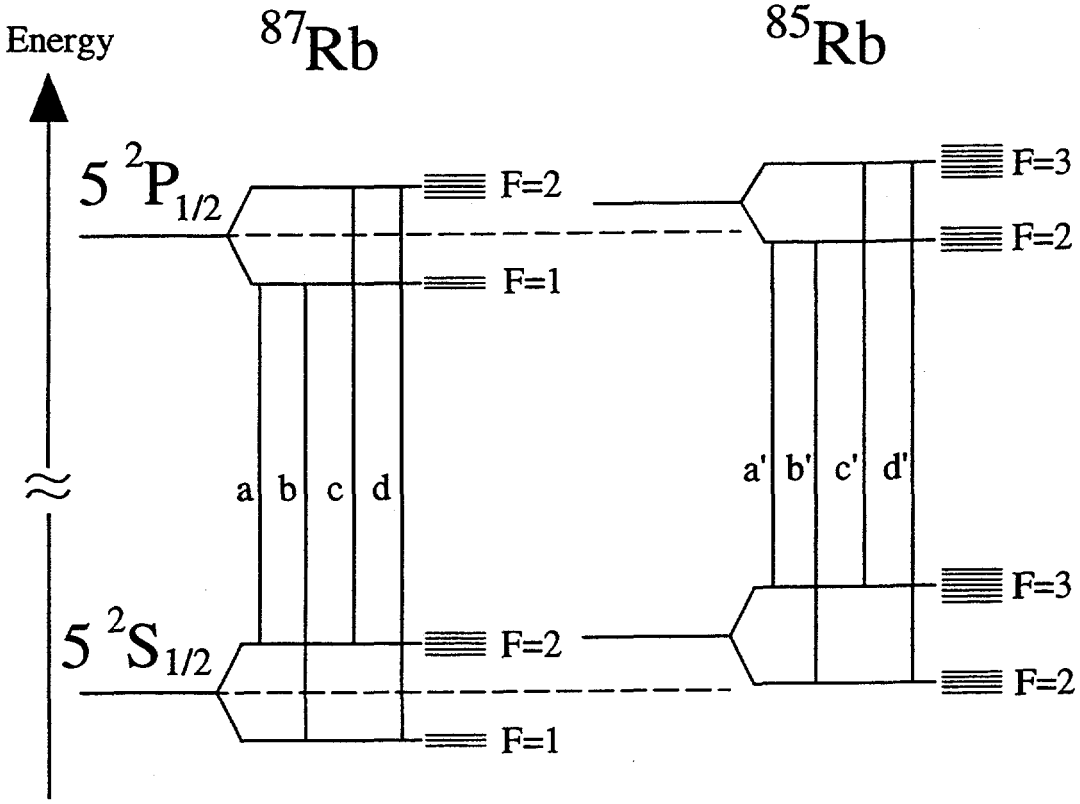

Figure 4.2 Energy level diagram of rubidium with the hyperfine transitions identified.

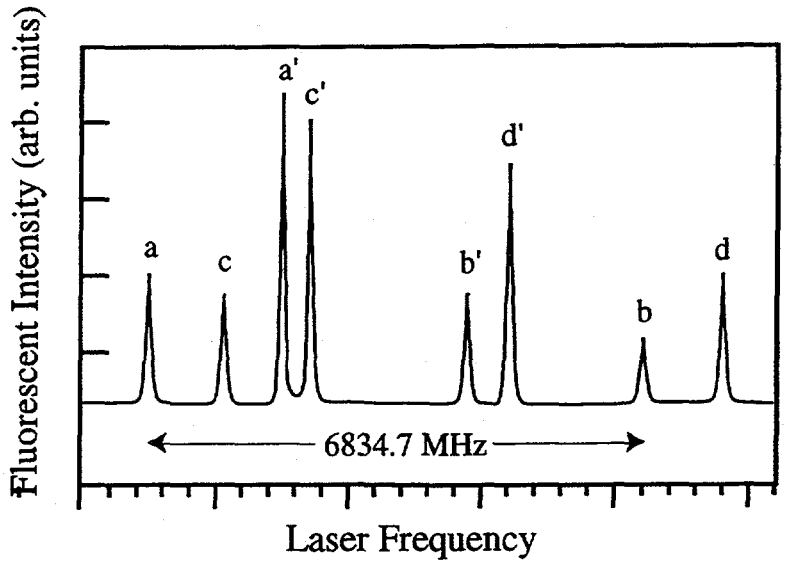

Figure 4.3 Schematic natural abundance rubidium fluorescence spectrum. The letters above the resonances correspond to the transitions in Figure 4.2.

The nuclear spin may be neglected since the Doppler broadening at the temperatures optical pumping is performed at is greater than the hyperfine splitting. Therefore, only one transition is allowed when Rb is illuminated along the direction of the magnetic field with $\sigma+$ polarized light. The effects of spin orbit coupling may be neglected because the $^2P_{3/2}$ energy level is split by 232714 cm^{-1} from the $^2P_{1/2}$ energy level. The D2 transition ($^2S_{1/2} \rightarrow {}^2P_{3/2}$) is therefore completely out of resonance at 780 nm.

Spontaneous emissions from the excited m = 1/2 state take place to either ground state within about 30 ns. The branching ratios of the decay, 1/3 and 2/3, are given by the Clebsch-Gordon coefficients and indicated in Figure 4.4. At the Rb pressures in a typical optical pumping experiment, the Rb atoms collide before they decay, causing the excited state to mix. The branching ratios become 1/2 and 1/2. The net result of this optical pumping cycle is to leave the ground state m = + 1/2 highly polarized, since the relaxation time of the ground state approaches 1 s.

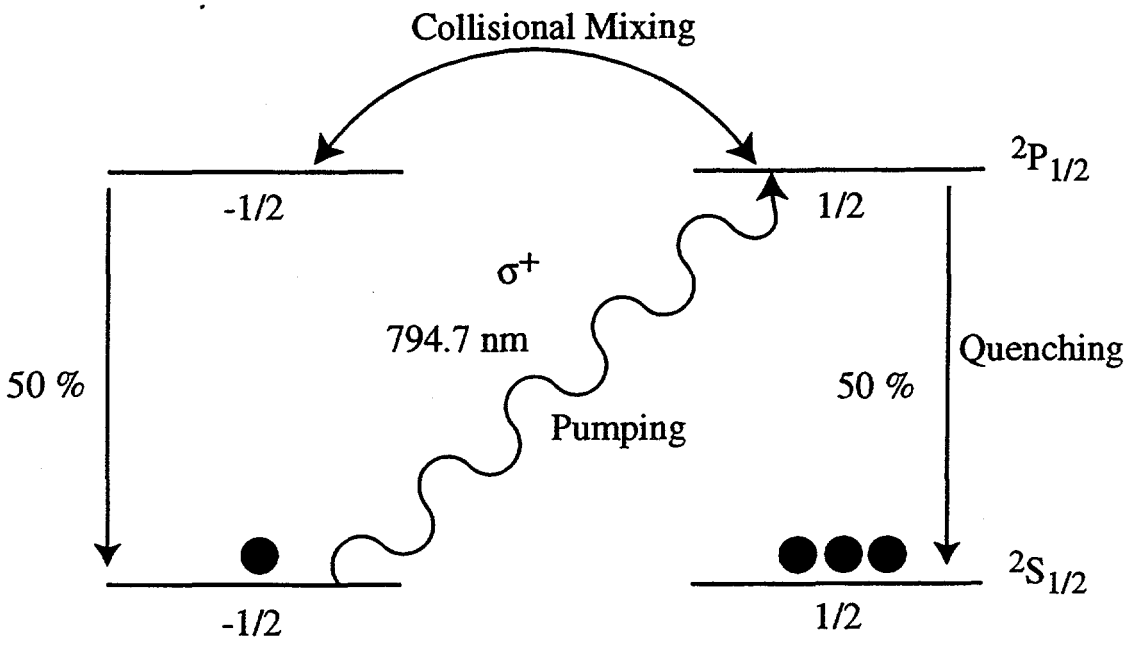

Figure 4.4 Optical pumping scheme for Rb. Circularly polarized light excites the m=-1/2 to m=1/2 transition. Due to collisional mixing of the excited state, spontaneous emission occurs to both ground states.

4.2.2 Spin Exchange

Spin-exchange collisions make it possible to achieve spin polarization in systems that cannot be polarized directly. Spin-exchange can be represented schematically by the following equation: $A(\uparrow)+B(\downarrow)\rightarrow A(\downarrow)+B(\uparrow)$ (4.6)

Before the collision the spin of species A is up, while the spin of species B is down. After the collision the spin orientation of the two species has been exchanged. Dehmelt first suggested that spin-exchange collisions between optically pumped alkali vapor and a second species could be used to transfer polarization.[127] Xenon is a particularly favorable spin-exchange partner with Rb because it forms a long lived

van der Waals molecule.[128-131] The major spin interactions in the Rb-Xe van der Waals pair are described by the Hamiltonian:[132]

$$\mathcal{H} = A\vec{S}\cdot\vec{I} + \gamma\vec{S}\cdot\vec{N} + \alpha\vec{S}\cdot\vec{K} + g_S\mu_B\vec{B}\cdot\vec{S} + g_I\mu_B\vec{B}\cdot\vec{I} + g_K\mu_B\vec{B}\cdot\vec{K} + \ldots \quad (4.7)$$

where $A\vec{S}\cdot\vec{I}$ denotes the contact interaction between the rubidium electronic $\vec{S}$ and nuclear spin $\vec{I}$, and $\alpha\vec{S}\cdot\vec{K}$ the exchange interaction between $\vec{S}$ and the xenon nuclear spin $\vec{K}$ and with the g-factors denoted $g_{S,\,I,\,K}$ and the Bohr magneton μ_B. The angular momentum vectors are depicted in Figure 4.5.

The fermi contact interaction given by

$$\alpha\vec{S}\cdot\vec{K} = \frac{8\pi}{3}\gamma_e\gamma_{Xe}|\Psi(0)|^2\vec{S}\cdot\vec{K} \quad (4.8)$$

is responsible for the spin-exchange. $|\Psi(0)|^2$ represents the probability for finding unpaired electron spin density at the xenon nucleus. The Fermi contact interaction is enhanced in Rb-Xe complexes due to the electron exchange interaction between the Rb 5s electron and the core s orbitals of Xe. The enhancement is on the order of 10^3.[133]

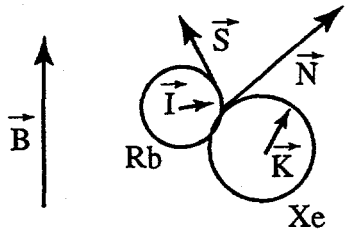

Figure 4.5 Schematic of a Rb-Xe van der Waals molecule with the angular momentum vector labeled. N represents the rotational angular momentum of the complex.

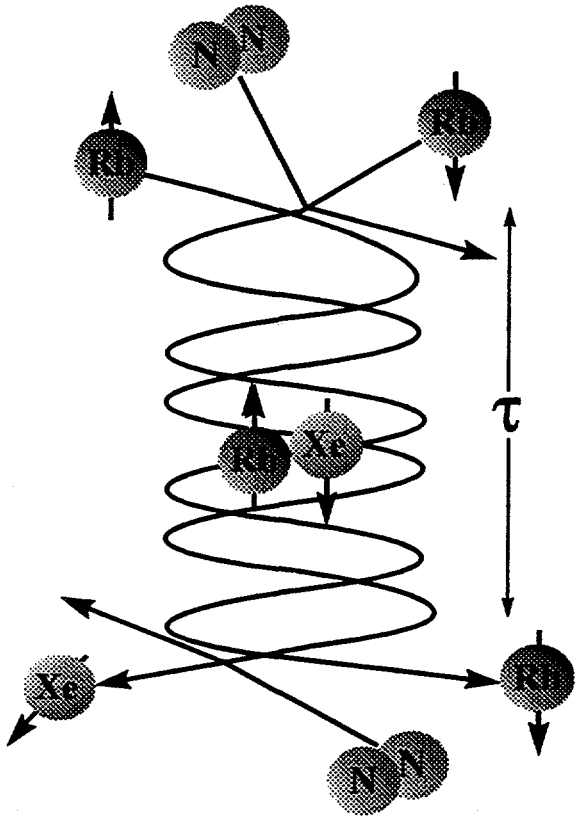

Figure 4.6 Schematic of Rb-Xe spin van der Waals interaction.

The $\vec{S}\cdot\vec{K}$ term in (4.8) may be expanded to $\vec{S}\cdot\vec{K} = S^{+}K^{-} + S^{-}K^{+} + S_{z}K_{z}$, (4.9)

where $S^{+}K^{-} + S^{-}K^{+}$ denote the flip-flop terms that allow spin-exchange. The polarization not transferred to the Xe is lost to the rotational angular momentum of the complex, which is subsequently dissipated as translational energy when the complex is collisionally broken apart. The lifetimes of these complexes, τ, depend on the pressure and are on the order of hundreds of nanoseconds for gas pressures of a few torr and one nanosecond at pressures of about one atmosphere. Because the spin exchange probability is proportional to the square of the lifetime of the complex, the van der Waals mechanism for spin-exchange is dominant when the collision limited lifetime of the complex is sufficiently long and the magnetic field strengths are less than 100 G, despite the fact that three-body collisions are less probable than two-

body collisions. This mechanism is schematically illustrated in Figure 4.6. In higher fields and/or higher pressures, binary collisions, with durations of only picoseconds, become the dominant mechanism for spin-exchange.[134]

It would be convenient to directly polarize a system of interest, rather than polarize a secondary species and transfer the polarization. In order to be directly optically polarized, a molecular species must have an accessible transition with selection rules that will allow the establishment of non-thermal populations. Secondly, the relaxation time of the polarized state must be sufficiently long to allow the accumulation of polarization. Alternatively, in order to spin-exchange a system with optically polarized Rb, it must not react with the rubidium vapor (not necessarily a trivial requirement!). There must be some probability of finding the Rb electron at the nucleus of the system of interest and, again, the relaxation times must be sufficient to allow for the accumulation of polarization. ^{3}He is the only noble gas that can be easily polarized directly by pumping a metastable state.[135]

4.3 Experimental Approach

A schematic diagram of the optical pumping apparatus used in the Pines laboratory is shown in Figure 4.7.[136] The optical pumping cell is constructed of glass and consists of a 35 cc cylindrical cell with connections to allow for evacuation of the glassware and sample and measurement of the xenon pressure. The optical-pumping apparatus is typically assembled one of two ways. It is either located in the fringe magnetic field beneath a superconducting magnet with the sample region in the probe connected to the pumping cell through a glass transfer line and separated by a series of stopcocks. Alternatively, the pumping cell is located on a laser table in a 30 G field provided by a

pair of Helmholtz coils connected to a detachable sample tube. The preparation and assembly of the optical pumping apparatus is discussed in detail in Appendix A.

The pumping cell is coated with a thin film of rubidium and can be heated by flowing nitrogen gas to maintain the temperature in the range of 80 - 100 °C during laser irradiation. The elevated temperature increases the rubidium vapor pressure to ~6 x 10^{-6} torr, which is sufficient to absorb the laser light. The cell is illuminated by circularly polarized light from a 2 W Titanium-Sapphire ring laser (Schwartz Electro-Optics), typically operated at 1 - 1.5 W, which is pumped with a 10 W Argon laser (Coherent Laser Group Inc.).

Circular polarization is achieved by insertion of a quarter wave plate in the path of the pumping beam. Deviations from linear polarization of the infrared laser light can be minimized by inserting a linear polarizer in the beam path before the light passes through the quarter wave plate. The laser wavelength is tuned to the rubidium D1 optical transition at 794.7 nm, and the rubidium fluorescence is monitored with an infrared viewer. Alternatively, a photodetector allows detection of the optical absorption of the rubidium by monitoring the intensity of the transmitted light. The tuning of the laser and alignment of the optics is discussed in Appendix B.

Enriched ^{129}Xe (80%, EG+G Mound) is stored in a sidearm that also contains rubidium. (The rubidium reacts with impurities in the xenon and serves to purify it before it is loaded into the pumping cell.) Typically, 200-400 torr of xenon (~ 3 x 10^{-4} moles) are loaded into the pumping cell and irradiated for 20-30 minutes. The cell is then cooled to 40 °C to lower the vapor pressure of the rubidium.

In the case in which the pumping cell is connected directly to the sample in the probe, the xenon gas is introduced, typically in small portions, to the evacuated and, if necessary, precooled sample by opening a stopcock which separates the optical

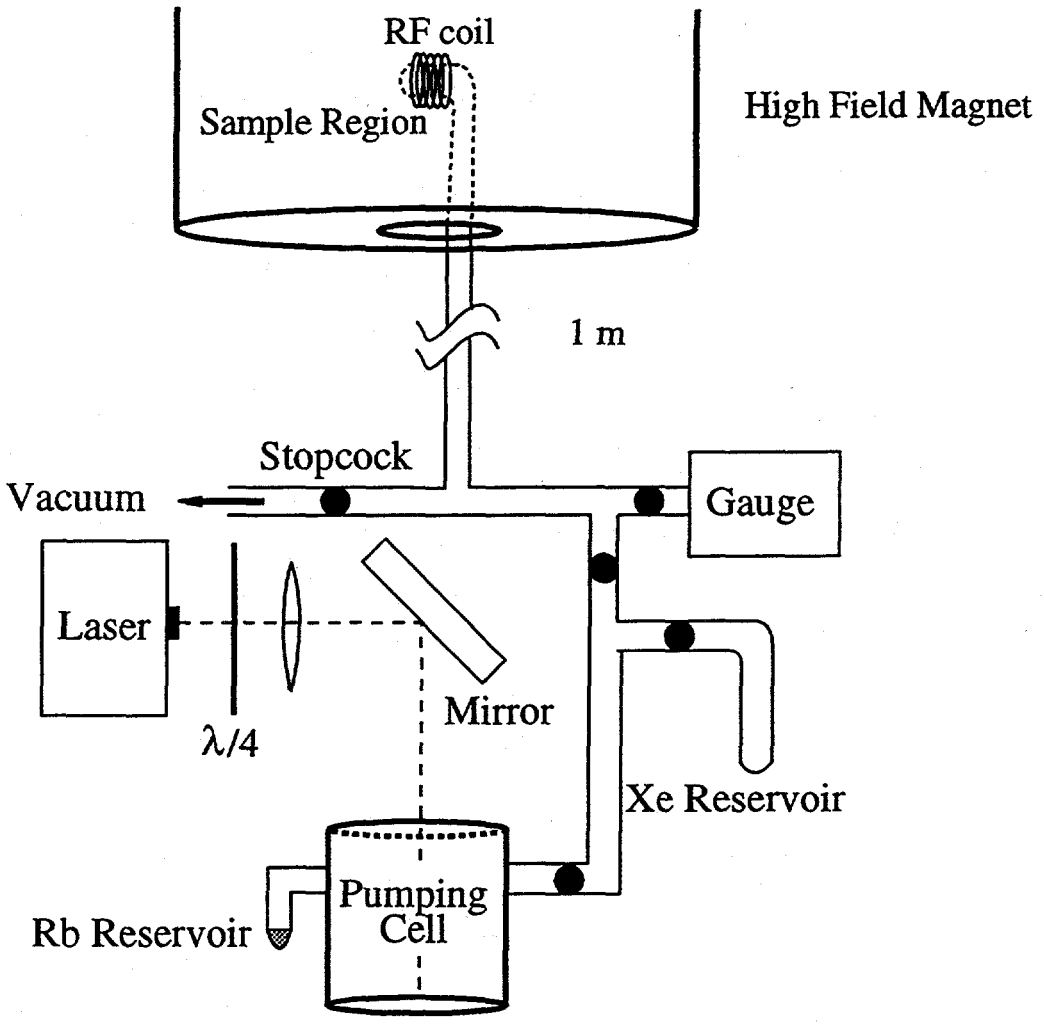

Figure 4.7 Optical pumping apparatus, consisting of a 35 cc cylindrical glass cell, Rb reservoir, and a xenon reservoir. These components are linked by glass vacuum lines with a series of stopcocks. One glass line extends into the probe and to the sample. The laser beam passes through a circular polarizer and illuminates the cell where optical pumping takes place. See text for details.

pumping cell from the sample region. The xenon is allowed to equilibrate with the sample surface for a few seconds (5 -10) before NMR spectra are acquired. The xenon adsorption is monitored with a pressure gauge. The equilibrium pressures are related to the amount of adsorbed xenon through the heat of adsorption.[83]

In the case where the optical pumping cell is connected to a detachable sample tube, the polarized xenon is either expanded into the sample tube volume or condensed into the tube in a small magnetic field, provided either by a permanent magnet or a second pair of Helmholtz coils. The sample is then transported to the superconducting magnet for acquiring the NMR signal. It should be emphasized that this xenon nuclear polarization is a non-equilibrium polarization that is destroyed upon the application of radio frequency pulses and cannot be restored by spin lattice relaxation.

4.4 A Surface Study of Poly(acrylonitrile)

4.4.1 Introduction

Polymers are technologically important due to their wide variety of structural, mechanical and thermal properties. The surface characteristics of polymers lend them many of their important material properties. For example, interfacial phenomena play a role in bio-compatibility, wettability, and diffusion barriers. Traditional UHV techniques are not amenable to the surface study of powdered polymers. NMR is an inviting technique because of its sensitivity to structure, conformation, and dynamics. However, it lacks the sensitivity to probe any but the highest surface area materials.[137] For systems with protons residing exclusively at the surface (e.g. silica), one approach to overcoming the sensitivity to problem is to cross-polarize from the surface protons.[138] This approach is limited to samples with sensitive nuclei residing solely at the surface. An alternative approach is to adsorb polarized xenon

onto the surface and acquire pressure and temperature dependent ^{129}Xe NMR spectra. The chemical shift of the xenon at the surface reveals details of the Xe-surface interaction. With a systematic study of polymers, this interaction can be correlated to physical properties of the polymers.

4.4.2 Experimental

For studies of surfaces, preparation of a clean surface is of critical importance. Powdered samples can not be treated with the traditional methods of surface science such as sputtering or annealing. However, every attempt was made to clean the surface as rigourously as possible. The polymer sample was evacuated to 10^{-5} torr while heated to 60° C in the probe. This treatment seemed to be sufficient to remove the physisorbed water, which is a major contaminant and will interfere with the NMR experiments by decreasing the relaxation time of the adsorbed Xe.[29]

The experiments utilized a home-built low temperature NMR probe equipped with a solenoid coil and operating at a Larmor frequency of 49.45 MHz for ^{129}Xe. The 90° pulse length was 8 μs; typically, a pulse length of 4 μs was applied in the experiments. Cooling of the probe was achieved with a flow of cold nitrogen gas to the dewared sample region. The optical pumping cell was assembled beneath the superconducting magnet with glassware extending into the probe to connect the sample region. The sample region was slowly cooled and brought to thermal equilibrium at the desired experimental temperatures of 125, 130, 136, 146, 151, 161 K and controlled to ±1 K. The cooling apparatus is described in Section 2.5.2.

Xenon gas was polarized according to the method described in Section 4.3. After condensing the rubidium, a small amount of xenon was added to the sample region by opening a stopcock separating the optical pumping cell and sample region. After

adding a controlled amount of xenon, usually between 5 and 20 torr, one minute was allowed for equilibration before acquiring data. A single acquisition was acquired. Another aliquot of polarized xenon was introduced to the sample region, and signal acquired in an identical manner. This procedure was typically repeated 4 - 5 times at each temperature to allow for a range of coverages to be studied. After the last acquisition, the sample was allowed to warm, and the xenon was recovered to the sidearm by condensing it with liquid nitrogen.

Nitrogen and xenon isotherms were carried out to measure the surface areas and adsorption energies of xenon on the polymer sample. Details of the experimental procedure and analysis are described in Section 2.5.2. The N_2 and Xe isotherms are shown in Figure 4.8, 4.9, and 4.10. The xenon heat of adsorption on poly(acrylonitrile), 3.96 kcal/mol, was determined using equation (2.44). The data from the isotherms are summarized in Table 4.1.

Gas	Temperature (K)	Adsorption Energy (kcal/mol)	Surface Area (m^2/g)
N_2	77	2.01	18.2
Xe	146	3.97	16.4
Xe	155	3.96	21.3

Table 4.1 Parameters determined from BET isotherm analysis of Xe and N_2 adsorbed onto poly(acrylonitrile).

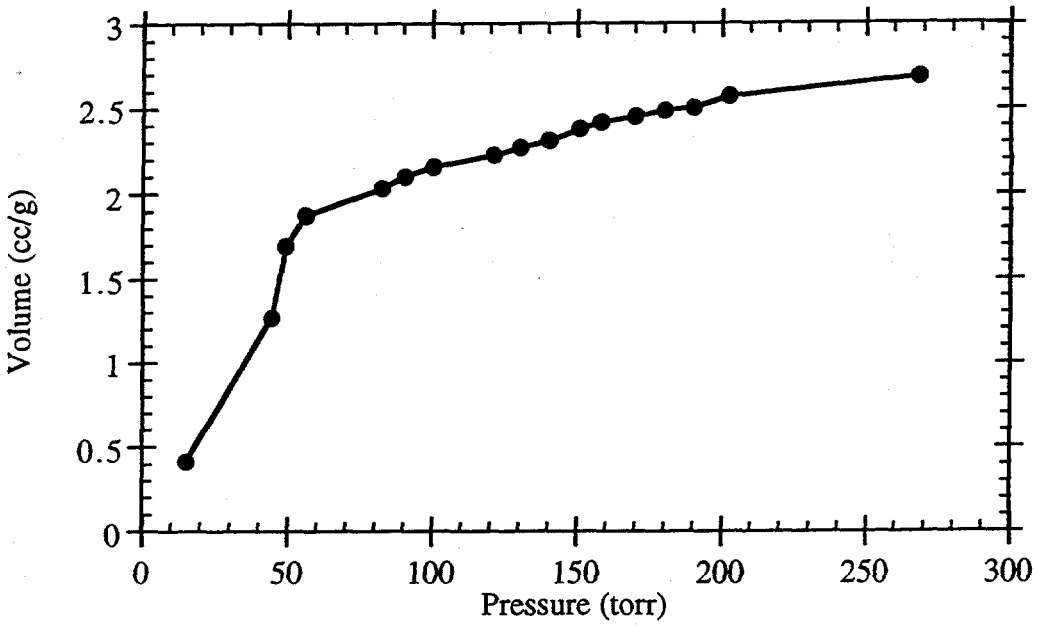

Figure 4.8 BET adsorption of N_2 on poly(acrylonitrile). The lines connect the points to guide the eye.

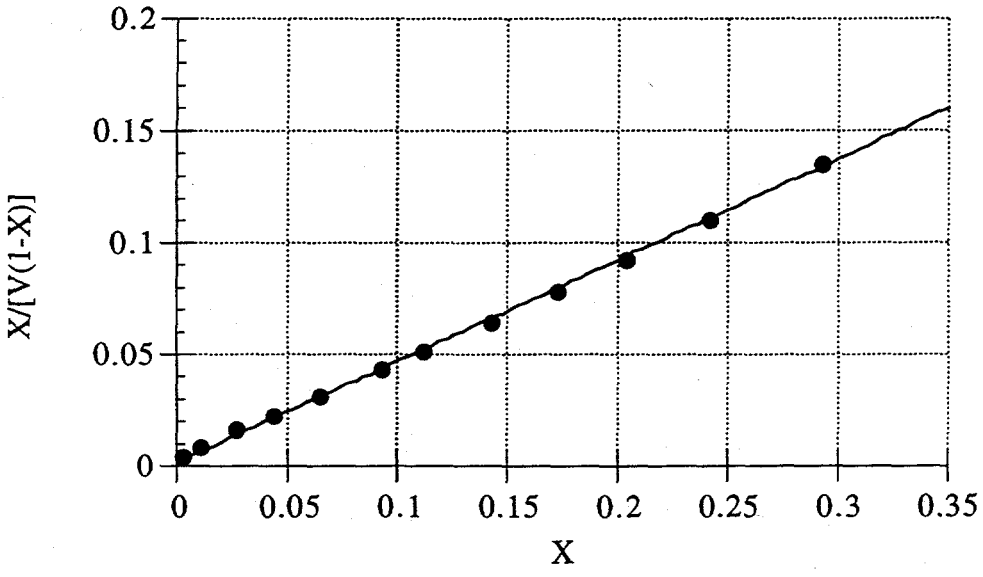

Figure 4.9 Linearized BET adsorption isotherm of N2 on poly(acrylonitrile).

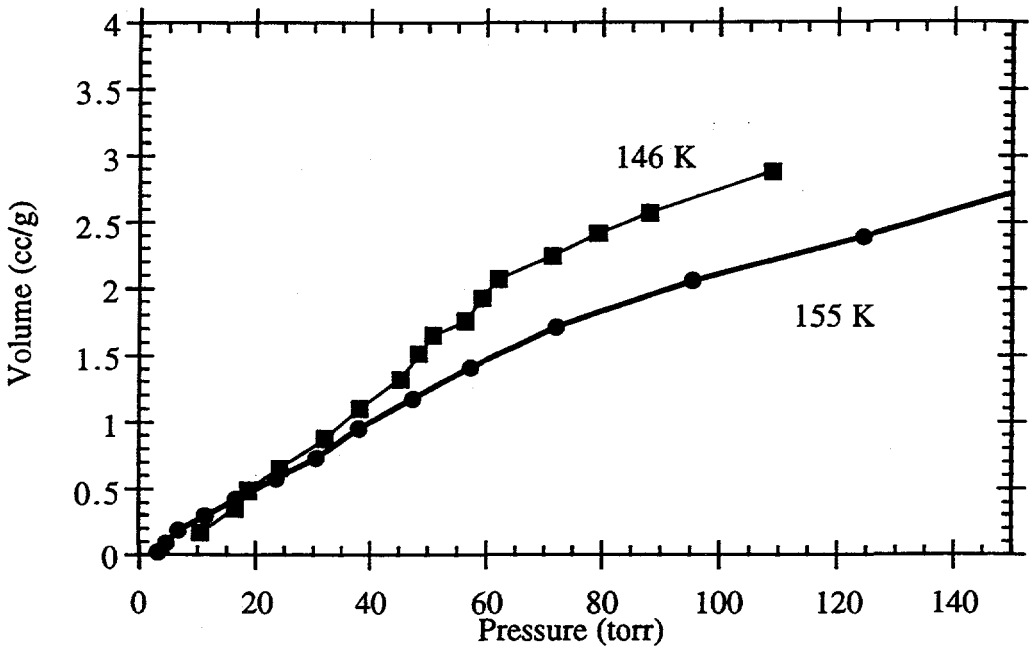

Figure 4.10 BET adsorption of Xe on poly(acrylonitrile) at 146 K and 155 K. The lines connect the points to guide the eye.

4.4.3 Results and Discussion

Representative spectra of polarized xenon adsorbed onto poly(acrylonitrile) are shown in Figure 4.11. The spectra displayed were obtained using xenon coverages, θ, between 0.001 and 2.5. The chemical shift of xenon adsorbed on the surface of poly(acrylonitrile) as a function of temperature and coverage are displayed in Figure 4.12. The chemical shift shows a linear dependence on the xenon coverage, which indicates that only Xe-Xe interactions are important at the coverages studied.

As discussed in the case of xenon adsorbed on metal oxides in Section 2.5, the shift of xenon adsorbed on poly(acrylonitrile) results from rapid exchange of the xenon atoms between the gas phase and the surface adsorbed phase. Hence, the total chemical shift is equal to the shift due to interactions at the surface (δ_S) plus that of the gas

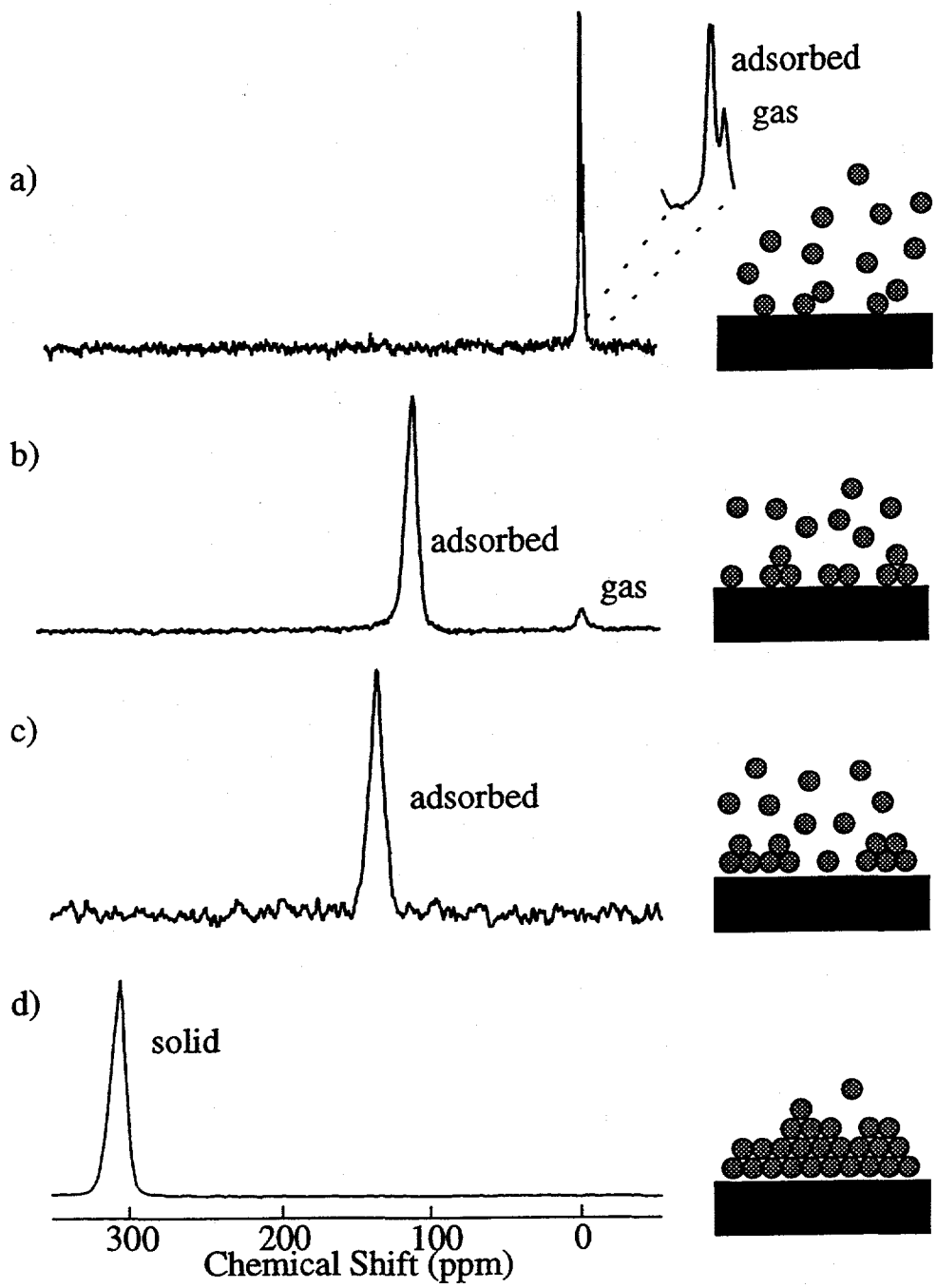

Figure 4.11 Representative spectra of polarized xenon adsorbed onto poly(acrylonitrile) at various temperatures and coverages. (a) T=298, Θ = 0.001; (b) T=151 K, Θ = 0.2; (c) T = 135 K, Θ = 0.3; and (d) T = 130 K, Θ = 2.5. The gas signals in (a) and (b) arise from xenon not in contact with the sample region.

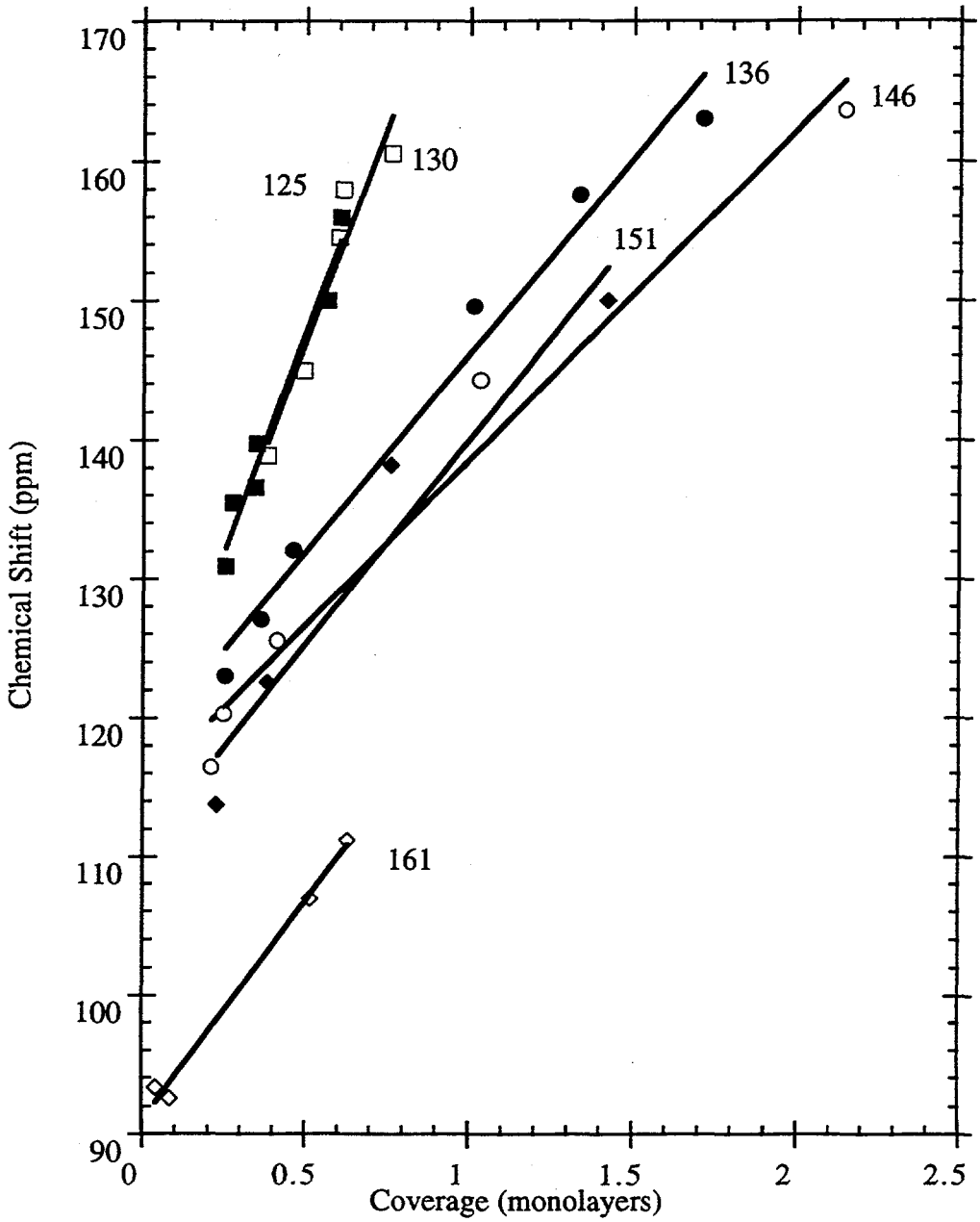

Figure 4.12 ^{129}Xe Chemical shift (ppm) of xenon adsorbed on poly(acrylonitrile) as a function of temperature (K) and coverage (in monolayers). Lines represent linear least-squares fits to the data each temperature.

phase (δ_g), weighted by the relative probabilities of the xenon atom being on the surface, ($P_s(T)$) and in the gas phase ($P_s(T)$).

$$\delta(T,\theta) = \delta_g(T,\theta)\, P_g(T) + \delta_s(T,\theta)\, P_s(T) \qquad (4.10)$$

The shift of xenon at low pressure is used as an external standard and defined as 0 ppm. Following a completely analogous derivation as given in Chapter 2, the intrinsic chemical shift of xenon at the surface is given by:

$$\delta(T,\theta=0) = \sigma_0 \frac{e^{\Delta H_{ads}/kT}}{\tau_v/\tau_0 + e^{\Delta H_{ads}/kT}}. \qquad (4.11)$$

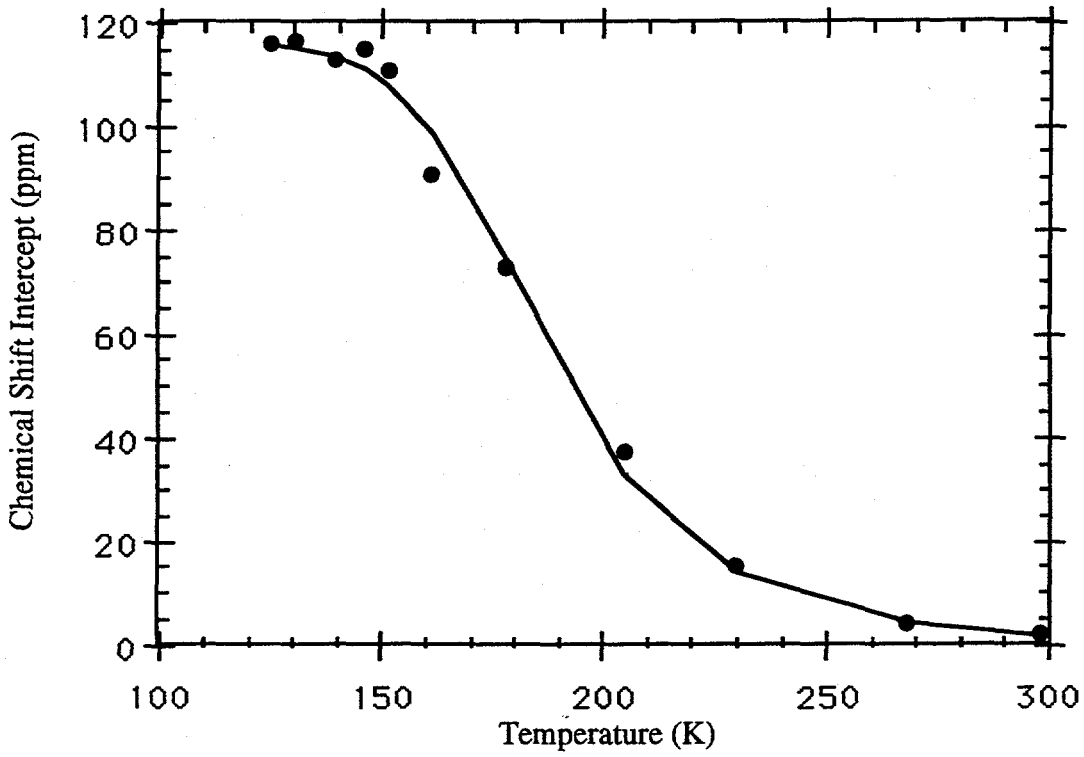

Figure 4.13 ^{129}Xe chemical shift intercepts (ppm) of xenon adsorbed on poly(acrylonitrile) versus temperature. The intrinsic chemical shift due to xenon-surface interactions is found to be 116 ppm.

With the average xenon heat of adsorption from Table 4.1, the chemical shift extrapolated to zero coverage, $\delta(T,\theta=0)$, as a function of temperature, is fit to equation 4.11. The fit and data are presented in Figure 4.13. The contribution to the chemical shift due to xenon-surface interactions (σ_0) is found to be 116 ± 2 ppm for poly(acrylonitrile).

4.4.4 Conclusions

The chemical shift of ^{129}Xe adsorbed on the surface of poly(acrylonitrile) depends linearly on the xenon coverage, and the intrinsic ^{129}Xe chemical shift due to xenon-surface interactions are 116 ± 2 ppm. This is the greatest shift of the polymers studied previously[12,29], indicating a strong interaction between the xenon and the surface. Whether this is due to the chemical or structural composition of the surface remains unclear. It would be desirable to extend these xenon studies to polymers with different functional groups. Additionally, it would be useful to study the surface morphology through complementary techniques, such as AFM, to determine to what extent the surface xenon chemical shift is due to surface morphology versus surface composition. Despite the incomplete explanation for the current results, with more studies this technique does promise to enable empirical correlation of the chemical shift of xenon to the chemical functional groups exposed on the surface!

4.5 A Study of the Enclathration of Polarized Xenon into a Hydrate Lattice

4.5.1 Introduction

Since the discovery of gas hydrates in 1811 by Davy[139] and noble gas hydrates by Villard[140] and de Forcrand,[141] clathrate hydrates have been the subject of intense research. Clathrate hydrates are potentially important for the safe storage and transport of energy.[142] The energy density stored in hydrates is considerably higher than of conventional natural gas.[143] Recent investigations consider the possibility of disposing industrially produced methane as a hydrate in deep ocean to prevent further release into the atmosphere as a greenhouse gas.[144] Clathrate formation can be a nuisance, however, as hydrate plugs in offshore oil wells and pipelines for transport of unprocessed fluids present a problem of high economical impact. The ability to stimulate and inhibit clathrate formation depends on a detailed understanding of the clathrate formation mechanism.

Xenon serves as a good model for methane with respect to size and shape. Xenon also forms a clathrate hydrate with water, the structure of which consists of six larger tetrakaidecahedral and two smaller pentagonal dodecahedral cages per unit cell. The free diameter of the larger cages is 0.59 nm, that of the smaller cages 0.52 nm, resulting in a maximum of eight xenon atoms (diameter 0.44 nm) per unit cell, with one xenon atom residing in each cage.[145-147] For the purpose of NMR investigations, xenon is a more favorable nucleus than carbon due to the high polarizability of its electron cloud and the resulting large chemical shift range. Ripmeester and coworkers initiated the use of ^{129}Xe NMR to the study of anisotropic cavities,[148] including xenon clathrate hydrates. Using ^{129}Xe NMR spectroscopy, they were able to differentiate between structure I, structure II and structure H clathrate hydrates[149] because the ^{129}Xe chemical shift is a function of the cage space available to the xenon.[150,151] The

major drawback of this technique is the occurrence of long spin lattice relaxation times for ^{129}Xe in clathrate hydrates (on the order of minutes[31]) which prohibits the study of non-equilibrium samples. It is possible to decrease the acquisition time from four hours (at 275 K) to 24 minutes (at 265 K) by using proton to xenon cross polarization.[152] However, as the xenon clathrate hydrate formation occurs on the timescale of minutes,[153] it is still not possible to monitor the uptake of the xenon by conventional ^{129}Xe NMR spectroscopy. The kinetics of the clathrate formation have been studied previouslyby a volumetric method,[153,154] a technique that does not allow the differentiation between the xenon uptake of the small and the large cages. As the equilibrium occupancy ratios (large cage/small cage) often differ substantially from the stoichiometrical value of three, even after long equilibration times,[31] it is of particular interest to follow the occupancies of the individual cage sizes. Conventional ^{129}Xe NMR is a useful tool for monitoring the occupancy of each cage size, but its sensitivity is far too low to detect signals on the timescale required to study clathrate formation. The use of optically polarized xenon, however, allows the signal detection following a single radio frequency pulse with sufficient sensitivity.[136]

4.5.2 Experimental Details

The experiments utilized a home-built low temperature NMR probe equipped with a saddle coil and operating at a Larmor frequency of 100.277 MHz for ^{129}Xe. The 90° pulse length was 14 μs; a pulse length of 8 μs was applied in the experiments. Cooling of the probe was achieved with a flow of cold nitrogen gas to the dewared sample region.

The sample consisted of powdered ice prepared by dripping D_2O (Aldrich) in liquid nitrogen. The ice was ground up in a mortar, and quickly transferred into the NMR

sample tube, cooled and immediately evacuated to minimize the amount of included oxygen. The sample was equilibrated for at least one hour in a slush bath prior to addition of the polarized xenon, prepared by the process described in detail in the first section of this chapter. A 10 mm NMR tube equipped with a high vacuum stopcock and a sidearm for the xenon served as a sample tube and is depicted in Figure 4.14. The sidearm was kept at ambient temperature during the equilibration of the ice. Equilibration temperatures were 258 K, 233 K, 217 K, 195 K and 170 K.

Prior to the NMR experiment, the sidearm of the sample tube was immersed in liquid

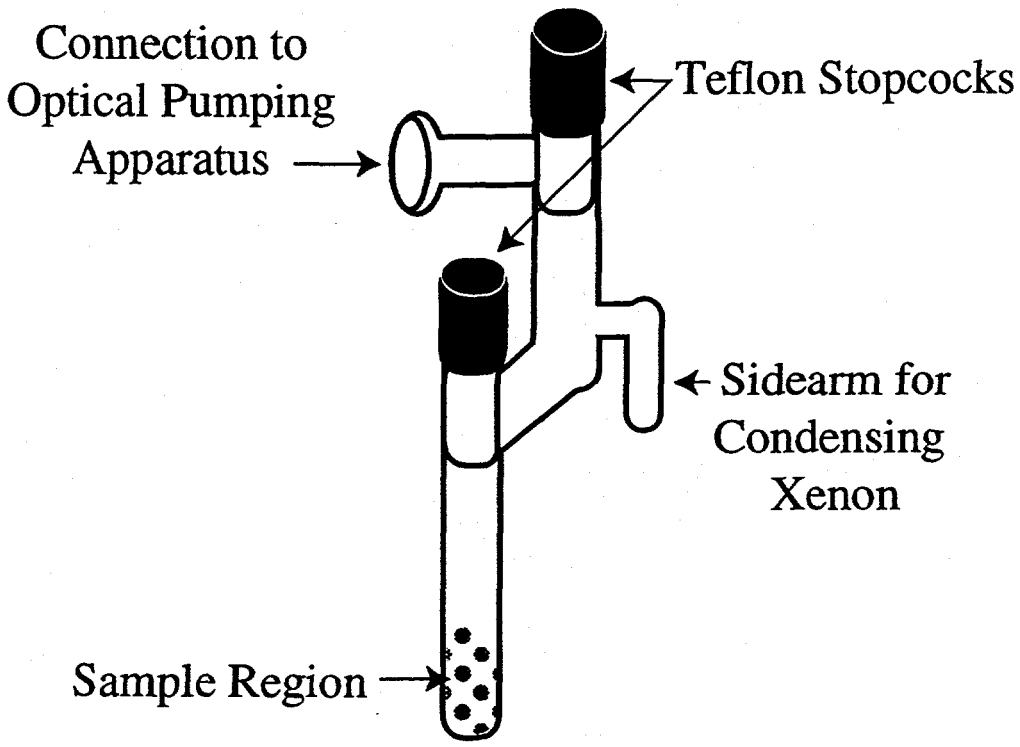

Figure 4.14 Schematic of the sample tube used in the clathrate experiments. The sample region was maintained at the desired temperature by immersion in an organic slush bath. The sidearm was immersed in liquid N_2 to condense the polarized Xe. The Teflon stopcocks and connection to the optical pumping apparatus are also depicted.

nitrogen in order to freeze the optically pumped xenon from the optical pumping cell into the sidearm. The amount of xenon varied in the different experiments. The pumping cell was loaded with 337 torr xenon at 258 K; 305 torr at 233 K; 64 torr at 217 K; 281 torr at 195 K and 280 torr at 170 K. During the freezing procedure, the sample tube was maintained in a magnetic field of 100 G, also provided by a pair of Helmholtz coils, to slow the xenon relaxation.[155] After freezing the xenon, the sample tube was transferred to the high field NMR magnet (8.52 T) for detection, where the probe was precooled to the same temperature as the sample. The moment of sample insertion into the magnet was defined as t = 0. The transfer of the sample tube to high field was normally accomplished in 5 seconds.

Following the NMR experiments, the xenon was recovered by connecting the sample tube to the vacuum line and immersing the sample region in a bath of dry ice/ethanol. It is important to note that merely opening the sample tube to the vacuum led to only a partial release of the xenon; complete recovery could only be achieved after warming the ice to free the enclathrated xenon. Selective freezing of the water in the ethanol bath allows xenon recovery, because freezing of water in the presence of xenon (at the reported pressures) only causes clathrate formation upon agitation.[156]

4.5.3 Results and Discussion

Figure 4.15 shows three typical ^{129}Xe NMR single scan spectra obtained at different times t elapsed from the time of insertion of the sample into the magnet. The gas peak is referenced to 0 ppm. The signal at 160 ppm is attributed to xenon in the larger tetrakaidecahedral cages, and the one at 240 ppm to xenon in the smaller dodecahedral cages.[31] Instead of observing the expected narrow lineshape of the gas signal (< 0.25 ppm) a broad signal is observed, whose linewidth is dependent both on

temperature and time (Figure 4.16). The steep increase of the linewidth in the first 200 s is very likely due to xenon subliming in the sidearm of the sample tube, as the xenon was transferred to the magnet while frozen. This is consistent with the observation that the gas signal intensity first *increases* with time.

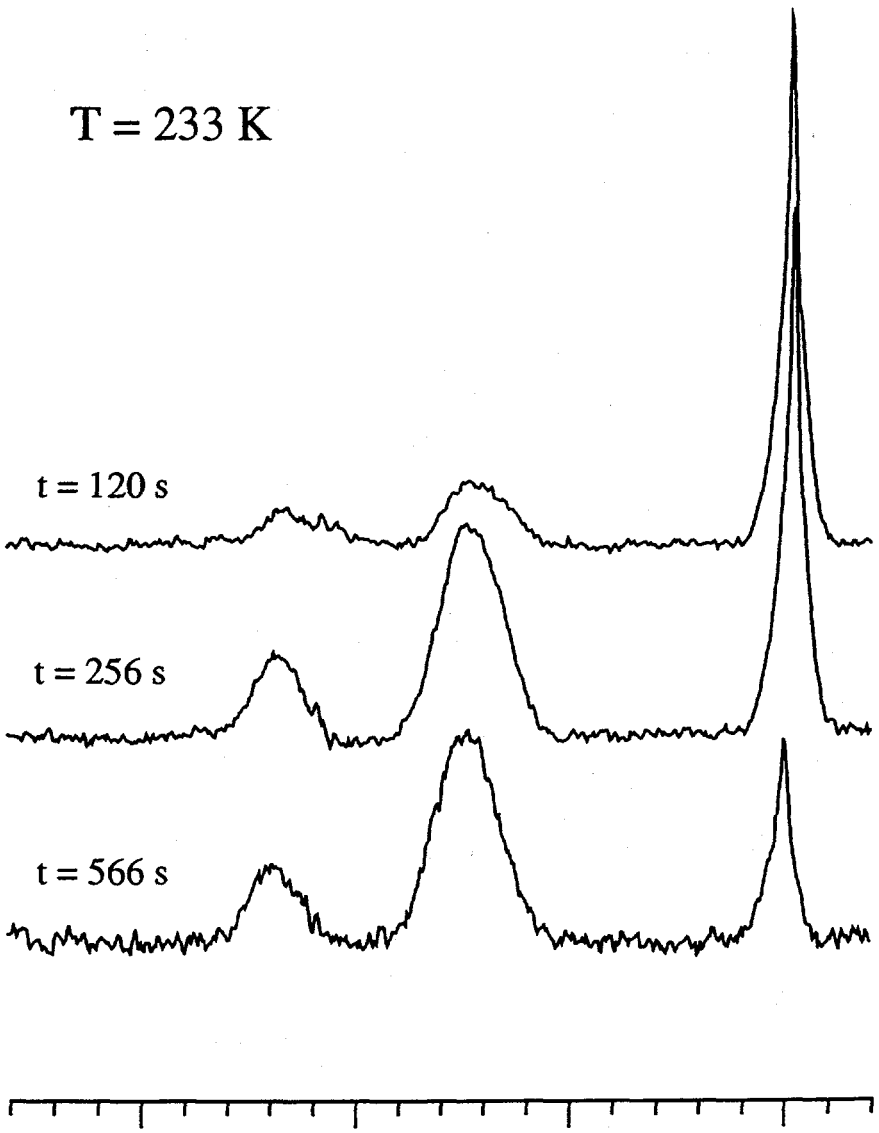

Figure 4.15 ^{129}Xe NMR spectra of the formation of a xenon clathrate hydrate at 233 K and time t after admission of the xenon to the powdered ice sample.

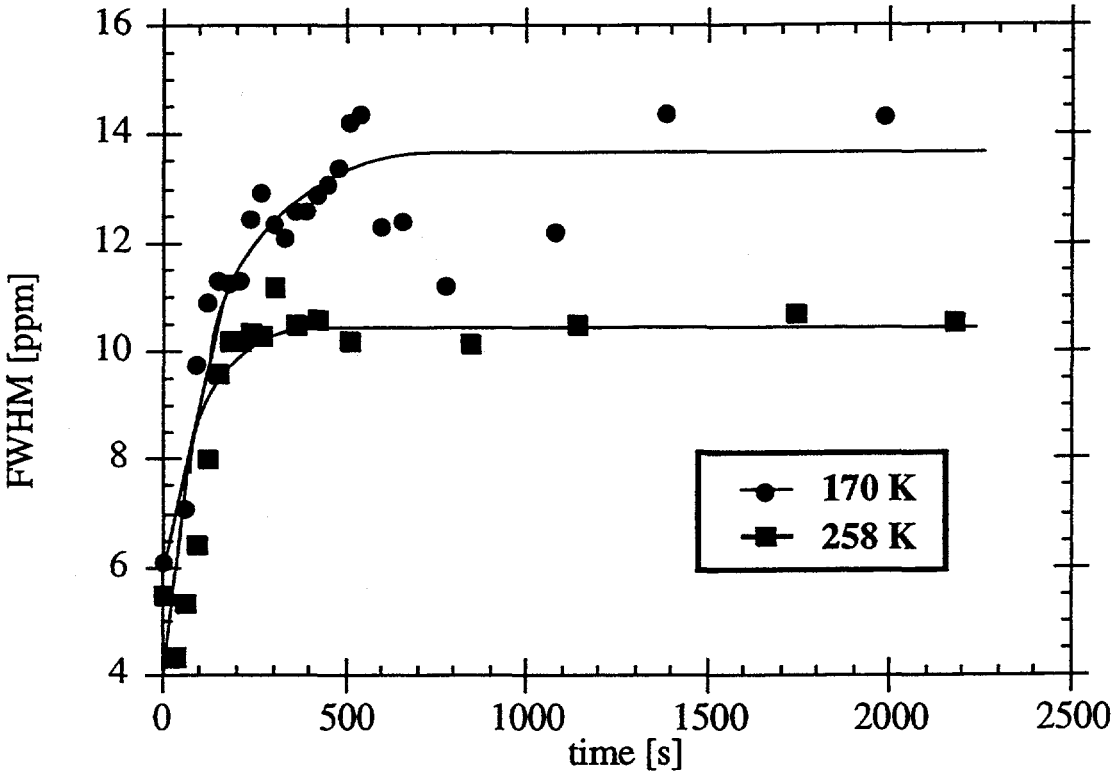

Figure 4.16 ^{129}Xe NMR linewidth (full width at half maximum, FWHM) of xenon gas in presence of powdered ice as a function of time after the admission of the xenon at different temperatures.

Only about 20% of the total sample tube volume is located in the dewared region of the probe. This creates a small temperature and pressure gradient in the sample tube, which contributes to the linewidth. A xenon gas sample of comparable density experienced a shift of 4 ppm when changing the temperature from 250 to 300 K.[23]

Furthermore, the gas signal is the sum of the signal of xenon gas inside *and* outside the pickup coil, due to the high polarization. Xenon in the void spaces close to the surface of the ice crystals might experience a different susceptibility than xenon in the free gas space, so the linewidth may also be due to susceptibility broadening.

The spectra were analyzed by integrating the signals and plotting the values as a function of time. The formation of the xenon clathrate hydrates at 217 K is shown in Figure 4.17. The time axis in Figure 4.16 terminates at t = 12 min although the experiment was performed over a timescale of 43 min. At times t > 12 min, the (larger) peak of the xenon in the large cages as well as the gas signal can still be observed, but the signal to noise ratio decreased, prohibiting reliable data analysis.

The onset of clathrate formation is delayed by 1.5 min after inserting the sample tube in the magnet. In this period of time, the frozen xenon warms until the pressure has reached at least the dissociation pressure of the clathrate at the prevailing temperature. A rapid increase in the xenon pressure in the first minutes is consistent with the steep increase in the linewidth of the gas signal. The dissociation pressures[157] and the initial xenon pressures are listed in Table 4.2. Although water was present in stoichiometric excess with respect to xenon, and the xenon pressure decreases during each experiment due to enclathration, it is known that the xenon forms a clathrate layer on the surface of the ice crystal, which is impenetrable by the xenon.[158] Therefore, it is assumed that excess xenon was available throughout the experiments. The permanent presence of the xenon gas signal in the spectra supports

T [K]	170	195	217	233	258
P_{diss} [10^5 Pa]	0.004	0.045	0.16	0.27	0.78
P_0 [10^5 Pa]	2.62	2.62	0.60	2.85	2.85

Table 4.2 Xenon clathrate hydrate dissociation pressures P_{diss} and initial xenon pressures P_0 (calculated for room temperature) used in the NMR experiments. P_{diss} and P_0 are listed for the temperatures T at which the experiments were performed.

this assumption as well as the fact that the sample tubes were still pressurized when they were opened for xenon recovery.

To determine the kinetics of the reaction, a model for the reaction mechanism is required. Bishnoi and coworkers[159] formulated a semi-empirical model to correlate their experimental data, which were obtained by contacting methane with water upon vigorous stirring. The rate of hydrate formation is dependent on the supersaturation of the liquid water, a situation that is not comparable to this one. Holder and coworkers[160,161] used an experimental design with a fixed gas-water or gas-ice interfacial area. Their experiments were initially carried out at 263 K using gas pressures as high as 12 MPa. However, they only observed clathrate formation when warming the gas temperature above the melting point of ice, which led to the conclusion that melting ice provides a template for hydrate nucleation. In the experiments presented here, hydrate formation was observed at temperatures as low as 195 K at a gas pressure of only 0.3 MPa, conditions which exclude the presence of liquid water. Sloan and Fleyfel[154] proposed a molecular mechanism for gas hydrate nucleation from ice. The authors modeled Falabella's data,[162] which show that for the formation of xenon clathrate hydrate from ice there is no induction period, a result consistent with or data and those of Barrer and Edge.[153] Sloan and Fleyfel propose a mechanism that involves the presence of transient liquid water on a local scale, since the formation of one cavity requires the relocation of 20 ice lattice molecules. Falabella used a shaking ball-mill apparatus similar to the one of Barrer and Edge. The impinging balls on the ice/hydrate surface provide sufficient mechanical energy to form liquid water locally even at low temperatures.[154] However, as indicated above, the data from the experiments utilizing polarized xenon suggest that the presence of transient liquid water is not a necessary condition for hydrate formation.

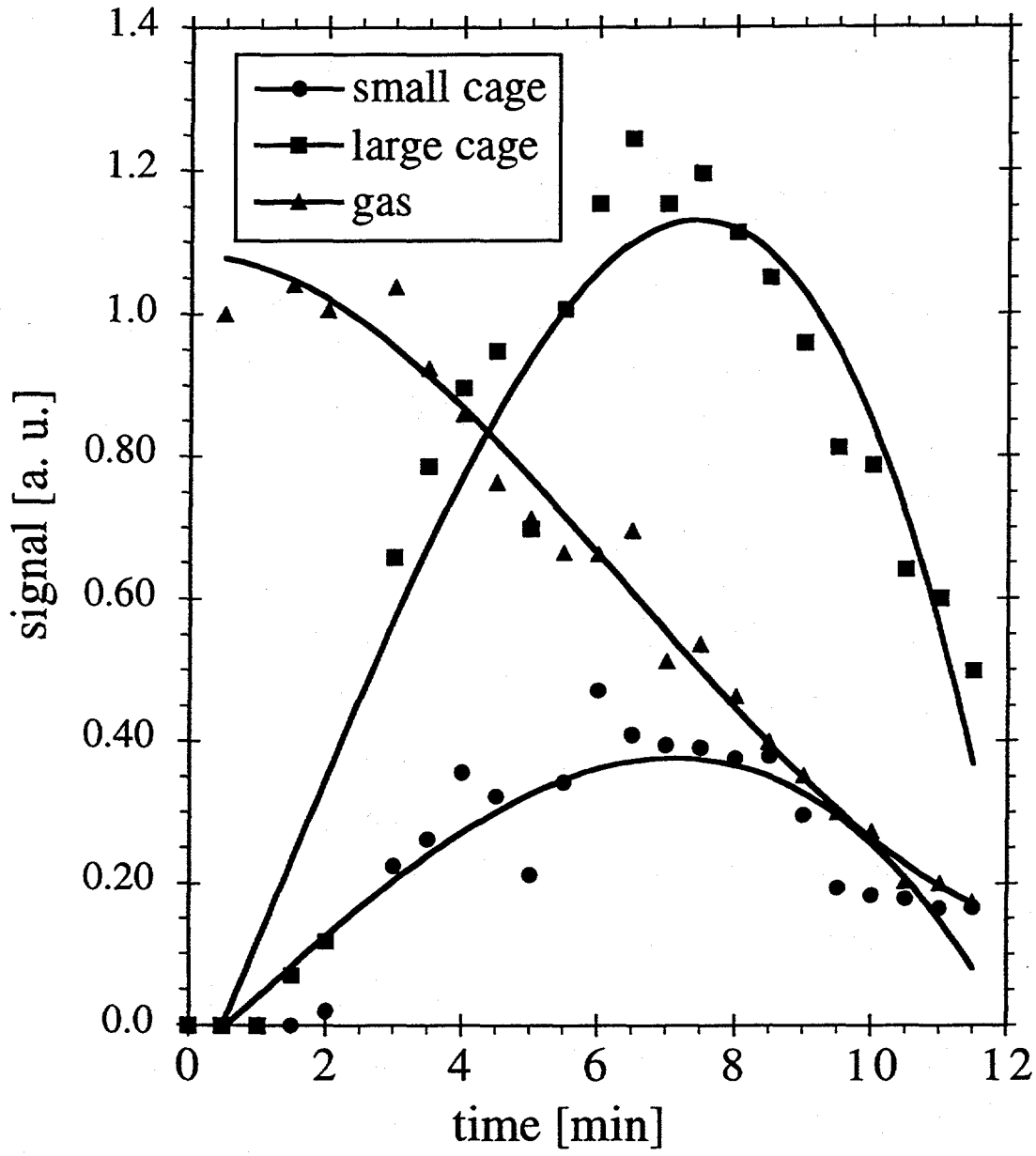

Figure 4.17 Formation of a xenon clathrate hydrate at 217 K monitored by the change in the integrated intensities of the ^{129}Xe NMR signals with time t after admission of the xenon. The curves serve merely to guide the eye.

The high sensitivity of the optically pumped xenon detection method compared to the volumetric methods discussed above makes it possible to observe hydrate formation on a much smaller scale. Whereas Falabella's data are reported in percent conversion[154], this method enables observation of clathrate formation in the ppm conversion range. This estimate is made by assuming that the total amount of ice used in the experiments is converted into an empty structure I hydrate lattice. With the optical pumping enhancement, a detection sensitivity of one occupied cage in 10^6 empty cages is obtained.

A simple model was used to describe the kinetics of hydrate formation in this experimental approach. There is general agreement in the literature that hydrate formation can be divided into two basic steps. In the first step, the gas is adsorbed onto the ice surface, accompanied by a relocation of the ice lattice molecules. The adsorption of the xenon is a reversible process that can occur at any xenon pressure. This intermediate structure is termed Xe_{ads}. It is assumed that the amount of ice converted into clathrate is very small compared to the initial amount of ice present, since no mechanical device is used to destroy the impenetrable clathrate layer covering the ice surface.[158] In the second step, the intermediate phase Xe_{ads} converts irreversibly into the clathrate hydrate lattice structure, referred to as Xe_{clath}. This model assumes that a minimum number of adsorbed xenon atoms is required for nucleation, and that the conversion of Xe_{ads} into Xe_{clath} occurs when this critical number is reached. The concentration of Xe_{ads} is assumed to be constant and Xe_{clath} depends only on the xenon pressure [Xe]. The rate coefficients for the individual steps cannot be determined from our data and are therefore expressed as an effective rate coefficient k. The processes can be described by the following scheme:

$$[Xe] \underset{k_{des}}{\overset{k_{ads}}{\rightleftarrows}} Xe_{ads} \xrightarrow{k_{clath}} Xe_{clath} \qquad (4.12)$$

$$\frac{d[Xe_{ads}]}{dt} = 0 \tag{4.13}$$

$$[Xe_{ads}] = \frac{k_{ads}}{k + K_{des}} \cdot [Xe] \tag{4.14}$$

$$\frac{d[Xe_{clath}]}{dt} = k_{clath} \cdot [Xe_{ads}] = \frac{k_{clath} k_{ads}}{k_{clath} + k_{des}} \cdot [Xe] = k \cdot [Xe] \tag{4.15}$$

The clathrate concentration is proportional to the integrated signal intensity of the NMR resonances from the small and large cages. However, it is necessary to account for the fact that the ^{129}Xe NMR signal intensity decays with time due to spin-lattice relaxation and, in particular, due to the NMR rf pulses. The correction for the decay due to rf pulses is required because the initial polarization is not the equilibrium Curie law polarization, but is created by the optical pumping process. Both effects are expressed as an overall time constant T_{decay}. Integration of the equation (4.15) and addition of an exponential decay term depending on the time constant T_{decay} yields the fitting function (4.16):

$$M(t) = k\, t\, [Xe] \exp[-\frac{t}{T_{decay}}] \tag{4.16}$$

where M(t) is the time-dependent integrated intensity of the signal of the enclathrated xenon in the large and small cages. Results of the fits are shown in Figure 4.18; the fitting parameters are summarized in Table 4.3. The errors of the fits listed in Table 4.3 are due to a decrease in signal-to-noise-ratio with time and severe phase and baseline correction, which are necessary for integration.

The data for the rate coefficients *k* in Table 4.3 reveal a temperature and pressure dependence. The rate decreases with increasing temperature, a result indicative of a negative activation energy. A negative Arrhenius energy has been experimentally observed previously[159] and has been recently confirmed theoretically.[157] At 217 K, the

T [K]	cage	k [MPa•min.]$^{-1}$	Δk [MPa•min.]$^{-1}$	T_{decay} [min.]	ΔT_{decay} [min.]	R
195	large	0.69	0.12	1.54	0.16	0.74
	small	0.68	0.16	1.49	0.20	0.65
217	large	0.91	0.07	4.34	0.25	0.94
	small	0.97	0.10	3.95	0.28	0.92
233	large	0.23	0.02	3.40	0.17	0.94
	small	0.27	0.02	3.07	0.16	0.91

Table 4.3 Rate coefficients k and decay constants T_{decay} for the formation of xenon clathrate hydrates, determined for inclusion of xenon in the large and in the small cages. k and T_{decay} are listed for the temperatures at which clathrate formation was observed. R is the correlation coefficient of the fits.

rate seems faster than at 195 K, but at 217 K the initial xenon pressure was substantially lower than in the other runs, thus raising the value of k in the applied model.

In Figure 4.19, the ratios of the rate coefficients of the large to the small cages are plotted versus temperature. These ratios are independent of pressure and unknown parameters such as the volume of the void spaces between ice crystals and the penetration depth of the xenon into the ice, and should depend only on temperature. With increasing temperature, the smaller cages are occupied more rapidly than the larger cages. Since the ease of clathrate formation decreases with increasing temperature, this may indicate that the intermediate phase Xe_{ads} resembles the

smaller cage structure. This result is supported by comparing the individual occupancy ratios of the cages for the various temperatures (Figure 4.20). Due to the difficulties in phasing the NMR spectra mentioned earlier, the individual cage ratios cannot be determined to better than ±10%, but two general trends can be observed.

First, the ratios of the cage occupancies have reached their equilibrium value after a short time (one to two minutes). The observed equilibrium values of the ratios range for the higher pressure samples (at 195 K and 233 K) from about 3.8 to 3.9, consistent with the value obtained by Ripmeester for a well equilibrated sample.[31] Secondly, the ratios seem lower at 217 K where the xenon pressure was also considerably lower compared to that at the other temperatures. However, the errors in integration are quite large and the differences between each temperature are small. To confirm these differences, more experiments at different temperatures and pressures should be performed. Nonetheless, it seems likely that at this lower pressure, the conversion from the Xe_{ads} phase to the clathrate hydrate structure Xe_{clath} is incomplete. This is again consistent with the first data points in Figure 4.20 at 233 K and 195 K, which exhibit a considerably smaller ratio of the cage occupancy, until the equilibrium value is reached.

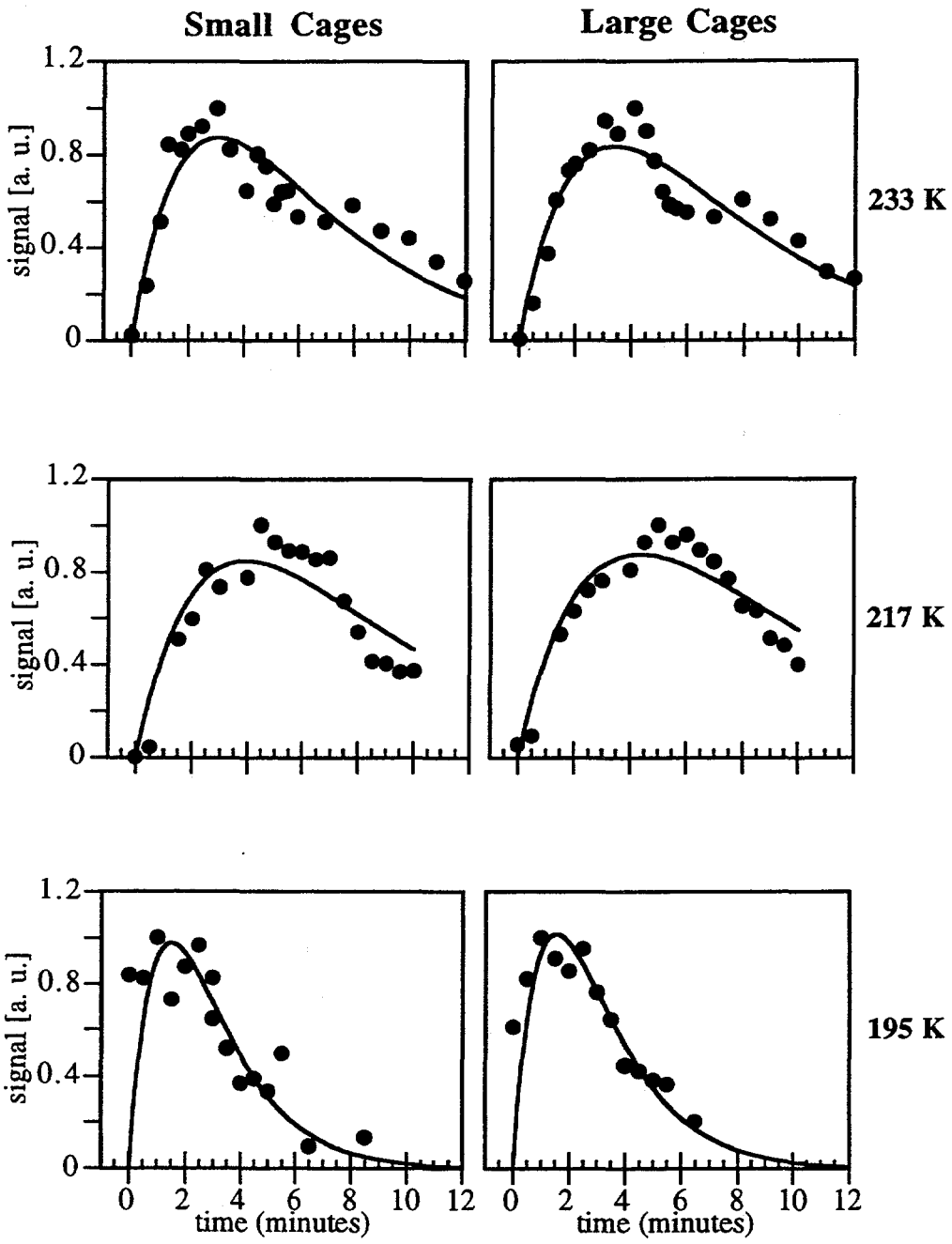

Figure 4.18 Xenon clathrate hydrate kinetic model. Experimental data points (dots), determined from the ^{129}Xe NMR spectra, approximated by the model function (line) for the large and the small cages at the given temperatures (see text).

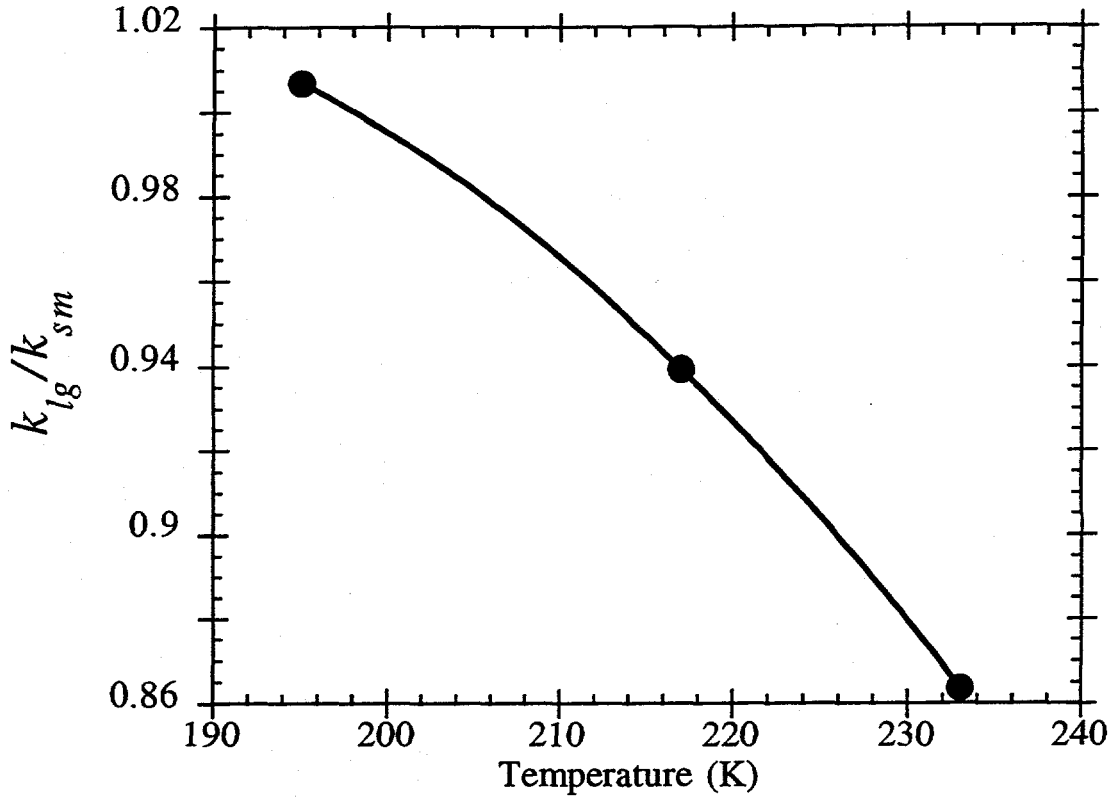

Figure 4.19 Temperature dependence of the ratios of the rate coefficients for the large over the small cages from table 4.3. The curve serves as a guide to the eye.

The decay constant T_{decay} listed in Table 4.3 is the same within experimental error for the small and the large cages. The effect of one pulse is evidently the same for both the xenon in the large and the small cages. The spin-lattice relaxation time T_1 of xenon occluded in the two cage types has not been determined explicitly, and the results in Table 4.3 suggest that it is the same for both cage sizes. The xenon spin-lattice relaxation time in the gas phase increases with decreasing pressure[25,163,164] and decreasing temperature.[164] Since in these experiments the majority of the xenon is in the gas phase and about 80% of the volume of the sample tube is at ambient temperature, the pressure effect on the xenon relaxation should dominate over the temperature effect. Therefore the longest spin-lattice relaxation times are expected at

the lowest pressure at 217 K, in agreement with the results. At the lowest temperature, the shortest decay constant T_{decay} is observed. Since it is primarily the xenon in the coil region which is depolarized by rf pulses, i. e., the enclathrated xenon, the destruction of the polarization is expected to be most efficient for the fastest enclathration process at 195 K, also in agreement with our data. At 170 K and 258 K no clathrate formation could be observed. At the lowest temperature (170 K), the formation of liquid xenon occurred after about 10 minutes. It has been observed previously that the condensation of xenon in porous systems is not instantaneous.[165] The liquid xenon was identified by its narrow ^{129}Xe NMR resonance at 240 ppm.

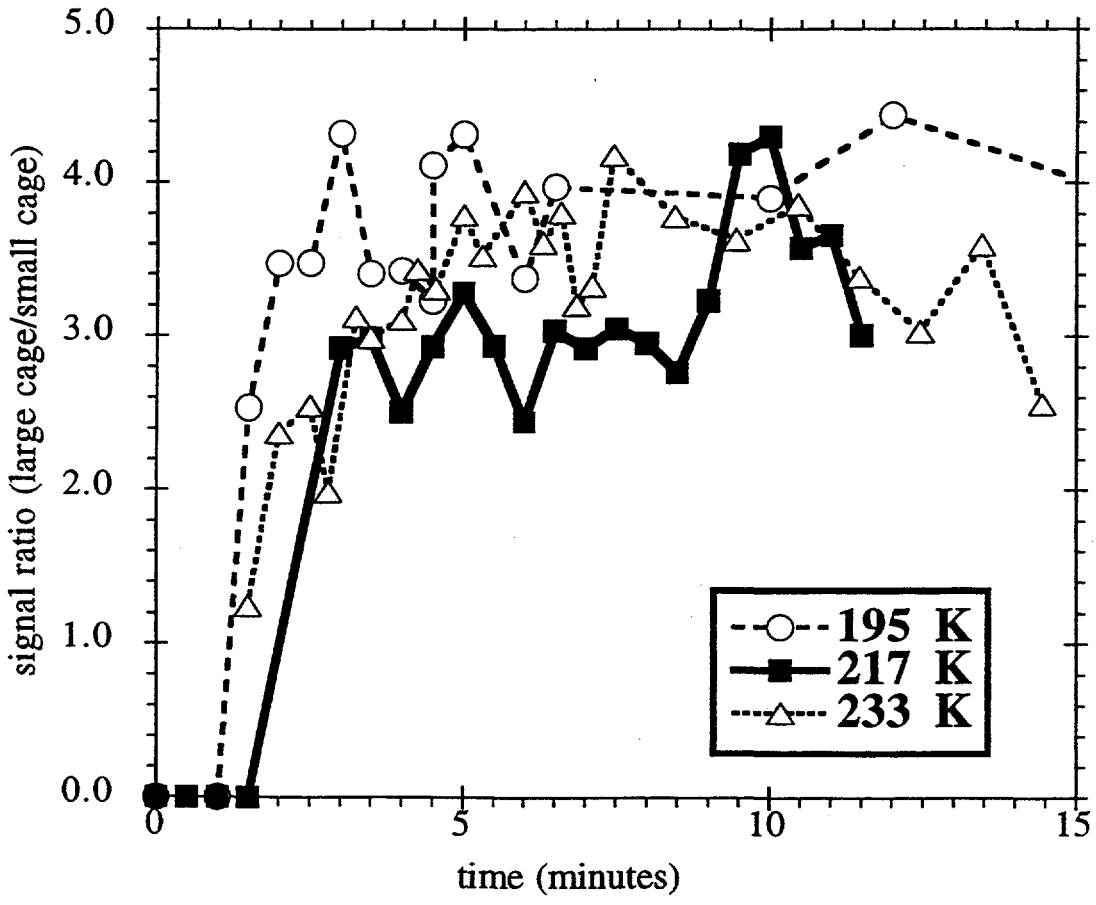

Figure 4.20 ^{129}Xe NMR signal ratios of xenon in the large to the small cages as a function of time after admission of the xenon.

At the highest temperature, 258 K, an interesting effect was observed. Following a period of 36.3 min, in which the sample was cooled from 258 K to 231 K, a period of 10.4 min was allowed for equilibration of the sample. The spectrum at t = 46.7 min revealed the two signals for enclathrated xenon and the gas signal. The formation of the clathrates was monitored for 17.2 min with a spectrum recorded every 2 min, indicating a slight increase in the magnitude of the clathrate peaks. At t = 63.9 min the sample was rapidly warmed to 258 K. The spectrum recorded 2 min later revealed only the gas signal, with complete disappearance of the two clathrate signals even in absence of sample equilibration. This observation emphasizes the narrow temperature/pressure range in which clathrate formation is observable. Moreover, it is a confirmation of the reproducibility of the applied method of xenon NMR.

4.5.4 Conclusions

This study represents the first investigation of a reaction involving polarized xenon. Previous results, the absence of an induction period, and a negative Arrhenius energy for the formation process are consistent with the results of the optical pumping experiments. The high detection sensitivity of this approach, when compared to volumetric methods, allowed the observation of clathrate formation at an early stage. These results imply that the presence of transient liquid water is not a necessary condition for clathrate formation. The pressure, temperature and time dependence of the occupancy ratios of the large over the small cages and of the ratios of the rate coefficients suggest that the intermediate phase, in which xenon is adsorbed onto the ice and has not yet converted into the clathrate hydrate structure, may resemble the structure of the smaller cages.

4.6 Conclusions

The use of optically polarized xenon extends the applicabilty of ^{129}Xe NMR investigations to systems which are inaccesible to thermally polarized xenon due to sensitivity limitations. For instance, polarized xenon may be used to investigate surfaces, providing information unattainable through other methods. In addition to the polymer system discussed here, polarized xenon studies have been performed on semi-conductor nanocrystals[166] and porous silicon.[167] Despite the utilty of the xenon NMR experiments, the information gained from these experiments is somewhat indirect. Of course it would be immensely useful to observe the surface resonances *directly*. This observation is not possible without the increased sensitivity of the polarized xenon. However, the possiblity of transferring the magnetization of the polarized xenon to surfaces is discussed in the next chapter.

Chapter 5

Polarization Transfer of Optically Polarized Xenon

5.1 Introduction

One of the most exciting potential applications of polarized xenon is its use as a magnetization source in polarization transfer experiments, which are ubiquitous in NMR spectroscopy. Techniques that exploit cross polarization,[121,122] the Overhauser effect,[168,169] and the solid effect[123,124] have been used to increase the small thermal-equilibrium nuclear polarization. The application of these techniques to polarization transfer between highly polarized xenon and a low sensitivity material creates the possibility of very large signal enhancements. This chapter opens with a discussion of the theory of cross polarization and continues with specific examples of low-field and high-field polarization transfer.

5.2 Cross Polarization in NMR

One of the fiercest ongoing battles in NMR is the fight against insensitivity. At some point, conventional approaches of increasing sensitivity will fail. There is a limit to the field strength available in superconducting magnets; moreover, at high field strengths, certain interactions increase, obscuring spectral information. On the other hand, there are also difficulties in performing experiments at cryogenic temperatures. Finally, spectrometer time is nearly always limited, so endless signal averaging is not the answer. One elegant solution is the use of double resonance, using the magnetization of a sensitive nucleus to enhance the magnetization of a less sensitive nucleus. This chapter discusses cross polarization experiments from polarized xenon utilizing two experimental approaches: low field thermal mixing and high field Hartmann-Hahn matching.

5.3 Low-Field Cross Polarization from Optically Polarized Xenon to $^{13}CO_2$

5.3.1 Introduction

For magnetization transfer between different types of nuclei, the energy levels of the two nuclei must somehow be matched. A very simple method of matching the energy levels is to reduce or remove the external magnetic field. The Zeeman interaction is then absent or strongly reduced and the spins can mix via the dipolar interaction to reach a common spin temperature.[170,171]

5.3.2 Theory of Cross-Relaxation[170,171]

Initially, the density matrix of the system of sensitive I spins and insensitive S spins is given by $\rho_{initial} = \beta_1 \omega_I I_z + \beta_2 \omega_S S_z$. (5.1)

The I and S spins are at different inverse spin temperatures β_1 and β_2, respectively. At low fields, the dipolar energy reservoir can make up the difference in the mismatch of the residual Zeeman energies and the system can reach a common spin temperature. The equilibrated system is described by the density matrix:

$$\rho_{final} = \beta(\omega_I I_z + \omega_S S_z). \tag{5.2}$$

Neglecting relaxation processes, the system evolves at constant energy, such that:

$$Tr(\rho_{initial}\mathcal{H}) = Tr(\rho_{final}\mathcal{H}) = \beta Tr(\mathcal{H}^2). \tag{5.3}$$

Solving for the common final inverse spin temperature β,

$$\beta = \frac{Tr(\rho_{initial}\mathcal{H})}{Tr(\mathcal{H}^2)} = \frac{\beta_1 \omega_I^2 N_I I(I+1) + \beta_2 \omega_S^2 N_S S(S+1)}{\omega_I^2 N_I I(I+1) + \omega_S^2 N_S S(S+1)}. \tag{5.4}$$

This can be rewritten as $\beta = \frac{\beta_1 + \alpha\beta_2}{1+\alpha}$, (5.5)

where $\alpha = \frac{\gamma_S^2 N_S S(S+1)}{\gamma_I^2 N_I I(I+1)}$. (5.6)

5.3.3 Background

The possibility of low field cross polarization from polarized xenon was first demonstrated by Gatzke et. al.[155] in cross-relaxation experiments from ^{129}Xe to ^{131}Xe in frozen laser-polarized xenon. They performed a number of experiments in which the magnetic field was momentarily lowered to a mixing value of less than or equal to 100 G. The resulting ^{131}Xe polarization was estimated to be 5 %. The subject of this section is the transfer of ^{129}Xe spin order to *molecules*, constituting a chemically relevant method of sensitivity enhancement for solid state and surface NMR. Cross polarization of $^{13}CO_2$ embedded in solid laser-polarized xenon was achieved by thermal mixing in low-field.

5.3.4 Experimental Methods

The optical pumping apparatus described in Chapter 4 was assembled on the laser table, and connected to an L-shaped NMR sample tube. The experimental timing sequence is illustrated in Figure 5.1. The polarized xenon was combined with 500 torr-cc of 99% isotopically enriched $^{13}CO_2$ (Isotec Inc.) at room temperature and allowed to mix for about 45 s. The mixture was frozen rapidly into the NMR sample tube immersed in liquid nitrogen. During the freezing process, a magnetic field of 150 G was applied to lengthen the spin-lattice relaxation time of the ^{129}Xe.[155] The cross relaxation was accomplished by rapidly switching the magnetic field to a value of B_{mix} for a duration τ_{mix} and then returning the field to 150 G. The sample was then transferred to a 4.2 T field for ^{13}C NMR detection. Similar results were obtained for values of {B_{mix} and τ_{mix} } of {0.1 G , 200 ms}, {35 G, ~200 ms}, {35 G, ~ 10 s} and Xe:CO_2 ratios of 6:1, 4:1, 1:1, and 1:6.

5.3.5 Results and Discussion

The sensitivity enhanced spectra of the 4:1 Xe:CO_2 solid mixture is shown in Figure 5.2(a). This spectrum was obtained with right circularly polarized light. The measured values for $\sigma_\perp$ = 232.8 ± 2.3 and $\sigma_\parallel$ = -82.5 ± 2.3 ppm for the axially symmetric chemical shift tensor, extracted from the fit of the spectrum with the best signal-to-noise ratio, differ slightly from the $\sigma_\perp$ = 245 ppm and $\sigma_\parallel$ = -90 ppm as reported by Beeler *et al.*[172] for CO_2 in a methane-doped argon matrix at 20 K.

The spectrum in Figure 5.2(b) demonstrates the inversion of the NMR signal occurring when the helicity of the optical pumping light is changed from positive to negative because the density matrix of the xenon following optical pumping corresponds to positive spin

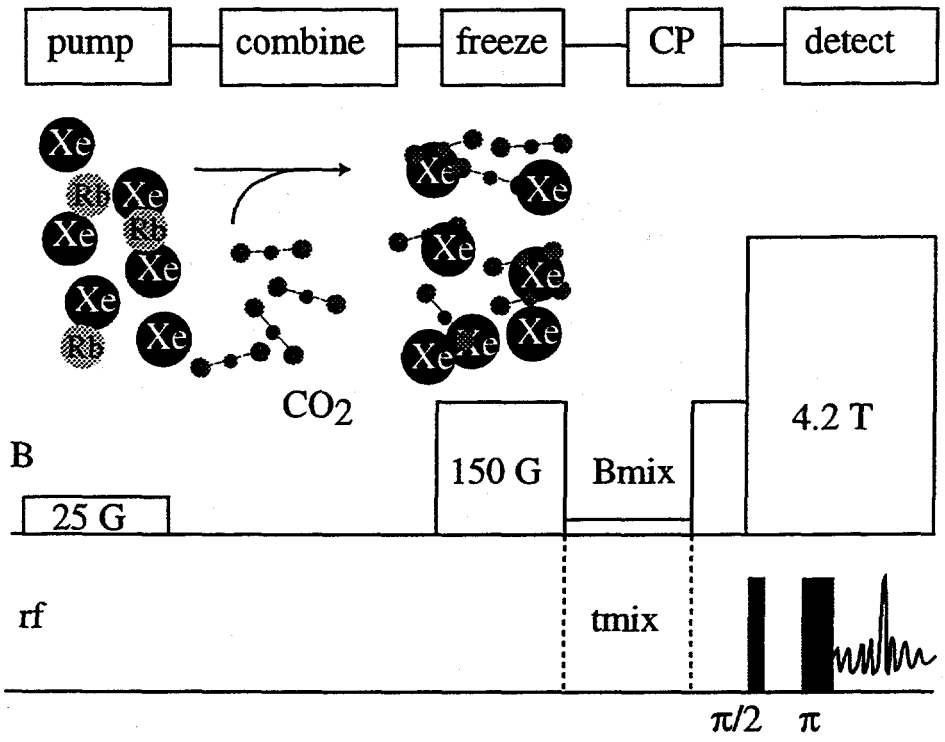

Figure 5.1 Timing diagram of the experimental procedure for Xe CO_2 experiment. Rubidium is laser-irradiated in the presence of xenon for ~20 minutes to allow for optical pumping and spin exchange. After separation from the rubidium, the xenon is combined with CO_2 gas, mixed for 45 s and expanded into the precooled sample cell in a field of 150 G. The field is then reduced to a value of B_{mix} for a period of τ_{mix} during which thermal mixing occurs. The sample is subsequently removed from the nitrogen bath and immediately transported to high field where the signal is observed using a spin echo pulse sequence.

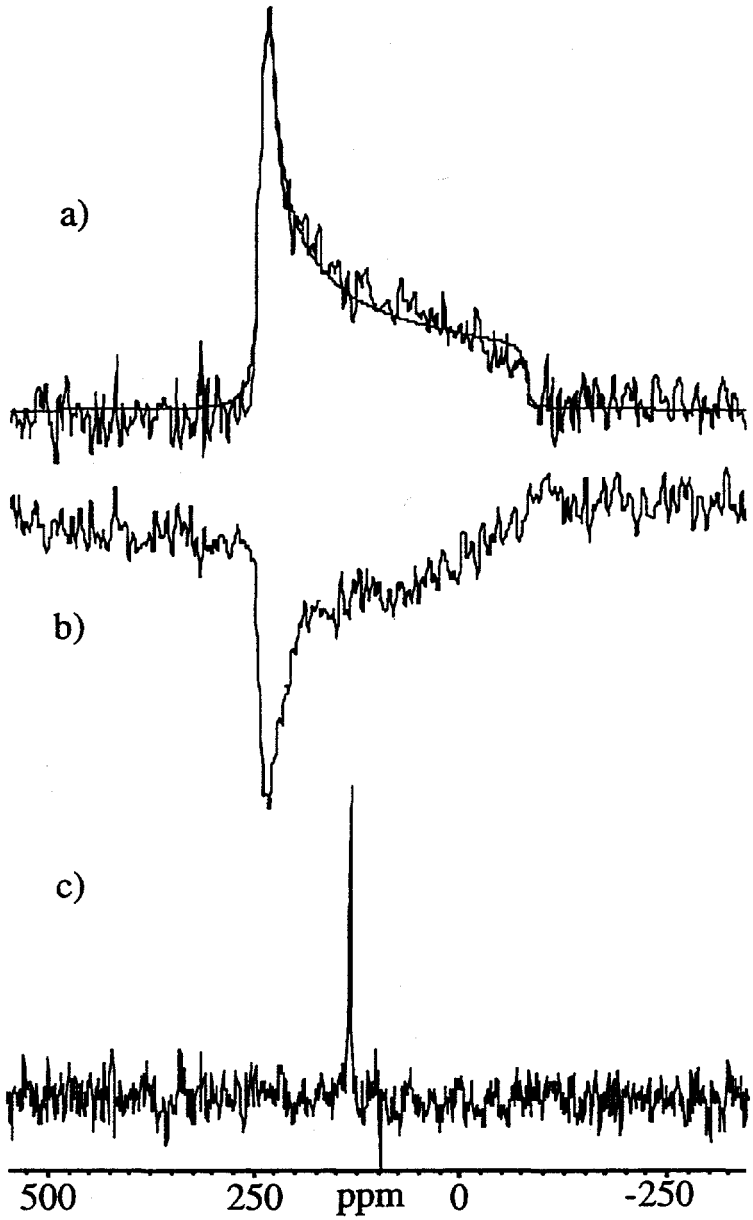

Figure 5.2 CO_2 spectra (a) ^{13}C NMR spectrum of 1.6 x 10^{19} $^{13}CO_2$ molecules obtained after thermal mixing in zero field at 77 K with 6.4 x 10^{19} laser-polarized ^{129}Xe atoms. The optical pumping light was σ^- circularly polarized. The solid line represents a fit of the theoretical anisotropic chemical shift lineshape to the experimental spectrum. (b) Spectrum obtained with the same procedure as in (a), but with σ^+ light. (c) ^{13}C NMR spectrum of 5 x 10^{18} $^{13}CO_2$ molecules at 300 K after 64 averaged scans. The chemical shift of 124.6 ppm is referenced to an external standard of liquid TMS.

temperature for σ^- light and to negative spin temperature for σ^+ light. The population inversion may be interpreted as a reversal in sign of the spin temperature. Demagnetization of the spin system to low field, wherein the difference in Larmor frequencies between ^{129}Xe and ^{13}C is comparable to the heteronuclear dipolar interaction, conserves the sign of the spin temperature. After thermal mixing during a time on the order of T_2, the density matrix becomes proportional to exp ($-\beta H$), where H is the low-field Hamiltonian and β is the common inverse spin temperature. The sign of β is thereby determined by the sense of the circular polarization of the light. Negative spin temperatures correspond to emissive NMR transitions as illustrated in Figure 5.2(b).

As a frequency and sensitivity reference, the conventional NMR spectrum of gaseous $^{13}CO_2$ for a similar number of molecules if presented in Figure 5.2 (c). The enhancement is estimated to be 200 by a comparison of the integrated intensity of the laser-enhanced signal with that of the $^{13}CO_2$ gas reference, corrected for the difference in the number of ^{13}C spins. The xenon enhancement factor is approximately 18 000, corresponding to a polarization of about 10%. Using equation (5.6), assuming an equal number of ^{129}Xe and ^{13}C nuclei, the final magnetization of the ^{13}C is predicted to be 0.45 times the initial Xe magnetization. Clearly, optimal polarization transfer has not been attained. However this calculation does not account for the possibility that only a fraction of the total number of CO_2 molecules are in dipolar contact with the polarized xenon. The solid mixtures were prepared by opening a stopcock separating the two gases, waiting 45 s, and allowing them to expand into a pre-cooled sample region. No special measures were taken to confirm that a homogeneous matrix was formed. It is quite possible that the solid xenon and cabon dioxide were largely segregated and only a small percentage of eh different nuclei were in sufficient contact for magnetization exchange.

Xenon enriched to 80% isotopic purity of ^{129}Xe and depleted to 1.2% ^{131}Xe was used to avoid potential losses due to low-field cross relaxation from the former to the latter. This is the dominant spin-lattice relaxation mechanism at 4.2 K for magnetic fields lower than 1000 G. The spin lattice relaxation time for the xenon in the mixture was extremely long, as is characteristic of the pure solid.

5.3.6 Conclusions

The Xe-CO_2 polarization transfer was a promising first step towards polarization transfer to surface nuclei. The number of surface spins on 1 m^2 of typical powdered solid is on the order of 10^{19}, approximately the same number of ^{13}C nuclei detected in this experiment. However, this method relies on xenon freezing reasonably well with the polarization transfer target. Moreover, the measured nuclei must have long T_1s at low fields. These experimental requirements proved to be quite rigorous, and attempts to transfer polarization from xenon to other molecules, such as carbon monoxide, acetylene, trichloroetheylene were all unsuccessful. The next section details a high-field approach, which circumvents these limitations, to polarization transfer between xenon and surface protons.

5.4 Cross Polarization from Polarized Xenon to Surface Protons

5.4.1 Introduction

A high-field method of matching the energy levels of nuclei with different γ was discovered by Hartmann and Hahn.[121] In the doubly rotating frame, the flip-flop

transitions between two different types of spin-1/2 nuclei are conserving when the Hartmann-Hahn condition is met:

$$\gamma_I B_{1I} = \gamma_S B_{1S}. \tag{5.7}$$

Basically, the experiment works as follows: the abundant I spin system is brought into equilibrium with the lattice at an inverse temperature $\beta_L=(kT_L)^{-1}$. The I spins are then brought into contact with the rare S spins, which are considered to have an infinite spin temperature. The contact can be achieved by irradiating the I and S spins at their resonant frequencies. The strengths of the rf fields are chosen such that the Hartmann-Hahn condition is satisfied, and the mutual I and S spin flips via the I-S dipolar interaction become energy conserving and cause the system to equilibrate. The result is a cooling of the S-spin system and a small heating of the I spin reservoir. The effect on the I spins is usually quite small since the S spins are rare. The procedure may be repeated multiple times. This technique as it is practiced today is known as cross polarization and was first developed by Pines, Gibby, and Waugh.[122]

5.4.2 Theory of Cross Polarization

The Hamiltonian of the spin system described above has the form

$$\mathcal{H} = \mathcal{H}_z + \mathcal{H}_d + \mathcal{H}_{1I}(t) + \mathcal{H}_{1S}(t). \tag{5.8}$$

where H_Z is the Zeeman interaction of the I and S spins with the external field, H_d is the full dipolar interaction, and H_{1I} (t) and H_{1S}(t) describe the coupling of the I and S spins with rf irradiation. In the doubly rotating frame the Hamiltonian becomes:

$$\mathcal{H}_R = \mathcal{H}_d^0 + \mathcal{H}_{1I} + \mathcal{H}_{1S} + \mathcal{H}(t), \tag{5.9}$$

where $\mathcal{H}_d^0$ is the truncated dipolar Hamiltonian and

$$\mathcal{H}_{1I} = -\gamma_I \hbar B_{1I} \sum_i I_{ix} \tag{5.10}$$

$$\mathcal{H}_{1S} = -\gamma_S \hbar B_{1S} \sum_i S_{ix} \tag{5.11}$$

The phase of rotation is chosen to put B_{1S} along the x axes in the I and S rotating frames. The two terms H_{1I} and H_{1S} are reservoirs of Zeeman energy that exchange energy via the dipolar coupling. The system ultimately approaches a thermal equilibrium in the rotating frame. It can be described by the density matrix:

$$\rho_R^{eq} = \frac{\exp(-\beta \mathcal{H}_R)}{Tr[\exp(-\beta \mathcal{H}_R)]}. \tag{5.12}$$

In the high temperature approximation, $\rho_R^{eq} = Z^{-1}[1 + \beta(\mathcal{H}_{1I} + \mathcal{H}_{1S})]$, (5.13)

where Z = Tr{1}. In general, each reservoir can approach a different equilibrium spin temperature.

$$\rho_R^{eq} = Z^{-1}[1 + \beta_I \mathcal{H}_{1I} + \beta_S \mathcal{H}_{1S}] \tag{5.14}$$

The Zeeman energy of the system is given by:

$$E = -Tr\{\rho_R \mathcal{H}_R\} = E_I + E_S = -\beta_I C_I B_{1I}^2 - \beta_S C_S B_{1S}^2 \tag{5.15}$$

where C_I and C_S are Curie constants given by $C_I = \frac{1}{3}\gamma_I^2 \hbar^2 I(I+1)N_I$, (5.16)

and similarly for C_S. N_I and N_S are the total number of I and S spins, respectively. The x component of the magnetization in the rotating frame is given by:

$$M_I = \gamma_I \hbar \langle I_x \rangle = \gamma_I \hbar \, Tr\{\rho_R I_x\} = \beta_I C_I B_{1I}. \tag{5.17}$$

In a cross polarization experiment, the I spins are allowed to equilibrate with the lattice, yielding a magnetization $M_I^0 = \beta_L C_I B_0$. (5.18)

The density matrix for the I-spin system in the rotating frame is

$$\rho_R^{(0)} = Z^{-1}(1 + \beta_0 \mathcal{H}_{1I}). \tag{5.19}$$

and from (5.17), the magnetization is given by $M_I^0 = \beta_0 C_I B_{1I}$. (5.20)

Combining (5.14) and (5.15), the definition of βo is apparent, $\beta_0 = \beta_L \frac{B_0}{B_{1I}}$. (5.21)

So the inverse spin temperature in the rotating frame corresponds to a cooling of the I-spin reservoir.

The S spins are then coupled to the I spins by tuning the rf irradiation in the S rotating frame such that the I and S spin systems come to a common equilibrium spin temperature, β_1, described by the density matrix:

$$\rho_R^{(1)} = Z^{-1}[1 + \beta_1(\mathcal{H}_{1I} + \mathcal{H}_{1S})] \tag{5.22}$$

Since energy is conserved, $\beta_1 C_I B_{1I}^2 + \beta_1 C_S B_{1S}^2 = \beta_1 C_I B_{1I}^2$. (5.23)

The final equilibrium spin temperature may be solved for $\beta_1 = \beta_0(1+\varepsilon)^{-1}$, (5.24)

where $\varepsilon = \frac{\gamma_I^2 C_S}{\gamma_S^2 C_I} = \frac{S(S+1)N_S}{I(I+1)N_I}$. (5.25)

The S magnetization following contact with the I spins is given by

$$M_S^{(1)} = \beta_1 C_S B_{1S} = \beta_1 C_S \frac{\gamma_I}{\gamma_S} B_{1I}. \tag{5.26}$$

Using (5.21), (5.24), and (5.25), the S magnetization becomes:

$$M_S^{(1)} = \frac{\gamma_I}{\gamma_S}(1+\varepsilon)^{-1} \beta_L C_S B_0. \tag{5.27}$$

Assuming $\varepsilon << 1$, $M_S^{(1)} = \frac{\gamma_I}{\gamma_S}(1-\varepsilon)\beta_L C_S B_0$.

If the contact procedure is repeated n times, the magnetization of the S spin reservoir is given by $M_S^{(n)} = \frac{\gamma_I}{\gamma_S}(1-\varepsilon)^n M_S^{(0)}$. (5.28)

5.4.3 Background

Cross-polarization (CP)[122] has been used successfully to selectively probe surface nuclei when the magnetization source, usually protons, resides exclusively at the surface. Maciel and Sindorf have utilized ^{1}H-^{29}Si CP-MAS to investigate the resonances of surface silicon atoms in silica.[138] Oldfield and coworkers used ^{1}H-^{17}O CP to observe surface hydroxyl groups of high surface area metal oxides that are difficult to detect by conventional NMR.[173] This technique is also useful for investigating interfaces. Zumbulyadis and O'Reilly have used ^{1}H-^{29}Si CP to estimate the proximity of the backbone of a polymer to the surface of silica.[174]

For many systems of interest, such as polymers, there are no such distinctive surface nuclei. A new method of detecting surface species in such a system is to adsorb optically polarized xenon-129 onto a surface and use the polarized xenon as the source of magnetization in a CP experiment.[175]

The high field cross polarization methods should be advantageous in allowing nuclear spin selectivity in the transfer step as well as circumventing relaxation and transport problems of the low field method discussed in the previous section. In work discussed in this section, contact between laser polarized xenon and surface spins was achieved in high field by Hartmann-Hahn matching of the energy levels in the rotating frame with direct NMR detection of the polarized species.[121,122] Proton spins are observed due to their abundance at the surface and the dominant dipolar interactions with adsorbed xenon.

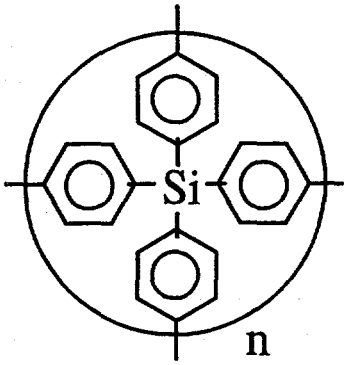

Figure 5.3 Structure of poly(tetrabiphenylsilane), surface area 1035 m^2/g.

5.4.4 Experimental

Sample Preparation

The samples utilized were poly(triarylcarbinol), poly(tetraphenylsilane), and Aerosil R812. Poly(triarylcarbinol), the subject of conventional ^{129}Xe NMR investigations discussed in Chapter 2, and poly(tetraphenlysilane), shown in Figure 5.3, are microporous and have BET surface areas, obtained by nitrogen isotherms, of 835 m^2/g and 1069 m^2/g, respectively.[176] Due to the large surface area, at low temperatures these polymers rapidly adsorb most of the optically polarized xenon present ($\approx 5 \times 10^{19}$ atoms). Aerosil R812 is a commercial sample of silica with methyl capping groups, reported by Degussa to have a surface area of 260 m^2/g. The total surface area present in the sample tubes was approximately 300 m^2 for the poly(triarylcarbinol) and poly(tetrabiphenylsilane) samples and 30 m^2 for Aerosil R812 sample. The samples were loosely packed into 10 mm diameter L-shaped sample tubes, evacuated to 5×10^{-5} torr at $\approx 50°$, and cooled to either 10 or 90 K before the introduction of polarized xenon. Typically 5-10 seconds were waited after adding the xenon before starting the pulse sequence. The T_1 of the ^{129}Xe on the sample surfaces is about 20 seconds.

Pulse Sequences

For the ^{129}Xe *to* ^{1}H cross polarization experiments, Figure 5.4 (a) shows the multiple contact pulse sequence used. After the polarized xenon is adsorbed on the polymer surface and allowed to equilibrate, the proton resonance of the sample is saturated either by a train of 45° pulses or by a single pulse of 1 ms duration to destroy any thermal polarization. A 90° pulse is applied to the xenon spins, which are then spin-locked for the duration of the acquisition. A Hartmann-Hahn matching pulse is applied to the proton spins for a time τ to establish a dipolar contact between ^{1}H and ^{129}Xe, and the proton signal is detected immediately afterward either directly or by refocussing using a dipolar echo to reduce the effects of the spectrometer dead time. This ^{1}H-^{129}Xe contact and signal acquisition are repeated up to 8 times while the xenon spins remain spin-locked. The transmitter power levels for the Hartmann-Hahn matching condition were optimized using a xenon quinol clathrate compound[177] at room temperature. The matching times were optimized by proton to xenon cross polarization in a sample of poly(triarlycarbinol) sealed with 375 torr ^{129}Xe.

Figure 5.4(b) shows the sequence used to examine the efficiency of polarization transfer from the xenon to the proton reservoir. The first step of the sequence is a proton to xenon cross-polarization to establish the xenon signal. The enhanced xenon magnetization is then stored along the z axis for at time τ. The xenon and proton reservoirs are again brought into dipolar contact and the xenon magnetization is consequently drained away. The xenon signal is measured as a function of the second contact time. This sequence is referred to as the DRAIN experiment.

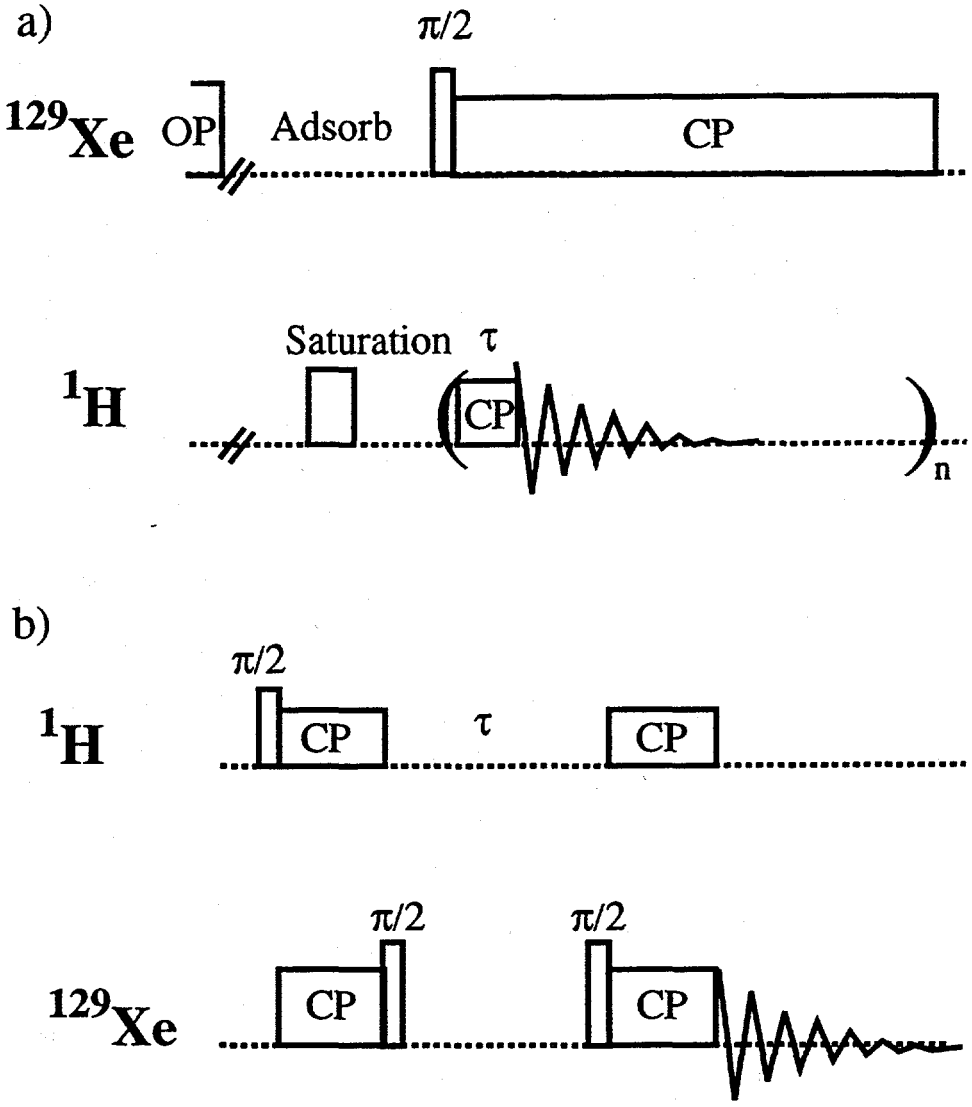

Figure 5.4 Pulse sequences used in cross polariztion experiments a) Multiple contact pulse sequence. Following optical pumping and adsorption of the xenon, the proton spins of the sample are saturated and then repeatedly cross polarized by Hartmann-Hahn matching to the xenon. b) Pulse sequence used in the DRAIN experiment. An initial CP sequence is followed by storage of xenon magnetization along the z-axis for a fixed time τ, and a second cross-polarization step. The second contact time is varied and τ is set to 1s.

Probes

The xenon and proton NMR frequencies are 49.45 MHz and 178.75 MHz, respectively. Two probes were used for the experiments. The first is the Doty design-based probe discussed in Chapter 2 which utilizes cold flowing nitrogen gas to control the temperature of a Dewared sample region. The 90° pulse lengths used for this probe are 8.5 μs for xenon and 4.5 μs for proton. Figure 5.5 shows a schematic drawing the second probe, a modified commercial double resonance probe (Chemagnetics). The main modification is the small size of the cold region; this facilitates fast change of sample temperature. A vacuum insulated liquid helium transfer line is used to inject cooled nitrogen gas or liquid helium into the sample region from the top of the magnet. The exit gas is vented through another vacuum insulated line. A shielded thermocouple is installed very close to the sample. The probe can be cooled to liquid nitrogen temperature in about 10 minutes and can be warmed quickly when flushed with warm nitrogen gas. When liquid helium is used, the sample can be cooled to ~10 K. The temperature in the probe can be controlled to an accuracy of a few Kelvins. The 90° pulse lengths used are 6 μs for xenon and 4 μs for proton. The advantage of this probe over the first is its smaller proton background and its ability to go to lower temperatures; however, this is offset by the disadvantage of temperature gradients, which broaden the NMR signals.

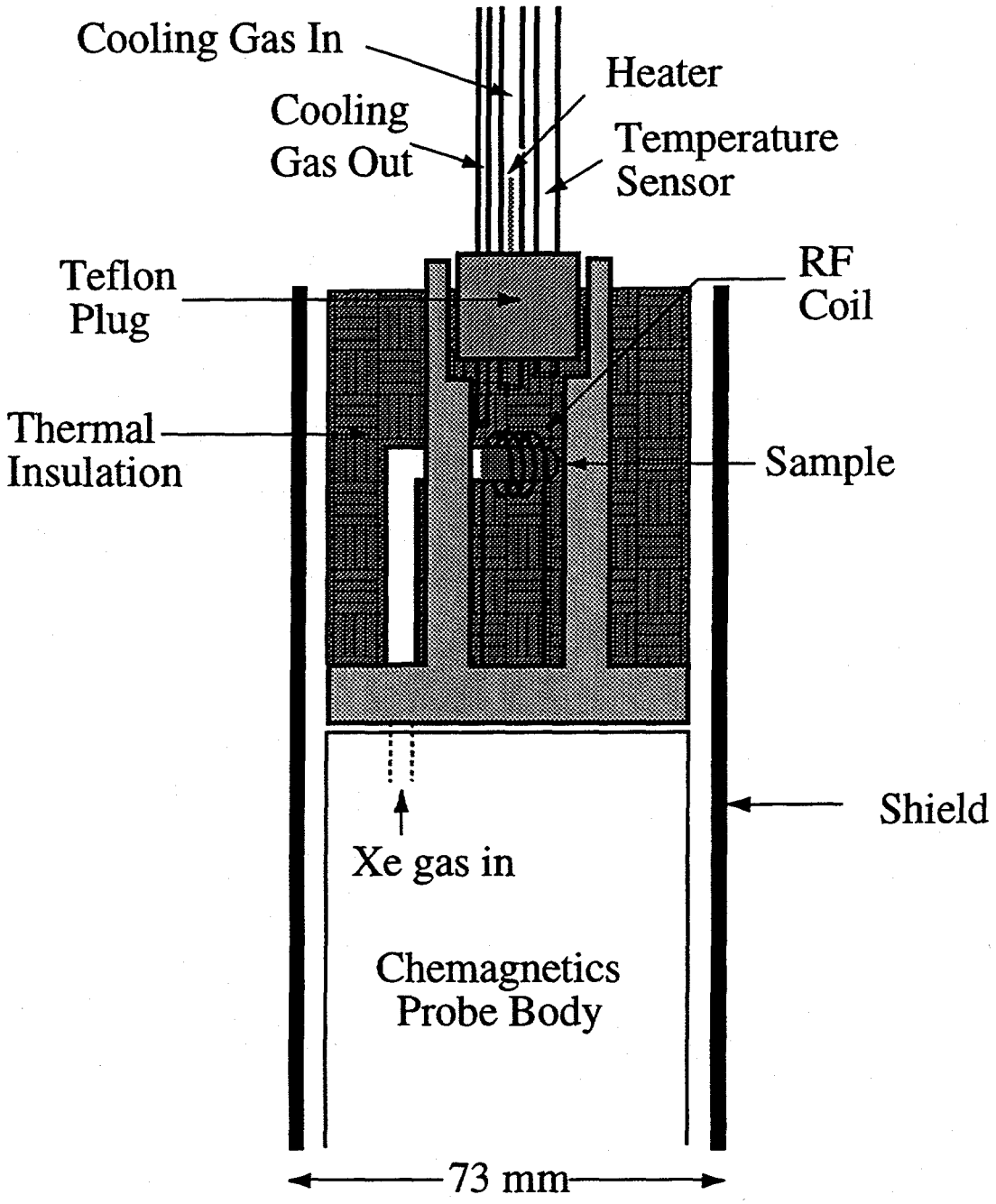

Figure 5.5 A schematic drawing of the probe. The probehead consists of an RF coil in a small sample region, surrounded by thermal insulation. A vacuum insulated liquid helium transfer line is used to inject cooled nitrogen gas or liquid helium, which is resistively heated, into the sample region from the top of the magnet. The exit gas is vented through another vacuum insulated line. A shielded thermocouple is installed close to the sample.

5.4.5 Results and Discussion

Xenon NMR

The ^{129}Xe NMR spectrum of xenon adsorbed on poly(triarylcarbinol) at 113 K is shown in Figure 5.6. The two resonances correspond to frozen xenon (~320 ppm) and xenon adsorbed on the polymer (~170 ppm).

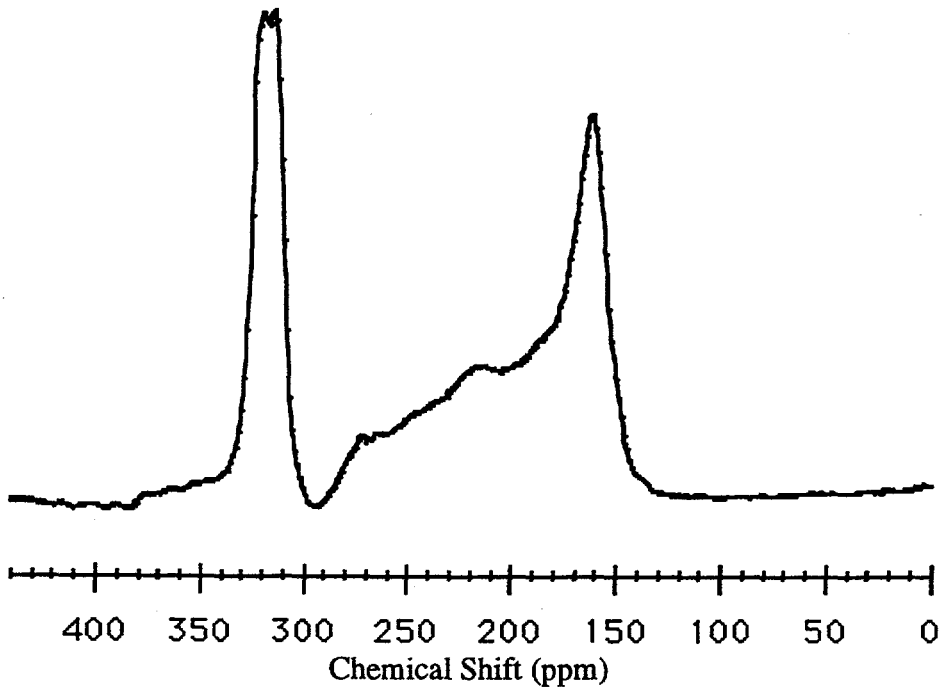

Figure 5.6 NMR spectrum of ^{129}Xe adsorbed on poly(triarylcarbinol) at T=-160°C, approximately 10 seconds after the xenon was introduced into the sample region (referenced to low pressure xenon gas).

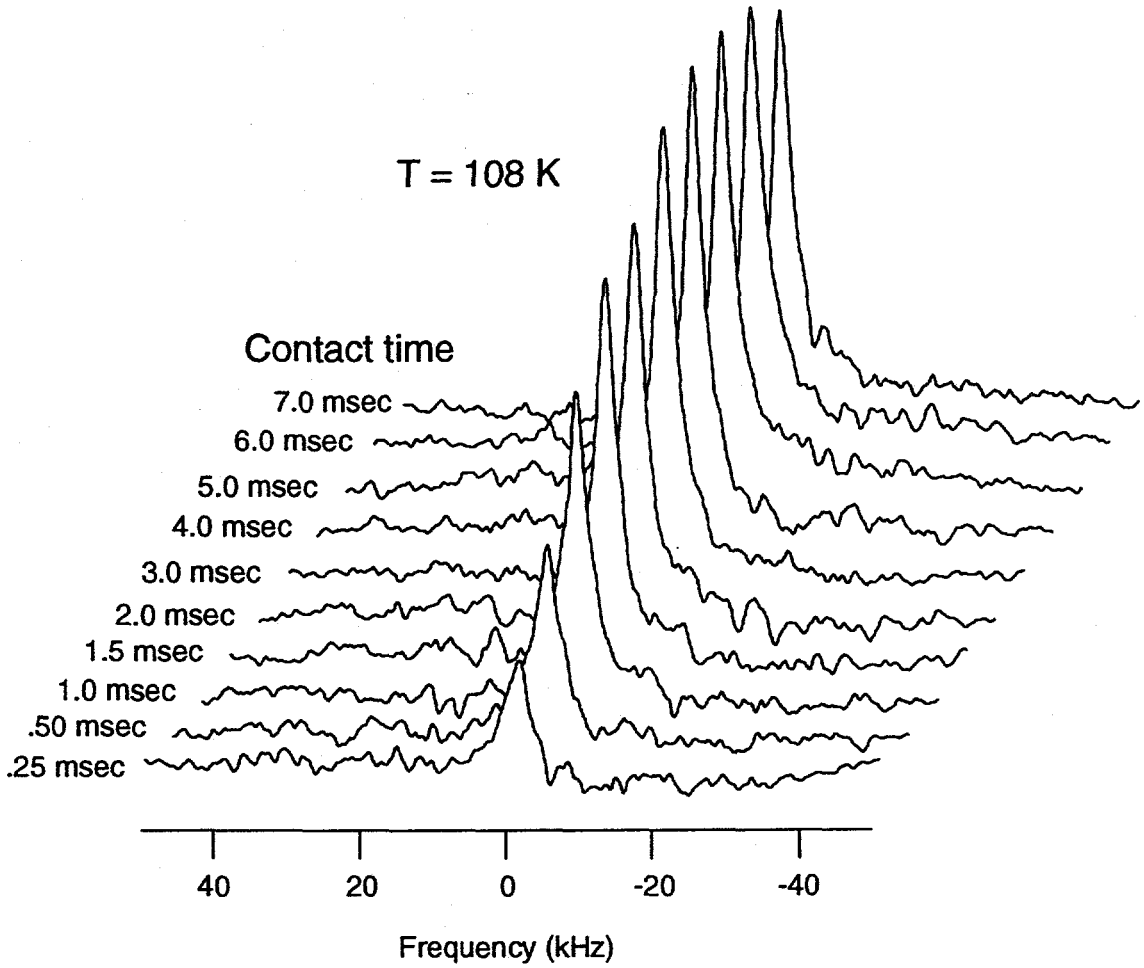

Figure 5.7 Magnetization build-up for ^{1}H to ^{129}Xe cross polarization in a sample of poly(triarylcarbinol) sealed with 375 torr of xenon gas. Optimal cross polarization at 109 K is 5 ms.

Proton to Xenon Cross-Polarization

Cross-polarization *from* protons *to* xenon has been demonstrated in poly(triarylcarbinol)[178] below about 133 K, indicating heteronuclear dipolar coupling with an optimal contact time of approximately 5 ms. Figure 5.7 shows a typical magnetization buildup curve for the xenon with the growth due to polarization transfer, followed by an exponential decay due to spin-lattice relaxation in the rotating frame.

Xenon to Proton Cross-Polarization on Poly(triarylcarbinol)

The spectra resulting *from* optically polarized xenon to proton cross-polarization in poly(triarylcarbinol) are shown in Figure 5.8. The figure also shows the resulting spectrum when the helicity of pumping light is inverted. The bottom spectrum shows the difference spectrum.

The change in helicity of the pumping light from σ^+ 5.8 (top) to σ^- 5.8 (middle) results in a 180 phase shift in the spectrum, which confirms that xenon indeed constitutes the polarization source for the proton spins. No signal from the polymer was obtained when the sequence was run immediately before the xenon was added or when the Hartmann-Hahn matching field amplitudes were deliberately misset. The sharp feature slightly out of phase, near the center of the spectra arises from proton spins not in contact with xenon, mostly from the probe background of the Doty design-based probe. Note that this feature is subtracted out in the difference spectrum of Figure 5.8 (bottom) since it is invariant to inversion of the xenon polarization.

Depth-Profiling

The ^1H signal of poly(triarylcarbionol) was studied at several matching times, using a single contact experiment, and found to be consistent with the expected exponential dependence on the ^{129}Xe-^1H contact time. At short contact times ($\leq$ 0.5 ms), the signal was very weak but could be enhanced by employing a multiple contact sequence. The spectrum at the shortest contact time (0.2 ms) was perceptibly broader (43 kHz) than the equilibrium spectrum obtained by a simple echo sequence (36 kHz). At longer contact times the line width approached the bulk equilibrium value, probably due to proton spin diffusion, consistent with a spin diffusion coefficient estimated to be $\approx$0.6 nm^2/ms.[179]

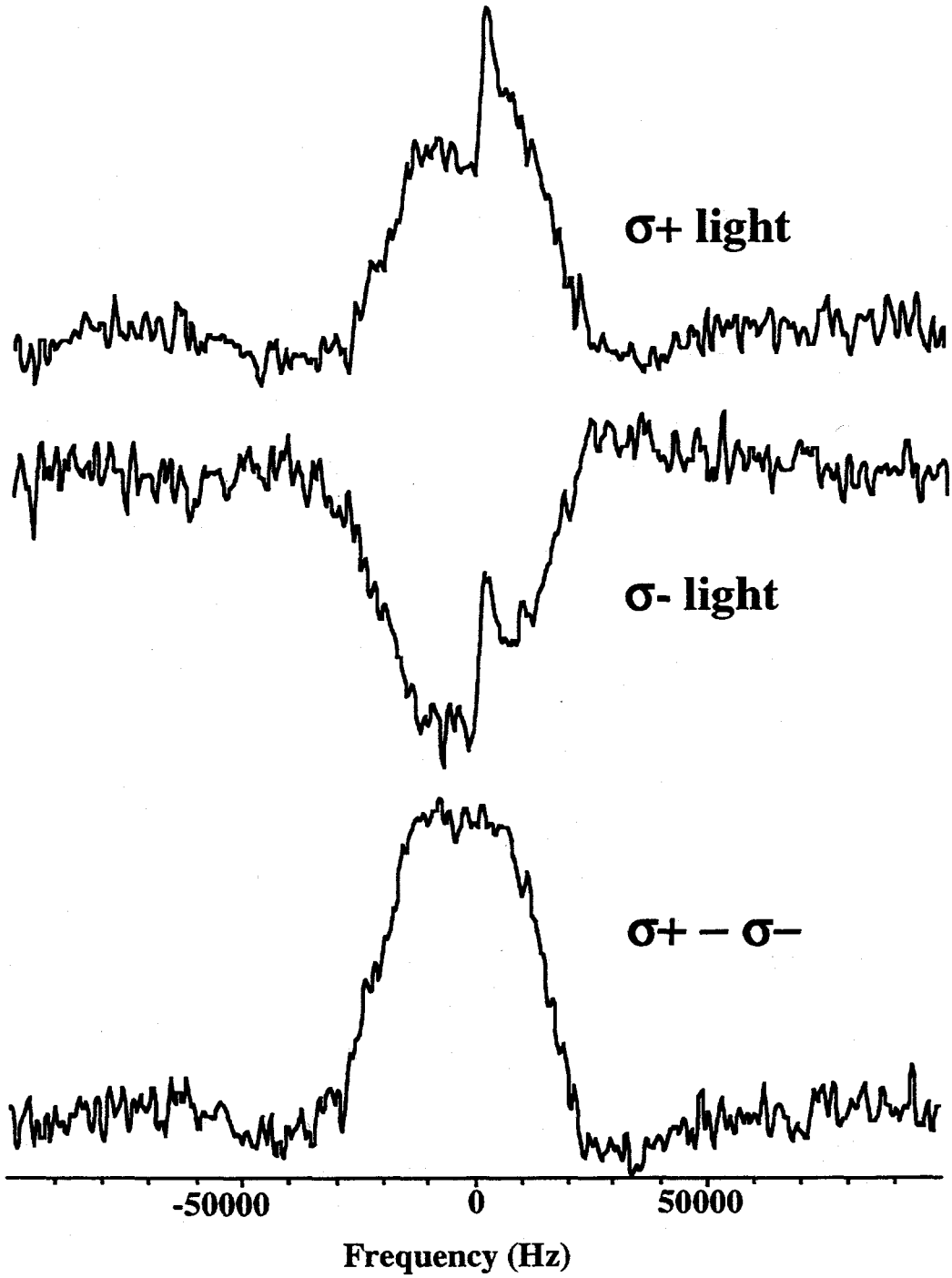

Figure 5.8 Cross polarization spectra from polarized xenon to surface hydrogens (top) ^{1}H spectrum of the surface protons of poly(triarylcarbinol) resulting from cross polarization from polarized xenon polarized with σ^{+} light, (middle) Same as above, but with σ^{-} light,. (bottom) Difference spectrum. Note that the background feature is invariant to polarization of light and is removed by subtraction of two spectra.

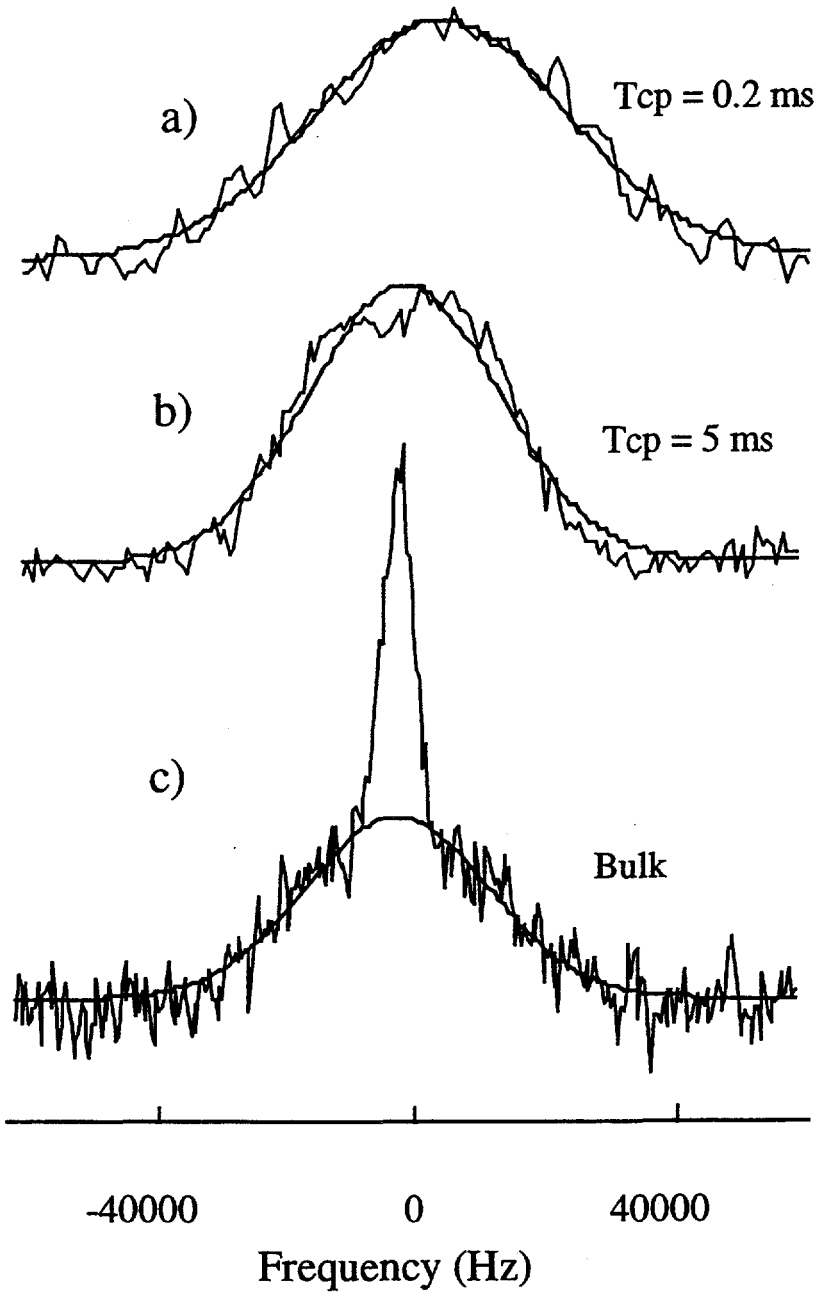

Figure 5.9 Depth profiling using cross polarization (a) ^{1}H spectrum following cross polarization from ^{129}Xe. T_{cp} = 0.2 msec. FWHM = 43 kHz (b) Same as above, T_{cp} = 5 msec, FWHM = 36 kHz. (c) ^{1}H bulk spectrum FWHM = 33 kHz.

Multiple Contact Studies

Figure 5.10 shows a typical multiple contact signal for the ^{129}Xe-^{1}H OPCP of xenon adsorbed on poly(tetrabiphenyl silane) at 90 K. Each of the signals is a FID immediately after one contact. The acquisition time for each FID is 128 μs. In this example, there are 8 contacts of 4 ms each, with resulting signals in the first seven contacts.

These multiple contact studies were undertaken to monitor the complete magnetization transfer process. The basic idea is that the observed ^{1}H signal is proportional to the ^{129}Xe magnetization prior to the cross polarization contact, and thus it is a measure of the decay of ^{129}Xe polarization during the complete CP experiment. Moreover, this experiment may yield multiple signals from a single OPCP run, and it is possible to combine these signals to further increase the signal-to-noise ratio. The FID signal intensity decays with each contact.

It is clear that the ^{129}Xe spin magnetization is not transferred completely to the ^{1}H spins during the first contact period. The CP process can be understood as the

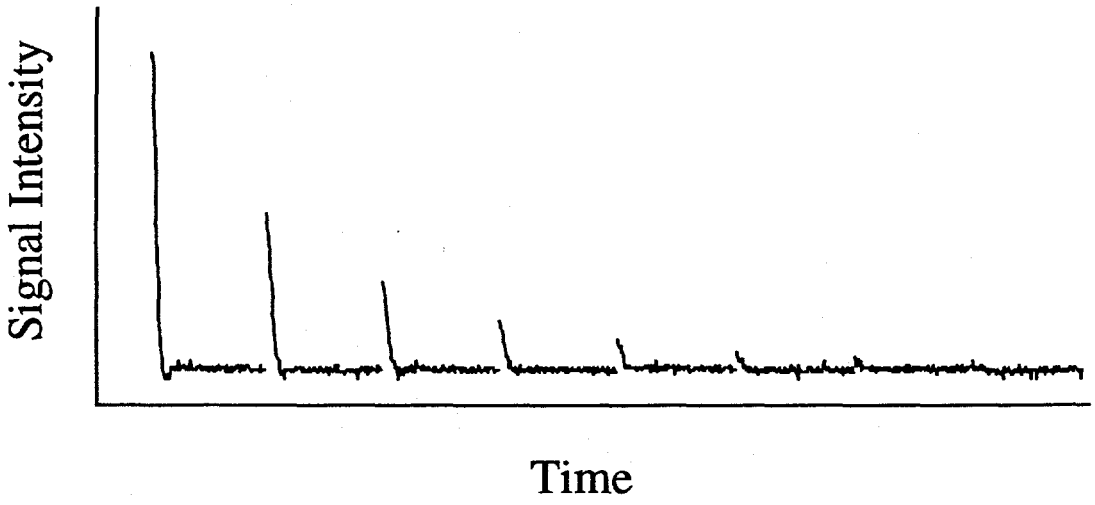

Figure 5.10 ^{1}H signals from the poly(tetrabiphenylsilane) sample in a multiple contact OPCP experiment. Contact time is 4 ms.

transfer of nuclear Zeeman energy in the rotating frame. The energy of each nuclear spin reservoir is given by $N \bullet (\gamma B_1) \bullet P$, where N represents the number of spins, B_1 is the radiofrequency (RF) magnetic field for each nucleus, and γ is the gyromagnetic ratio of the nucleus, and P is the polarization of each nuclear species. Conservation of energy dictates that the energy gain in the proton spin reservoir equals the energy loss in the xenon spin reservoir,

$$N_H \bullet (\gamma B_1)_H \bullet P_H = N_{Xe} \bullet (\gamma B_1)_{Xe} \bullet (P_o - P_{Xe}) \tag{5.29}$$

where P_0 represents the initial xenon polarization prior to the contact period. Under the Hartmann-Hahn matching condition, the ratio of the rf field at the NMR frequency of ^{129}Xe and ^1H equals the inverse of the γ ratio, $(\gamma H_1)_{Xe} = (\gamma H_1)_H$. We assume that during the contact period, a thermal equilibrium is reached between the proton and xenon spin systems in the rotating frame, so that the final polarizations of the two spin systems are the same, $P_{Xe} = P_H \equiv P$. The final polarization after each contact becomes:

$$P = P_o(1 + \frac{N_H}{N_{Xe}})^{-1} \tag{5.30}$$

If $N_H = N_{Xe}$, then $P = 0.5\ P_o$. Therefore, if the number of protons is equal to the number of xenon atoms, each signal in the multiple contact sequence should be half the intensity of the previous signal. If $N_{Xe} >> N_H$, there should be little decay of the signal in subsequent contacts. Conversely, if $N_H >> N_{Xe}$, then the proton signal should decay rapidly. For multiple contact experiments, one would expect the intensity of each subsequent FID to decay exponentially:

$$P_n = P_{n-1} \bullet (1 + \frac{N_H}{N_{Xe}})^{-1} = P_o \bullet \exp(-\alpha \cdot n) \tag{5.31}$$

where $\alpha = \ln(1 + N_H / N_{Xe})$.

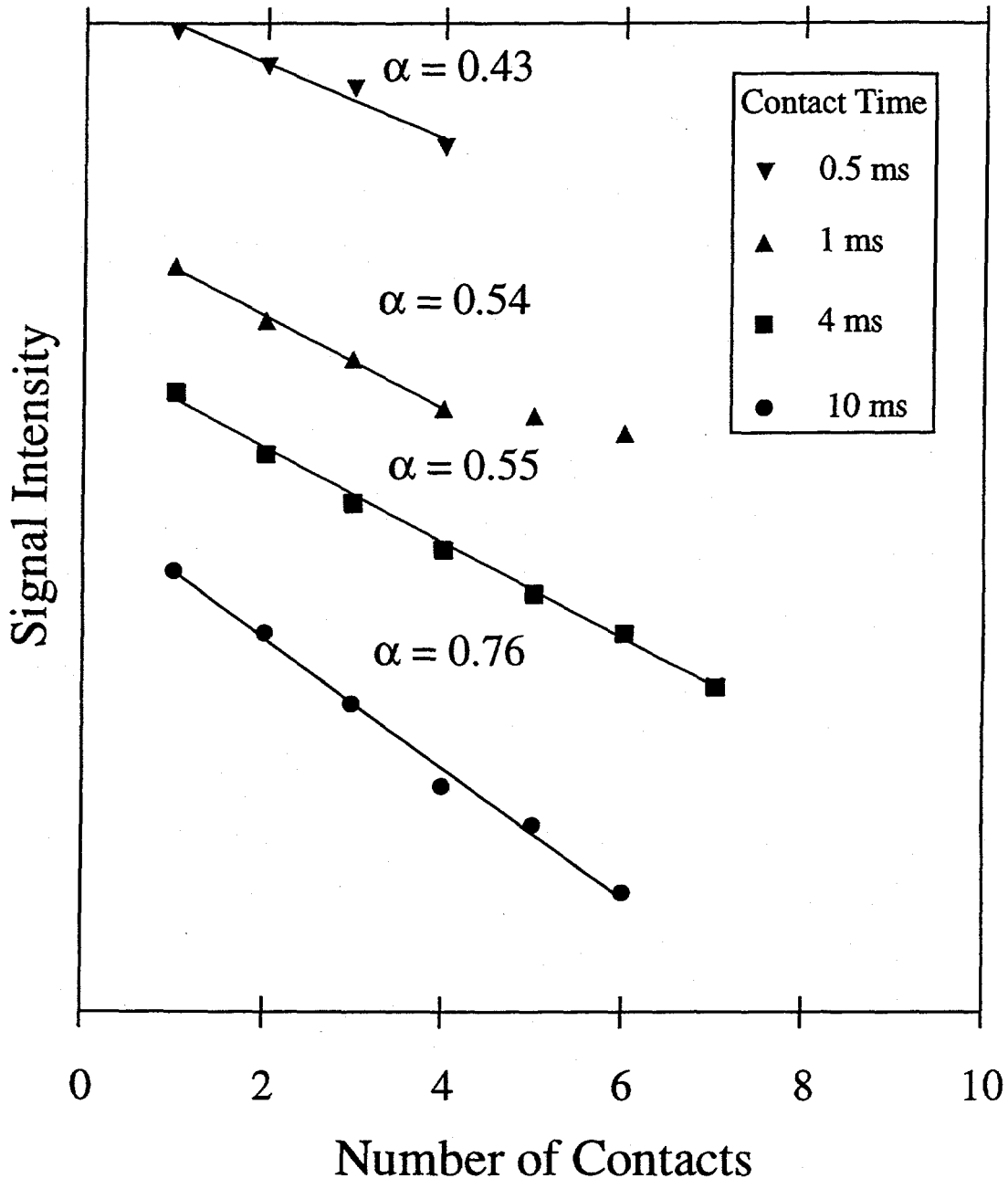

Figure 5.11 Signal intensity versus number of contacts for contact times of 0.5, 1, 4, and 10 ms, obtained by OPCP experiments on poly(tetrabiphenylsilane). The signal intensities have been scaled for clarity.

If the thermal equilibrium is not reached, the decay factor α may also be dependent on the length of the contact time, and, in general, should be smaller than $\ln(1+N_H/N_{Xe})$. Experimentally, the observed decay factor α is close to ln(2). Figure 5.11 shows the signal intensity as a function of the number of dipolar contacts for the contact times of 0.5, 1, 4, and 10 ms for OPCP on the poly(tetrabiphenylsilane) sample. The decay factors α for the four contact times are 0.43, 0.54, 0.55, and 0.76, respectively. The dependence of α on contact time is qualitatively consistent with the above considerations. Nuclear relaxation certainly contributes to the signal decay, however, since the T1ρ of xenon under these conditions is measured to be 33 ms, this contribution may be neglected in all but the longest contact time experiments.

DRAIN Studies

To further address the question of CP efficiency, the ^{129}Xe signal as a function of the contact time in the DRAIN experiment was observed. This experiment was performed on a sample of poly(triarylcarbinol) sealed with 375 torr of xenon gas and a poly(tetrabiphenyl silane) sample connected to the glassware of the optical pumping cell with ^{129}Xe pre-adsorbed and equilibrated for at least 20 minutes. The results from both samples are similar. The data for the poly(triarylcarbinol) sample are displayed in Figure 5.12.

The xenon signal observed after a proton matching pulse decays very rapidly, while the xenon signal observed when the experiment is performed without the proton matching pulses shows only a very slight decay, likely due to (rotating frame) spin-lattice relaxation of ^{129}Xe magnetization. The proton matching pulse establishes dipolar contact between ^{129}Xe and ^{1}H and effectively drains away the xenon nuclear Zeeman energy in the rotating frame. The polarization is transferred completely from the xenon to the proton spin reservoir within a 4 - 5 ms contact period, indicating

efficient magnetization transfer. The effects of xenon spin diffusion were also investigated by varying the delay times between the contacts in the DRAIN experiment, and preliminary results indicate that xenon spin diffusion does not limit the cross polarization efficiency.

In the DRAIN experiment the xenon magnetization is completely transferred in 4-5 ms; however, in the multiple contact experiments, signal is still obtained after seven 4 ms contacts! This implies that in the multiple contact experiment ^{129}Xe magnetization is added into the xenon spin reservoir during or after each contact period. One possible explanation is that after xenon is released into the sample region, some of the xenon atoms may not contact the surface immediately. Due to the long T_1 of

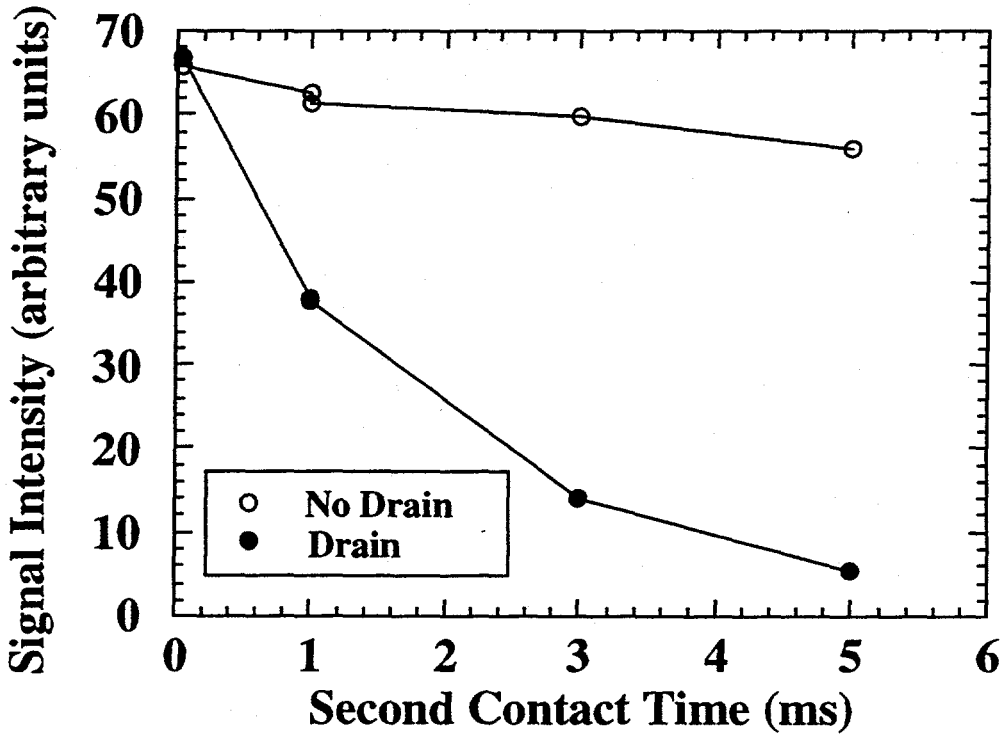

Figure 5.12 The DRAIN experiment The ^{129}Xe signal intensity is compared with and without the second proton matching pulse. Without the matching pulse, the xenon signal intensity decays quite slowly. With the matching pulse, the xenon signal is essentially drained with a 5 ms contact time.

xenon in the gas phase, these xenon atoms remain polarized. As these xenon atoms condense onto the surface during the course of the experiment, they can replenish the polarization of the xenon reservoir and contribute to the second and subsequent CP ^{1}H signals.

The DRAIN sequence was also used to calculate the enhancement of the surface ^{1}H signal obtained using OPCP. For this purpose, however, the ^{1}H signal, rather than the xenon signal, was detected. By utilizing the two CP steps in this manner, only the surface protons (i.e., the protons near xenon) contribute to the detected signal. This proton signal obtained by signal averaging can be compared directly to the signal obtained via the OPCP experiment, which also detects only surface protons. Thirty-two signal averages using the DRAIN sequence were accumulated on the sample of poly(triarylcarbinol) after xenon gas was adsorbed at 90 K in the same fashion as in an OPCP experiment. A single shot acquisition of xenon adsorbed on poly(triarylcarbinol) using OPCP resulted in an enhancement of roughly 800. Although encouraging, this factor is still an order of magnitude less than the direct enhancement in the ^{129}Xe signal obtained for laser-polarized xenon over thermal ^{129}Xe. These figures suggest that not all of the polarized xenon is in close contact with the surface for magnetization transfer to occur, which is consistent with Figure 5.6. The main difference in the procedure of the DRAIN and OPCP experiments, besides the polarization of ^{129}Xe, is that in the OPCP experiment the xenon is introduced rapidly to the sample and may not be sufficiently cooled to the sample temperature prior to the execution of the experiments. This difference introduces the possibility that the cross-polarization enhancement obtained using OPCP is partly limited by diffusion of the xenon from the gas phase to the sample surface.

Low Temperature Cross Polarization

Cross-polarization experiments from ^{1}H to ^{129}Xe adsorbed on poly(triarylcarbinol) at 10 K have been performed. Figure 5.13 shows a comparison of the signal intensity as a function of the contact time for the CP experiments at 10 and 90 K. At 10 K the signal reaches the maximum after a 2 ms contact time, while at 90 K, the signal reaches the maximum around 8 - 10 ms. These results suggest that significant motion of the adsorbed xenon atoms occurs on the time scale of a few milliseconds at 90 K. From a two-exponential fit to the 10 K experiment, we have obtained a value of 0.7 ms for T_{IS}, which is comparable to the values expected for ^{13}C-^{1}H (~0.1 -1 ms).[122]

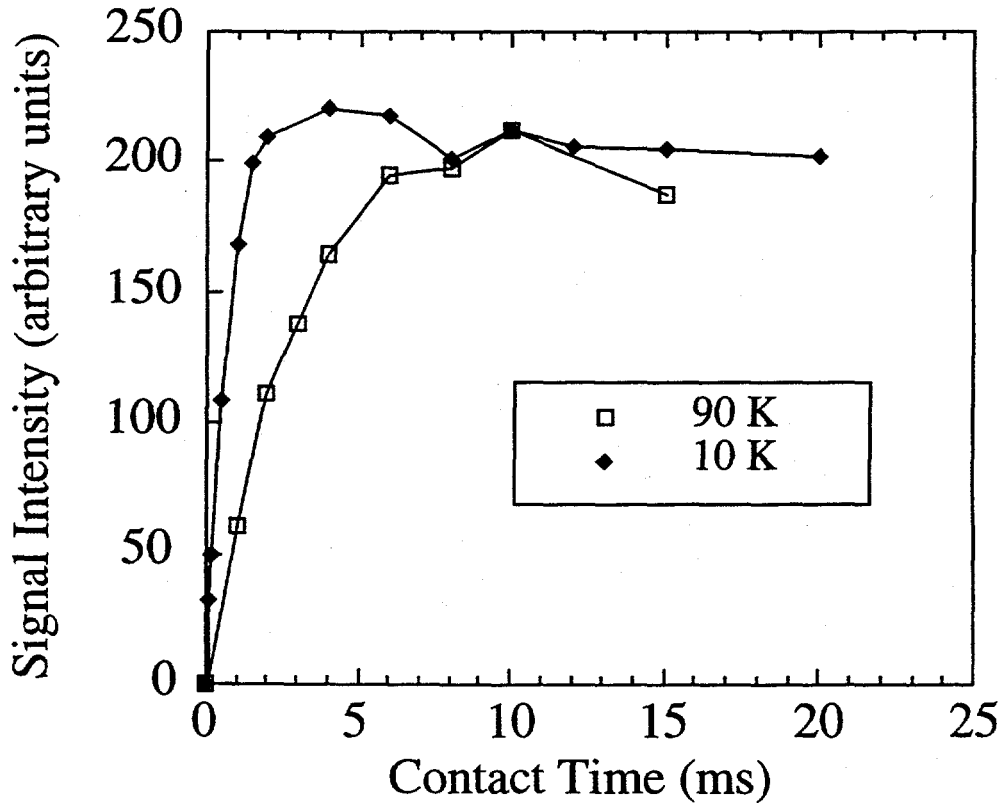

Figure 5.13 The contact time dependence of ^{129}Xe signal from CP from ^{1}H on poly(triarylcarbinol) at 10 K at 90 K. The lines are provided to guide the eye.

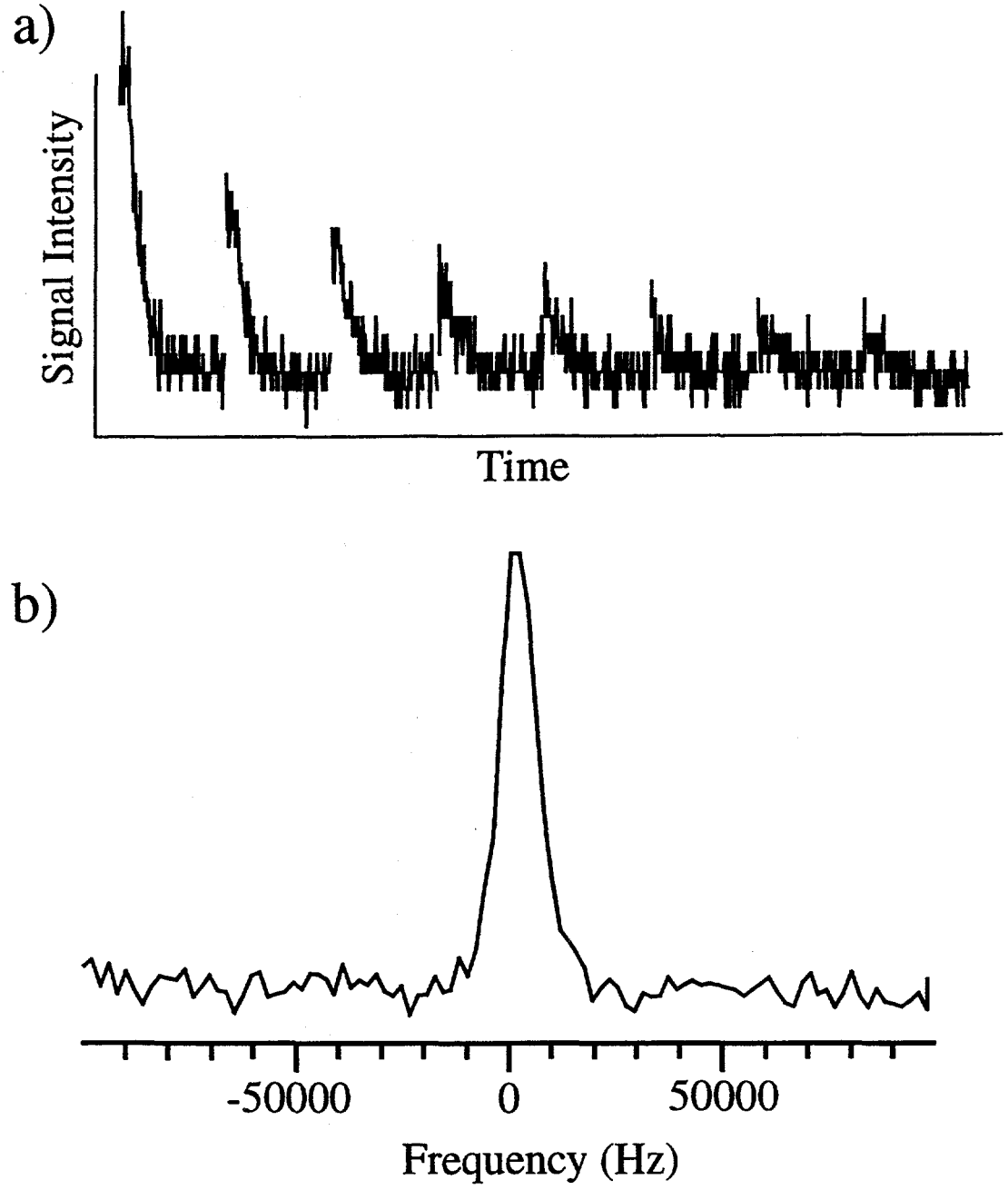

Figure 5.14 Cross polarization to a lower total surface area sample. a) ^{1}H signals from the Aerosil R812 sample in a multiple contact optical pumping cross-polarization experiment performed at 90 K. b) The spectrum obtained by fourier transform of the first signal in (a). The FWHM is 20 kHz.

Cross Polarization to Lower Surface Areas

The first OPCP ^1H spectra obtained from a lower total surface area sample, Aerosil R812, are shown in Figure 5.14. (The digitization noise in the spectra reveals a problem unique to OP NMR--the problem of predicting in advance how much attenuation is required before the pre-amplifier. In this case, too much attenuation was inserted.) The previous experiments were all performed on poly(triarylcarbinol) or poly(tetrabiphenyl silane), both of which are ultra-high surface area and microporous. The surface area of the Aerosil R812 is quite high, 260 m^2/g, yet the sample mass used in our study was only 0.1 g. Thus the total surface area of this sample is around 30 m^2, a factor of 10 less than for the other two samples. Obtaining OPCP surface ^1H signals from the Aerosil sample represents an encouraging step toward investigating lower surface areas. Adsorbing xenon onto samples with a stronger xenon-surface interaction may produce more effective wetting and, therefore better proton-xenon dipolar contact; this should enable lower surface area materials to be studied by this method.

5.4.5 Conclusions

These investigations have shown that Optical Pumping Cross Polarization can be an effective way of obtaining surface selective NMR signals, particularly when combined with techniques such as multiple contact CP. The magnetization transfer process depends not only on the contact times used during the CP experiments, but also on the diffusion of polarized xenon to the surface. The continual diffusion of polarized xenon allows for a number of acquisitions to be obtained and possibly averaged. The signal enhancement of the surface protons was found to be approximately 10^3, although this might be improved by dispersing the sample onto the cold surface of the sample cell and allowing the xenon to equilibrate longer before beginning acquisition. The first

OPCP experiment on a sample with 30 m^2 total surface area is reported, representing an encouraging step towards observing low surface area materials. Transferring magnetization to other nuclei such as ^{13}C or ^{29}Si, which are more sensitive to local structural and chemical properties, would be another valuable extension of this method. Experimental efforts in this direction are currently in progress in our laboratory.

5.5 Conclusions

The primary goal of the optical pumping cross polarization experiment is to select and enhance NMR signals from surface nuclei. While this goal has been achieved in specialized samples, the experiment is still by no means routine. The difficulties in accomplishing a complete xenon to proton magnetization transfer are twofold. The first difficulty is the possible inefficiency of the CP process. It is of course desirable to utilize the *full* xenon magnetization for the enhancement of the surface proton signal. Multiple contact and very low temperature cross polarization methods more efficiently utilize the xenon polarization. A second difficulty is that at temperatures below 100 K, a necessary condition for the CP experiment in order to reduce xenon mobility, xenon tends to freeze into the bulk solid phase. (See Figure 5.6) This is by far the more vexing problem. The maximum number of xenon atoms that will adsorb on the surface is *thermodynamically* limited. One possible strategy is to use large amounts of sample to increase the *total* surface area and hence increase the number of adsorbed xenon atoms. Of course this approach has limited practacility and returns. Nonetheless, if these difficulties can be overcome, this technique will revolutionize surface NMR.

Chapter 6

Nuclear Magnetic Resonance Imaging using Polarized Xenon Gas

6.1 Introduction

The use of NMR to obtain two and three dimensional images has extended the technique into the realm of medicine. In 1973 Lauterbur[180] and Mansfield and Grannell[181] independently proposed the use of NMR to form images. Since then magnetic resonance imaging, or MRI, as it is known in the medical community, has become a common diagnostic tool in hospitals. Concurrently, NMR microscopy has been developed as a tool for studying materials. Callagahan has written an excellent book on the subject.[182] This chapter deals with the use of polarized xenon in NMR imaging, a relatively new approach which has potential impact in both medicine and microscopy.

6.2 The Basic Idea

The basic concept of NMR imaging is straightforward. Ideally, the sample should have a narrow resonance in a uniform static magnetic field. (This would seem to immediately exclude solids as imaging candidates; however, line-narrowing techniques are being developed which enable imaging of suitable solids.[183]) Water is a common imaging sample. If a constant field gradient is applied in the z-direction, the magnetic field component B_z, parallel to the uniform field is

$$B_z = B_o + z\left(\frac{\partial B_z}{\partial z}\right) \tag{6.1}$$

Planes of constant z correspond to planes of constant precession frequency. The total NMR intensity within a given frequency interval bounded by two planes of constant z is proportional to the number of nuclei lying between those two planes. Thus the NMR absorption spectrum provides a projection of the sample spin density integrated over planes perpendicular to the gradient direction. By applying gradients in multiple directions, a series of projections can be used to reconstruct an image of the object.

6.3 Polarized Xenon in Imaging

Nuclear magnetic resonance is an established technique for imaging and microscopy in a wide variety of systems.[182] One attractive method for imaging porous materials is to saturate the sample with a high sensitivity contrast agent and thereby obtain a "negative" image, which depicts the void structure. Proton containing solvents, such as water, are ideal contrast agents due to their high intrinsic sensitivity, but in some cases they can react with the material and modify its structure. In these cases inert

gases such as xenon, which is used extensively in NMR as a probe of its surroundings, [184,185] are an attractive alternative, and despite their low intrinsic sensitivity due to low spin density, there have been several successful gas imaging studies. Lizak, Conradi, and Fry imaged C_2F_6 gas imbibed into a porous ceramic matrix - ceramic fiber composite.[186] As part of a study to ascertain the feasibility of studying nuclei in low concentrations with a whole-body imaging spectrometer, Pfeffer and Lutz imaged a xenon-oxygen mixture.[187] One approach to overcoming the limitations of low sensitivity of gases, is the use of optically polarized xenon or helium. The density of gaseous xenon at 1 atm pressure is 4×10^{-5} mol/cm^3, and with the polarizations attainable through optical pumping, the magnetization density of polarized xenon becomes comparable to the proton magnetization in water, 0.1 mol/cm^3, making it possible to attain images of a gas without the need for extensive signal averaging. This method has been used to obtain biological images of the gas space in rat and guinea pig lungs.[188,189]

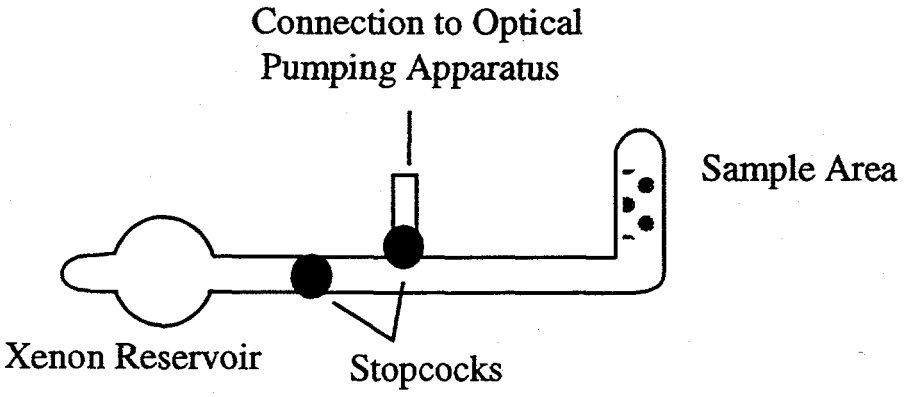

Figure 6.1 Imaging Sample Cell consists of a xenon reservoir and sample area separated by stopcocks.

6.4. Polarized Xenon Images of Phantoms

6.4.1 Introduction

The use of polarized xenon to image materials has not received as much attention as polarized gas imaging applied to biological systems. In order to determine the experimental conditions required to image materials, an image of a structured phantom was acquired. From this image an upper limit on resolution could be estimated.

6.4.2 Experimental

The imaging experiments were performed on a commercial micro-imaging spectrometer (Quest 4300, Nalorac Cryogenics Inc.) using cylindrical micro-imaging gradients (Nalorac Cryogenics Inc.) and a home-built probe. At the magnetic field of 4.3 T, the ^{129}Xe resonance frequency is 51 MHz. The polarized xenon was created in the optical pumping apparatus described in Chapter 4 and transported frozen in a magnetic field to the imaging spectrometer. The sample cell used for the imaging experiments is pictured in Figure 6.1. The xenon gas pressure used in the sample cell ranged from 1 - 3 atm. A standard FLASH (Fast Low Angle SHot) sequence, [190] shown in Figure 6.2, was used for the two dimensional imaging experiments. The tipping angle used was 10 degrees and the magnetic field gradient strength was 3.8 kHz/mm. Sixty four phase-encoding steps were used to produce a 128 x 64 time domain data set. The phantom was composed of three nested glass tubes with outside diameters of 9 mm, 6 mm, and 4 mm. Because of the way these tubes rest within each other, they form gaps varying continuously in diameter, providing a convenient gauge for image resolution. The three tubes were also carefully treated with SurfaSil prior to the experiment to reduce relaxation effects.

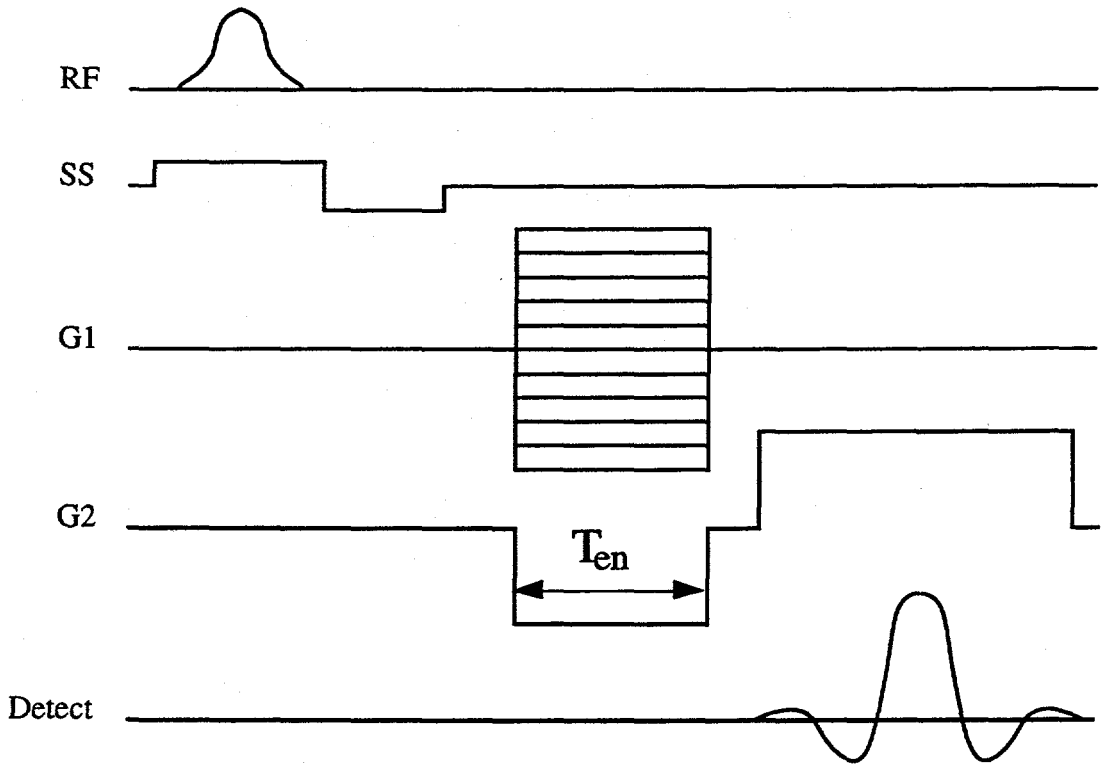

Figure 6.2 A schematic of the FLASH imaging sequence. Typical encoding time T_{en} was 580 μs using a read gradient G2 of 3.8 kHz/mm. Acquisition were made for 64 phase encoding gradient pulses G1.

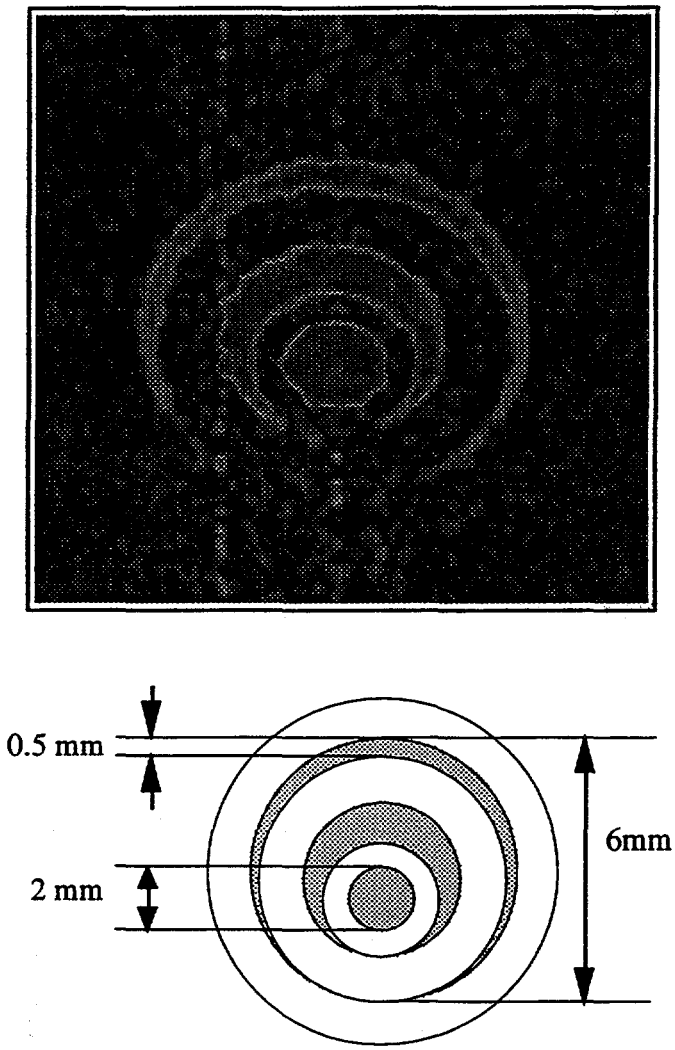

Figure 6.3 Two dimensional image of a phantom made of three nested glass tubes. The sizes of the tubes are shown in the cross-sectional sketch, below. Since the three tubes rest within each other, the gaps between tubes (shaded area in the sketch) continuously change from 0 to 2 mm.

6.4.3 Results

Figure 6.3 shows a sketch of the phantom together with a cross-sectional xenon image, indicating a spatial resolution of about 0.1 mm. The tubes did not noticeably increase the relaxation rate of xenon magnetization during imaging experiments. An alternative to using images for the characterization of small-scale heterogeneities is the use of NMR Patterson functions.[191] These NMR Patterson functions are analogous to the density auto-correlation functions of x-ray diffraction, except that nuclear rather than electronic density provides contrast and the spatial resolution is determined by magnetic field gradient strength rather than the momentum transfer in x-ray scattering. Figure 6.4 shows the NMR image and the Patterson function, showing the radial density distribution, of a bundle of hollow Teflon tubes. Both the image and the Patterson function are consistent with an inner diameter of ~0.3 mm, limited by the digital resolution and the overlapping signals caused by the misalignment of the Teflon tubes over the slice selection length of 15 mm.

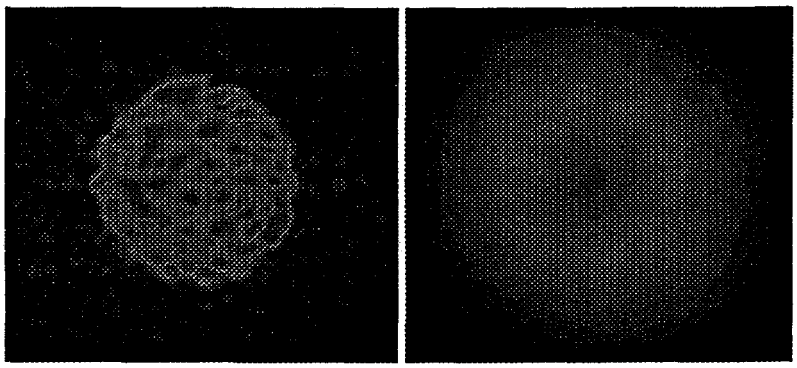

Figure 6.4 Image of Teflon tubes(a) Two dimensional image (box dimensions: 13 mm x 12 mm) of ^{129}Xe gas in bundled Teflon tubes, with 1 mm OD and 0.3 mm ID. The overlapping signals are due to the misalignment of the Teflon tubes over the slice selection length of 15 mm. (b) Patterson function (box dimensions: 13 mm x 12 mm) of same sample showing polarized xenon density distribution function.

6.4.4 Discussion

An estimate of the effects of xenon gas diffusion on imaging resolution can be made. During the application of the gradient pulses, lasting 1.16 ms, the root mean squared displacement at the pressures the phantom image was acquired at is ~60 μm, smaller than the resolution achieved. However, the root mean squared displacement for 1 atm of xenon is 100 μm, so the diffusion-limit to resolution is controlled by experimental parameters. In fact, fast diffusion of xenon gas can be advantageous in some cases, as diffusion of xenon from outside the selected slice replenishes magnetization destroyed by previous rf pulses. A delay of 5-10 seconds between acquisitions was sufficient to allow polarized ^{129}Xe to diffuse into the sample region, thus further enhancing the signal to noise ratio. Moreover, the ability to perform multiple acquisitions can be exploited for phase cycling and signal averaging.

6.5 Xenon Imaging of Materials

6.5.1 Background

One important application of gas imaging is the study of solid materials that are chemically sensitive to water and other liquids, or which may in some other way be altered upon exposure to moisture. Examples of such materials include food products, polymers, catalysts, and aerogels. Aerogels are a class of porous materials typically based on silica, [192] other metal oxides,[193] or organic polymers.[194] Their preparation involves standard sol-gel hydrolysis and condensation steps followed by solvent exchange and supercritical drying.[195] The supercritical drying step eliminates the destructive forces caused by liquid-vapor interfaces, and preserves the original gel structure. For silica aerogels, this structure consists of silica particles 2-5 nm in diameter, linked in a meandering three-dimensional network. Typical apparent bulk

densities range from 0.003 to 0.25 g/cm^3. Specific surface areas as high as 800-1000 m^2/g (~ 100 m^2/cm^3) are common. The remainder of the bulk volume of an aerogel is an open pore network. Pore diameters (derived from adsorption/desorption isotherms) range from 2-100 nm, with a mean of ~20 nm. Many of the proposed applications of aerogels require a detailed understanding of gas dynamics within the aerogel matrix. NMR imaging may provide valuable information concerning gas diffusivity and dynamics in aerogel as well as images of the uniformity and defects of the material itself.

6.5.2 Experimental

In order to study xenon gas penetration into a sample of aerogel prepared by basic catalysis of tetraethyl orthosilicate, and dried using supercritical carbon dioxide one dimensional imaging experiments have been performed. The final density of the sample was 0.1 g/cm3. For this experiment, the optically enhanced ^{129}Xe was stored separately and was not introduced into the sample region until immediately before acquisition of images. The aerogel sample was a cylinder 4 mm in diameter and 7 mm in length and was prepared by forcing a glass tube into a larger block of the aerogel material.

6.5.3 Results and Discussion

One dimensional images are shown in Figure 6.5, taken at various times after xenon was released into the sample region. A 90 degree pulse was used for each experiment. The two high ridges in the spectra indicate the edges of the sample. The overall shapes of all the spectra are similar, indicating that gas penetration occurred before our first acquisition, about 3 s after xenon gas entered the sample region. However, all the images show low intensity in a few regions, suggesting that xenon gas does not penetrate into these parts of the sample easily and that the sample is

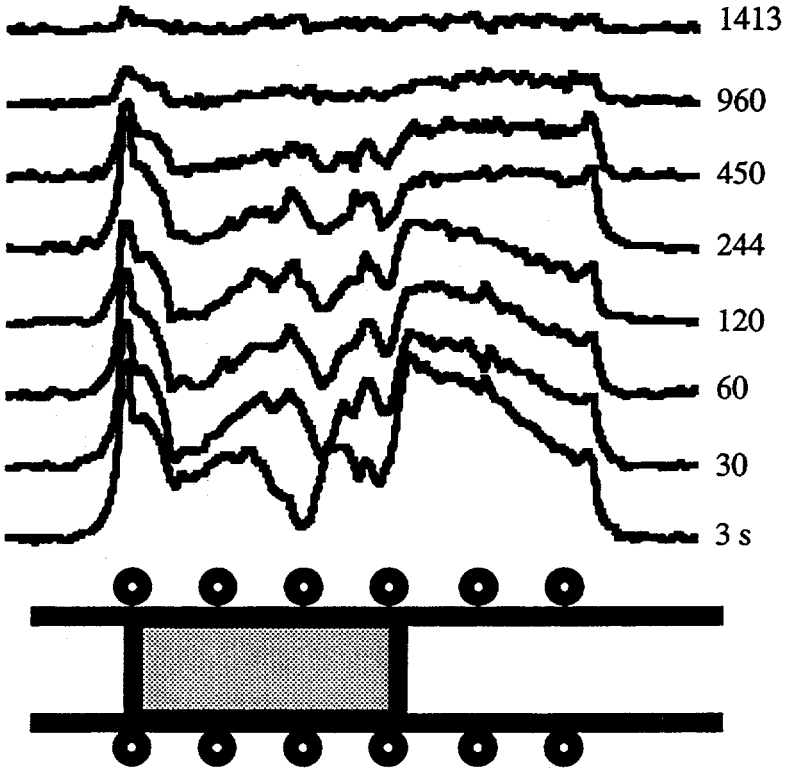

Figure 6.5 One dimensional images of ^{129}Xe penetration into an aerogel sample. The schematic shows the arrangement of the sample (dimensions: 4 mm diameter, 7 mm length), the radio-frequency coil and the glass tube container. Images were taken at increasing delay times after xenon entered the sample region. Note the consistently low intensity areas within the sample, indicative of sample or penetration inhomogeneity.

not uniform on a millimeter length scale demonstrating the applicability of this technique to the study of porous and heterogeneous materials.

6.6 Conclusions

In conclusion, using optically polarized ^{129}Xe as a contrast agent, one may obtain NMR images with a resolution of 0.1 mm in FLASH experiments. Fast diffusion of xenon may actually improve the images acquired by allowing fresh ^{129}Xe magnetization to replenish the polarization lost due to RF pulses. Polarized xenon may be used to demonstrate the effects of restricted diffusion on microscopic NMR imaging, which have been simulated.[196] It is also possible to use this technique for the investigation of material inhomogeneity and perhaps sample morphology, which for certain samples, may not be possible by NMR imaging of water. Alternative imaging methods, including echo planar imaging,[197,198] would be a desirable extension of this method. Additionally, construction of a flowing polarized xenon apparatus would enable more lengthy two-dimensional experiments by replenshing the xenon polarization.

Chapter 7

Outlook for Optical Pumping in NMR

The various chemical applications of highly spin polarized xenon in NMR experiments demonstrate the wide range of applicability of this novel technique. The limitations of the technique point to the necessary future developments. The experiments involving optically polarized ^{129}Xe NMR detection have been developed to a level of nearly routine performance. Future possible applications include the extension of the technique to solution studies, including biological systems. Before the experimentally more demanding cross polarization experiments become routine, development of techniques to localize the xenon more strongly on the surface is required. Furthermore, Hartmann-Hahn cross polarization to nuclei other than protons would be a valuable extension of the method, but is more difficult due to the reduced dipolar interactions and natural abundance and is still in development. Once the high field cross polarization experiment to heteronuclei has been achieved successfully, the optical pumping technique must be linked to other solid state NMR techniques. In order to obtain high resolution spectra, a combination of magic angle spinning[199,200] and optical pumping of xenon will then be desirable. Though experimentally

demanding, a combination of these techniques does not seem impossible when considering the experiments of Haw and coworkers,[201] in which a gas is introduced into a spinning sample. An additional desirable technical advance would be the assembly of a flowing polarized xenon apparatus, allowing for continual introduction of freshly polarized xenon to the sample. This development would be particularly crucial for extending the polarized xenon imaging studies and other multi-dimensional experiments, where many pulses are required.

Additional studies may be performed with other polarized atoms. In principle, all noble gas nuclei with a nuclear spin $I \neq 0$ as well as atomic hydrogen and deuterium[202-204] can be optically polarized via spin exchange with alkali metal atoms.[205] A variety of experiments has already been performed with ^{131}Xe [59,206-212] which exhibits a quadrupole moment. With its high gyromagnetic ratio, nuclear spin I = 1/2, and typically long spin lattice relaxation times,[213] ^{3}He presents an interesting probe for medical and materials imaging. Although the chemical shift range is very small, its much smaller size in comparison to ^{129}Xe should allow the imaging of smaller void spaces.

Optical pumping of semiconductors has been coupled with low field NMR[214] and, more recently, with high field NMR detection.[215] Magnetic resonance techniques in combination with optical pumping are widely applied in semiconductors, *e. g.* in ODNMR (Optically Detected NMR),[216] but only the combination with high field NMR allows the exploitation of the enormous variety of multipulse techniques, and moreover, the selective detection of impurities in low concentrations. The sensitivity enhancements available through optical polarization combined with clever applications will make possible experiments which are inconceivable today.

References

(1) *Purcell, E. M.; Torrey, H. C.; Pound, R. V. Phys. Rev.* ***1946****, 69, 37.*

(2) *Bloch, F.; Hansen, W. W.; Packard, M. Phys. Rev.* ***1946****, 69, 127.*

(3) *Proctor, W. G.; Yu, F. C. Phys. Rev.* ***1950****, 77, 717.*

(4) *Abragam, A. Priciples of Nuclear Magnetism; Clarendon Press: Oxford, 1961.*

(5) *Ernst, R. R.; Bodenhausen, G.; Wokaun, A. Priciples of Nuclear Magnetic Resonance in One and Two Dimensions; Clarendon Press: Oxford, 1987.*

(6) *Farrar, T. C.; Becker, E. D. Pulse and Fourier Transform NMR: Introduction to Theory and Methods; First ed.; Academic Press: New York, NY, 1971.*

(7) *Fukushima, E.; Roeder, S. B. W. Experimental Pulse NMR: A Nuts and Bolts Approach; First ed.; Addison-Wesley: Reading, MA, 1981.*

(8) *Harris, R. K. Nuclear Magnetic Resonance Spectroscopy: A Physicochemical View; First ed.; Longman Scientific & Technical: Essex, England, 1986.*

(9) *Mehring, M. Principles of High Resolution NMR in Solids; 2nd ed.; Springer: Berlin, 1983.*

(10) *Slichter, C. P. Principles of Magnetic Resonance; 3rd. ed.; Springer-Verlag: Berlin, 1990.*

(11) *Raftery, M. D. PhD. Thesis, University of California, Berkeley, 1992.*

(12) *Long, H. W. Ph. D. Thesis, University of California, Berkeley, 1993.*

(13) *Sladky, F. O.; Bulliner, P. A.; Bartlett, N.; Boer, B. G. D.; Zalkin, A. J. Chem. Soc., Chem. Commun.* ***1968****, 1048.*

(14) *Sladky, F. O.; Bulliner, P. A.; Bartlett, N. J. Chem. Soc., Dalton Trans.* ***1969****, 2179.*

(15) *Gillepsie, R. J.; Schrobilgen, G. J. J. Chem. Soc., Chem. Commun.* ***1974****, 1543.*

(16) *Gillespie, R. J.; Landa, B.; Schrobilgen, G. J. J. Chem. Soc., Chem. Commun.* ***1971****, 1543.*

(17) *Gillespie, R. J.; Schrobilgen, G. J. Inorg. Chem.* ***1974****, 13, 2370.*

(18) *DesMarteau, D. D.; Eisenberg, M. Inorg. Chem.* ***1972****, 11, 2641.*

(19) *Lamb, W. Phys. Rev.* ***1941****, 60, 817.*

(20) *Malli, G.; Froese, C. Inter. J. of Quant. Chem.* ***1967****, 1, 99.*

(21) *Ramsey, N. F. Phys. Rev.* ***1950****, 78, 699.*

(22) *Ramsey, N. F.* ***1952****, 86, 243.*

(23) *Jameson, C. J.; Jameson, A. K.; Cohen, S. J. Chem. Phys.* ***1973****, 59, 4540.*

(24) *Jameson, C. J. Bull. Magn. Reson.* ***1980****, 3, 3.*

(25) *Torrey, H. C. Phys. Rev.* ***1963****, 130, 2306.*

(26) *Adrian, F. Phys. Rev.* ***1964****, 136, A980.*

(27) *Jameson, C. J. Chem. Rev.* ***1991****, 91, 1375.*

(28) *Ito, T.; Fraissard, J. Zeolites* ***1988****, 8, 350.*

(29) *Raftery, D.; Reven, L.; Long, H.; Pines, A.; Tang, P.; Reimer, J. J. Phys. Chem.* ***1993****, 97, 1649.*

(30) *Ito, T.; Fraissard, J. In 5th International Conference on Zeolites; Heyden: Naples, 1980; pp 150.*

(31) *Ripmeester, J. A.; Davidson, D. W. J. Mol. Struct.* ***1981****, 75, 67.*

(32) *Miller, K. W.; Reo, N. V.; Stengle, D. P.; Stengle, T. R.; Williamson, K. L. Proc. Natl. Acad. Sci. USA* ***1981****, 78, 4946.*

(33) *Fraissard, J.; Ito, T. Zeolites* ***1988****, 8, 350 - 361.*

(34) *Dybowski, C.; Bansal, N.; Duncan, T. M. Ann. Rev. Phys. Chem.* ***1991****, 42, 433.*

(35) *Barrie, P. J.; Klinowski, J. Prog. in NMR Spec.* ***1992****, 24, 91.*

(36) *Raftery, M. D.; Chmelka, B. F. In NMR Basic Principles and Progress; B. Blümich and R. Kosfeld, Ed.; Springer-Verlag: Berlin, 1993; Vol. 30; pp 111-158.*

(37) *Jokisaari, J. Prog. in NMR Spec.* ***1994****, 26, 1.*

(38) *Webster, O. W.; Gentry, F. P.; Farlee, R. D.; Smart, B. E. Polm.Prepr. Am. Chem. Soc., Div. Polym. Chem.* ***1991****, 32, 412.*

(39) *Webster, O. W.; Kim, Y. H.; P.Gentry, F.; Farlee, R. D.; Smart, B. E. Polm. Prepr., Am. Chem. Soc., Div. Polym. Chem.* ***1992****, 33, 186.*

(40) *Webster, O. W.; Gentry, F. P.; Farlee, R. D.; Smart, B. E. Makromol. Chem., Macromol. Symp.* ***1992****, 54/55, 477.*

(41) *Davenkov, V. A.; Tsyrupa, M. P. Polym. Mater. Sci. Eng.* ***1992****, 66, 146.*

(42) *Stengle, T. R.; Williamson, K. L. Macromolecules* ***1987****, 20, 1428.*

(43) *Kennedy, G. J. Polymer Bulletin* ***1990****, 23, 605.*

(44) *Ferrero, M. A.; W., W. S.; Conner, W. C.; Bonardet, J. L.; Fraissard, J. Langmuir* ***1982****, 8, 2269.*

(45) *Walton, J. H.; Miller, J. B.; Rowland, C. M. J. Polym. Sci. B* ***1992****, 30, 527.*

(46) *Walton, J. H.; Miller, J. B.; Roland, C. M.; Nagode, J. B. Macromolecules* ***1993****, 26, 4052.*

(47) *Brownstein, S. K.; Roovers, J. E. L.; Worsfold, D. J. Magn. Res. Chem.* ***1988****, 26, 392.*

(48) *Miller, J. B.; Walton, J. H.; Roland, C. M. Macromolecules* ***1993****, 26, 5602.*

(49) *Jameson, A. K.; Jameson, C. J.; Gutowsky, H. S. J. Chem. Phys.* ***1970****, 53, 2310.*

(50) *Cheung, T. T. P.; Fu, C. M.; Wharry, S. J. Phys. Chem.* ***1988****, 92, 5170.*

(51) *Chmelka, B. F.; Raftery, D.; McCormick, A. V.; Menorval, L. C. d.; Levine, R. D.; Pines, A. Phys. Rev. Lett.* ***1991****, 66, 580.*

(52) *Larsen, R.; Shore, J.; Schmidt-Rohr, K.; Emsley, L.; Long, H.; Pines, A.; Janicke, M.; Chmelka, B. F. Chem. Phys. Lett.* ***1993****, 214, 220-226.*

(53) *Yen, W. M.; Norberg, R. E. Phys. Rev.* ***1963****, 131, 269.*

(54) *Bond, G. C.; Konig, P. J. J.Catal.* ***1982****, 77, 309.*

(55) *Gasior, M.; Gasior, I.; Grzybowska, B. Appl. Catal.* ***1984****, 10, 87.*

(56) *Wainwright, M. S.; Foster, N. R. Catal. Rev.* ***1979****, 19, 211.*

(57) *Bosch, H.; Janssen, F. Catal. Today* ***1988****, 19, 369.*

(58) *Bond, G. C.; Bruckman, K. Faraday Discuss. Chem. Soc.* ***1981****, 72, 235.*

(59) *Wachs, I. E.; Saleh, R. Y.; Chan, S. S.; Cherisch, C. C. Appl. Catal.* ***1985****, 15, 339.*

(60) *Eckert, H.; Wachs, I. E. J. Phys. Chem.* ***1989****, 93, 6796.*

(61) *Roozeboom, F.; Mittelmeijer-Hazeleger, M. C.; Moulijn, J. A.; Medema, J.; de Beer, V. H.; Gellings, P. J. J. Phys. Chem.* ***1980****, 84, 2783.*

(62) *Haber, J.; Kozlowska, A.; Kozlowki, R. J. J. Catal.* ***1986****, 52, 5831.*

(63) *Chan, S. S.; Wachs, I. E.; Murrell, L. L.; Wang, L.; Hall, W. K. J. Phys. Chem.* ***1984****, 88, 5831.*

(64) *Cristiani, C.; Forzatti, P.; Busca, G. J. J. Catal.* ***1989****, 116, 586.*

(65) *Went, G. T.; Leu, L.-J.; Bell, A. T. J. Catal.* ***1992****, 134, 479.*

(66) *Bansal, N.; Dybowski, C. J. Magn. Reson.* ***1990****, 89, 21.*

(67) *de Menorval, L. C.; Raftery, D.; Lui, S. B.; Takegoshi, K.; Ryoo, R.; Pines, A. J. Phys. Chem.* ***1990****, 94, 27-31.*

(68) *Ryoo, R.; Pak, C.; Ahn, D. H.; de Menorval, L. C.; Figueras, F. Catal. Lett.* ***1990****, 7, 417.*

(69) *Cheung, T. T. P. J. Phys. Chem.* ***1989****, 93, 7549.*

(70) *Conner, W. C.; Weist, E. L.; Ito, T.; Fraissard, J. J. Phys. Chem.* ***1989****, 93, 4138.*

(71) *Bansal, N.; Dybowski, C. J. Phys. Chem.* ***1988****, 92, 2333.*

(72) *Boddenberg, B.; Hartmann, M. Chem. Phys. Lett.* ***1993****, 203, 243.*

(73) *de Menorval, L. C.; Fraissard, J.; Ito, T.; Primet, M. J. Chem. Soc. (Faraday Trans. 1)* ***1982****, 78, 403.*

(74) *Ito, T.; Fraissard, J. J. Chem. Soc. (Faraday Trans. 1)* ***1987****, 83, 451 - 462.*

(75) *Ahn, D. H.; Lee, J. S.; Nomura, M.; Sachtler, W. M. H.; Moretti, G.; Woo, S.; Ryoo, R. J. Catal.* ***1992****, 133, 191.*

(76) *Ryoo, R.; Cho, S. J.; Pak, C.; Kim, J.-G.; Ihm, S.-K.; Lee, J. Y. J. Am. Chem. Soc.* ***1992****, 114, 76.*

(77) *Boudart, M.; de Menorval, L. C.; Fraissard, J.; Valenca, G. P. J. Phys. Chem.* ***1988****, 92, 4033.*

(78) *Valenca, G. P.; Boudart, M. J. Catal.* ***1991****, 128, 447.*

(79) *Boudart, M.; Ryoo, R.; Valenca, G. P.; Van Grieken, R. Catal. Lett.* ***1993****, 17, 273.*

(80) *Topsoe, N.-Y.; Slabiak, T.; Clausen, B. S.; Sruak, T. Z.; Dumesic, J. A. J. Catal.* ***1992****, 134, 742.*

(81) *Tanaka, K.; White, J. M. J. Phys. Chem.* ***1982****, 86, 4708.*

(82) *Shoemaker, D. P.; Garland, C. W.; Steinfeld, J. I.; Nibler, J. W. Experiments in Physical Chemistry; Fourth ed.; McGraw-Hill: 1981.*

(83) *Brunauer, S.; Emmet, P. H.; Teller, E. J. Am. Chem. Soc.* ***1938****, 60, 309.*

(84) *Kirk-Othner Concise Encyclopedia of Chemcial Technology; John Wiley & Sons: 1985, pp 585.*

(85) *Barrett, E. P.; Joyner, L. G.; Halenda, P. P. J. Am. Chem. Soc.* ***1951****, 73, 373.*

(86) *Gregg, S. J.; S.W., S. K. Adsorption, Surface Area and Porosity; Academic Press: New York, 1967, pp 177.*

(87) *Freeman, M. P.; Halsley, G. D. J. Phys. Chem.* ***1956****, 60, 1119.*

(88) *Cook, G. A. Argon, Helium and the Rare Gases; Interscience: New York, 1961; Vol. 1.*

(89) *Ripmeester, J. A.; Ratcliffe, C. I. Anal. Chim. Acta* ***1993****, 283, 1103-1112.*

(90) *Springuel-Huet, M. A.; Fraissard, J. Chem. Phys. Lett.* ***1989****, 154, 299-302.*

(91) *CRC Handbook of Chemistry and Physics; 66 ed.; CRC Press: Boca Raton, 1985.*

(92) *Schadt, M. Liq. Cryst.* ***1989****, 5, 57.*

(93) *Depp, S. W.; Howard, W. E. In Scientific American; 1993; pp 90.*

(94) *Greeff, C. W.; Lu, J.; Lee, M. A. Liq. Cryst.* ***1993****, 15, 75-85.*

(95) *Doane, J. W. In Magnetic Resonance of Phase Transitions; C. P. Poole and H. A. Farach, Ed.; Academic Press: 1979; pp 171.*

(96) *Khetrapal, C. L.; Becker, E. D. Magn. Res. Rev.* ***1991****, 16, 35.*

(97) *Lowenstein, A.; Brenman, M. Chem. Phys. Lett.* ***1978****, 58, 435.*

(98) *Jokisaari, J.; Ingman, P.; Lounila, J.; Pulkkinen, O.; Diehl, P.; Muenster, O. Mol. Phys.* ***1993****, 78, 41.*

(99) *Ingman, P.; Jokasaari, J.; Diehl, P. J. Mag. Reson.* ***1991****, 92, 163.*

(100) *Jokisaari, J.; Diehl, P.; Muenster, O. Mol. Cryst. Liq. Cryst.* ***1990****, 188, 189.*

(101) *Jokisaari, J.; Diehl, P. Liq. Cryst.* ***1990****, 7, 739.*

(102) *Crawford, G. P.; Steele, L. M.; Ondris-Crawford, R.; Iannacchione, G. S.; Yeager, C. J.; Doane, J. W.; Finotello, D. J. Chem. Phys.* ***1992****, 96, 7788.*

(103) *Ondris-Crawford, R. J.; Crawford, G. P.; Zumer, S.; Doane, J. W. Phys. Rev. Lett.* ***1993****, 70, 194.*

(104) *Hsiung, H.; Rasing, T.; Shen, Y. R. Phys. Rev. Lett.* ***1986****, 57, 3065.*

(105) *Crawford, G. P.; Yang, D. K.; Zumer, S.; Finotello, D.; Doane, J. W. Phys. Rev. Lett.* ***1991****, 66, 723.*

(106) *de Gennes, P. G. The Physics of Liquid Crystals; Oxford University Press: 1974.*

(107) *Allender, D. W.; Crawford, G. P.; Doane, J. W. Phys. Rev. Lett.* ***1991****, 67, 1442.*

(108) *Diehl, P.; Jokisaari, J. Chem. Phys. Lett.* ***1990****, 165, 389.*

(109) *Harbison, G. S.; Vogt, V. D.; Spiess, H. W. J. Chem. Phys.* ***1987****, 1206.*

(110) *Muenster, O.; Jokisaari, J.; Diehl, P. Mol. Cryst. Liq. Cryst.* ***1991****, 206, 179-186.*

(111) *Crawford, G. P.; Ondris-Crawford, R.; Zumer, S.; Doane, J. W. Phys. Rev. Lett.* ***1993****, 70, 1838-1841.*

(112) *Jeener, J.; Meier, B. H.; Bachmann, P.; Ernst, R. R. J. Chem. Phys.* ***1979****, 71, 4546.*

(113) *Tomaselli, M.; Meier, B. H.; Robyr, P.; Suter, U. W.; Ernst, R. R. Chem. Phys. Lett.* ***1993****, 214, 1-4.*

(114) *Tomaselli, M.; Meier, B. H.; Robyr, P.; Suter, U. W.; Ernst, R. R. Chem. Phys. Lett.* ***1993****, 205, 145-152.*

(115) *States, D. J.; Haberkorn, R. A.; Ruben, D. J. J. Magn. Res.* ***1982****, 48, 286 - 292.*

(116) *Drobny, G.; Pines, A.; Sinton, S.; Weitekamp, D. P.; Wemmer, D. Faraday Symp. Chem. Soc.* ***1979****, 13, 49.*

(117) *Bodenhausen, G.; Vold, R. L.; Vold, R. R. J. Magn. Reson.* ***1980****, 37, 93.*

(118) *Crawford, G. P.; Stannarius, R.; Doane, J. W. Phys. Rev. A* ***1991****, 44, 2558.*

(119) *Bellini, T.; Clark, N. A.; Muzny, C. D.; Wu, L.; Garland, C. W.; Schaefer, D. W.; Oliver, B. J. Phys. Rev. Lett.* ***1992****, 69, 788-791.*

(120) *Somorjai, G. A. Chemistry in Two Dimensions: Surfaces; Ithaca, NY, Cornell University Press, 1981.*

(121) *Hartmann, S. R.; Hahn, E. L. Phys. Rev.* ***1962****, 128, 2042.*

(122) *Pines, A.; Gibby, M.; Waugh, J. S. J. Chem. Phys.* ***1973****, 59, 569.*

(123) *Carver, R. R.; Slichter, C. P. Phys. Rev.* ***1956****, 102, 975.*

(124) *Carver, R. R.; Slichter, C. P. Phys. Rev.* ***1953****, 92, 212.*

(125) *Hall, D.; Becerra, L.; Gerfen, G.; Inah, S.; Spindler, H.; Singel, D.; Griffin, R. In Experimental NMR Conference; Boston, MA USA, 1995; pp 300.*

(126) *Kastler, A. J. Phys. Radium* ***1950****, 11, 255.*

(127) *Dehmelt, H. G. Phys. Rev.* ***1958****, 109, 381.*

(128) *Bouchiat, C. C.; Bouchiat, M. A.; Pottier, L. C. Phys. Rev.* ***1969****, 181, 144.*

(129) *Bouchiat, M. A.; Brossel, J.; Pottier, L. C. J. Chem. Phys.* ***1972****, 56, 3703.*

(130) *Grover, B. C. Phys. Rev. Lett.* ***1978****, 40, 390.*

(131) *Volk, C. H.; Kwon, T. M.; Mark, J. G.; Kim, Y. B.; Woo, J. C. Phys. Rev. Lett.* ***1980****, 44, 136.*

(132) *Happer, W.; Miron, E.; Schaefer, S.; Schreiber, D.; Wijngaarden, W. A. v.; Zeng, X. Phys. Rev. A* ***1984****, 29, 3092.*

(133) *Herman, R. M. Phys. Rev.* ***1965****, 137, 1062.*

(134) *Bhaskar, N. D.; Happer, W.; McClelland, T. Phys. Rev. Lett.* ***1982****, 49, 25.*

(135) *Walters, G. K.; Colegrove, F. D.; Schearer, L. D. Phys. Rev. Lett.* ***1962****, 8, 439-442.*

(136) *Raftery, D.; Long, H.; Meersmann, T.; Grandinetti, P. J.; Reven, L.; Pines, A. Phys. Rev. Lett.* ***1991****, 66, 584.*

(137) *Ansermet, J.; Slichter, C. P.; Sinfelt, J. H. Prog. NMR Spectrosc.* ***1990****, 22, 401-421.*

(138) *Maciel, G. E.; Sindorf, D. W. J. Am. Chem. Soc.* ***1980****, 102, 7606.*

(139) *Davy, H. Phil. Trans. Roy. Soc. (London)* ***1811****, 101, 1.*

(140) *Villard, P. C. R. Hebd. Seances. Acad. Sci.* ***1896****, 123, 377.*

(141) *de Forcrand, R. C. R. Hebd. Seances Acad. Sci.* ***1923****, 176, 335.*

(142) *Teal, A. G.; Westerman, J. F.; Ott, V. J. In Apr. 18, 1989; pp .*

(143) *McDonald, G. T. Annu. Rev. Energy* ***1990****, 15, 53.*

(144) *Englezos, P.; Hatzikiraiakos, S. G. Ann. N. Y. Acad. Sci.* ***1994****, 715, 270.*

(145) *Pauling, L.; Marsh, R. E. Proc. Natl. Acad. Sci. U.S.* ***1952****, 38, 1123.*

(146) *v. Stackelberg, M.; Mueller, H. R. Naturwissenshaften* ***1975****, 39, 20.*

(147) *Claussen, W. F. J. Chem. Phys.* ***1951****, 19, 1425.*

(148) *Lee, F.; Gabe, E.; Tse, J. S.; Ripmeester, J. A. J. Am. Chem. Soc.* ***1988****, 110, 6014.*

(149) *Ripmeester, J. A.; Ratcliffe, C. I. J. Phys. Chem.* ***1990****, 94, 7652-7656.*

(150) *Ripmeester, J. A.; Ratcliffe, C. I.; Tse, J. S. J. Chem. Soc., Faraday Trans. 1* ***1988****, 84, 3731.*

(151) *Cheung, T. T. P.; Chu, P. J. J. Phys. Chem.* ***1992****, 96, 9551.*

(152) *Davidson, D. W.; Handa, Y. P.; Ripmeester, J. A. J. Phys. Chem.* ***1986****, 90, 6549.*

(153) *Barrer, R. M.; Edge, A. V. J. Proc. Roy. Soc. (London)* ***1967****, 90, 6459.*

(154) *Sloan, J., E. D.; Fleyfel, F. AIChE Journal* ***1991****, 37, 1281.*

(155) *Gatzke, M.; Cates, G. D.; Driehuys, B.; Fox, D.; Happer, W.; Saam, B. Phys. Rev. Lett.* ***1993****, 70, 690.*

(156) *Pietraß, T.; Bowers, C. R.; Gaede, H. C.; Bifone, A.; Pines, A.* ***1993****, unpublished results*

(157) *Tanaka, H.; Nakanishi, K. Molecular Simulation* ***1994****, 12, 317.*

(158) *Barrer, R. M.; Ruzicka, D. J. Trans. Faraday. Soc.* ***1962****, 58, 2262.*

(159) *Vysniauskas, A.; Bishnoi, P. R. Chem. Eng. Sci.* ***1983****, 38, 1061.*

(160) *Holder, G. D.; Zele, S.; Enick, R.; LeBlond, C. Ann. N. Y. Acad. Sci.* ***1994****, 715, 345.*

(161) *Hwang, M. H.; Wright, D. A.; Kapur, A.; Holder, G. D. J. Inclusion Phenomena* ***1990****, 8, 103.*

(162) *Falabella, B. J. Ph.D. Thesis, University of Massachusetts, Amherst, MA, 1975.*

(163) *Hunt, E. R.; Carr, H. Y. Phys. Rev.* ***1961****, 130, 2302.*

(164) *Streever; Carr, H. Y. Phys. Rev.* ***1961****, 121, 20.*

(165) *Ripmeester, J. A. , unpublished results.*

(166) *Bowers, C. R.; Pietraß, T.; Barash, E.; Pines, A.; Grubbs, R. K.; Alivasatos, A. P. J. Phys. Chem.* ***1994****, 98, 9400-9404.*

(167) *Pietraß, T.; Bifone, A.; Pines, A. Surface Science* ***1995****, submitted,*

(168) *Overhauser, A. W. Phys. Rev.* ***1953****, 91, 476.*

(169) *Overhauser, A. W. Phys. Rev.* ***1953****, 92, 411.*

(170) *Abragam, A.; Procter, W. G. Phys. Rev.* ***1958****, 109, 1441.*

(171) *Goldman, M. Spin Temperature and Nuclear Magnetic Resonance in Solids; Oxford Univ. Press: Oxford, 1970.*

(172) *Beeler, A. J.; Orendt, A. M.; Grant, D. M.; Cutts, P. W.; Michl, J.; Zilm, K. W.; Downing, J. W.; Facelli, J. C.; Schindler, M. S.; Kutzelnigg, W. J. Am. Chem. Soc.* ***1984****, 106, 7672.*

(173) *Walter, T. H.; Turner, G. L.; Oldfield, E. J. Mag. Reson.* ***1988****, 76, 106-120.*

(174) *Zumbulyadis, N.; O'Reilly, J. M. Macromolecules* ***1991****, 24, 5294.*

(175) *Long, H. W.; Gaede, H. C.; Shore, J.; Reven, L.; Bowers, C. R.; Kritzenberger, J.; Pietrass, T.; Pines, A.; Tang, P.; Reimer, J. A. J. Am. Chem. Soc.* ***1993****, 115, 8491.*

(176) *Gentry, F. P., private communication.*

(177) *Ripmeester, J. A. J. Am. Chem. Soc.* ***1982****, 104, 289.*

(178) *Long, H. W.; Reven, L.; Tang, P.; Raftery, D.; Reimer, J. A.; Pines, A. In Experimental NMR Conference; Asilomar, Ca, 1992; pp .*

(179) *Clauss, J.; Schmidt-Rohr, K.; Spiess, H. Acta Polym.* ***1993****, 44, 1.*

(180) *Laterbur, P. C. Nature* ***1973****, 242, 190.*

(181) *Mansfield, P.; Grannell, P. K. J. Phys.* ***1973****, C6, L422.*

(182) *Callaghan, P. T. Principles of Nuclear Magnetic Resonance Microscopy; Clarendon Press: Oxford, 1991.*

(183) *Blümler, P.; Blümich, B. In Solid-State NMR I: Methods; P. Diehl, E. Fluck, H. Guenther, R. Kosfeld and J. Seelig, Ed.; Springer-Verlag: 1994.*

(184) *Ripmeester, J. A.; Davidson, D. W. Bull. Magn. Res.* ***1981****, 2, 139.*

(185) *Ito, T.; Fraissard, J. In 5th International Conference on Zeolites; Heyden: Naples, 1980; pp 150.*

(186) *Lizak, M. J.; Conradi, M. S.; Fry, C. G. J. Magn. Reson.* ***1991****, 95, 548-557.*

(187) *Pfeffer, M.; Lutz, O. J. Magn. Reson. A* ***1994****, 108, 106-109.*

(188) *Albert, M. S.; Cates, G. D.; Driehuys, B.; Happer, W.; Saam, B.; Jr., C. S. S.; Wishnia, A. Nature* ***1994****, 370, 199-200.*

(189) *Middleton, H.; Black, R. D.; Saam, B.; Cates, G. D.; al, e. Magnetic Resonance in Medicine* ***1995****, 33, 271-275.*

(190) *Haase, A.; Frahm, J.; Matthaei, D.; Hanicke, W.; Merboldt, K. D. J. Magn. Reson.* ***1986****, 67, 258.*

(191) *Barrall, G. A.; Frydman, L.; Chingas, G. C. Science* ***1992****, 255, 714-717.*

(192) *Kistler, S. S. Nature* ***1931****, 127, 741.*

(193) *Teichner, S. J. In Aerogels; J. Fricke, Ed.; Springer-Verlag: Berlin, 1986; pp 22.*

(194) *Pekala, R. W.; Kong, F. M. Revue de Physique Applique, Supp. No. 4* ***1989****, 24, 33.*

(195) *Tewari, P. H.; Hunt, A. J.; Lofftus, K. D. Mater. Lett.* ***1985****, 3, 363.*

(196) *Hyslop, W. B.; Lauterbur, P. C. J. Magn. Reson.* ***1991****, 94, 501-510.*

(197) *Mansfield, P. J. Phys. C.* ***1977****, 10, L55.*

(198) *Mansfield, P.; Pykett, I. L. J. Magn. Reson.* ***1978****, 29, 355.*

(199) *Andrew, E. R.; Bradbury, A.; Eades, R. G. Nature* ***1958****, 185, 1659.*

(200) *Lowe, I. Phys. Rev. Lett.* ***1959****, 2, 285.*

(201) *Haw, J. F. In 35th Experimental NMR Conference; Asilomar, CA, 1994; pp 61.*

(202) *Haroche, S.; Cohen-Tannoudji, C.; Audoin, C.; Schermann, J. P. Phys. Rev. Lett.* ***1970****, 24, 861.*

(203) *Redsun, S. G.; Knize, R. J.; Cates, G. D.; Happer, W. Phys. Rev. A* ***1990****, 42, 1293.*

(204) *Coulter, K. P.; Hoult, R. J.; Kinney, E. R.; Kowalczyk, R. S.; Potterveld, D. H.; Young, L.; Zeidman, B.; Zghiche, A.; Toporkov, D. K. Phys. Rev. Lett.* ***1992****, 68, 174.*

(205) *Happer, W. Rev. Mod. Phys.* ***1972****, 44, 169.*

(206) *Wu, Z.; Kitano, M.; Happer, W.; Hou, M.; Daniels, J. Applied Optics* ***1986****, 25, 4483.*

(207) *Wu, Z.; Happer, W.; Daniels, J. Phys. Rev. Lett.* ***1987****, 59, 1480.*

(208) *Wu, Z.; Schaefer, S.; Cates, G. D.; Happer, W. Phys. Rev. A* ***1988****, 37, 1161.*

(209) *Liu, Z.; Sun, X.; Zeng, X.; He, Q. Chin. Phys. Lett.* ***1990****, 7, 399.*

(210) *Raftery, D.; Long, H. W.; Shykind, D.; Grandinetti, P. J.; Pines, A. Phys. Rev. A* ***1994****, Phys. Rev. A , 50, 567.*

(211) *Appelt, S.; Wäckerle, G.; Mehring, M. Phys. Rev. Lett.* ***1994****, 72, 3921.*

(212) *Butscher, R.; Wäckerle, G.; Mehring, M. J. Chem. Phys.* ***1994****, 100, 6923.*

(213) *Newbury, N. R.; Barton, A. S.; Cates, G. D.; Happer, W.; Middleton, H. Phys. Rev. A* ***1993****, 48, 4411.*

(214) *Lampel, G. Phys. Rev. Lett.* ***1968****, 20, 491.*

(215) *Barrett, S. E.; Tycko, R.; Pfeiffer, L. N.; West, K. W. Phys. Rev. Lett.* ***1994****, 72, 1368.*

(216) *Hermann, C.; Lampel, G.; Safarov, V. I. Ann. Phys. Fr.* ***1985****, 10, 1117.*

(217) Zeng, X.; Miron, E.; Wijngaarden, W. A. v.; Schreiber, D.; Happer, W. *Phys. Lett. A.* **1983**, *96*, 191.

Appendix A

Preparation and Assembly of Optical Pumping Apparatus

A.1 Surface Treatment

All glassware is treated with a siliconizing agent (e. g. SurfaSil, Pierce Scientific) to reduce ^{129}Xe wall relaxation.[217] The clean, dry glassware is rinsed several times with cyclohexane. A 10% solution of SurfaSil diluted with cyclohexane is then rinsed through the glassware several times. The glassware then may, but need not, be dried in a warm oven. The coating may be tested by adding a drop of water to the treated glassware. The water should not "wet" the surface at all, but should bead readily. This surface treatment is particularly important for the pumping cell itself, as a reduced relaxation time will substantially lower the accumulation of polarization. It should be noted that the surface coating can be damaged by excessive heat.

A.2 Addition of Rb

Rubidium, which is needed in both the rubidium and xenon sidearms of the pumping cell, cannot be transferred in air. However, the transfer can be easily accomplished in a glovebox. The surface-treated pumping apparatus is evacuated and then introduced along with a sealed ampoule of rubidium, a heat gun, disposable pipettes, and pipette bulbs into the glovebox. The ampoule is opened in this inert atmosphere and the heat gun is used to melt the rubidium. The stopcocks are removed from the pumping apparatus and a pipette is used to transfer the molten rubidium to the pumping cell. If the rubidium resolidifies in the pipette, the heat gun may be used to reheat the rubidium in the pipette. After a suitable amount of rubidium has been added to the cell (~0.5 cm^3 the rubidium sidearm and 1-2 cm^3 in the Xe sidearm) the stopcocks are returned to the apparatus and closed. Remaining rubidium may be transferred from the ampoule to a glass container with a stopcock and either be left in the glovebox for future transfers or removed.

After adding rubidium to the pumping cell, the inert gas which diffused into the cell from the glovebox must be removed. The apparatus is attached to a vacuum rack and carefully evacuated. Bubbles of gas may be trapped in the solidified rubidium, which will slowly degas over time. To prevent the introduction of this gas to future experiments, it is best to remove the gas bubbles. This is accomplished by closing the stopcock between the rubidium and the vacuum rack and melting the rubidium with a heat gun while tapping on the glass to release the gas. The rubidium is allowed to cool and the stopcock is opened. This procedure is repeated until the pressure gauge reads 10^{-5} torr. Finally, the rubidium is distilled into the pumping cell by briefly passing a gas torch over the rubidium sidearm. The rubidium will vaporize and a small amount will condense into the pumping cell. When done perfectly, the pumping cell will adopt a blue sheen, caused by the thin film of rubidium deposited on the glass.

This procedure must be undertaken with great care in order to prevent the rubidium from bumping over in large amounts to the pumping cell. Careful removal of the gas bubbles should help prevent this occurrence. The additional precaution of clamping the pumping cell at an angle such that the pumping cell is directly above the sidearm will prevent liquefied rubidium from falling into the pumping cell.

A.3 Addition of Xenon

Xenon is added by connecting either a bulb or tank of xenon to the apparatus. The apparatus is also connected to the vacuum rack and a pressure gauge. The entire system is evacuated to at least 4 x 10^{-5} torr in order to avoid contaminating the xenon source. The stopcock to the xenon sidearm is closed at this point and is immersed in a small dewar of liquid nitrogen. A small amount of xenon is released into a known volume of the apparatus, so the final pressure of xenon into the sidearm can be estimated. The valve to the xenon source is closed and the valve to the xenon side arm is opened to allow the xenon to condense. This procedure is repeated as often as necessary to obtain the desired pressure of xenon in the sidearm. The use of isotopically enriched ^{129}Xe is highly advantageous, mainly due to a depletion in ^{131}Xe, which cross relaxes effectively with ^{129}Xe.[155]

A.4 Assembly of Apparatus

The pieces of the apparatus, which consist of the pumping cell, a "T", a pressure gauge, connection to the sample, and connections to the vacuum rack are held together by ball and socket glass joints or ultratorr unions. The optical pumping apparatus is assembled one of two ways: a) beneath the superconducting magnet, with glassware connecting the pumping cell directly to the sample in the probe and b) on the laser table, with glassware connecting the pumping cell to a detachable sample which is

transported to the probe after addition of polarized xenon. In either case, a plexiglass oven is mounted to a small breadboard. The breadboard also holds a vertical rail which has clamps to support the glassware and mounts for the optics, to be discussed in detail in Appendix B. In case a, the breadboard fits between the supporting legs of the superconducting magnet. The pumping cell sits in the plexiglass oven. A copper-constantan thermocouple is placed between the oven and the pumping cell to monitor the temperature in the cell. The ball joints are lubricated with Apeizon grease and fastened to connecting sockets with aluminum spring clamps. The "T" connects the pumping cell to the glassware leading to the sample in the probe. One horizontal connection leads to the vacuum rack, which consists of a mechanical rough pump, capable of maintaining pressures of 10^{-4} torr and a silicone oil glass diffusion pump, capable of maintaining pressures of 10^{-6} torr. The other horizontal connection leads to the thermocouple pressure gauge, which measures pressures from 0.1 - 1000 torr. The connection here is 1/4" glass from the "T" connected to the 1/4" connector from the pressure transducer with a stainless steel ultratorr union. Additional support is provided to the pressure transducer by a clamp attached to the leg of the superconducting magnet. All glassware is securely clamped to the supporting rail, and connections are checked for stress. The oven is heated with a warm flow of nitrogen gas. The heater, which consists of nicrome wire sealed in glass tubing, is connected to a variac. If low temperature experiments are to be performed, the cooling apparatus is also assembled. The cooling apparatus consists of a copper heat exchanger which is connected to a N_2 supply and a dewared transfer line which leads to the dewared sample region. The heat exchange sits in a dewar of l-N_2. In case b, where the apparatus is assembled on the laser table, the breadboard is screwed onto the laser table using 1/4"-20 screws. The pressure gauge is usually attached to the vertical site of the "T" and the horizontal openings are attached to the vacuum rack and to a sample. A pair of Helmholtz coils is used to provide a 30 G magnetic field. The

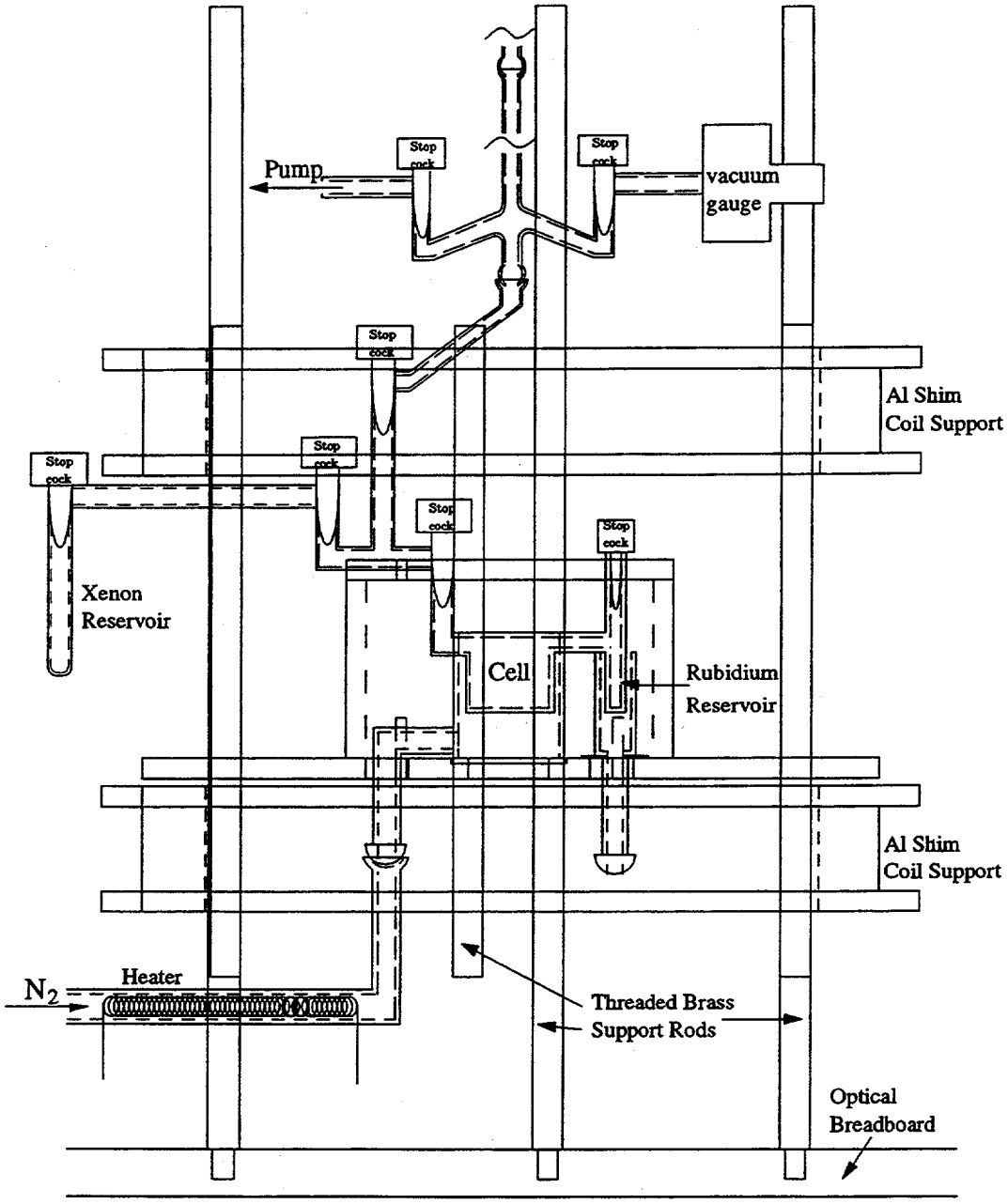

Figure A.1 Schematic of assembled optical pumping apparatus

sample either sits in another pair of Helmholtz coils or , when condensing the xenon into the sample region, a small permanent magnet is used to slow xenon relaxation.

A.5 Purification of Xenon

Before adding xenon to the pumping cell, it must be as pure as possible or else it will react with the rubidium vapor. Xenon loaded directly from the tank should be sufficiently pure; however, xenon recycled from a previous experiment may contain impurities from the sample. The method of purification is a freeze-pump-thaw cycle. The xenon is condensed into the sidearm and opened to the vacuum rack. The frozen xenon is allowed to evacuate to as low a pressure as possible. The stopcock is then closed and the heat gun is used to warm the sidearm while tapping on it gently . The rubidium should be visibly molten and jarring the sidearm a bit should expose fresh rubidium. The procedure should be repeated until the overpressure of the condensed xenon is 4×10^{-5} torr. This method sometimes leaves behind a whitish residue. When all the rubidium in the sidearm has reacted, it is necessary to remove the contaminated rubidium and add fresh rubidium in the glovebox.

A.6 The Pumping Experiment

The experiment begins by turning on the oven and allowing the cell to warm until the temperature reaches 70 - 80 °C. When this temperature is attained the optical resonance is found by the procedure described in Appendix B. The purified xenon may then be added to the cell. It is of course imperative that the stopcocks to the vacuum and sample are closed at this point. One can monitor the amount of xenon added

directly by leaving the stopcock to the pressure gauge open. Higher pressures of xenon may be loaded by leaving the stopcock to the pressure gauge closed. As long as the volumes are known, it is still possible to calculate the amount of xenon added. At this point, the xenon may quench the rubidium fluoresence if the xenon is insufficiently pure. If the fluoresence does not recover in 5 - 10 minutes, the oven must be cooled and the xenon recovered for additional purification. If the xenon is pure, often a visible purple glow may be observed! If the benchtop assembly is used, the magnet must be turned on. In either case, sample preparation (i.e. precooling) may be begun. The pumping is generally allowed to continue for 20 minutes. The cell should be monitored periodically because sometimes the Ti-Sapphire laser drifts. When sufficient pumping time has been allowed, the oven is turned off and allowed to cool to 40 °C. The stopcock to the vacuum must be closed (it is even worse to lose polarized xenon than freshly purified xenon!). The xenon may be added in aliquots by leaking a small amount from the cell. For high polarizations, 20 -30 dB of attentuation is required before the receiver on the gamma spectrometer. After the NMR experiments are finished, if necessary the sample is reattached to the glassware and the connecting area is evacuated. The sample is warmed enough to allow for xenon recovery. The xenon is condensed into the sidearm with liquid nitrogen and purified before the next experiment. Barring vacuum problems, as many as 4 - 6 runs can be accomplished in one day.

A.7 Troubleshooting

Sometimes, the xenon polarization is not as high as expected. There are several things to check if this is the case.

•*Is there rubidium in the cell?* Contaminants may have depleted the rubidium supply. If this is the case, more rubidium may be distilled over into the cell.

•*Is the xenon clean?* Although this problem would probably be noticed before the NMR detection part of the experiment, it can definitely contribute to poor polarization.

•*Was the magnet turned on during the experiment?* This is an easy thing to forget.

•*Was the laser aligned correctly? Was the power of the laser as high as expected? Did the laser stay on resonance for the entire experiment?* The treatment of the optics are discussed in Appendix B.

•*Did the polarized xenon actually reach the detection coil?* In the past, grease has occasionally plugged the glassware and prevented xenon from actually reaching the coil. Alternatively, stopcock leaks have occurred which can be detected upon xenon recovery.

Often not detecting high polarization is not a symptom that the optical pumping "isn't working." It can instead mean that the spectrometer is not correctly configured. Here is a checklist for common spectrometer errors.

Is the probe tuned? Is it connected to the receiver?

Is the amplifier turned on ?

Is the spectrometer configured correctly for ^{129}Xe detection? Is the frequency set correctly? Are pulses coming out of the spectrometer?

A.8 Redoing the Cell

If nothing at all seems to be wrong with the laser or spectrometer, and the xenon and rubidium are pure, but unsatisfactory signal enhancements persist, the cell may have to be "redone." This involves removing the xenon and rubidium currently stored in the

cell, reapplying a SurfaSil coating, and adding new rubidium and xenon. The used xenon is often stored in a bulb. If it seems pure, it can be readded to the cell. Otherwise, it is often stored in a bulb for use in sealed samples. Removing the rubidium is more tricky and, often, spectacular. The rubidium may be quenched by dripping water slowly into the cell which has been clamped into the hood. This reaction is violent and sparks and smoke are produced if there is any amount of unreacted rubidium in the cell. Alternatively, the entire cell may be plunged into a plastic tub may be filled with water. To slow the reaction, ethanol may be used instead of water and either solvent can be cooled.

Appendix B

Care of Lasers and Alignment of Optics

B.1 Laser Maintenance

B.1.1 General Cleaning Procedures

There are two established optic cleaning procedures. The first is the *drop and drag* technique. The optic to be cleaned is held in one hand and lens paper is gently laid across the optic. A drop of methanol or acetone is placed in the center of the lens paper. The lens paper should then be slowly dragged across the surface of the optic. The lens paper and optic should be dry before the drag is complete. The second is the *hemostat* technique. A lens tissue should be folded into a 1 cm wide strip. Do not touch the portion of the tissue that will be in contact with the optic. Fold this strip upon itself and grasp near the fold with the hemostat. Place a few drops of methanol on the fold and shake off the excess. Make a single wipe across the surface of the optic. With either method, do not reuse the lens paper as particles of dust picked up from the surface may scratch the optic.

B.1.2 Argon Ion Laser

The Ar+ laser has minimal maintenance requirements. Optics cleaning is not required as part of regular maintenance. Optics should only be cleaned as corrective action for marked power decrease or poor mode quality. The output mirror may need to be cleaned occasionally and the procedure is outlined quite clearly in the Coherent manual (pages 93 - 95.)

Occasionally the brewster window may become spotted with residue falling from the bellows. The symptoms of this problem are a continually dropping Ar+ laser power and failure of the power track to optimize the power levels. If this happens regularly, the bellows should be replaced by Coherent. In order to clean the window, the *electrical power should be turned off* and the Ar+ laser cover should be removed. The bellows should be slid gently back. Methanol should be used with high quality lens paper and a hemostat. One stroke should be made from top to bottom. If methanol does not successfully remove the spots, a harsher "etching" procedure should be used. A 10-12% ww ammonium bifluoride solution should be prepared. One drop should be placed on the window with a pipette and allowed to sit for 30 seconds. The drop should be removed with lens tissue. The window should be thoroughly rinsed with distilled water. No residual acid should remain! The window can also be subsequently cleaned with methanol. The bellows should be slid over the window carefully before recovering the laser.

Other very occasional maintenance issues include replacement of fuses located behind the fan in the laser power supply and replacement of the water filter.

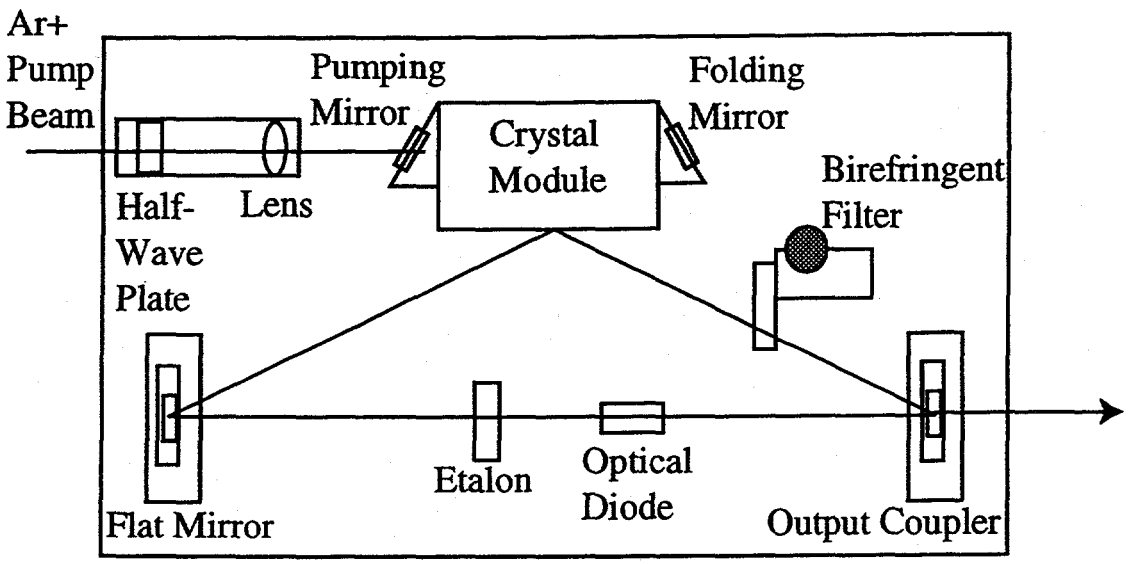

Figure B.1 Schematic of Titanium - Sapphire Laser

B.1.3 Titanium Sapphire Laser

The Ti-Sapphire laser requires much more attention to keep it operating properly. The crystal should be cleaned almost every day. This is accomplished using the hemostat and *methanol*. (Acetone should not be used since it will dissolve the adhesive which mounts the crystal!!) The crystal should be wiped once on each side along the direction of the crystal cut. A more detailed cleaning procedure should be performed approximately once every two weeks for optimal performance. The cleaning procedure is outlined below:

Birefringent Filter (BRF)

The silver knob should be unscrewed to release the BRF. The crystal face should be cleaned on both sides using the hemostat and either acetone or methanol. The BRF can then be remounted by rescrewing the large silver knob. The power should be optimized using the procedure described in Section B.3.

Etalon

The etalon should be unscrewed from its mount using 5/32" allen wrenches. Either the hemostat method or the drop and drag method can be used to clean the etalon. Methanol and not acetone should be used. After replacing the optic, the power should be optimized using the procedure described in Section B.3.

Optical Diode

The small plate should be removed and cleaned with the hemostat. The plate should then be returned and the power optimized using the procedure described in Section B.3. The cover on the magnet should be unscrewed using a 1/16" allen wrench. The cover and magnet should be removed. The crystal inside should be cleaned with the hemostat and either acetone or methanol. Take care to return the magnet with the same orientation. The power should be optimized using the procedure described in Section B.3.

Output Coupler

Turn the right hand knob's coarse adjustment clockwise 5 times to allow for removal of the lens holder. Unscrew the blue bevel. With lens tissue push out lens. Both sides of the lens should be cleaned with the drop and drag method. The lens should be reinserted with same side facing the crystal. (An arrow marked on the edge should always point to the crystal.) Screw the lens holder in quite tightly. Turn coarse knob counterclockwise 5 times. If the laser is not lasing, insert the beam height alignment tool (BHAT) as close to the flat mirror as possible. Center the beam reflected from the turning mirror on the center hole of the BHAT. Using the IR viewer to monitor the procedure, turn the coarse knobs of the output coupler until the beam reflected from the output coupler passes through the center hole of the BHAT. The reflected beam

should be "fuzzy" and about 1 cm in diameter. Remove the BHAT. If the laser is still not lasing, tape a business card to the exit port. Through the IR viewer one should be able to see two IR reflections on the business card. Use the coarse knobs of the output coupler to move the less intense spot into the more intense spot. When the two spots meet, lasing should occur and be immediately apparent when looking through the IR viewer. The power should be optimized using the procedure described in Section B.3.

Flat Mirror

This procedure is identical to the output coupler except that it is unnecessary to first turn the coarse knob in order to remove the lens holder. After cleaning and returning the lens, if lasing does not occur, follow the same realignment procedure outlined above. As always, optimize the power of the laser.

Pump Mirror and Folding Mirror

Use small allen wrenches to remove one of the optics. Clean both sides using drop and drag procedure. Reinsert lens with same angular orientation. Reoptimize power by gently turning allen wrenches. Repeat the procedure with the other mirror.

B.2 Operation of Lasers

The first step in the operation of the lasers is always to turn on the cooling water. In the case of the Ar+ laser, always open the exit valve before turning on the water in order not to risk bursting the plasma tube. The Ar+ laser has a built-in water meter which automatically turns off the laser if the water flow is too low. The Ti-Sapphire

laser cooling water has an external flow meter. The water should be turned on at such a rate that the bead makes about one revolution per second.

The Ar+ laser is switched on by turning the key on the power supply and pressing the on button on the control module. The laser should be allowed to warm up for about ten minutes before any adjustments are made.

In shutting down the lasers, the power button the control module of the Ar+ laser should be turned off. The water should be allowed to flow for approximately ten minutes (or until the exit pipe is cold to the touch). The water for the Ar+ valve should be shut off before the exit valve. The laser is ultimately shut off by turning the key on the power supply. The Ti-Sapphire cooling water should also be turned off.

B.3 Optimizing Power of Ti-Sapphire Laser

The power of the Ti-Sapphire laser is measured using the Coherent power meter. The power meter should be placed just outside the exit port of the Ti-Sapphire laser. The power can be optimized either at high setting or low setting of the Ar+ laser. The fine horizontal adjustment of the output coupler should be adjusted for maximum power. The procedure should be repeated with the fine horizontal adjustment of the flat mirror. Then the vertical fine adjustments of each mirror should be adjusted. This procedure should be repeated until no gain is observed. At 10 W of Ar+ power, the Ti-Sapphire should ideally produce 2.0 W; however, 1.5 W is probably a more realistic goal. If the power is considerably lower, the laser should be thoroughly cleaned. If cleaning does not restore the laser power, a call to Tom Kaffenberger of Schwartz Electro Optics is in order, as realignment of the laser may be called for.

B.4 Tuning the Laser

The laser is tuned by adjusting the BRF and the etalon. The BRF setting does not change very much and should be set near 537. With the oven at 70 - 80 °C and the laser beam directed through the cell, the BRF is rotated back and forth by about 90 °. If the resonance is not found, the knob on the etalon is adjusted by 1/4 turn and the BRF is again rotated. This procedure is continued until a bright green glow is apparent when viewing through the IR viewer. Scattered light is always visible in the cell and that should not be confused for "finding the line." The resonance should be very obvious: a slight turn of the BRF should completely detune the laser. It is as obvious as turning a light bulb off and on. The etalon can be turned slightly without detuning the laser, especially after the xenon has been loaded and the line is pressure-broadened.

The laser can also be tuned by mounting a photodetector beneath the optical pumping cell. The photodetector is connected to an oscilloscope. With the laser beam blocked, the oscilloscope should be zeroed. The scale should be adjusted so that when the beam is unblocked the oscilloscope trace remains on the screen. When the laser is on resonance, the laser light is absorbed and fewer photons are captured by the photodetector. If the laser light is completely absorbed, the oscilloscope should give a zero reading.

B.5 Aligning the Optics

When the optical pumping apparatus is assembled beneath the magnet, the laser beam must be steered across the room. *The entire alignment procedure should be undertaken with great care as the beam is invisible.* The Ti-Sapphire beam comes out

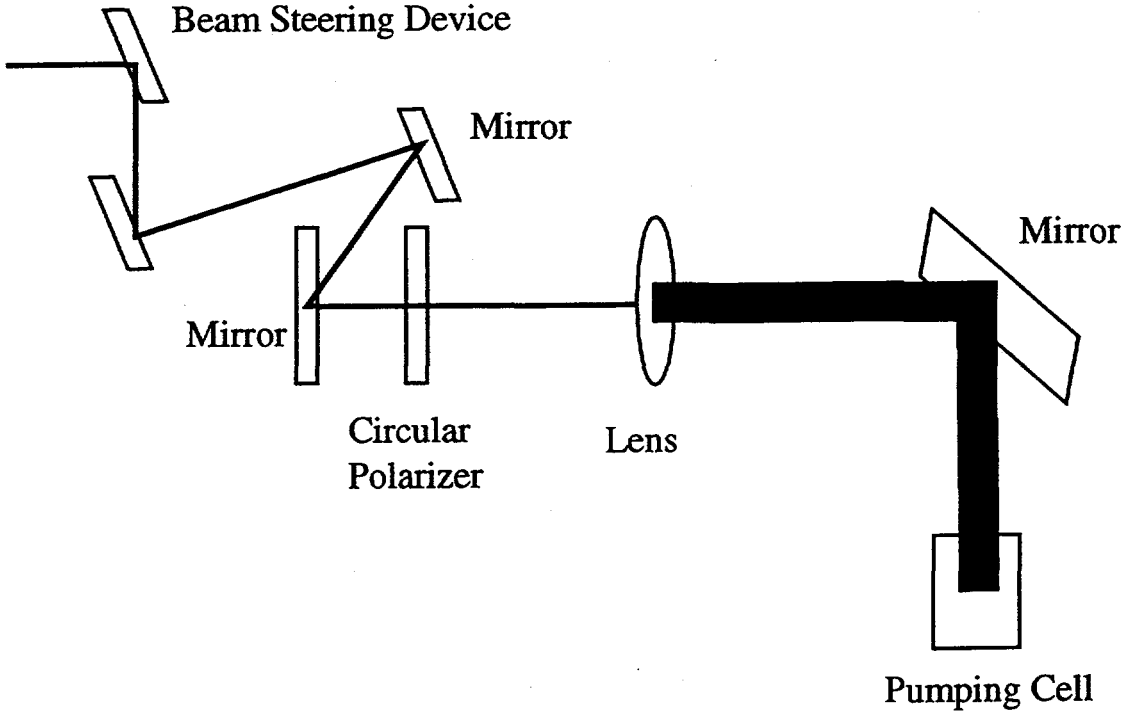

Figure B.2 Schematic of Optics for Beneath the Magnet Assembly.

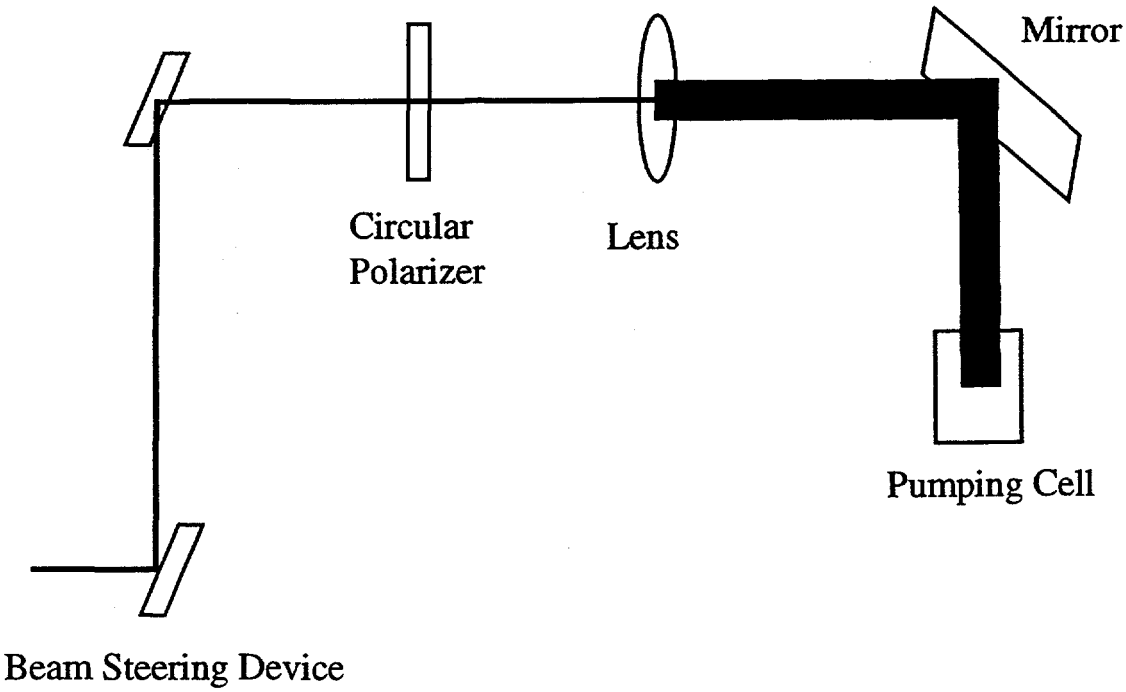

Figure B.3 Schematic of Optics for Benchtop Assembly.

of the laser and hits the beam steering device mounted on the end of the laser table. The beam steering device consists of two mirrors which can be used to change the height of the beam as well as its direction. The top mirror is adjusted so that the beam hits the center of the bottom mirror. The bottom mirror is adjusted so that the beam hits the first mirror mounted to breadboard. This mirror is in turn adjusted so that the beam hits the second mirror on the breadboard. The beam then passed through a $\lambda/4$ and perhaps a lens. A final mirror mounted above the pumping cell turns steers the beam through the cell. The beam should be adjusted so that the beam illuminates as much of the cell as possible. Additionally, the beam should travel parallel to the magnetic field.

When the optical pumping apparatus is mounted to the laser table, the alignment procedure is similar. The beam steering device is still used; however, the beam travels directly to the $\lambda/4$ with no intervening mirrors.

B.6 Adjusting the Circular Polarization

The circular polarization may be monitored by inserting a linear polarizer behind the circular polarizer. If the light is truly circularly polarized, adjusting the linear polarizer should have no effect on the output. The output can be monitored with a power meter or with the photodetector connected to an oscilloscope. The setting on the circular polarizer is systematically varied, and subsequently monitored by adjusting the linear polarizer. When there is very little or no change in the output power, the circular polarizer is set correctly.